Development of Zn(II) Complexes for Efficient Triplet Emission

Thesis

for obtaining the academic degree of Doctor of the Natural Sciences (Dr. rer. nat.)

from the Faculty of Chemistry and Chemical Biology
of the Technical University of Dortmund

submitted by
Mousree Mitra, M. Sc.
from Krishnagar, India

Dortmund, 2026

Submitted to the Faculty of Chemistry and Chemical Biology on: May 22, 2026

Reviewer of the written thesis:

1. Reviewer: Prof. Dr. Andreas Steffen

2. Reviewer: Prof. Dr. Sebastian Henke

Examiners of the public doctoral colloquium:

1. Examiner: Prof. Dr. Andreas Steffen

2. Examiner: Prof. Dr. Sebastian Henke

Chairman of the Examination Board:

Day of the public doctoral colloquium:

To My Family

আমরা যা দেখি, যা অনুভব করি,

পুরোটাই কেবল স্বপ্নের ভেতর আরেকটা স্বপ্ন মাত্র!

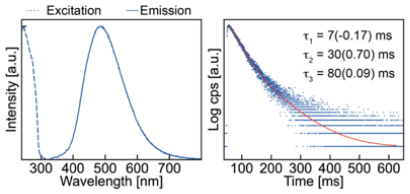
All that we see or seem, is but a dream within a dream.

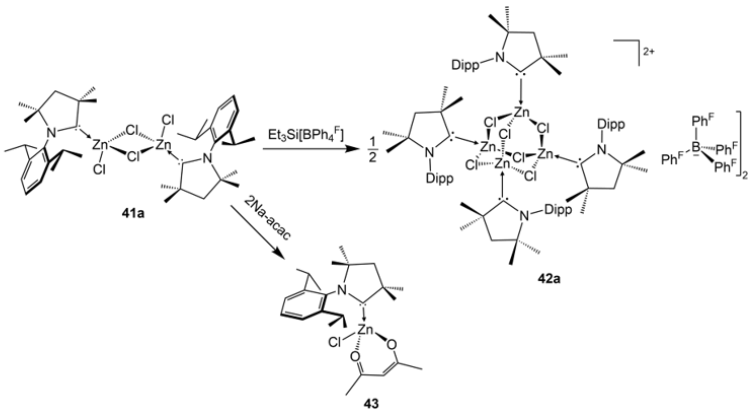
- Edgar Allan Poe

Abstract

In the recent past, luminophores based on zinc(II) have gained increasing attention as a promising alternative to expensive 4d and 5d metal-based luminophores due to its abundant availability, cost-effectiveness, and stable d^{10} electron configuration. Despite these advantages, the number of literature-known zinc(II) luminescent complexes that involve emission from triplet excited states is very limited.[1,2] Recent studies on cyclic (alkyl)(amino) carbene (cAAC) complexes of zinc(II) halides demonstrate ultra-long phosphorescence associated with LLCT states.[3] However, these complexes undergo fast photo-induced transformations under continuous high-energy UV irradiation at room temperature, which are linked to asymmetric rotation of the carbene ligand and photo-chemical transformations such as halide dissociation.

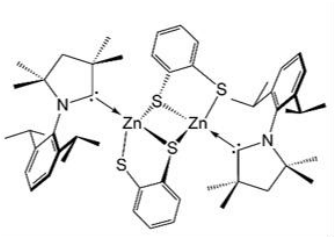
This doctoral thesis focuses on the chemical modification of cAAC-based zinc halide complexes, such as $[Zn_2Cl_4(^{Me}cAAC)_2]$ (**41a**), to improve photostability and modulate their photophysical properties through halide abstraction and halide exchange routes. Halide abstraction from **41a** using a triethylsilylium-like reagent, $[Et_3Si][B(C_6F_5)_4]$, results in the formation of a stable tetrameric cluster $[(^{Me}cAAC)_4Zn(\mu\text{-}Cl)_6][B(C_6F_5)_4]_2$ (**42a**), while treatment with acetylacetonate or related congeners yields a monomeric complex of the type $[(^{Me}cAAC)Zn(acac)(Cl)]$ (**43**). Both new structural motifs exhibit phosphorescence, but, more importantly, their photostability is significantly improved compared to the starting dimeric structure. These promising results highlight the high structural versatility and tunability of the photophysical properties of rare phosphorescent zinc(II) complexes based on cAAC chromophore ligands.



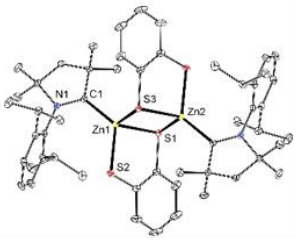


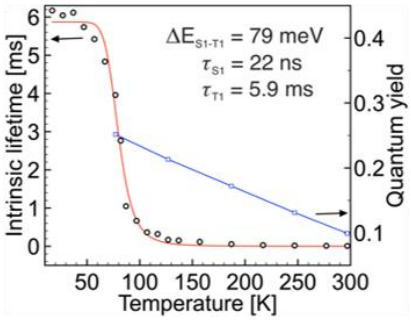
In the second project, an electron-rich dithiophenolate ligand (benzene-1,2-dithiolate) was employed to synthesize the dimeric $[(^{Me}cAAC)_2Zn_2(bdt)_2]$ (**45**), where the dithiophenolate ligand coordinates to the metal center in a bridging mode, providing high stability toward air and moisture.[4] The complex exhibits visible light emission when incorporated into polymer matrices, with a very high radiative rate constant of 1.5×10^5 s^{-1}. Variable-temperature lifetime measurements reveal TADF emission with a small singlet-triplet energy gap, $\Delta E_{(S_1-T_1)}$= 79 meV. The long-lived excited state was also explored for its potential in Dexter energy transfer, and it was found to be faster than the standard $[Ru(bpy)_3]^{2+}$ in the photo-isomerization of E-stilbene. Although the major disadvantage of this complex lies in its weak photo-

efficiency, with the highest value of photoluminescence quantum yield being only 0.10 in a PMMA matrix, it still shows potential for further optimization.



45

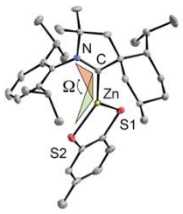




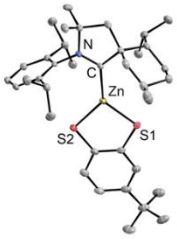
To overcome the drawbacks of the previous dimeric Zn(II)-bridged dithiophenolate complex, sterically more demanding menthyl-substituted cAAC ligands were employed to synthesize the next generation of zinc(II) TADF emitters, referred to as **CZT**s (carbene-zinc-thiolate).[5] The **CZT**s exhibit bright yellow-orange luminescence in the solid state, with photo-efficiency enhanced by 6-15 times compared to the previous dimer. Additionally, structural control over the excited-state properties of **CZT**s is achieved by isolating different polymorphs of **CZT3**. Detailed photophysical studies and quantum mechanical calculations reveal that the dihedral angle (Ω) between the carbene and the S-Zn-S unit controls the relative rates of k_{ISC} and k_{rISC}, thus influencing the TADF efficiency. The tilted conformation (Ω= 33-36°) in **CZT3** is found to be the most efficient orientation, leading to a radiative rate constant (k_r) of up to 1.2×10^6 s^{-1} at room temperature — a record value for zinc(II)-based emitters, even competitive with well-established rare-metal-based emitters.



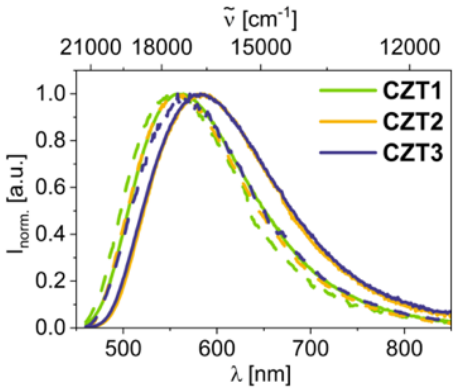
CZT1
Ω = 45.0°



CZT2
Ω = 54.3 and 59.2°



CZT3a
Ω = 6.4-43.1°
CZT3b
Ω = 29.9 and 36.2°



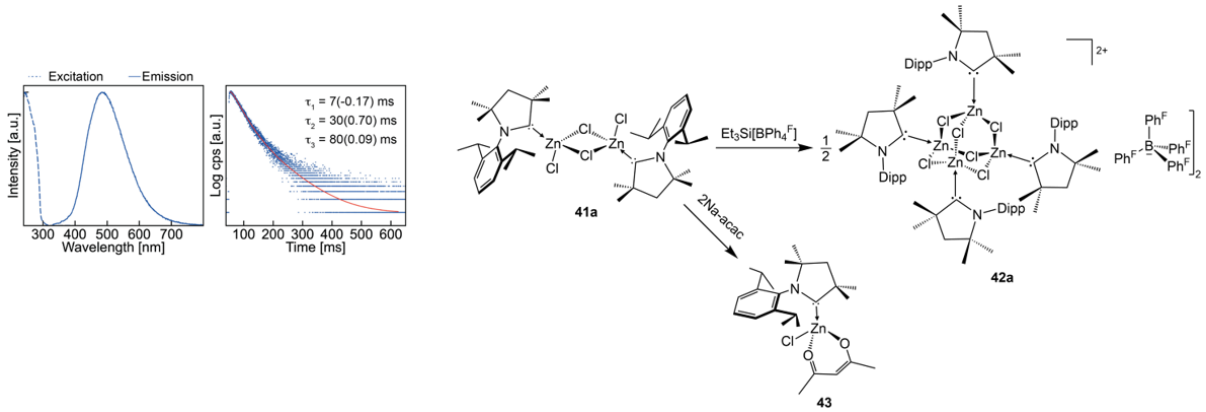


The next work presents a systematic development of Zn(II)-based carbene–thiolate complexes as efficient thermally activated delayed fluorescence (TADF) emitters using rigid bicyclic (BicAAC) ligands. Structural tuning from monomeric to dimeric architectures enables control over geometry, rigidity, and ligand-to-ligand charge transfer (LLCT) excited states. The complexes exhibit weak emission in solution but show near-unity quantum yield (Φ_{PL} up to 0.9) in the solid state due to suppressed non-radiative decay. Temperature- and environment-dependent studies confirm efficient TADF governed by small singlet–triplet energy gaps and optimal dihedral angles.

Zusammenfassung

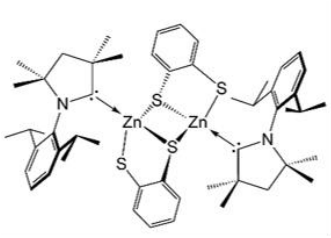
In jüngster Zeit haben Luminophore auf der Basis von Zink(II) als vielversprechende Alternative zu teuren Luminophoren auf 4d- und 5d-Metallbasis zunehmend an Aufmerksamkeit gewonnen, da sie reichlich verfügbar und kostengünstig sind und eine stabile d^{10}-Elektronenkonfiguration aufweisen. Trotz dieser Vorteile ist die Zahl der in der Literatur bekannten lumineszierenden Zn(II)-Komplexe, bei denen die Emission aus angeregten Triplett-Zuständen erfolgt, sehr begrenzt[1,2]. Jüngste Studien über zyklische (Alkyl)(Amino) Carben (cAAC)-Komplexe von Zn(II)-Halogeniden zeigen eine ultralange Phosphoreszenz in Verbindung mit LLCT-Zuständen.[3] Diese Komplexe erfahren jedoch unter kontinuierlicher hochenergetischer UV-Bestrahlung bei Raumtemperatur schnelle photoinduzierte Umwandlungen, die mit einer asymmetrischen Rotation des Carbenliganden und photochemischen Umwandlungen wie der Dissoziation des Halogenids verbunden sind.

Diese Doktorarbeit befasst sich mit der chemischen Modifizierung von Zinkhalogenidkomplexen auf cAAC-Basis, wie z. B. $[Zn_2Cl_4(^{Me}cAAC)_2]$ (**41a**), um die Photostabilität zu verbessern und ihre photophysikalischen Eigenschaften durch Halogenidabstraktion und Halogenidaustausch zu modulieren. Die Halogenidabstraktion von **41a** mit einem Triethylsilylium-ähnlichen Reagenz, $[Et_3Si][B(C_6F_5)_4]$, führt zur Bildung eines stabilen tetrameren Clusters $[(^{Me}cAAC)_4Zn(\mu\text{-}Cl)_6][B(C_6F_5)_4]_2$ (**42a**), während die Behandlung mit Acetylacetonat oder verwandten Kongeneren einen monomeren Komplex vom Typ $[(^{Me}cAAC)Zn(acac)(Cl)]$ (**43**) ergibt. Beide neuen Strukturmotive zeigen Phosphoreszenz, aber, was noch wichtiger ist, ihre Photostabilität ist im Vergleich zur dimeren Ausgangsstruktur deutlich verbessert. Diese vielversprechenden Ergebnisse unterstreichen die große strukturelle Vielseitigkeit und Abstimmbarkeit der photophysikalischen Eigenschaften seltener phosphoreszierender Zn(II)-Komplexe auf der Basis von cAAC-Chromophorliganden.

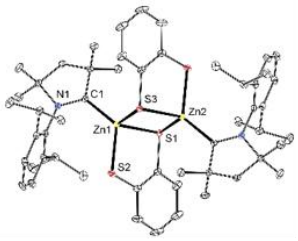


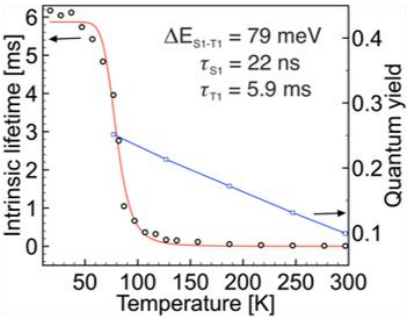
Im zweiten Projekt wurde ein elektronenreicher Dithiophenolat-Ligand verwendet, um einen dimeren Zink(II)-Carben-Komplex (**45**) zu synthetisieren, bei dem der Dithiophenolat-Ligand das Metallzentrum verbrückend koordiniert und eine hohe Stabilität gegenüber Luft und Feuchtigkeit aufweist.[4] Der Komplex emittiert sichtbares Licht, wenn er in Polymermatrizen eingebaut wird, mit einer sehr hohen Strahlungsgeschwindigkeit von 1.5×10^5 s^{-1}. Messungen der Lebensdauer bei variabler Temperatur zeigen eine TADF-Emission mit einer kleinen Singulett-Triplett-Energielücke, $\Delta E_{(S_1-T_1)}$= 79 meV. Der langlebige angeregte Zustand wurde auch auf sein Potenzial für den Dexter-Energietransfer hin

untersucht, und es zeigte sich, dass er bei der Photoisomerisierung von E-Stilben schneller ist als das Standard-$[Ru(bpy)_3]^{2+}$. Obwohl der größte Nachteil dieses Komplexes in seiner schwachen Photo-Effizienz liegt - der höchste Wert betrug nur 0,10 in einer PMMA-Matrix, zeigt er dennoch Potenzial für weitere Optimierungen.

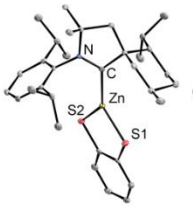


45

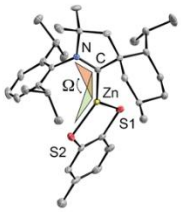




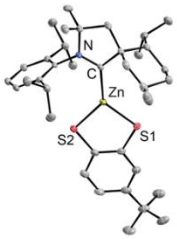
Um die Nachteile des früheren dimeren Zn(II)-verbrückten Dithiophenolat-Komplexes zu überwinden, wurden sterisch sperrige Menthyl-substituierte CAAC-Liganden verwendet, um die nächste Generation von zink(II)-TaDF-Emittern zu synthetisieren, die als **CZT**s (Carben-Zink-Thiolat) bezeichnet werden.[5] Die **CZT**s zeigen im festen Zustand eine leuchtend gelb-orange Lumineszenz mit einer um das 6- bis 15-fache gesteigerten Photo-Effizienz im Vergleich zum vorherigen Dimer. Durch die Isolierung verschiedener Polymorphe von **CZT3** lassen sich die Eigenschaften der **CZT** im angeregten Zustand strukturell kontrollieren. Detaillierte photophysikalische Studien und quantenmechanische Berechnungen zeigen, dass der Flächenwinkel (Ω) zwischen dem Carben und der S-Zn-S-Einheit die relativen Raten von k_{ISC} und k_{rISC} steuert und somit die TADF-Effizienz beeinflusst. Die geneigte Konformation (Ω= 33-36°) in **CZT3** erweist sich als die effizienteste Orientierung, die zu einer Strahlungsgeschwindigkeitskonstante (k_r) von bis zu 1.2×10^6 s^{-1} bei Raumtemperatur führt - ein Rekordwert für Zn(II)-basierte Emitter, der sogar mit etablierten Seltenmetall-Emittern konkurriert.



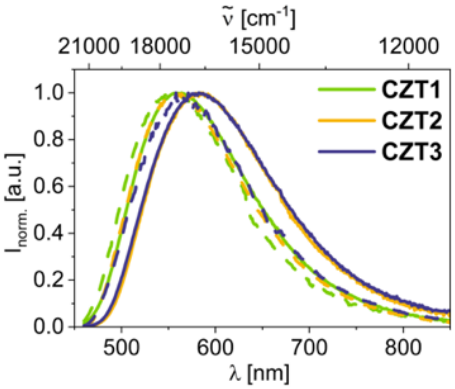
CZT1
Ω = 45.0°



CZT2
Ω = 54.3 and 59.2°



CZT3a
Ω = 6.4-43.1°
CZT3b
Ω = 29.9 and 36.2°





Die vorliegende Arbeit präsentiert eine systematische Entwicklung von Zn(II)-basierten Carben-Thiolat-Komplexen als effiziente Emitter für thermisch aktivierte verzögerte Fluoreszenz (TADF) unter Verwendung starrer bizyklischer (BicAAC) Liganden. Die strukturelle Anpassung von monomeren zu dimeren Architekturen ermöglicht die Steuerung von Geometrie, Steifigkeit und den durch Liganden-zu-Liganden-Ladungstransfer (LLCT) angeregten Zuständen. Die Komplexe zeigen in Lösung eine schwache Emission, weisen jedoch im festen Zustand aufgrund des unterdrückten nichtstrahlenden Zerfalls eine Quantenausbeute nahe Eins (Φ_{PL} bis zu 0,9) auf. Temperatur- und umgebungsabhängige Untersuchungen bestätigen eine effiziente TADF, die durch kleine Singulett-Triplett-Energielücken und optimale Diederwinkel bestimmt wird.

Complete List of Publications

Excerpts of this work have already been published in journals and at conferences.

Structural Control of Highly Efficient Thermally Activated Delayed Fluorescence in Carbene Zinc (II) Dithiolates

M. Mitra[#], O. Mrózek[#], M. Putscher, J. Guhl, B. Hupp, A. Belyaev, C. M. Marian, A. Steffen, *Angew. Chem. Int. Ed.* **2024**, *63*, e202316300.

Enhanced Intersystem Crossing, Yet Still Fluorescence Upon Introduction of Intermediate Charge-Transfer States in Hemicaged [Zn(bpy)3]2+

J. Kuhnt, M. Mitra, S. Maity, B. Hupp, C. M. Marian, A. Steffen, *J. Phys. Chem. Lett.* **2024**, *15*, 6409-6414.

An Air-and Moisture-stable Zinc (II) Carbene Dithiolate Dimer Showing Fast Thermally Activated Delayed Fluorescence and Dexter Energy Transfer Catalysis

O. Mrózek, M. Mitra, B. Hupp, A. Belyaev, N. Lüdtke, D. Wagner, C. Wang, O. Wenger, C. M. Marian, A. Steffen, *Chem.−Eur. J.* **2023**, e202203980.

Carbazolophane Enhances the Efficiency of Thermally Activated Delayed Fluorescence in Carbene Coinage Metal Amides

I. Sen, O. Mrózek, M. Mitra, A. Belyaev, C. Si, E. Zysman Colman, J. Seibert, S. Bräse, A. Steffen, *chemrxiv*. **2023**.

Ultra-Long Lived Luminescent Triplet Excited States in Cyclic (Alkyl)(amino)carbene Complexes of Zn (II) Halides

O. Mrózek, M. Gernert, A. Belyaev, M. Mitra, L. Janiak, C. M. Marian, A. Steffen, *Chem. Eur. J.* **2022**, *28*, e202201114.

Synthesis, structural characterization and rigidity dependent dual phosphorescence behavior of high-energy phosphorescent zinc(II) cyclic(alkyl)(amino)carbene complex

M. Mitra, O. Mrózek, A. Belyaev, L. Janiak, C. M. Marian, A. Steffen, *Dalton Trans.*, **2026**, *55*, 5519.

Photoactive Zn(II)-cAAC Complexes on the Rise

M. Mitra, O. Mrózek, A. Steffen, *17. Koordinationschemie-Treffen*, Jena, Presentation.

Strategic Modification of Donor-acceptor Motifs in Zn(II) Triplet Emitters

M. Mitra, O. Mrózek, A. Steffen, *Ligand design workshop*, Cologne, Presentation.

List of abbreviations

A	Acceptor	**MC**	*Metal centered*
ac	*avoided crossing*	**mCP**	9-(3-Carbazol-9-ylphenyl)carbazole
acac	acetylacetonate	**Me**	Methyl
BINAP	2,2'-Bis(diphenylphosphino)-1,1'-binaphthyl	**Menth**	Menthyl
^{t}Bu	*tert*-Butyl	**MLCT**	*Metal to ligand charge transfer*
cAAC	Cyclic Alkyl(amino)carbene	**n.d.**	Not detected
cAArC	Cyclic Amino(aryl)carbene	**NIR**	Near-infrared
CMA	Carbene-Metal-Amide	**NHC**	N-heterocyclic carbene
Cp	cyclopentadienyl	**NMR**	Nuclear magnetic resonance
CPL	Circular Polarised Luminescence	**OLED**	*Organic light emitting diode*
CT	*charge transfer*	**PES**	Potential energy surface
cz	Carbazolate	**Ph**	Phenyl
CZT	Carbene-Zinc-Thiolate	**PL**	photoluminescence
D	Donor	**PMMA**	polymethylmethylacrylate
DAC	Diamidocarbene	**^{i}Pr**	*iso*-propyl
DCM	Dichloromethane	**PS**	Polystyrene
DFT	Density Functional Theory	**RT**	Room temperature
Dipp	2,6-Di-iso-propylphenyl	**S_0**	Singlet ground state
EL	Electroluminescence	**SOC**	Spin orbit coupling
EQE	External Quantum Yield	**SOCME**	*spin-orbit coupling matrix element*
Et	Ethyl	**TADF**	*Thermally activated delayed fluorescence*
FCWD	FRANCK-CONDON-*weighted density of states*	**TD**	*Time dependant*
eqv.	equivalent	**THF**	Tetrahydrofuran
et al.	(lat.) *et alii*, and others	**Vide supra**	(lat.) see above
HOMO	*highest occupied molecular orbital*	**Vis**	Visible
IC	*Internal Conversion*	**VR**	Vibrational relaxation
ILCT	*Intra-ligand charge transfer*	**XLCT**	*Halide to ligand charge transfer*
ISC	*Inter system crossing*	**Z_{eff}**	Effective nuclear charge
K	Rate constant	**ZFS**	Zero-field splitting
LC	*Ligand-centered*		
LLCT	Ligand to ligand charge transfer		
LUMO	*lowest occupied molecular orbital*		

Table of Contents

1 Introduction 1

1.1 General Photo-physical Processes 1

1.2 Intersystem Crossing 2

1.3 Phosphorescence 5

1.4 Emitters based on 4d- and 5d- metal Complexes 6

1.5 Thermally Activated Delayed Fluorescence 9

1.6 Emitters based on 3d-metal Complexes 12

1.9 Objective of this Thesis 29

2 Result and Discussion 31

2.1 Synthesis, structural characterization and rigidity dependent dual phosphorescence behavior of high-energy phosphorescent zinc(ii) cyclic (alkyl)(amino)carbene complexes 31

2.2 An Air- and Moisture-stable Zinc(II) Carbene Dithiolate Dimer Showing Fast Thermally Activated Delayed Fluorescence and Dexter Energy Transfer Catalysis 49

2.3 Structural Control of Highly Efficient Thermally Activated Delayed Fluorescence in Carbene Zinc(II) Dithiolates 63

2.4 TADF Zn(II) Bicyclic(Alkyl)(Amino)Carbene Thiolate Complexes with Near-Unity Quantum Yield 78

2.5 Discussion 90

3 Summary and Outlook 99

4 References 102

5 Appendix 107

5.1 Supporting information for chapter 2.1 (Synthesis, structural characterization and rigidity dependent dual phosphorescence behavior of high-energy phosphorescent zinc(ii) cyclic (alkyl)(amino)carbene complexes) 107

5.2 Supporting information for chapter 2.2 (An Air- and Moisture-stable Zinc(II) Carbene Dithiolate Dimer Showing Fast Thermally Activated Delayed Fluorescence and Dexter Energy Trans fer Catalysis) 130

5.3 Supporting information for chapter 2.3 (Structural Control of Highly Efficient Thermally Activated Delayed Fluorescence in Carbene Zinc(II) Dithiolates) 159

5.4 Supporting Information for TADF Zn(II) Bicyclic(Alkyl)(Amino)Carbene Thiolate Complexes with Near-Unity Quantum Yield 195

1 Introduction

Photoactive transition metal complexes are of significant interest due to their diverse applications in fields such as organic light-emitting diodes (OLEDs),[6] photocatalysis (including energy and electron transfer),[7] dye-sensitized solar cells,[8] imaging,[9] and photodynamic therapy.[10] Despite the limited availability of 4d and 5d transition metals, complexes containing these metals are predominantly used in the aforementioned applications.[11] While considerable advancements have been made in developing first-row transition metal complexes such as Cr(0/III),[12] Mn(I),[13] Fe(II/III),[14] Co(III),[15] Ni(II),[16] and Cu(I)[62]—which exhibit remarkable photophysical properties, the search for earth-abundant alternatives to precious metal complexes continues to challenge researchers. Gaining a deeper understanding of luminescence phenomena and the excited state behaviour of 3d metal complexes, along with strategic modifications to their ligand spheres, has led to various research avenues aimed at competing with rare-earth metals. Among these, d^{10} copper(I) complexes stand out as promising candidates for use as triplet emitters in OLEDs, showcasing significant potential.[16] However, the exploration of isoelectronic zinc(II) complexes as efficient triplet emitters remains limited.[1, 2] This limitation arises primarily from zinc's high ionization potential, which hinders the formation of metal-to-ligand charge transfer (MLCT) states that are essential for facilitating efficient spin-orbit coupling (SOC) to generate triplet excitons. In the following chapters, we will discuss the relevant design criteria and photophysical properties necessary for enhancing the performance of zinc(II)-based complexes as triplet emitters. By addressing these challenges, we aim to unlock the potential of zinc(II) complexes in photonic applications and further contribute to the development of sustainable alternatives to precious metal-based systems.

1.1 General Photo-physical Processes

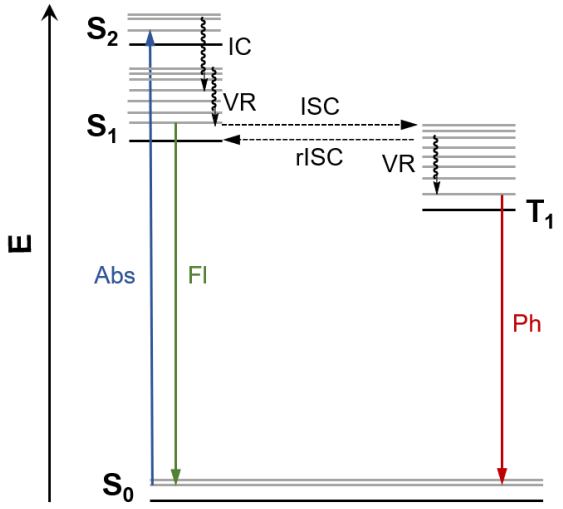


Figure 1. Simplified Jablonski diagram showing processes followed by absorption (Abs) of photon and corresponding radiative and non-radiative processes (Fl - fluorescence, Ph- phosphorescence, IC - internal conversion, VR - vibrational relaxation, ISC - intersystem crossing, rISC - reverse intersystem crossing). Created based on reference [17].

Photophysics encompasses the study of the interaction between light and matter, elucidating how molecular systems respond to electromagnetic radiation. The general photophysical processes can be visually represented using a Jablonski diagram (**Figure 1**).

At the core of these processes is the absorption of light by a molecule, which excites the system from its ground state (S_0) to a higher singlet excited state (S_n). This excitation is typically followed by vibrational relaxation (VR), where the excited molecule loses excess vibrational energy and settles into the lowest vibrational level of the first excited singlet state (S_1). Subsequently, internal conversion (IC) may occur, allowing for a transition between different electronic states of the same spin multiplicity. This sequence of events is crucial for understanding various photophysical phenomena, including fluorescence, phosphorescence, and non-radiative decay processes.

From the S_1 state, various radiative and non-radiative processes can occur, influenced by the energy gap between the S_1 and S_0 states. When there is a large energy barrier between these states, internal conversion (IC) to the ground state becomes improbable due to negligible coupling, which corresponds to a small Franck-Condon (FC) overlap for the transition between them. In such cases, fluorescence is favored. Since the spin multiplicity is conserved during fluorescence, this process occurs relatively quickly, typically on a timescale of 10^{-9}-10^{-7} seconds. Alternatively, a triplet state (T_n) can be populated via intersystem crossing (ISC) from an excited singlet state. This pathway provides an alternative to IC or fluorescence. Once in the triplet state, ISC can occur again to transition back to a singlet state, followed by either radiationless transitions or phosphorescence. It is important to note that the relaxation from the triplet state to the ground state involves a change in spin multiplicity, making it a spin-forbidden process. As a result, this transition occurs more slowly than fluorescence, typically on a timescale of microseconds to milliseconds (μs to ms).

1.2 Intersystem Crossing

Spin-orbit Coupling

Spin-orbit coupling (SOC) is a critical factor in the photophysics and photochemistry of organic and transition metal (TM) complexes, as the efficiency of spin-forbidden processes—such as intersystem crossing (ISC) and phosphorescence—depends on the effectiveness of SOC in rendering these transitions spin-allowed. Spin-forbidden transitions involve a change between electronic states with different spin multiplicities, which, in principle, would violate the conservation of angular momentum.[18] However, conservation can still occur if there is a simultaneous change in orbital angular momentum along with the change in spin angular momentum. In this context, SOC acts as a relativistic effect that influences both orbital and spin angular momentum, enabling the mixing of these degrees of freedom and facilitating coupling between electronic states of differing multiplicities.Within the framework of the one-center approximation, the degree of SOC can be mathematically expressed using the SOC operator, as represented in **Equation 1**.[19] This operator quantifies the strength of coupling between electronic states, providing insights into how SOC enhances the likelihood of transitions that would otherwise be spin-forbidden.

$$\hat{H}_{SO}^{eff} = \frac{1}{2m_e^2c^2}\sum_I \sum_i \frac{z_I^{eff}}{r_{iI}^3}\hat{l}_i\hat{s}_i \quad (\mathbf{1})$$

Where $\hat{l}_i$ is the orbital angular momentum operator, $\hat{s}_i$ is the spin angular momentum operator of electron *i*, z_I^{eff} and r_{iI}^3 is respectively atom's effective nuclear charge and distance of *i* electron from the nucleus. The later two factors along with the other constants can be combined to the atom specific spin-orbit coupling constant, $\zeta_c = \frac{z_I^{eff}}{2m_e^2c^2r_{iI}^3}$. Thus, SOC mediated by 4d or 5d metals outperforms the lighter elements owing their higher effective nuclear charge. This so-called heavy atom effect significantly improves ISC allowing triplet population either by participating directly in the transition or externally. This leads to a rough approximation of the dependence of spin-orbit coupling (SOC) and, consequently, intersystem crossing (ISC) on the heavy atom effect, while excluding the nature of the orbitals involved in the transition. The influence of the electronic transition's nature on the rate of ISC can be described by El-Sayed's rules, which state that "the rate of intersystem crossing, such as from the lowest singlet state to the triplet manifold, is relatively large if the radiationless transition involves a change of molecular orbital type."[20] In simpler terms, to conserve total angular momentum during ISC, the nature of the orbitals involved must change to accommodate the spin reversal. This principle can be illustrated using simple organic chromophores that contain nitrogen or oxygen as heteroatoms. For instance, in acetone, the transition between the $^1n\pi^*$ and $^3\pi\pi^*$ states is allowed. The rate of ISC is higher in this case because the change in spin multiplicity is accompanied by a change in the nature of the orbitals involved, specifically in their orbital angular momentum, thus conserving total angular momentum. El-Sayed's rules also find applicability in organometallic complexes to explain SOC, as observed in the metal-to-ligand charge transfer (MLCT) states of Au(I) and Cu(I) complexes. [21] Interestingly, the SOC for Cu(I) complexes can sometimes exceed that of Au(I) complexes, despite the latter's heavier atomic nature. This discrepancy can be attributed to the involvement of the metal's d_π orbitals in MLCT states, which are less accessible in Au(I) complexes due to larger crystal field splitting. However, it is important to note that El-Sayed's rules are based on purely electronic transitions within the framework of the Born-Oppenheimer approximation. This approach loses its validity when mixing occurs between different states, particularly when vibronic transitions accelerate ISC. In such cases, the influence of vibrational modes can significantly enhance the coupling between states, complicating the straightforward application of El-Sayed's rules. The effect of SOC on intersystem crossing (ISC) is apparent when applying Fermi's Golden Rule (**Equation 2**), which links transition rates to the matrix element of the perturbation (SOC) and the density of final states (DOS).[18]

$$k_{ISC}^{nm} = \frac{2\pi}{h}\langle S_m|\hat{H}_{SOC}|T_n\rangle^2 . FCWD \quad (\mathbf{2})$$

The rate constant of ISC is influenced by two primary factors: SOC between the S_m and T_n states, and the Franck-Condon weighted density of states (FCWD). The FCWD refers to the density of lower-energy states that are energetically accessible to the system from the initial (higher-energy) state. A higher FCWD corresponds to a larger number of energetically available states that can couple with the initial excited state, increasing the transition rate. Together, the SOC and FCWD determine the overall transition rate by influencing both the electronic and vibrational coupling mechanisms. The rate constant

increases with stronger SOC and higher FCWD, which together enhance the transition probability between the S_m and T_n states. 3d metals and organic molecules often exhibit weak or negligible spin-orbit coupling (SOC). In these cases, other mechanisms are responsible for promoting efficient intersystem crossing (ISC), indicating that SOC is not the sole factor facilitating coupling between electronic states.

Spin-vibronic Coupling

The application of **Equation (1)** with a one-center approximation to determine SOC, along with El-Sayed's rules, is limited to specific nuclear configurations and assumes that nuclear motion does not significantly influence electronic transitions. The Born-Oppenheimer approximation underpins this approach, positing that electron dynamics occur on a much shorter timescale than nuclear movements.[22] This assumption allows for the separation of the nuclear contribution (encompassing vibrational and rotational degrees of freedom) from the electronic contribution to the molecular wavefunction. Consequently, in this framework, the nuclear motion does not interact with the electronic states. However, when the timescales of nuclear and electronic motions converge, the Born-Oppenheimer approximation breaks down.[23] This breakdown allows the nuclear part to meaningfully contribute to the molecular wavefunction, leading to a coupling between electronic and vibrational degrees of freedom—termed spin-vibronic coupling. This interaction can facilitate the coupling of electronic states and promote ISC.

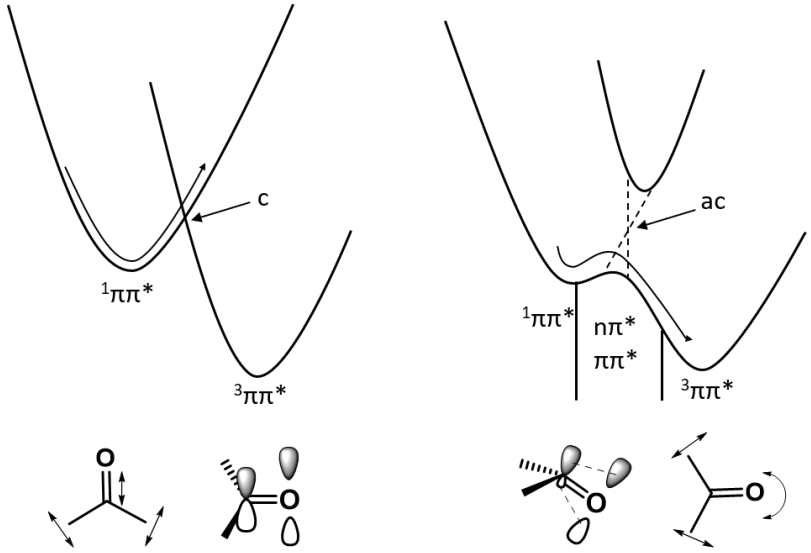


Figure 2. Spin-vibronic couping in the case of acetone: state diagram of the stretching vibrations (left) and the bending vibrations (right) as well as the corresponding orbitals. A crossing (c) occurs between the potential curves during the stretching vibrations and an avoided crossing (ac) occurs during the bending vibrations. Figure created based on reference [24, 25].

For acetone and other carbonyl compounds[24, 25], the transition from the singlet state $^1\pi\pi^*$ to $^3\pi\pi^*$ is considered El-Sayed forbidden, rendering it initially unsuitable for intersystem crossing (ISC). However, spin-vibronic coupling can facilitate this transition by influencing the geometry of the states and the character of the electronic transitions. **Figure 2** illustrates the potential energy surfaces of the singlet state S_1 and the triplet state T_1, alongside the stretching vibrations in the molecular plane and the

bending vibrations that occur perpendicular to it. In the case of stretching vibrations, the distortion of the molecular geometry occurs without significantly altering the nature of the orbitals involved in the π bonding, as the relevant carbon and oxygen orbitals remain perpendicular to the plane of vibration. Conversely, bending vibrations cause a more profound transformation, changing the hybridization of the carbonyl carbon atom from sp^2 to sp^3. This alteration increases the s-character of the carbon atom's p orbitals, resulting in a nπ* transition state characterized. This configuration can lead to an avoided crossing between the singlet and triplet potential energy surfaces, facilitating the $^1\pi\pi^* \rightarrow {}^3\pi\pi^*$ transition. The ability of vibrational modes to mediate this transition underscores the significance of spin-vibronic coupling in enabling ISC in systems that would otherwise be restricted by El-Sayed rules. By coupling electronic states through vibrational dynamics, these processes demonstrate a complex interplay that broadens our understanding of non-radiative transitions in carbonyl compounds.

1.3 Phosphorescence

As the T_1 state can be populated via intersystem crossing (ISC), either through spin-orbit coupling (SOC) or spin-vibronic coupling, the system can return to the ground state radiatively, allowing phosphorescence to occur. Phosphorescence also involves a spin reversal, which necessitates SOC to perturb the system sufficiently for singlet-triplet mixing. This mixing means that the molecule does not exist in a pure singlet or triplet state; instead, there is an admixture of singlet character within the triplet state and vice versa (**Figure 3**). This phenomenon allows for transitions that would typically be forbidden by spin selection rules. The degree of singlet-triplet mixing is critical for facilitating radiative decay back to the ground state, as it enables the system to access pathways that allow for the emission of light. The efficiency of phosphorescence is influenced by the strength of SOC and the nature of the

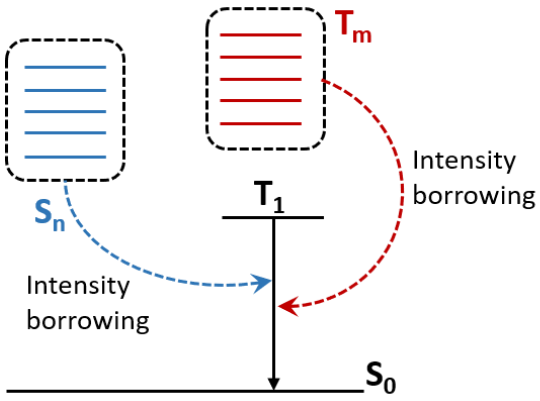


Figure 3. Singlet -triplet mixing: phosphorescence gaining intensity via singlet admixture to T_1 and triplet admixture to S_0. Figure created based on reference [26].

molecular environment, including factors such as ligand field effects and vibrational couplings, which can enhance the mixing of states and thus promote the likelihood of phosphorescent emission.

The influence of coupling of singlet and triplet state on the radiative rate constant of phosphorescence can be visualized according to **Equation (3)**.[25,27]

$$k_p\,(i) = \frac{4\,e^2}{3\,c^3\,h^4}\;(E(T_1 - E(S_0))^3 \times \left|\sum_{m=0}^{\infty} \frac{\langle S_m|\hat{H}_{so}|\,T_{1,i}\rangle}{E(S_m)-E(T_1)}\;\langle S_0|\sum_j e\vec{r_j}|S_m\rangle + \right.$$

$$\left.\sum_{n=1}^{\infty} \frac{\langle S_0|\hat{H}_{so}|T_{n,i}\rangle}{E(T_n)-E(S_0)}\;\langle T_{n,i}|\sum_j e\vec{r_j}|T_{1,i}\rangle\right|^2 \qquad (3)$$

The equation can be divided into three distinct parts: the blue section represents the energy gap between the T_1 and S_0 states; the red section accounts for the singlet admixture into the T_1 state; and the green section describes the triplet admixture into the S_0 state. A greater energy gap between T_1 and S_0 typically results in a higher radiative rate, whereas a smaller energy gap tends to enhance the rate of non-radiative processes. The red component indicates that to ensure oscillator strength for the transition from $T_1 \rightarrow S_0$, the T_1 state must "borrow" intensity from the singlet manifold, denoted as S_m . Conversely, the green section highlights that S_0 must borrow intensity from the triplet excited states, T_n. Strong SOC is particularly effective when the nature of the orbitals involved in the transitions differs significantly. Additionally, the energy gap between the coupled states and the density of states play crucial roles in this process. A smaller energy gap between the states enhances coupling strength, making transitions more likely. Furthermore, a high density of states is advantageous as it increases the coupling between T_1 and singlet excited states or vice versa, thereby facilitating the necessary interactions for effective ISC and phosphorescent emission.

It is important to note that the spin-orbit coupling operator, $\hat{H}_{so}$, plays a significant role in the equation, particularly in heavy metal complexes. The large SOC constants associated with these metals can lead to efficient phosphorescence, especially when the metal's orbitals are involved in the transitions. While phosphorescence can occur in some organic molecules, it tends to be inefficient, with lifetimes typically ranging from milliseconds to seconds. This inefficiency can be attributed to the relatively small SOC constants present in organic molecules. When a transition metal is introduced into the molecular structure, the electronic states often acquire a metal-to-ligand charge transfer (MLCT) character due to the involvement of the metal's d orbitals. This, combined with the internal heavy atom effect and the multitude of possible transitions between the metal and its ligands, results in an increase in the radiative rate constant and a corresponding lifetime in the microsecond range. Consequently, there has been significant research interest in complexes containing heavy transition metals, with numerous efficient emitters based on iridium(III) and platinum(II) already documented in the literature. [28,29]

1.4 Emitters based on 4d- and 5d- metal Complexes

Luminescent transition metal complexes have become the focus of extensive research over the past few decades, primarily due to their promising applications in organic light-emitting diodes (OLEDs), dye-sensitized solar cells, and lighting technologies. These complexes, particularly those based on 4d and 5d transition metals, have gained significant attention for their unique electronic properties, which enable efficient and tunable light emission. In addition to the elevation of non-radiative d-d* transitions, late transition metals offer the additional advantage of pronounced spin-orbit coupling due to their high nuclear mass. The ability to harness both singlet and triplet excited states makes these complexes

particularly attractive for OLED applications, where high efficiency and stability are paramount. Among the various transition metals, Ru(II), Re(I), Os(II), Ir(III), and Pt(II) are the most extensively studied due to their favorable luminescent properties.[28, 29] These metals, often referred to as noble metals, exhibit strong spin-orbit coupling (SOC), enabling phosphorescence. These transition metal complexes, especially in their stable oxidation states (such as Ru(II), Os(II), and Ir(III)), often have a d^6 (Ru, Os) or d^8 (Ir, Pt) electron configuration, which significantly influences their geometry and bonding properties. In these configurations, the complexes typically adopt octahedral or square-planar geometries depending on the metal center and the type of ligands coordinated to the metal. The emission from these complexes originates primarily from the ^{3}MLCT or ^{3}LC states, or from an admixture of both. However, due to the presence of partially filled d-orbitals, metal-centered (^{3}MC) d-d* transitions can also compete with phosphorescence, potentially affecting the overall emission properties. In the example presented in **Figure 4**, the high-energy excitation promotes the occupation of higher vibrationally excited states of the ^{3}MLCT or ^{3}LC, which provides the activation energy for the ^{3}MLCT→^{3}MC radiationless transition.[40, 41] The d* orbitals typically exhibit a dissociative character concerning the metal-ligand bond, as evidenced by the horizontal shift in the metal-centered (MC) potential curve. Due to strong coupling with the ground state, this often results in a radiationless transition or bond cleavage due to the dissociative MC chracter. Additionally, the expansion of the metal-ligand bond in the excited state can alter the reactivity of the compound and promote photochemical reactions. These processes, which are undesirable for emissive systems, can be

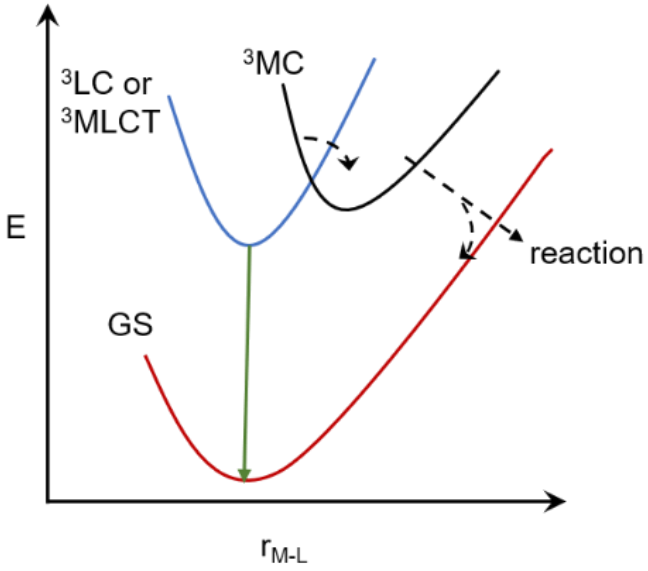


Figure 4 schematic representation of electronic transition of transition metal complexes with partially filled d orbitals, dotted line denotes radiationless transition. Figure created based on the reference [40, 41].

suppressed by increasing the ligand field splitting. A higher ligand field splitting shifts the d* orbitals to higher energies, effectively separating radiative and non-radiative transitions. Notably, ligand field splitting is generally stronger for late transition metals compared to 3d metals, and can be further enhanced by using strong-field ligands.

As already mentioned before, there is large number of reaseraches[40, 41, 47] known in the literature for photo-active late transition metal complexes, only selected examples will be mentioned in this chapter.

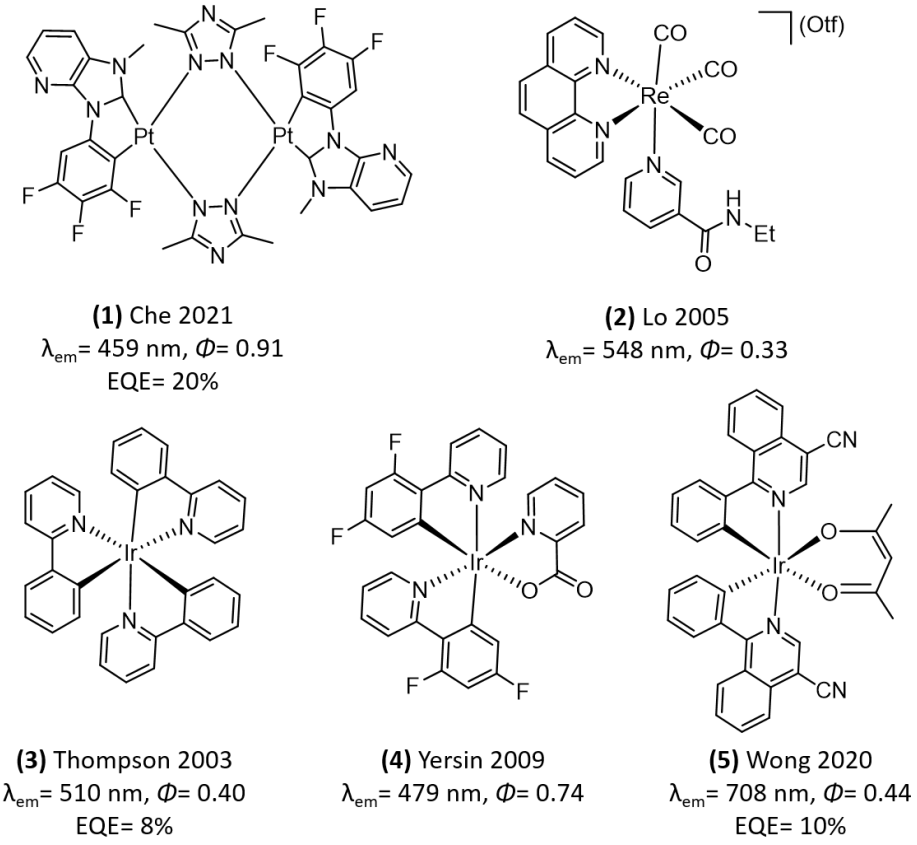


Figure 5. Molecular structure and important photophysical data of some emissive late transition metal complexes.[42, 43,44,45,46]

While the emission efficiency of the complexes is typically high in the green to orange region of the spectrum, it tends to drop significantly at the extremes of the visible range (i.e., in the red and blue regions). This drop in efficiency can be attributed to several factors, including the nature of the electronic transitions involved. In high-energy emitters, one of the primary challenges arises from MC transitions, which often result in significant efficiency losses. For many complexes, especially those with high ligand field splitting, this separation of radiative and non-radiative transitions is sufficient across large portions of the visible spectrum. However, achieving blue emission, characterized by a relatively high energy is

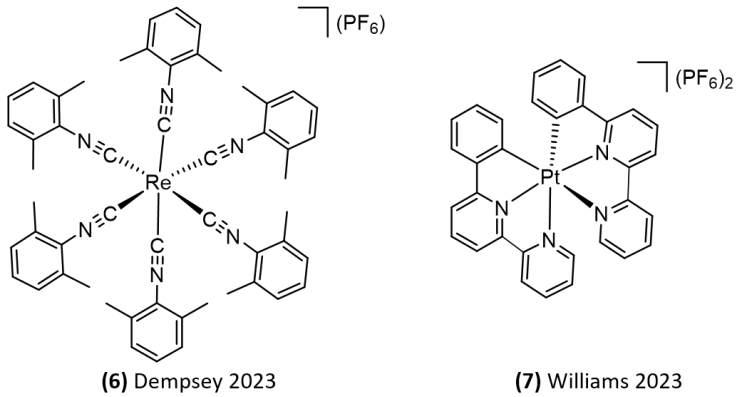


Figure 6. Molecular structure of some recent examples of emissive late transition metal complexes in less known oxidation state.[48,49]

more challenging. In this case, a large energy gap between the occupied and unoccupied molecular orbitals is required which often results in the competitive population of the metal-centered states. Clever ligand design to decrease the HOMO energy without changing the energy level of LUMO helps to achieve blue emission in significant quantum yield in case of **4** as shown by Yersin and his group.[45] Similarly, another significant challenge is the development of efficient emitters in the low-energy red and near-infrared (NIR) regions, due to the energy gap law (vide supra). Researchers are exploring numerous classes of compounds and a variety of strategies to address these issues. One common approach to obtain transition metal complexes with NIR emission is to modify the ligands of a visible light emitter in such a way as to achieve a redshift of the emission. Several strategies are being pursued to achieve this goal, and they include the use of stronger-field ligands, modification of the ligand geometry, and incorporation of specific donor-acceptor motifs to modulate the electronic structure of the complex. The recent work by Wong and his group demonstrated that a simple strategy to decrease the LUMO energy by introducing the strongly electron-withdrawing CN group into an isoquinoline ligand yields the NIR-emitting Ir(III) complex **5** with appreciable EQE when applied in an OLED.[46] Despite the challenges, significant ongoing research continues to focus on improving blue and NIR emitters. In particular, new trends are emerging that explore the structural versatility of these complexes. Additionally, compounds featuring metals in less conventional oxidation states and coordination geometries are gaining attention.[48, 49] For example, the depicted Re(II) complex **6** exhibit significant LMCT contributions, in contrast to the more commonly observed MLCT transitions while the Pt(IV) complex **7** shows new research directions involving platinum.

By incorporating these new design principles, researchers hope to overcome the limitations of conventional emitters and develop more efficient and versatile materials for different light emission. However, classical 4d and 5d metal complexes generally come with high costs and sustainability concerns. Moreover, the radiative rate constant k_P of heavy metal emitters cannot be increased indefinitely with rising SOC.[30] Empirically, a limitation of approximately $k_P \approx 10^6\ s^{-1}$ has been attributed to the zero-field splitting (ZFS) of the triplet levels within the T_1 state. Given these constraints, alternative emission mechanisms involving triplet excitons are of high interest, particularly for organic molecules and lighter metal complexes. Such mechanisms do not rely on the use of rare elements and offer the potential for increased radiative rate constants k_r compared to traditional phosphorescence. This opens up exciting avenues for research and development in the field of photonic materials.

1.5 Thermally Activated Delayed Fluorescence

An alternative emission mechanism that could circumvent the inefficiencies of phosphorescence in organic chromophores or lighter metal complexes is thermally activated delayed fluorescence (TADF). This mechanism was first identified in 1961 and is also referred to as E-type fluorescence, a name derived from its initial description using the luminescence of eosin as an example. [31] TADF has gained considerable attention, particularly regarding its application in organic light-emitting diodes (OLEDs), since the late 2000s, when research by Adachi and his colleagues has highlighted TADF as a potentially efficient mechanism for enhancing the performance of optoelectronic devices.[32] The key advantage of

TADF lies in its ability to harness both singlet and triplet excitons for light emission, effectively converting normally unutilized triplet states back into singlet states through thermal activation. Since thermally activated delayed fluorescence (TADF) utilizes both singlet and triplet excitons, TADF emitters can achieve 100% internal quantum efficiency (IQE) in devices. This characteristic has led to TADF being referred to as "singlet harvesting", similar to phosphorescence.[33] Additionally, TADF allows for high oscillator strengths and radiative rate constants that surpass those of pure triplet state emitters. This advantage arises because the emission process is derived from the spin-allowed $S_1 \rightarrow S_0$ transition, which is inherently more favorable than transitions involving triplet states. This process not only improves the overall efficiency of light emission but also reduces the reliance on heavy metals, making TADF materials more sustainable and cost-effective. As a result, TADF has emerged as a promising avenue for developing next-generation OLEDs and other photonic devices, contributing to advancements in organic electronics and lighting technologies.

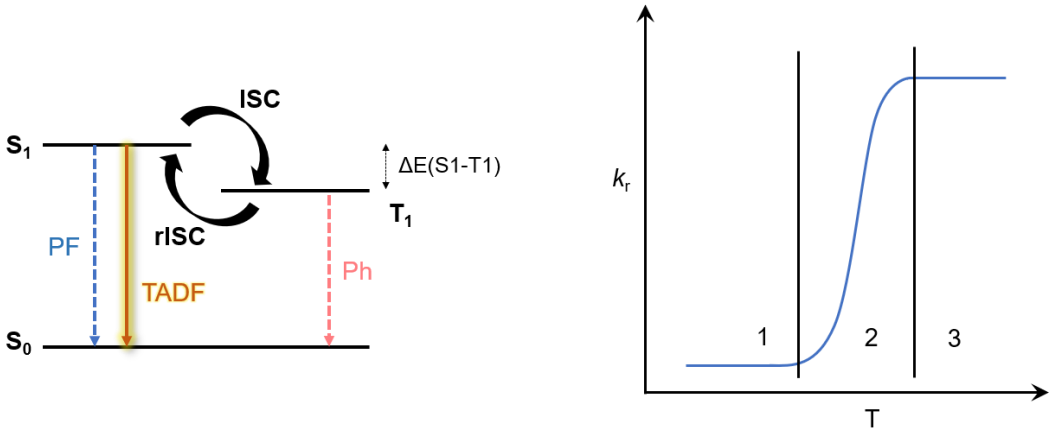


Figure 7. Simplified Jablonski diagram showing Prompt fluorescence (PF), phosphorescence (Ph) and TADF. Illustration created based on reference [25].

TADF involves a thermal equilibration between the lowest energy singlet (S_1) and triplet (T_1) excited states at room temperature, provided the singlet-triplet energy gap is sufficiently small (typically less than 1500 cm^{-1}).[25] When this gap is small enough, emission can occur directly from the S1 state, bypassing the traditionally inefficient phosphorescence process, as illustrated in **Figure 7**. A critical aspect of efficient TADF is the reverse intersystem crossing (rISC) from the T_1 state to the S_1 state. This rISC process plays a pivotal role in replenishing the singlet state, which then radiatively relaxes to the ground state, generating fluorescence. The efficiency of TADF is highly temperature-dependent, as rISC is thermally activated. The rate of rISC can be described by the Boltzmann distribution, which governs the population equilibrium between the singlet and triplet states as a function of temperature, as expressed in **Equation 4**.[25]

$$k_{rISC} \propto e^{\left(\frac{\Delta E_{(S_1-T_1)}}{k_B T}\right)} \quad (4)$$

Here, k_B stands for Boltzmann constant, T is temperature and $\Delta E_{(S_1-T_1)}$ is the energy gap between the singlet S_1 and triplet T_1 excited states. At higher temperatures, the thermal energy favors the reverse transition from T_1 to S_1, thus enhancing the TADF efficiency

The radiative rate constant of TADF can be expressed as follows:

$$k_r = \frac{\left[3k_r(T_1)+k_r(S_1).e^{\left(\frac{\Delta E(S_1-T_1)}{k_B T}\right)}\right]}{\left[3+\ e^{\left(\frac{-\Delta E(S_1-T_1)}{k_B T}\right)}\right]} \quad (\mathbf{5})$$

Similarly, the overall radiative rate constant for the TADF process depends on both the energy gap between the singlet (S_1) and triplet (T_1) excited states and the temperature. A plot of the radiative rate constant as a function of temperature typically produces a sigmoidal curve, as shown in **Figure 7**. At sufficiently high temperatures (region III), as described by **Equation 5**, the population of the singlet excited state (S_1) is sufficiently high that emission from the S_1 state dominates, resulting in an increased radiative rate constant (k_r). As the temperature decreases (region II), the population of the S1 state decreases, and the system shifts towards a higher population of the triplet state (T_1) which results in an increased contribution from phosphorescence, characterized by a longer emission lifetime and a lower k_r. At very low temperatures (region I), the thermal population of the singlet state is minimal, and the system is essentially dominated by the T_1 state. In this regime, the radiative rate constant is reduced to the low value characteristic of pure phosphorescence, and the emission reaches a plateau, where the contribution from phosphorescence becomes dominant, and fluorescence is essentially quenched.

The general design criteria for TADF molecules are primarily governed by three key factors: a small $\Delta E_{(S_1-T_1)}$ to facilitate efficient rISC, sufficient SOC to promote the coupling between singlet and triplet states, and molecular rigidity to minimize thermal deactivation processes. Small $\Delta E_{(S_1-T_1)}$ can be achieved by creating spatial separation between the Mos involved in the transition that would result a small exchange integral (J). The dependence of energy gap on the molecular orbital overlap can be expressed as follows:[32, 34]

$$\Delta E_{(S_1-T_1)} = 2J = 2 \iint \Phi_{HOMO}\ (r_1)\Phi_{LUMO}\ (r_2)\frac{1}{|r_2-r_1|}\Phi_{HOMO}\ (r_2)\Phi_{LUMO}\,.(r_2)\ dr_1 dr_2 \quad (\mathbf{6})$$

In this context, where Φ_{HOMO} and Φ_{LUMO} represent the spatial distributions of the HOMO and LUMO, respectively, e denotes the charge, and ϵ_0 is the dielectric constant, r_1 and r_2 are position vectors. A small overlap integral results in a reduced exchange integral, which in turn leads to a smaller energy gap between the singlet and triplet states. Spatial separation of the molecular orbitals (MOs) involved in the transition is therefore beneficial for achieving a small singlet-triplet energy gap. This separation can be effectively realized in charge-transfer (CT) complexes, where the donor and acceptor units are spatially distinct, resulting in reduced orbital overlap. The reduction in spatial overlap between orbitals in TADF emitters weakens the oscillator strength of the radiative transition ($S_1 \rightarrow S_0$), thus lowering the fluorescence efficiency. Consequently, the challenge lies in finding a balance between achieving a small $\Delta E_{(S_1-T_1)}$ for efficient reverse intersystem crossing (rISC) and maintaining a sufficiently large oscillator strength for the $S_1 \rightarrow S_0$ radiative transition.

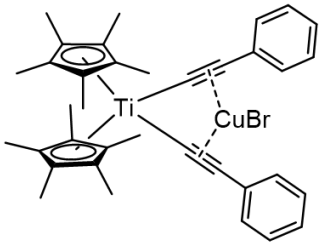
In recent years, earth-abundant 3d transition metal complexes have gained increasing attention as promising candidates for TADF emitters. By leveraging the unique properties of transition metal compounds such as stronger SOC and a high density of states, researchers aim to develop more efficient TADF materials that could potentially outperform traditional emitter materials in high-performance applications.

1.6 Emitters based on 3d-metal Complexes

The weaker ligand field effects in 3d metal complexes often pose challenges for achieving efficient emission, particularly for complexes with d^3–d^8 electronic configuration. The lower spin-orbit coupling of early transition metals also results in smaller rate constants for phosphorescence. Despite these challenges, contemporary research has increasingly shown the potential of first-row transition metal complexes in photonic applications and has opened up new design strategies to improve their photophysical properties. In the following sections, a selection of recent developments in the field of photochemically active molecular compounds from the past will be discussed. Finally, zinc (II) complexes are given particular attention due to their relevance to the present work.

Scandanium and Titanium group ($3d^0$)

Complexes of Sc(III) and Ti(IV) with a d^0 electronic configuration are promising candidates for emission from LMCT states, owing to the absence of metal-centered (MC) excited states that typically facilitate non-radiative deactivation. Several d^0 complexes have demonstrated emission from LMCT states, with metallocenes being the most extensively studied class. One of the earliest examples of LMCT emission from a d^0 complex is $[Cp^*_2ScCl]$, which was shown to emit in fluid solution at room temperature with a luminescence lifetime of 2.0 µs.[50] Similarly, titanocene derivatives, such as Cp_2TiX_2, are known to emit



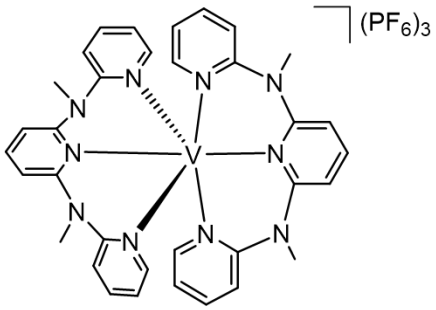
(8) Wagenknecht 2022
λ_{em}= 639 nm, Φ= <0.01

Figure 8. Emissive d^{10}/d^0 heterobimetallic titanocene tweezer.[52]

from the ^{3}LMCT state, although typically only at cryogenic temperatures.[51] At room temperature, Cp_2TiX_2 exhibits weak emission, but rapid photodecomposition hinders its practical use. Recent advances in this area have focused on improving the photostability and emission efficiency of these complexes. One recent development involves replacing the Cp ligand with the more sterically demanding Cp* and incorporating copper(I) halide, CuX, between alkyne ligands.[52] The resulting complex, $[Cp^*_2Ti(C_2Ph_2)_2CuBr]$ (**8**), shows enhanced photostability and room-temperature emission predominantly from the ^{3}LMCT state (Cp* to Ti) at 693 nm in THF solution. This improvement of photo-stabilty is attributed to the coordination of CuX, which lowers the excited state energies. However, the

quantum yield of the emission still remains low (1.3 ×10^{-3}). Despite these challenges, Ti(IV)-based complexes remain highly relevant for photochemical applications, especially in areas like photoredox catalysis, where stable and cost-effective photosensitizers are in high demand.

Vanadium group ($3d^2$/ $3d^3$)



(9) Heinze 2020
λ_{em}= 396 nm , Φ= 0.02
λ_{em}= 982, 1088, 1109 nm, Φ= <0.01

Figure 9. Molecular structure of emissive vanadium (III) complex .[53]

Vanadium can adopt both d^2 and d^3 electronic configurations, which are accessible in its different oxidation states, specifically in V(II) and V(III) . The photochemistry of vanadium(II) complexes is dominated by mixed ²MC/²MLCT states, which undergo rapid intersystem crossing (ISC) and internal conversion (IC), leading to fast ground-state recovery.[54] These states also exhibit faster non-radiative decay compared to their chromium(III) analogs, owing to inherent geometric distortions and stabilization effects. In contrast, the first vanadium(III) complex to exhibit near-infrared (NIR) luminescence at room temperature in fluid solution is mer--$[V(ddpd)_2]^{3+}$ (**9**), where ddpd is a strong-field ligand that helps create a rigid ligand environment, enhancing the ligand field effect.[53] The complex displays intense visible absorption bands extending into the NIR region, and it emits high-energy blue fluorescence at 396 nm with a quantum yield of 2.1%, attributed to transitions from the ³LMCT states. Additionally, it exhibits long-lived phosphorescence in the NIR region at room temperature in solution.

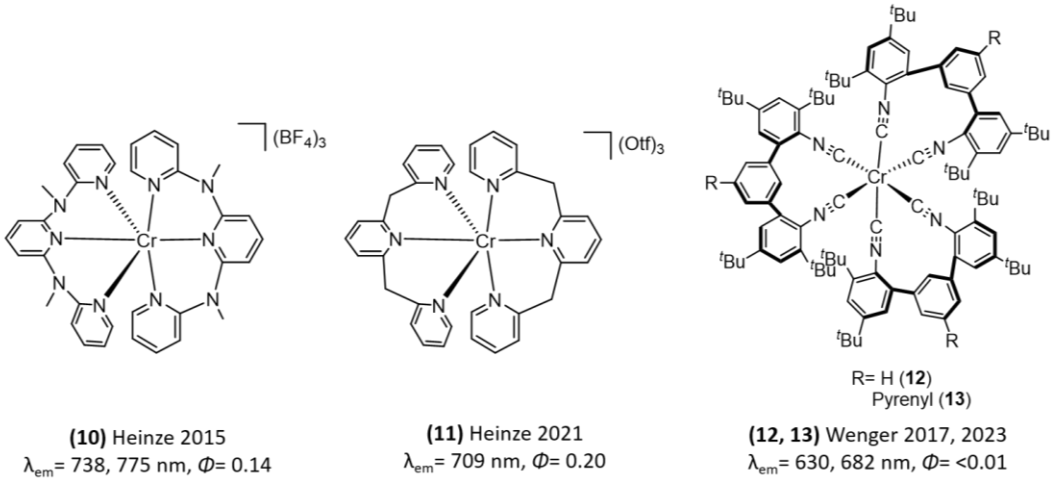
The weak phosphorescence bands observed at 982, 1088, and 1109 nm are assigned to spin-forbidden transitions from the $^1T_2$/¹E states to the split components of the $^3T_1$ ground state. Molecular dynamics simulations reveal that when the complex is excited into a ³LMCT state, only a small fraction of the population transitions to the ¹MC states, which can then radiatively decay back to the ground state. mer-$[V(ddpd)_2]^{3+}$ represents a rare example of a vanadium(III) complex exhibiting ambient temperature NIR luminescence, with its emission properties shaped by a delicate balance between slow ISC and the competition between radiative and non-radiative decay processes. These features highlight the potential of vanadium(III) complexes in applications requiring dual blue and NIR emission, despite the challenges posed by slow ISC and the relatively low quantum yields.

Chromium group ($3d^3$/ $3d^6$)

Photoactive complexes of chromium can be broadly classified into two major types: Cr(0) and Cr(III), with Cr(III) complexes, particularly those exhibiting ligand field luminescence, have gained significant attention due to their unique spin-flip emission properties. Heinze's group was among the pioneers in investigating Cr(III)-based emitters, synthesizing the $Cr(ddpd)_2^{3+}$ complex (**10**), which is often referred to as "molecular ruby" due to its intense and stable near-infrared (NIR) emission.[12a] This complex exhibits unexpectedly long-lived and efficient NIR luminescence for a Cr(III) emitter. The $Cr(ddpd)_2^{3+}$ complex features the ddpd ligand, a tridentate amine-bridged tripyridine ligand, which is key to its remarkable photophysical behavior. The bite angle of the ligand facilitates an optimal octahedral coordination geometry around the chromium center, which enhances the electronic properties of the complex. The strong σ-donating ability of the ddpd ligand contributes to substantial ligand field splitting, resulting in a high-energy barrier for excited-state deactivation and stabilizing the metal center. This ligand field effect plays a crucial role in controlling the spin-forbidden transitions that lead to the observed NIR emission. The Cr(III) center remains in a relatively stable electronic configuration, allowing for efficient radiative decay from the excited state. The complex exhibits intense NIR emission in acetonitrile at room temperature, with emission maxima at 738 nm and 775 nm. In addition to its NIR emission, the complex demonstrates a high quantum yield of 12% and a long-lived excited state with a lifetime of 899 µs. These photophysical properties are exceptional, especially compared to other chromium(III) NIR emitters, which typically have quantum yields well below 1%.

In a recent study[12b], Heinze's group introduced an interesting modification to the ddpd ligand by replacing the -NMe unit with $-CH_2$ groups. This substitution resulted in a blue shift of the emission, with the $Cr(bpmp)^{3+}$ complex (**11**) now emitting at 709 nm, compared to the original 775 nm emission in $Cr(ddpd)_2^{3+}$. This shift is significant because it moves the emission closer to the visible spectrum while still maintaining strong luminescent properties. The modified complex, $Cr(bpmp)^{3+}$, exhibits even higher luminescence efficiency, surpassing not only the MLCT emission of $Ru(bpy)_3^{2+}$[55] but also the MC emission of the often used Eu(III)-based red emitters. These results underscore the versatility of Cr(III)-based emitters and their potential to outperform other well-known chromophores in terms of both efficiency and emission tunability.

Beyond traditional fluorescence and phosphorescence, some Cr(III) complexes based on dqp ligands have been developed as circularly polarized luminescence (CPL) emitters.[56] These complexes show high g_{lum} values, indicating efficient chiroptical properties that make them attractive for applications in optical switches, 3D displays, and stereochemical sensing. Additionally, Cr(III)-based polypyridine complexes have been explored for their NIR-II emission (1000-1700 nm), particularly in low-temperature environments. For example, a Cr(III) polypyridine complex exhibited strong emission at 1067 nm in frozen acetonitrile at 77 K, an achievement that expands the range of emission wavelengths available for NIR imaging and photonics.[57]



(10) Heinze 2015
λ_{em}= 738, 775 nm, Φ= 0.14

(11) Heinze 2021
λ_{em}= 709 nm, Φ= 0.20

(12, 13) Wenger 2017, 2023
λ_{em}= 630, 682 nm, Φ= <0.01

Figure 10. Molecular structure of $Cr(ddpd)_2^{3+}$, $Cr(bpmp)^{3+}$ and emissive Cr(0) complex based on isonitrile ligands.[12]

Analogous to Ru(II) and Ir(III), Cr(0) features a d^6 electronic configuration, which can be efficient for ^{3}MLCT emission. The low oxidation state of the chromium center is typically stabilized by strongly π-accepting ligands, such as carbonyls and isocyanides. These ligands stabilize the metal center and tune the electronic properties of the complex through their electron-withdrawing nature, which facilitates metal-to-ligand charge transfer (MLCT) processes via π-back donation. A notable advancement in the field came from the Wenger group, which developed a series of Cr(0) complexes using chelating isocyanide ligands to stabilize octahedral coordination around the chromium center.[12c, 12d] These ligands are unique in that they shield the metal atom effectively using *tert*-butyl groups positioned in the ligand backbone. This bulky shielding prevents photodegradation and substitution reactions, which are common in Cr(0) complexes. Compound **12** exhibits emission from the ^{3}MLCT states, centered around 630 nm, but with relatively low quantum efficiency (10^{-5}) and a short excited-state lifetime of around 2 ns. The low photoluminescent efficiency is primarily attributed to rapid internal conversion (IC) to lower-lying metal-centered states. This behavior, similar to that observed in octahedral Fe(II) complexes, results in non-radiative decay to the lower-energy MC states, reducing the overall emission efficiency.

Recent reports show that substitution with pyrenyl groups on the periphery enhances emission efficiency by up to 90 times. This improvement is attributed to the delocalization effect, where the MLCT state becomes mixed with pyrene character, reducing the distortion of the MLCT excited state. As a result, **13** exhibits the longest MLCT lifetime (6.1 ns) observed so far for 3d metal complexes in solution at room temperature.

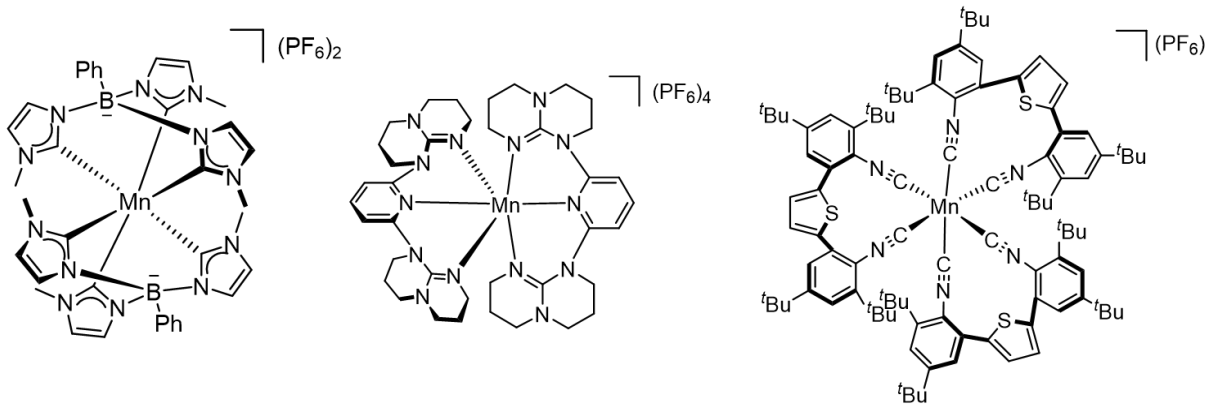
While these complexes have potential in areas like photocatalysis or light-emitting devices, their photophysical inefficiency means that they may be more suited for applications that do not rely heavily on high quantum yields, such as in photoactive materials or sensitizer systems for reactions that do not require strong or prolonged emission.

Manganese group ($3d^3$/ $3d^6$)

Despite its high abundance, photophysical research on Mn(I) and Mn(IV) complexes is still in its infancy. A significant breakthrough came from the Tesler group, who first synthesized an Mn(IV) complex (**14**)

using the electron-donating tris(carbene)borane ligand.[13a] **14** exhibits ruby-like red luminescence at 815 nm from metal-centered (MC) states in the solid state at room temperature, akin to many isoelectronic Cr(III) complexes. Additionally, the complex shows green luminescence from ligand-to-metal charge transfer (LMCT) states. Recent photophysical investigations of **14** in solution state by Hammerstorm group, reveal an exceptionally long LMCT lifetime of 15 ns along with remarkably high excited-state reduction potential of E^*_{red} = 2.0 V vs. SCE, making it an excellent candidate for use as a photo-oxidant.[58]

Heinze and her group recently demonstrated the potential of $Mn(dgpy)_4^+$ (**15**) as a low-energy photosensitizer.[13b] The complex exhibits panchromatic absorption across the entire visible spectrum, but, unlike **14**, no spin-flip emission was observed when irradiated with 360 nm or 500 nm light. However, excitation with low-energy NIR light results in emission at 1435 nm, originating from a ^{2}LMCT state, with a lifetime of 1.6 ns. The high excited-state reduction potential (E^*_{red} = 2.4 V vs SCE) of complex **15** makes it particularly useful for photo-oxidation reactions of substrates with extremely high oxidation potentials, such as naphthalene and nitriles, using low-energy light.



(14) Tesler 2017
λ_{em}= 600, 815 nm

(15) Heinze 2022, 2024
λ_{em}= 1470 nm

(16) Wenger 2021
λ_{em}= 485 nm, Φ= 0.05

Figure 11. Molecular structure of emissive Mn(IV) and Mn(I) complexes.[13]

The Wenger group first reported a series of emissive Mn(I) complexes based on isonitrile ligands (**16**).[13c] For complex **16**, very weak metal-to-ligand charge transfer (MLCT) emission was observed in solution at ambient temperature, with an exceptionally short-lived excited state (< 2 ns). Despite the short excited state lifetime, these complexes were proved useful for photo-induced energy and electron transfer processes, making Mn(I) based photosensitizer highly attractive for future application.

Iron group ($3d^5$/$3d^6$)

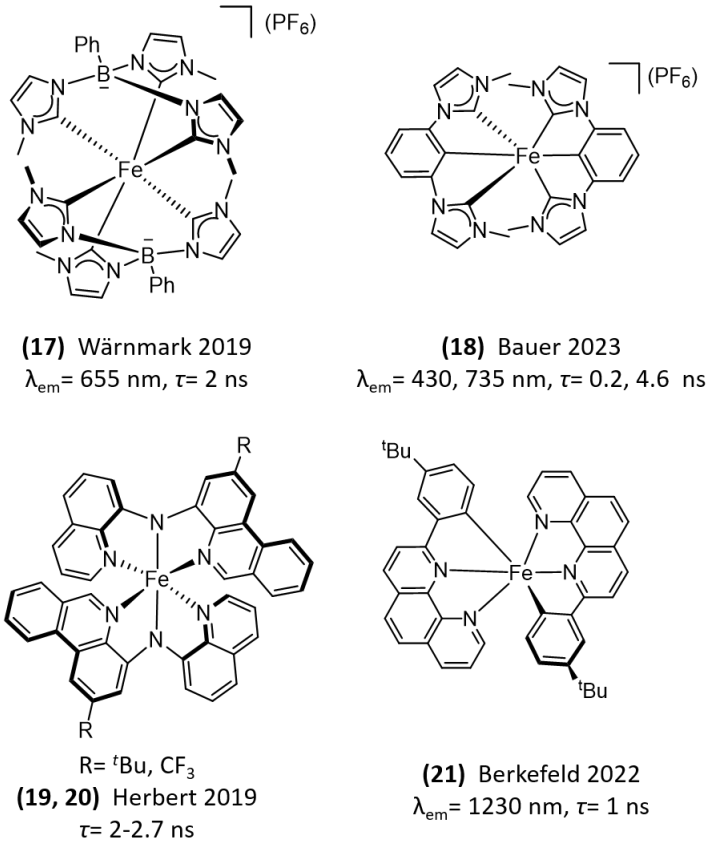
The search for iron-based photosensitizers capable of replacing the widely used Ru(II) complexes has driven significant research in recent years. Despite the promise of iron as a more Earth-abundant and potentially less toxic alternative, the weak ligand field strength of Fe(II) often leads to rapid deactivation of the metal-to-ligand charge transfer (MLCT) excited state via low-energy metal-centered (MC) states. To address this challenge, several innovative ligand design strategies have been employed to stabilize and enhance the MLCT excited states. These include the use of push-pull ligand sets, cyclometalating

ligands, N-heterocyclic carbenes (NHCs) and meso-ionic carbenes (MIC) carbenes.[59] In addition to Fe(II)-based complexes, Fe(III) complexes with a d^5 electronic configuration have garnered increasing attention. The isolation of the $Fe(btz)_3^{3+}$ complex (where btz is 3,3'-dimethyl-1,1'-bis(p-tolyl)-4,4'-bis(1,2,3-triazol-5-ylidene), which surprisingly exhibited photoluminescence, marked a breakthrough in the understanding of Fe(III)-based luminescent species.[14a] Unlike Fe(II) complexes, Fe(III) complexes do not suffer from the same rapid deactivation pathways, and the emission observed from the LMCT excited state at room temperature was unusual and promising for potential applications. A key advancement in this field came with the work of Wärnkmark and his colleagues, who modified the ligand environment of Fe(III) complexes to further enhance their photophysical properties.[14b] By using a more σ-donating $PhB(MeIm)_3$ ligand, they succeeded in increasing the energy of the MC excited state even more, thereby prolonging the excited-state lifetime and improving the emission efficiency. In their study, they found that the emission from iron(III) complex **17** occurs via a spin-permitted transition from a ^{2}LMCT state to the doublet ground state. The resulting photophysical data were impressive: the complex exhibited an extraordinarily high radiative rate constant ($k_r = 1.1 \times 10^7\ s^{-1}$), leading to a lifetime of approximately 2 ns and a quantum yield of 2%. However, despite these promising results, the complex undergoes self-quenching in acetonitrile solution. This self-quenching results in the formation of Fe(II) and Fe(IV) photoproducts in 4% yield, indicating that further optimization of the ligand design and experimental conditions may be necessary to reduce these non-productive pathways and improve the overall efficiency of the system.

Recently, the Bauer group has employed a combination of strongly electron donating N-heterocyclic carbene (NHC) ligands and cyclometalating σ- and π-donors to design iron complexes that displays particularly unusual and intriguing photoluminescent behavior.[14c] For complex **18**, two distinct emission bands were observed, originating from different excited states. The first emission, at 735 nm, was attributed to a ^{2}LMCT transition and exhibited a very short excited-state lifetime of only 0.2 ns. The second emission, at a higher energy of 430 nm, was assigned to a ^{2}MLCT transition. Remarkably, this ^{2}MLCT emission exhibited a much longer lifetime of 4.6 ns, which, at the time, was claimed to be the longest MLCT lifetime recorded for any iron-based compound. According to the author's analysis, the stabilization of the Fe(IV) oxidation state and the presence of energetically accessible π* orbitals from the phenyl/NHC played a critical role in enabling the observation of MLCT emission. However, the reliability of the dual emission behavior has come into question. The manuscript, after its initial submission and peer review, was accompanied by an editor's note that cast doubt on the robustness of the data supporting the two distinct emissions. The editor's note highlighted concerns about the reproducibility of the dual emission and suggested that further experimental validation was needed to confirm the presence of the two separate excited states.

As previously mentioned, the rapid deactivation of the Metal-to-Ligand Charge Transfer (MLCT) state in Fe(II) complexes presents a significant challenge, typically resulting in very short MLCT lifetimes (~10-20 ps)[60, 61], often only measurable using transient absorption spectroscopy. Exceptionally long MLCT lifetimes, however, have been achieved in the case of $Fe(btz)_3^{2+}$ (0.5 ns), where the use of mesoionic carbenes has been shown to enhance the ligand field strength. The mesoionic carbenes

provide strong π-acceptor properties while maintaining robust σ-donation ability, similar to N-heterocyclic carbenes (NHCs), thus stabilizing the MLCT state.



(17) Wärnmark 2019
λ_{em}= 655 nm, τ= 2 ns

(18) Bauer 2023
λ_{em}= 430, 735 nm, τ= 0.2, 4.6 ns

R= ^{t}Bu, CF_3
(19, 20) Herbert 2019
τ= 2-2.7 ns

(21) Berkefeld 2022
λ_{em}= 1230 nm, τ= 1 ns

Figure 12. Molecular structure of emissive Fe(III) (**17**,**18**) and Fe(II) (**19**, **20**, **21**) complexes.[14]

Additionally, the Herbert group has employed a completely different approach, utilizing the concept of HOMO inversion to extend the MLCT lifetime to the range of 2.0-2.7 ns (**19**, **20**).[14d] In their work, tridentate ligands incorporating π-donating amido groups enable strong mixing between the metal t_{2g} orbitals and the filled ligand orbitals. This mixing leads to a significant ligand character in the highest occupied molecular orbital (HOMO), and the complete inversion of the HOMO from being metal-based to ligand-centered results in the exceptionally long excited-state lifetimes observed.

More recently, a mononuclear Fe(II) complex (**21**) exhibiting radiative MLCT emission was reported by the group of Berkefeld.[14e] Using phenylphenanthroline-based ligands, they synthesized a doubly cyclometallated iron(II) complex that demonstrates MLCT emission in the near-infrared (NIR) region at room temperature, with a lifetime of approximately 1 ns in solution state. Notably, this complex also displays a ^{3}MLCT reduction potential of −2.0 V vs. Fc/Fc^{+}, which makes it an effective photosensitizer for promoting radical cross-coupling reactions, such as between chlorobromobenzene and benzene.

Overall, the work presented here represents a significant advancement in the field of photochemically active iron compounds over the past years. Given that iron is the fourth most abundant element, substituting iron for ruthenium in photosensitizers and photoredox catalysts is a crucial step toward achieving greater sustainability in these technologies.

Cobalt group ($3d^6$)

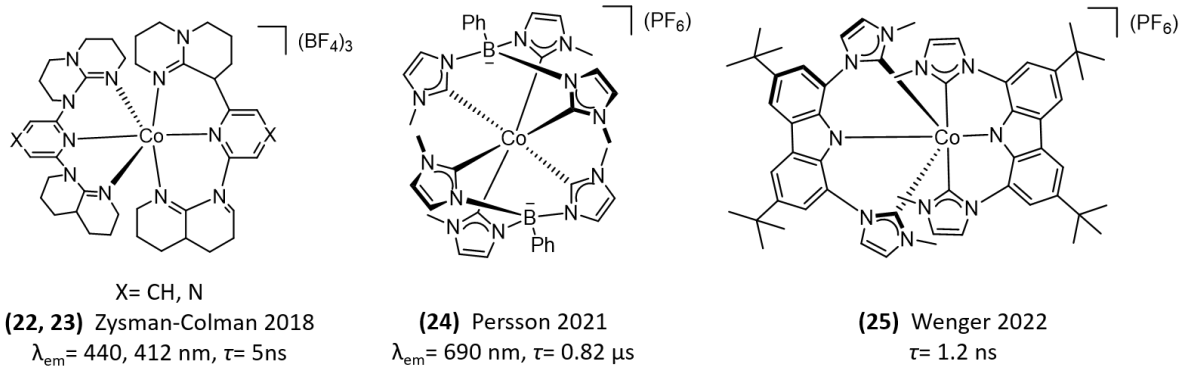


Figure 13. Molecular structure of photo-active Co(III) complexes involving different excited state.[15]

The isoelectronic configuration of Co(III) ($3d^6$) with Ru(II) and Fe(II) makes cobalt a particularly interesting candidate for photophysical applications. Despite this, the photochemistry of cobalt compounds has been relatively underexplored. Efforts to achieve LMCT emission using electron-rich pyridine-/pyrazine-based ligands led to the development of the first blue luminescent cobalt compounds (**22** and **23**), which exhibit room-temperature emission from a short-lived ^{3}LMCT state.[15a] Notably, the large bite angle of the ligands plays a crucial role in facilitating emission from the LMCT state by shifting non-emissive MC states to higher energies. The high excited-state reduction potential of these complexes (2.26 V and 2.75 V for **22** and **23**, respectively) renders them effective photo-oxidants, making them promising candidates for photo-redox catalysis such as the reported trifluoromethylation of polycyclic aromatic hydrocarbons (PAHs).

The high oxidation state of Co(III) results in a stronger ligand field, which, when combined with strong σ-donating ligands like $PhB(MeIm)_3$, facilitates emission from the MC state, as demonstrated by Persson and his co-workers (**24**).[15b] Complex **24** exhibits orange photoluminescence in acetonitrile at room temperature, with an exceptionally long-lived excited-state lifetime of approximately 1 µs. However, the emission from the $^3T_{1g}$ state to the ground state is spin-forbidden, leading to competition with non-radiative decay processes and resulting in a very low emission efficiency (0.01%) at room temperature.

As discussed earlier, the high oxidation potential and the electron-donating ligands often promote LMCT or MC emission in Co(III) complexes, making the MLCT excited state energetically inaccessible. However, Wenger group recently employed a bimca ligand consisting of a central carbazolate donor with two imidazole-based carbene substituents to achieve an MLCT as the low-energy excited state.[15c] The ligand's strong π-donating ability, coupled with its rigid strong-field coordination, shifts the MC excited state to higher energy by increasing the ligand field strength to prevent MC deactivation. However, the MLCT excited state in complex **25** is still non-emissive, although, transcient absorption spectroscopy reveals a significantly long lifetime of 1.2 ns, attributed to a mixture of MLCT and ILCT states in acetonitrile at room temperature.

Nickel group ($3d^8/3d^{10}$)

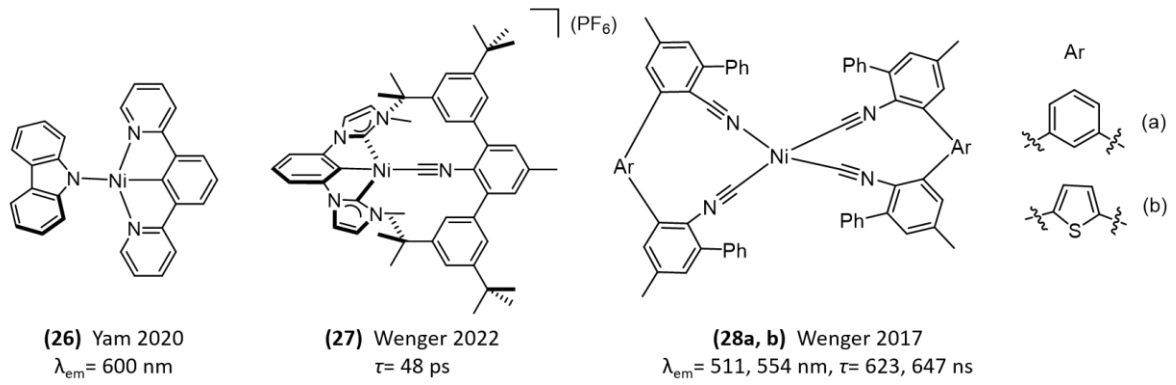


Figure 14. Molecular structure of emissive Ni(II) (**26**,**27**) and Ni(0) (**28a**, **b**) complexes.[16]

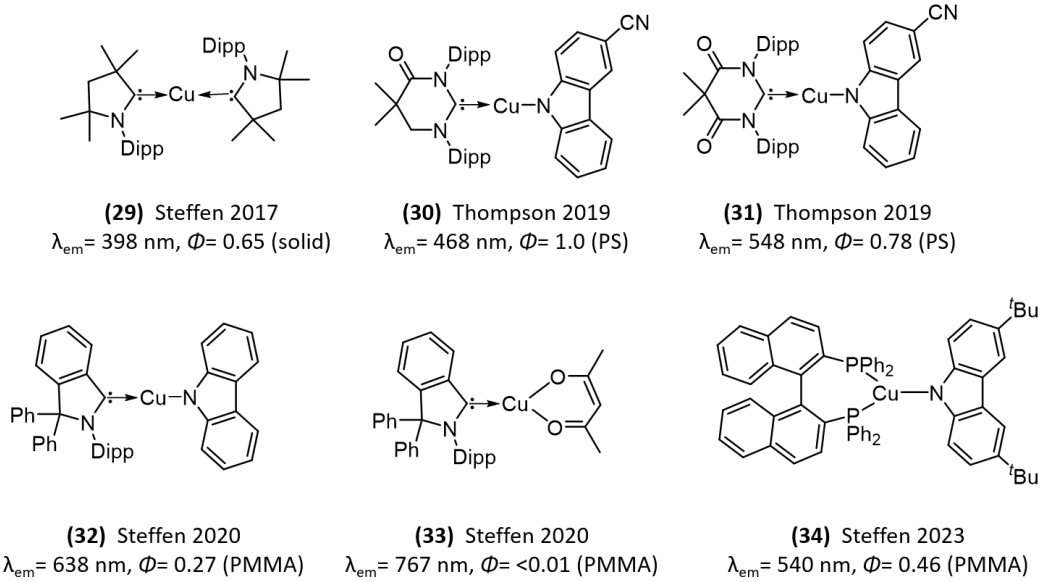
Emissive Ni(II) complexes are of importance due to their potential applications in light-driven cross-coupling catalysis and as sustainable alternatives to iso-electronic Pt(II) emitters.[61] However, the challenge with Ni(II) complexes lies in their energetically low-lying MC states, which often lead to non-radiative deactivation. The Yam group addressed this issue by employing cyclometallated N-C-N ligands and strong σ-donating carbazolyl ligands to prepare a square-planar Ni(II) complex (**26**) that exhibits weak emission around 600 nm in the solid state at room temperature.[16a] The lowest energy absorption band of these complexes was attributed to a mixture of ILCT and MLCT transitions, as confirmed by TD-DFT.

In a more recent study, Wenger and co-workers designed square-planar Ni(II) complexes incorporating tridentate N-heterocyclic carbene (NHC) and isonitrile ligands to achieve a stronger ligand field around the metal center (**27**).[16b] These modifications also protect the Ni(II) center from nucleophilic attack via steric shielding from the ligands. They observed a short-lived (48 ps) ^{3}MLCT excited state in DCM, but relaxation to the ^{3}MC state occurred rapidly, preventing the observation of photo-luminescence.

The problem of MC state deactivation, however, can be circumvented by using Ni(0), which lacks d-d* transitions due to its d^{10} electronic configuration. In this context, Wenger's group synthesized two tetrahedral Ni(0) complexes (**28a** and **28b**), featuring bidentate isonitrile ligands.[16c] Both complexes exhibited strong MLCT absorption bands in THF at 420-425 nm, with emissions observed at 511 nm and 554 nm, respectively, in frozen toluene solution at 77 K. The absence of room temperature ^{3}MLCT luminescence can be attributed to Jahn-Teller distortions and solvent coordination effects, similar to those observed in copper(I)-phenanthroline complexes. However, the insights gained from copper(I) compounds are expected to be transferable to Ni(0) complexes, suggesting that these systems hold promise for future applications in photophysics and catalysis.

Copper group ($3d^{10}$)

Photoactive Cu(I) complexes have gained significant attention over the past few decades due to considerable progress in enhancing their luminescent properties through structural modifications. The d^{10} electronic configuration of Cu(I) is particularly advantageous, as it prevents non-radiative deactivation via metal-centered (MC) transitions. Additionally, the low oxidation potential of the Cu(I)/Cu(II) redox couple facilitates the formation of metal-to-ligand charge transfer (MLCT) states, which are critical for the photophysical behaviour of these complexes. Historically, research on Cu(I) complexes was initially limited to pseudo-tetrahedral bis(imine) copper(I) complexes and their heteroleptic derivatives with diphosphine ligands.[63-64] Upon excitation, these complexes undergo Jahn-Teller distortions from the tetrahedral geometry to a more planar configuration, typical of Cu(I). This distortion, combined with exciplex formation (e.g., through solvent coordination), often leads to non-radiative deactivation, resulting in inefficient luminescence. In recent years, new classes of copper(I) compounds with linear and trigonal coordination geometries have been developed,[25]as these structures avoid the excited-state flattening distortions seen in tetrahedral complexes. This offers promising opportunities for the design of efficient and tunable photoactive materials. An additional factor driving the renewed interest in luminescent Cu(I) compounds is their potential as TADF emitter. Since the radiative transitions of Cu(I) complexes typically exhibit charge transfer character, they can feature a small $\Delta E_{(S1-T1)}$. This small gap promotes efficient reverse intersystem crossing (rISC), facilitating TADF (vide supra) in Cu(I) complexes and making them promising candidates for high-efficiency light-emitting devices. Given the vast body of research on luminescent Cu(I) complexes, the following discussion will focus on a selection of linear and trigonal Cu(I) complexes.



(29) Steffen 2017
λ_{em}= 398 nm, Φ= 0.65 (solid)

(30) Thompson 2019
λ_{em}= 468 nm, Φ= 1.0 (PS)

(31) Thompson 2019
λ_{em}= 548 nm, Φ= 0.78 (PS)

(32) Steffen 2020
λ_{em}= 638 nm, Φ= 0.27 (PMMA)

(33) Steffen 2020
λ_{em}= 767 nm, Φ= <0.01 (PMMA)

(34) Steffen 2023
λ_{em}= 540 nm, Φ= 0.46 (PMMA)

Figure 15. Molecular structure of selected emissive Cu(I) complexes.[62]

In the field of linear copper(I) complexes (see **Figure 15**), Steffen's group introduced the first phosphorescent copper(I) compounds (**29**) using cyclic alkyl amino carbene (cAAC) ligands.[62a] Compared to N-heterocyclic carbenes (NHCs), cAAC ligands are better σ-donors and stronger π-acceptors, which leads to significantly higher MLCT contribution to the T_1 state, facilitating spin-orbit coupling (SOC) and promoting coupling between the T_1 state and other singlet excited states, thereby

enabling efficient phosphorescence. The homoleptic complex, featuring two carbene chromophores, exhibits deep blue phosphorescent emission with an impressive quantum yield (Φ = 0.68).

Following the pioneering discovery of carbene-metal-amide (CMA) complexes[62b] by the Thompson group, these compounds have emerged as some of the most promising Cu(I) emitters. The linear geometry of CMA complexes, and combination of cAAC ligands with strongly σ-donating anionic amide groups, results in luminescence originating from an LLCT excited state. Notably, these complexes exhibit near-100% photoluminescence quantum yields both in the solid state and in solution at ambient temperature. The structural diversity of CMAs further extends to various carbene motifs, including monoamidocarbenes (MAC), diamidocarbenes (DAC), and cyclic amino aryl carbenes (cAArC.[62] Complexes **30** and **31**, featuring MAC and DAC ligands, respectively, exhibit extremely high radiative rate constants (in the range of 10^5 s^{-1}) and very high quantum yields in the solid-state and polystyrene films. The well-separated HOMO and LUMO in these complexes lead to a small $\Delta E_{(S1-T1)}$, promoting emission via TADF. The small $\Delta E(S_1–T_1)$ along with high k_r of emission make the CMAs highly efficient TADF emitters, resulting in impressive EQEs up to 20% in OLEDs.

Steffen and his colleagues were able synthesize **32**, employing cAArCs as acceptor moiety.[62d]The extended π-system and more electrophilic nature of the CAArC ligand facilitated a substantial red-shift in the lowest energy UV-Vis absorption, enabling the development of deep red TADF emitters (λ_{max} = 638 nm) with a radiative rate constant of 6.8 × 10^5 s^{-1} in PMMA for **32**. Single-photon correlation experiments for complex **32** also demonstrate its potential as a low-energy triplet emitter for future applications. The trigonal complex (**33**) using cAArC and acetyl-acetonate ligand even feature NIR emission with λ_{max} = 767 nm, although with very low photo-efficiency (Φ <0.01) due to the energy gap law (vide supra).

In a recent study, another trigonal Cu(I) complex (**34**), incorporating enantiomerically pure BINAP and carbazolate ligands, was found to exhibit TADF emission with considerable efficiency.[62f] This emission is also associated with circularly polarized luminescence (CPL), suggesting potential applications of Cu(I) emitters in circularly polarized electroluminescence (CP-EL).

In summary, copper(I) complexes have emerged as versatile and promising candidates for tuning emission properties, offering a wide range of possibilities for optimizing their photophysical characteristics. Researchers have established clear structure–property relationships that allow for the fine-tuning of luminescence efficiency. By modifying the ligand environment and coordination geometry, a variety of copper(I) complexes have been synthesized, covering a broad spectrum of emission wavelengths, including those in the visible range. These developments have led to the creation of efficient emitters across much of the visible spectrum, expanding their potential applications in lighting, display technologies, and sensing.

Despite these advances, low-energy emission (i.e., red and near-infrared) continues to present a significant challenge for copper(I) complexes. As with "classical" emitters, such as those based on platinum or iridium, the efficiency of copper(I) complexes with low-energy emission is often hindered by

nonradiative processes. Consequently, achieving high quantum yields for low-energy emission remains a key hurdle in developing copper(I) complexes for applications requiring red or near-infrared light.

However, the introduction of thermally activated delayed fluorescence (TADF) as a new emission mechanism has shown tremendous promise in overcoming these challenges. Copper(I) complexes that exhibit TADF have the potential to rival iridium(III)-based emitters, which are currently widely used in commercial applications such as organic light-emitting diodes (OLEDs) and other optoelectronic devices.

With further advances in ligand design, coordination chemistry, and a deeper understanding of the photophysics of copper(I) complexes, it is expected that these materials will play an increasingly important role in the development of efficient, low-cost, and sustainable emitters for a variety of optoelectronic applications, including lighting, displays, and beyond.

Zinc group ($3d^{10}$)

The high abundance of zinc (~75 ppm in the Earth's crust)[65] and its d^{10} electronic configuration, similar to Cu(I), play a significant role in preventing metal-centered transitions and minimizing non-radiative decay. This makes zinc an ideal candidate for various photonic applications. However, the creation of zinc-based emitters involving triplet excitons has been limited, primarily due to the high redox stability of zinc(II), which suppresses the formation of MLCT states essential for SOC and the promotion of triplet excitons. As a result, the zinc center generally plays a passive role in the emission process, acting more as a structural component than an active participant in the photophysics. Consequently, zinc(II)-based complexes tend to exhibit only ligand-centered fluorescence (LC) or intraligand charge transfer (ILCT) transitions.[66] When designing zinc-based photonic materials that involve triplet excitons, key strategies focus on promoting ligand-to-ligand charge transfer (LLCT) and intraligand charge transfer (ILCT) processes,[67] with a minor contribution from ligand-to-metal charge transfer (LMCT). These strategies aim to achieve sufficient SOC for effective triplet-state emission. However, the development of efficient zinc(II)-based triplet emitters remains an ongoing challenge, with only a few notable examples reportedin the literature. **Figure 16-17** presents selected zinc(II)-based emitters, which will be discussed in detail in the following section. The photophysical data for compounds **35**–**44** are summarized in **Table 1**.

One potential example of a zinc(II) compound involving triplet excitons is the work by Adachi et al.[2] They synthesized two new homoleptic zinc complexes, **35a** and **35b**, featuring phenylbenzoxazole derivatives. These complexes exhibited green emission with excellent quantum yields of up to 78%. Transient photoluminescence decay studies revealed an interplay between prompt fluorescence and TADF component. Compounds **35a** and **35b** demonstrated efficient TADF with quantum yields ranging from 50% to 60%. Notably, compound **35a** also achieved an external quantum efficiency (EQE) of 19.6% when used as an emitter material in an OLED device. The TADF emission in **35a** and **35b** is facilitated by an ILCT process between the phenylbenzoxazole acceptor and the phenoxazine donor unit. Although the zinc(II) center does not directly participate in the charge transfer, quantum chemical calculations support the role of zinc coordination in reducing the $\Delta E_{(S1-T1)}$. This is achieved by altering

the angle between the donor and acceptor units, thus resulting efficient TADF emission. A comparison with the pure ligand indicates that the coordination with zinc only slightly influences the occurrence of TADF, as the uncoordinated ligand also exhibits delayed fluorescence and a good quantum yield (Φ = 63%). However, the rate constant for k_{rISC} in the zinc complex (**35a**) is 25 times larger than that of the pure ligand, highlighting the significant impact of zinc coordination on enhancing the TADF process.

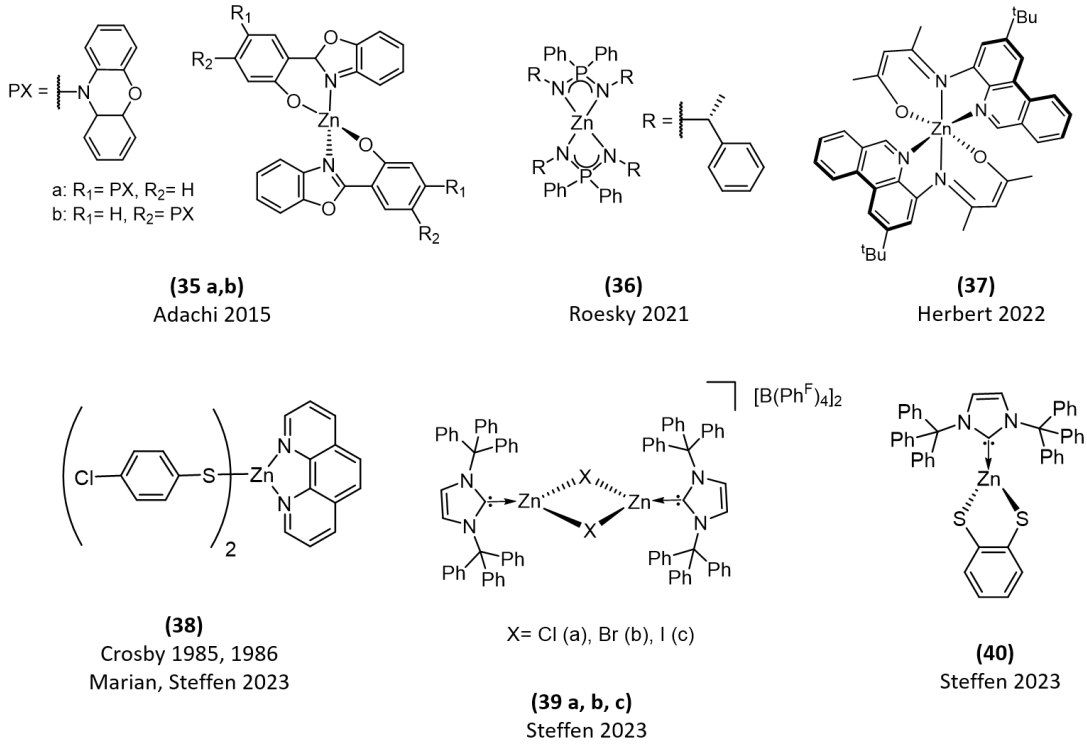


Figure 16. Molecular structure of selected emissive Zn(II) complexes. [1, 2, 68, 69, 70, 71]

In 2021, Roelsky and colleagues investigated the Zn(II) complex **36** using an iminophosphonamide ligand.[1] Compound **36** exhibits TADF emission in the solid state, driven by an ILCT mechanism. In compound **36**, the NPN ligands are strongly twisted relative to each other, enabling ISC and rISC due to the resulting $\Delta E_{(S1-T1)}$ of approximately 1000 cm^{-1}. In contrast, the parent compound with a planar ligand environment, exhibits only prompt fluorescence. Despite the small $\Delta E_{(S1-T1)}$ in compound **36**, the quantum yield at room temperature is relatively low (3%), primarily due to dominant non-radiative deactivation of the S_1 state. This study highlights the challenges in developing efficient TADF emitters based on zinc(II) complexes, emphasizing the delicate balance between geometry, energy gap, and non-radiative deactivation processes.

Recent work by the Herbert's group involved the preparation of a series of pseudo-octahedral zinc(II) complexes (**37**) featuring phenanthridine derivatives.[68] The key structural element is the use of benzannulated N^N^O pincer ligands, where the extended π-conjugation (via benzannulation) enhances light absorption and stabilizes excited states, while the tridentate coordination enforces rigidity. These complexes exhibited bright yellow phosphorescence in the solid state at room temperature, with quantum yields ranging from 1% to 6%. The emission is also driven by an ILCT

mechanism. Additionally, the less pronounced N_{amido} character of the ligand, through the combination of non-negligible pπ−dπ mixing in a stronger (pseudo)octahedral ligand field and delocalization through the acetylacetone-derived ligand arm, promotes emission from the long-lived triplet state in compound **37**.

Heteroleptic zinc(II) complexes (**38**) of 1,10-phenanthroline and thiophenolate ligands were studied by Crosby and his colleagues in 1980s, where they observed LLCT emission.[69] In particular, they identified that efficient phosphorescence in Zn(II) systems arises when ligands possess low-lying triplet states and sufficient spin–orbit coupling, often facilitated by ligand design rather than the metal itself. More recent work by Marian's and Steffen's groups,[70] using detailed spectroscopic experiments and quantum mechanical calculations, revealed the emission to be TADF with high k_r upto 3.5×10^5 s^{-1} at room temperature. It emphasizes that, despite the weak intrinsic spin–orbit coupling of Zn(II), efficient triplet population can still occur through ligand-centered excited states with appropriate orbital character (e.g., n→π* or charge-transfer states). The work further shows how subtle orbital mixing and vibronic coupling can enhance ISC rates, and how molecular rigidity and electronic delocalization govern the balance between radiative and non-radiative decay. However, the TADF efficiency for **38** is very low at room temperature, and the folding motion of the thiolate ligand upon excitation makes the complex highly susceptible to photodissociation.

Recently, Steffen's group synthesized low-coordinate trigonal zinc(II) complexes using sterically demanding N-heterocyclic carbene ligands, specifically (*N*,*N*′-bis(triphenylmethyl)imidazolylidene).[71] Complexes of the type $Zn(X_2)(ITr)_2[B(C_6F_5)_4]_2$ (**39a**, **39b**, **39c**) or Zn(bdt)(ITr) (**40**), exhibit long-lived phosphorescence from triplet excited states (^{3}LLCT or ^{3}LC) in the solid state at room temperature. The trigonal geometry and low coordination number allow for subtle structural and electronic flexibility in the excited state, which influences the emission properties. Notably, theoretical calculations show that the ITr carbene ligand is not photochemically innocent, as its phenyl substituents can transiently interact with the electron-deficient zinc center upon excitation, thereby stabilizing the excited state and affecting the electronic structure. The long-lived ^{3}LC state (τ = 9.03 ms) in complex **40** is particularly interesting for applications in photocatalysis.

Yang and co-workers[72] reported a series of square-pyramidal Zn(II) complexes (**41 a**, **b**) organized in a rigid dinuclear architecture, where the ligand framework enforces well-defined donor–acceptor orientations and thereby precisely controls both electronic coupling and conformational flexibility. These complexes exhibit bright green-to-yellow emission in the solid state at room temperature, with photoluminescence quantum yields reaching up to ~50%. The emissive behavior is attributed to thermally activated delayed fluorescence (TADF), arising from efficient reverse intersystem crossing (rISC) between closely spaced singlet and triplet charge-transfer states. The rigid dinuclear scaffold plays a decisive role in enabling this mechanism by suppressing non-radiative decay pathways, reducing structural relaxation in the excited state, and optimizing the energetic alignment between frontier orbitals. As a result, stabilized intramolecular charge-transfer (CT) excited states with a small singlet–triplet energy gap are formed, which facilitates efficient thermal upconversion from T_1 to S_1. A particularly noteworthy aspect of these systems is luminescence polymorphism, where different solid-

state packing motifs lead to distinct emission colors which arises from variations in intermolecular interactions, including π–π stacking, metal–ligand contacts, and conformational differences within the dinuclear core. These packing-dependent effects modulate the local electronic environment and, consequently, the relative stabilization of singlet and triplet excited states.

In 2007, Bernhard and his group[73a] synthesized the Zn(II) hemi-cage **42**, in which three 2,2′-bipyridine ligands are interconnected through aromatic bridges, forming a rigid hemicage architecture. This structural modification was shown to significantly alter the photophysical behavior compared to the parent $[Zn(bpy)_3]^{2+}$ complex. While the unmodified tris(bipyridine) Zn(II) system follows the expected behavior for a d^{10} metal center, displaying ligand-centered fluorescence at 326 nm—the hemi-cage complex **42** exhibits a much higher radiative rate constant and was initially interpreted as showing fast phosphorescence. The emission of the hemi-cage system (λ_{em} ~ 485 nm) with a short lifetime (~0.089 μs) and strong oxygen sensitivity led to the conclusion that aromatic bridging introduces an additional triplet state, enabling efficient intersystem crossing (ISC) and phosphorescence. However, later reinvestigation by Steffen and Marian group[73b] using temperature-dependent steady-state and time-resolved spectroscopy, combined with theoretical calculations revealed that $[Zn(bpy)_3]^{2+}$ and its hemicage derivative were found to primarily undergo fluorescence at room temperature, but with markedly different radiative rate constants (k_r ~ 2 × 10^8 s^{-1} for the parent complex versus 1.2 × 10^6 s^{-1} for **42**). Only weak phosphorescence was detected at low temperatures on the millisecond timescale. The key difference between the two systems lies in the electronic structure of the hemicage ligand framework, which introduces additional intraligand charge-transfer states. These states significantly accelerate intersystem crossing into the ligand-centered triplet state (^{3}LC), reducing the ISC timescale from ~350 s^{-1} in the parent complex to ~82 ns in the hemicage system, while simultaneously lowering the fluorescence rate constant.

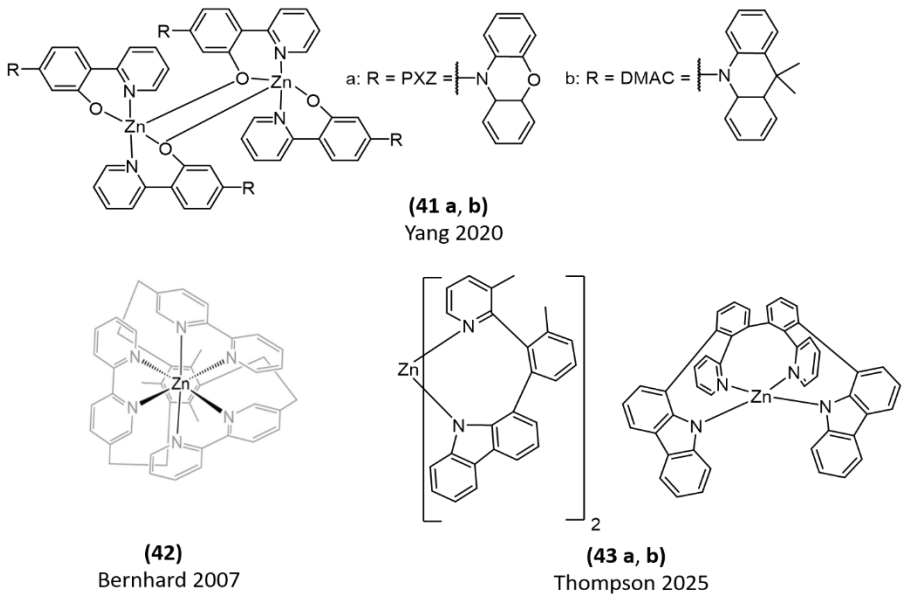
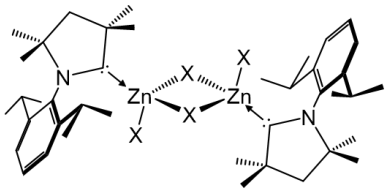


Figure 17. Molecular structure of selected emissive Zn(II) complexes. [72-74]

In 2025, Thomson group[74] designed Zn(II) complexes featuring carbazolate (Cz) donors electronically decoupled from pyridyl acceptors via an ortho-linked phenylene bridge, where methylation is used to restrict torsional motion and tune photophysical properties. Complex **43a** exhibit efficient thermally activated delayed fluorescence (TADF) with photoluminescence quantum yields up to ~30% in solution and small singlet–triplet gap of 34 meV. Methylation enhances intersystem crossing efficiency, giving higher delayed-to-prompt emission ratios and k_{ISC} values of (0.6 -1) × 10^8 s^{-1}, exceeding typical metal-free TADF systems by an order of magnitude. The authors also reported dual emission from **43a** due to low singlet-triplet gap. A major structural extension involves linking the bidentate ligands into a tetradentate, cradle-like framework ($H_2N_2R_2$), which enforces strong preorganization and increases through-bond conjugation. The resulting complex **43b** has comparatively higher singlet-triplet energy gap (86 meV), without any dual emission and with the most efficient ISC pathway in the series, while also enhancing absorption strength and molar absorptivity. Computational analysis further reveals that electronic communication is not limited to isolated donor–acceptor pairs but extends through interligand interactions (Cz···Cz and pyr···phenyl overlap), leading to cooperative exciplex-like behavior across the whole assembly.

Steffen and co-workers published a study on Zn(II) complexes **44a–c**, which are based on cyclic (alkyl)(amino)carbene (^{Me}cAAC).[3] The study includes both dimeric complexes with bridging halide ligands and monomeric complexes with coordinating acetonitrile. The bromide and iodide complexes alternate between monomeric and dimeric structures depending on the solvent or concentration. All the investigated complexes exhibit photoluminescence in the visible range, with the {(^{Me}cAAC)Zn} unit acting as the chromophore, and show ultra-long lifetimes in the millisecond range, which is characteristic of phosphorescence.



X= Cl (a), Br (b), I (c)

(44a, b, c)
Steffen 2022

Figure 17. Molecular structure of zinc(II) complex based on cAAC.[3]

In the crystalline solid state, upon excitation at a wavelength of 300 nm, all three compounds displayed dual emission: a high-energy band and a broad low-energy emission band. A photochemical transformation of these complexes was observed after a short measurement time, a decrease in the high-energy emission band intensity was associated with simultaneous increase in the low-energy emission band, resulting in the formation of several emissive species. According to quantum chemical calculations and low-temperature measurements (77 K), the high-energy, long-lived emission originates from a triplet state with XCT/LE_{CAAC} character while the low-energy emission band was assigned to a localized triplet state with Dipp $\pi\pi^*$ character. The population of this state is associated

with the asymmetric rotation of the ^{Me}cAACligand around the C-Zn bond and diverse photochemical changes including halide dissociation. Although, the low photostability of these complexes limits their use for further applications, this research highlights the potential of the cAAC ligand for photoactive zinc(II) complexes. Further modifications to the ligand sphere will be of interest for achieving improved photo-stability and enhanced photophysical properties.

Table 1. Photophysical data of complex **35-44** at RT.

complex	medium	λ_{max} [nm]	T	Φ	k_r [s^{-1}][a]	Ref
35a	mCBP (6 wt%)	542	12.8 ns, 37.8 µs	0.78	-	[2]
35b	mCBP (6 wt%)	523	-	0.58	-	[2]
36	Solid	448	24.8 µs	0.03	1210	[1]
37	Solid	539	27 ms	0.06	2.2	[68]
39a	Solid	584	80 µs	0.04	500	[71]
39b	Solid	594	68 µs	0.02	294	[71]
39c	Solid	610	14 µs	0.004	286	[71]
40	Solid	554	9.03 ms	0.04	4.4	[71]
41a	powder	538	2.09 µs	0.13	-	[72]
41b	powder	497	2.45 µs	0.50	-	[72]
42	powder	425	5.4 ns	0.08	1.2* 10^6	[73]
43a	toluene	532	7 ns, 0.81 µs	0.29	3.5	[74]
43b	toluene	525	7 ns, 5.5 µs	0.20	0.36	[74]
44a	Solid	360, 451	n.d	0.03	-	[3]
44b	Solid	370, 515	n.d	-	-	[3]
44c	Solid	355, 570	n.d	-	-	[3]

[a]Calculated with $k_r = \Phi/\tau$ unless specified in the reference. n.d (not detectable).

The examples presented here highlight both the challenges associated with designing efficient triplet emitters based on zinc(II) and the considerable potential of this class of compounds for future applications. The use of zinc(II) enables the development of not only phosphorescent emitters but also thermally activated delayed fluorescence (TADF) systems. Moreover, high quantum yields of up to 0.8 can be achieved, with emission spanning large portions of the visible spectrum (Table 1). Although the metal center itself does not directly participate in the radiative processes, owing to the high redox stability of zinc(II), its structural role nevertheless exerts a beneficial influence on the overall photophysical properties.

1.9 Objective of this Thesis

Zinc(II)-based efficient emitters offer ecologically sustainable alternatives to compounds containing rare metals and have the potential to make a significant contribution to environmental protection in various applications, such as OLEDs. However, the unique properties of zinc(II) present challenges in designing effective triplet emitters. Due to its high redox stability, the d-orbitals of the metal are not involved in the photophysical processes, limiting spin-orbit coupling (SOC). Despite these challenges, several promising studies highlight the high potential of this class of compounds. Within the framework of this doctoral thesis, several design strategies will be explored to explore the photophysical behaviours of Zn(II) complexes.

As presented in the previous section, the reported Zn(II) complexes (**44a–c**) supported by cyclic (alkyl)(amino)carbenes (MecAAC), exhibit visible photoluminescence with millisecond lifetimes, confirming phosphorescence from triplet states associated with the {(MecAAC)Zn} chromophore. However, upon UV excitation, they show dual emission that evolves over time due to photochemical processes such as halide dissociation and structural rearrangement that limits their potential application. From a design perspective, cyclic (alkyl)(amino)carbenes (cAACs) are particularly valuable ligands for Zn(II) photophysics because they combine strong σ-donation with π-accepting ability, enabling stabilization of metal–ligand charge-transfer states even in redox-inert d^{10} systems, while their modular and sterically tunable framework allows control over coordination geometry and excited-state accessibility. However, ligand flexibility and halide lability can introduce photochemical instability, suggesting that future design should focus on rigidifying the cAAC framework and stabilizing the coordination environment to achieve more robust and single-state emission behavior.

In this thesis, cyclic (alkyl)(amino)carbene (cAAC)-based ligands will be employed as electron-accepting chromophores coordinated to Zn(II), and their combinations with a range of donor ligands will be systematically explored to construct donor–acceptor (D–A) architectures. By varying the donor strength and electronic properties of the auxiliary ligands, the electronic structure of the complexes will be tuned, thereby modulating excited-state energies, charge-transfer character, and overall photophysical behavior. In parallel, differently substituted cAAC ligands will be investigated to evaluate how steric bulk and conformational constraints influence Zn–carbene bonding dynamics and emission properties.

To minimize photochemical instability arising from halide dissociation and Zn–carbene bond rotation observed in related systems, a synthetic strategy based on halide abstraction from the parent dimeric complex $[Zn_2(cAAC)_2X_4]$ will be employed.[75] This approach is expected to generate linear or low-coordinate Zn(II) complexes bearing strongly bound carbene chromophores, reducing structural lability. The resulting increase in positive charge at the metal center is anticipated to favor ligand-to-metal charge transfer (LMCT) states and enhance emissive excited-state formation.

Additionally, by introducing alternative monodentate ligands, different coordination environments around Zn(II) will be accessed to further tune geometry, rigidity, and electronic coupling. The

photophysical properties of all synthesized complexes will be investigated in detail using steady-state and time-resolved spectroscopy, supported by quantum chemical calculations to correlate structural features with excited-state dynamics and emission behavior.

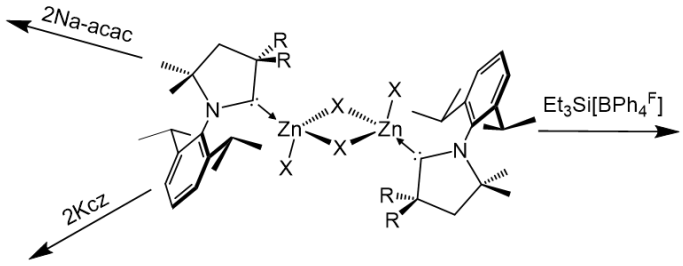


Figure 18. Halide abstraction and halide exchange to obtain low-coordinate zinc(II) complexes.[75]

Donor-M-acceptor motifs are extremely useful for achieving LLCT states, which are helpful for ensuring high radiative rates of transition and TADF. Building on this design principle, the second project focuses on the use of strongly electron-donating benzene-1,2-dithiolate ligands to construct a rigid, photostable dimeric Zn(II) complex incorporating a cAAC-based chromophore. This strategy aims to combine structural robustness with enhanced electronic coupling, enabling stabilized charge-transfer excited states and improved emissive performance.[4]

The overarching aim is also to establish a clear structure–property relationship for the rational design of Zn(II) luminophores exhibiting efficient thermally activated delayed fluorescence (TADF). To elucidate how structural factors govern TADF in Zn-based emitters, a next generation of dithiophenolate-based Zn(II) complexes has been developed in combination with cAAC-derived chromophores.

In this context, bulky ^{Menth}cAAC ligands will be employed to yield low-coordinate, trigonal Zn(II) complexes with variously substituted dithiophenolates, providing a structurally well-defined platform to probe the influence of coordination geometry, steric protection, and donor strength on excited-state behavior. The dithiophenolate ligands introduce strong electron donation and promote ligand-to-ligand charge transfer (LLCT) character, which is beneficial for accessing TADF-active states.[5]

To further enhance luminescence efficiency and suppress non-radiative decay pathways, sterically demanding carbene ligands will be used to rigidify the coordination environment and stabilize the Zn–ligand framework against photodecomposition. This combined strategy allows systematic tuning of electronic structure and excited-state dynamics, enabling direct correlation between molecular design, charge-transfer character, and TADF performance in Zn(II) luminophores.

2 Result and Discussion

2.1 Synthesis, structural characterization and rigidity dependent dual phosphorescence behavior of high-energy phosphorescent zinc(ii) cyclic (alkyl)(amino)carbene complexes

This subchapter as part of this partially cumulative dissertation work was published in collaboration with Royal society of chemistry.[75] Reprinted with permission from *Dalton Trans.,* **2026***,* ***55****,* 5519-5528. copyright © The Royal Society of Chemistry 2026.

Summary: The study explores the synthesis, structural characterization, and photophysical properties of cyclic (alkyl)(amino)carbene (cAAC) zinc(II) complexes, focusing on their unique rigidity-dependent dual phosphorescence. The synthesized complexes include tetrameric zinc halides and tetrahedral zinc(II) derivatives with acac or carbazolate ligands. The research reveals that these complexes exhibit rare triplet-state phosphorescence in zinc-based systems. High-energy excitation leads to emission primarily from high-energy states due to strong Franck-Condon overlaps, while low-energy excitation enables direct triplet state population and geometry-driven transitions. These behaviors, influenced by the molecular rigidity, highlight equilibrium between excited states and emphasize the impact of molecular structure on emission profiles.

Contribution to experimental part: approx. 70%

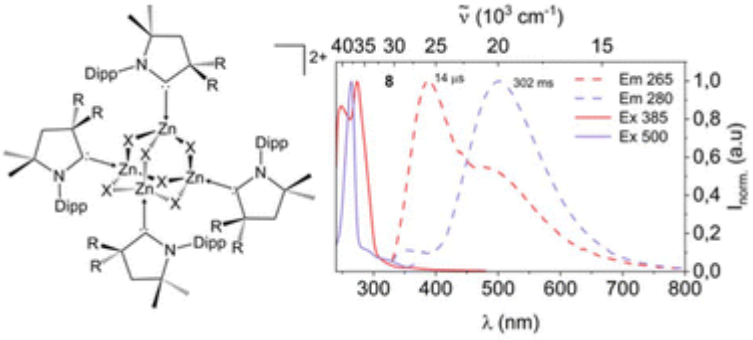
Contribution to the written part: approx. 70%

Synthesis, structural characterization and rigidity dependent dual phosphorescence behavior of high-energy phosphorescent zinc(ii) cyclic (alkyl)(amino)carbene complexes

Mousree Mitra, Ondřej Mrózek, Andrey Belyaev, Lars Janiak, Christel M. Marian and Andreas Steffen

Abstract

The study explores the synthesis, structural characterization, and photophysical properties of cyclic (alkyl)(amino)carbene (cAAC) zinc(II) complexes, focusing on their unique rigidity-dependent dual phosphorescence behavior. Starting from previously reported dimeric $[Zn_2X_2(\mu\text{-}X)_2(cAAC)_2]$ (X = Cl, Br), halide abstraction with Et_3Si^+ gives dicationic tetramers with an adamantyl-like Zn_4X_6 core, while the reaction with Na(acac) (acac = acetylacetonate) or KCz (Cz = carbazolate) leads to ligand exchange and isolation of [ZnCl(acac)(cAAC)] (**11**) and [ZnCl(Cz)(THF)(cAAC)] (**12**), respectively. While **12** displays orange phosphorescence from ^{3}LLCT (LLCT = ligand-to-ligand charge transfer) states both at room temperature and at 77 K, complex **11** and the tetrameric compounds exhibit excitation wavelength-dependent unusual high-energy UV-blue phosphorescence and green-yellow luminescence. The experimental data suggest that high-energy excitation leads to emission primarily from high-energy states due to strong Franck–Condon overlaps, while low-energy excitation enables direct triplet state population and geometry-driven transitions. This behavior, influenced by the molecular rigidity, appears to be the result of an equilibrium between different excited states and emphasizes the impact of the molecular structure on the emission profiles.



Introduction

Cyclic (alkyl)(amino)carbene (cAAC) complexes of transition metals (TM) are a highly interesting class of compounds with diverse applications in (photo)catalysis,[1–9] organic synthesis,[1–3] and the development of photoluminescent and photoactive materials,[10–12] which can be traced back to the unique electronic and steric properties of the carbene. Modifying the substituents on the α-carbon of the cAAC ligand provides steric control, enabling the formation of stable, unusual low-coordinate metal complexes, such as cationic $[Pd(allyl)(^{Menth}cAAC)]BF_4$ (Menth = menthyl),[13] $[Au(^{Ad}cAAC)(tol)][B(C_6F_5)_4]$[14] (Ad = adamantyl, tol = toluene) or [Zn(bdt′)(^{Menth}cAAC)] (bdt′ = benzene-1,2-dithiolate and its derivatives).[15] In addition to their steric effects, cAAC ligands exhibit significantly higher π-accepting properties than traditional N-heterocyclic carbenes (NHCs) of imidazolylidene and imidazoline-2-ylidene types, a critical component for stabilization of transition metals in unusual low oxidation states, as observed in Au^0, Ni^0, Mn^0, and Zn^0 complexes.[1,4–9]

Electrophilic cAAC ligands can also serve as highly efficient excited state π electron density acceptors, facilitating the generation of metal-to-ligand charge transfer (MLCT) or ligand-to-ligand charge transfer (LLCT) excited states that are important to realize visible light absorption and luminescence in TM complexes. In the last decade, d^{10} coinage metal (Cu/Ag/Au) cAAC complexes have been studied extensively regarding their photophysical and chemical properties.[12,16] The great potential and important influence of the carbene ligand on the excited state behaviour is nicely exemplified by analysis of linear $[Cu(^{Me}cAAC)_2]PF_6$ reported by Gernert *et al.*, which exhibits intense blue phosphorescence $T_1 \rightarrow S_0$ both in the solid state and in PMMA films with high radiative rate constants (k_r = 2.3–9.4 × 10^4 s^{-1}), making it one of the fastest phosphorescent Cu^I emitters known to date.[10] In contrast, structurally related $[Cu(IDipp)_2]PF_6$ bearing NHC ligands is barely emissive and lacks a visible MLCT band in the UV-Vis absorption spectrum.[10] This stark difference in luminescence behaviour can be attributed to the lower LUMO energy of the cAAC ligand compared to IDipp, leading to an enhanced MLCT contribution in the T_1 state, facilitating strong spin–orbit coupling (SOC) with singlet excited states to enable efficient phosphorescence. Subsequent studies have shown that construction of D–Cu^I–A (D = donor, A = acceptor) motifs greatly extends the space of photophysical properties. For example, carbene–metal–amides (CMA) can achieve outstanding k_r of up to 10^6 s^{-1} for blue to orange emission involving triplet states.[12,17] In these systems, the emission mechanism shifts from phosphorescence to thermally activated delayed fluorescence (TADF) due to a very small energy gap ΔE_{S1-T1} between singlet and triplet excited states of LLCT character, which allows thermal repopulation of the fluorescent S_1 state by reverse intersystem-crossing (rISC) at room temperature.[18, 19] Consequently, CMAs have successfully been incorporated into organic light-emitting diodes (OLEDs), demonstrating efficient electroluminescence and underscoring their potential for optoelectronic applications.

Despite the similar d^{10} electronic configuration, the number of thoroughly investigated luminescent Zn^{II} complexes is relatively small, with the majority being purely fluorescent.[20–29] This limitation arises primarily from zinc's high ionization potential $Zn^{II} \rightarrow Zn^{III}$, which prevents the formation of metal-to-ligand charge transfer (MLCT) states—essential for facilitating efficient spin–orbit coupling (SOC) required for formal spin-forbidden processes (r)ISC or phosphorescence. As a result, when designing zinc-based photonic materials that involve triplet excitons, key strategies focus on promoting $^{1/3}$LLCT and intraligand ($^{1/3}$IL) CT excited states with small energy gaps between the singlet and triplet excited states to reduce the significance of SOC and enable TADF.[18,19,30–33]

One notable approach involves the work by Adachi *et al.*,[34] who used phenylbenzoxazole derivatives to achieve a small ΔE_{S1-T1} *via* spatial separation of HOMO and LUMO. These complexes exhibit TADF with good quantum yields of up to 50–60% in mCPB matrices at room temperature, resulting in external quantum efficiencies (EQE) of 19.6% when used as emitters in OLEDs. In the 1980s, Crosby and colleagues studied a series of heteroleptic Zn^{II} complexes of 1,10-phenanthroline and thiophenolate ligands, observing weak phosphorescence from ^{3}LLCT states, and many subsequent works were built on this interpretation.[35–40] However, more recent work by our group, aided by detailed spectroscopic and quantum mechanical calculations, revealed that these complexes show TADF with high radiative

rate constant (k_r) up to 3.5 × 10^5 s^{-1} at room temperature, but non-radiative decay is more facile and thus the compounds are very inefficient emitters.[41]

Phosphorescence remains an even rarer phenomenon for zinc(ii)-based emitters with the exception of porphyrins.[23, 24] However, recent work has demonstrated a series of low-coordinate Zn^{II} complexes featuring sterically demanding ITr ligands to achieve long-lived phosphorescence from ^{3}LLCT or ^{3}LC state.[42] In 2022, we investigated the photophysical and photochemical properties of a series of dimeric and monomeric Zn^{II} halide complexes bearing cAAC ligands, which show rare ultralong-lived luminescence originating from ^{3}XLCT/LE_{cAAC} states.[43] However, these Zn^{II} cAAC complexes were found to be highly photolabile, most likely due to asymmetric distortion of the carbene ligand and halide dissociation among other unidentified processes. Despite this photo-instability, the study underscores the potential of cAAC ligands for expanding the photophysical properties of zinc(ii) complexes.

To address the limitations of photostability and explore the potential for more stable photoluminescent Zn^{II} cAAC compounds, we investigated the use of halide dimers as precursors for ligand exchange.[15,44] This approach allowed access to a variety of coordination geometries and ligand combinations, which modulated the photophysical properties of the resulting zinc(ii) carbene complexes. One such strategy involved synthesizing a new class of Zn^{II} TADF compounds by incorporating dithiophenolate ligands as electron-donating moieties and exploring different cAAC substitutions. Remarkably, these complexes demonstrated radiative rate constants (k_r) up to 1.2 × 10^6 s^{-1} at room temperature—setting a record for Zn^{II}-based emitters, and even competing with well-established rare-metal-based emitters.[15]

In this work, we further explore the structure–property relationships of cAAC-bearing Zn^{II} complexes attempting to access low-coordinated, primarily linear Zn^{II} complexes by halide abstraction. This approach is inspired by the successful design of $[CuL_2](PF_6)$-type compounds, which exhibit triplet excitons and have been instrumental in developing efficient luminescent materials.

Results and discussion

Synthesis and characterisation

We followed the reported synthetic strategy to prepare a series of carbene salts and their corresponding zinc(ii) halides **1**–**5**, which were obtained as crystalline solids in yields of 70–80% (Fig. 1, and SI).[43] Regardless of the *N*-substituent at the cAAC ligand, the chloride complexes consistently formed a dimeric arrangement of type $[Zn_2Cl_2(\mu\text{-}Cl)_2(^{R}cAAC)_2]$ (**1**, **2** and **4**), which was also observed for the bromide derivative **3** bearing ^{Me}cAAC as confirmed by single-crystal X-ray diffraction (SC-XRD). However, upon slow diffusion of *n*-pentane into the reaction mixture of $ZnBr_2$ with ^{Et}cAAC, the monomeric THF-coordinated bromide complex **5** was isolated (Fig. 1). This monomerization upon solvent coordination is typical for bromide and iodide complexes, attributed to the relatively weaker Zn–X bond strength, as previously observed for $[Zn_2X_2(\mu\text{-}X)_2(^{Me}cAAC)_2]$ (X = Br, I) with CH_3CN coordination.[43] While the Zn–$C^{carbene}$ bond lengths in compounds **1**–**4** are very similar (*ca.* 2.05 Å), it is slightly elongated in the monomeric complex 5 to 2.069(1) Å.

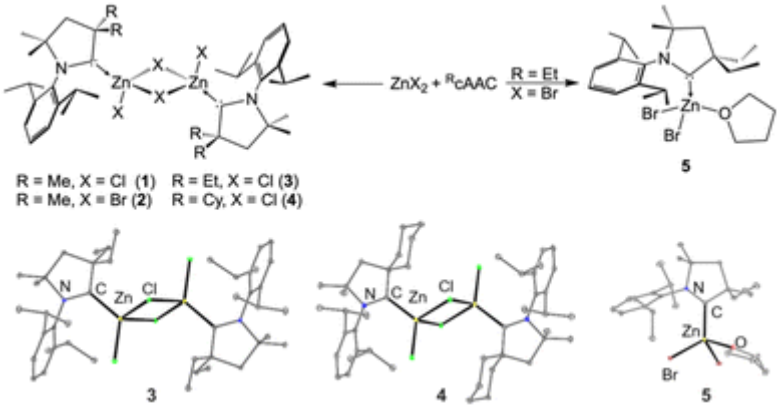


Fig. 1 Top: Synthesis of dimeric $[Zn_2X_2(\mu\text{-}X)_2(cAAC)_2]$ (**1**–**4**) and of monomeric [ZnBr(THF)(cAAC)] (**5**). Bottom: Molecular structures of **3**–**5** determined by SC-XRD.

We have recently reported the synthesis of tricoordinate Zn^{II} complexes employing the tropylium-substituted carbene ITr, where the aryl substituents induced a low-energy ^{3}LC state with millisecond lifetimes. [42] To enhance the charge transfer (CT) component in these low-coordinate zinc-based emitters, we employed a similar synthetic approach starting from **1**–**5** bearing more electrophilic cAAC ligands. Curious about the potential access to trigonal and linear complexes, we added one equivalent of the *in situ* prepared strongly halophilic silylium reagent $[(Et_3Si)(toluene)][B(C_6F_5)_4]$ [45,46] at room temperature to **1**–**5** suspended in toluene (Fig. 2). This reaction led to partial halide abstraction and the formation of Zn_4X_6 cluster-type tetramers **6**–**8** and **10** in 60–80% yield. However, we obtained only a very small amount of compound 9 following halide abstraction, which is likely due to an undesired side reaction between the coordinated THF and the silylium reagent.

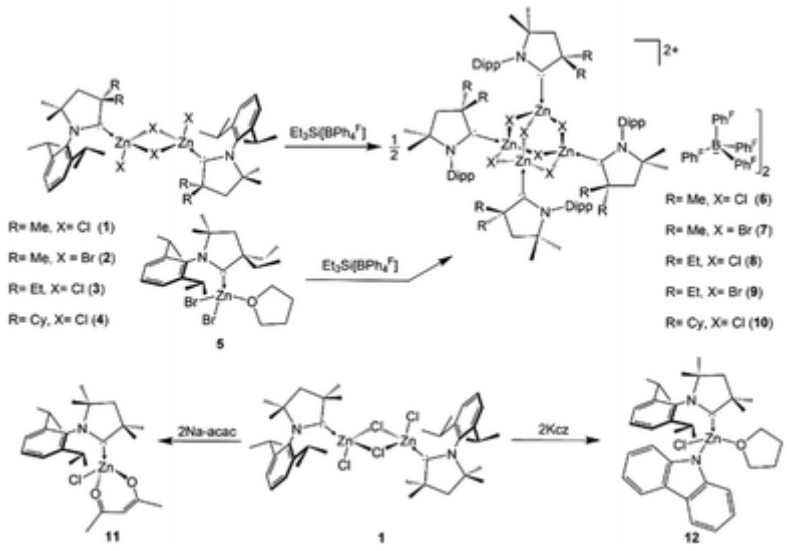


Fig. 2 Synthesis of tetrameric **6–10** by halide abstraction from **1–5**, and ligand exchange reactions of **1** to give [ZnCl(acac)(^{Me}cAAC)] (**11**) and [ZnCl(Cz)(THF)(^{Me}cAAC)] (**12**).

Interestingly, the steric demand of the cAAC ligands has a significant impact on product formation as no monomeric or dimeric products were observed. While the reaction proceeded smoothly with chloride

and bromide complexes, the corresponding iodide derivatives produced a complex mixture of products with no clear indication of the desired outcome, presumably due to thermodynamic instability.

Colourless single crystals suitable for X-ray diffraction studies were obtained for compounds **6**, **7**, and **9** by gas-phase diffusion of pentane into saturated DCM solutions. Compounds **8** and **10** could only be isolated as microcrystalline powders, regardless of the crystallization conditions. Compounds **6** and **7** are solvated with DCM and crystallized in the monoclinic *C*2/*c* space group, while **9** crystallized in the *Pbca* space group. The X-ray structures of **6**, **7** and **9** reveal a dicationic tetrameric cluster motif and two $[B(C_6F_5)_4]^-$ acting as counter anions (Fig. 3).

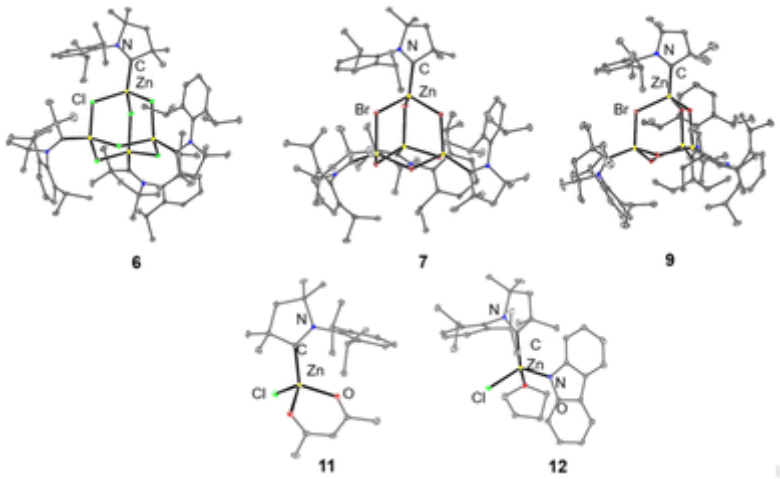


Fig. 3 Molecular structures of **6–12** in the solid state determined by SC-XRD studies. Hydrogen atoms, solvent molecules and counter anions are omitted for clarity.

The zinc(ii) ions exhibit a tetrahedral geometry, with all halides coordinated in a bridging mode. The structural motif resembles an adamantane-like framework, consisting of four zinc ions and six μ^2-bridging halides, with four carbene ligands terminally bound to each metal centre. Such cluster structures have been previously reported for zinc(ii) complexes, often involving bridging thiolate or selenolate ligands, and in some cases, methoxy groups with tertiary ammonium as counter cations. [47] The Zn–X bond lengths in compounds 6 (2.28–2.33 Å) and 7 (2.42–2.48 Å) represent the average of the bridging and terminal Zn–X bonds in the dimeric complexes **1** and **2**, while in compound **9**, the Zn–X bond length is 2.42–2.47 Å, similar to that in its monomeric counterpart **5** (2.3694(4)/2.3905(4) Å). In contrast, the Zn–$C^{carbene}$ bond length in the tetramers (2.030(3)/2.037(2) Å in 6, 2.030(3)/2.037(2) Å in 7, 2.046–2.059 Å in **9**) is slightly shorter than in the dimers **1–4** (*ca.* 2.05 Å) or the monomer **5** (2.069(2) Å), indicating increased electron deficiency at the metal center and enhanced σ donation from the carbene to zinc.

Attempts to further characterize compound **9** were not successful due to its low yield and obtained mixtures of various species. As a result, further characterization and photophysical measurements were carried out only for tetramers **6–8** and **10**. The ^{1}H-NMR spectra of compounds **6–8** and **10** in CD_2Cl_2 exhibit one set of sharp signals corresponding to the carbene ligands coordinated to the zinc atom. In the ^{13}C-NMR spectra, the most downfield signal appears at approximately 238 ppm, confirming the coordination of the deprotonated carbene to zinc, even after halide abstraction. The upfield shift of the

carbene carbon from 250 ppm (in **1–4**) to 238 ppm further suggests a stronger Zn–$C^{carbene}$ bond, which is attributed to halide cleavage and the formation of a cationic metal center, as also observed in the shorter Zn–$C^{carbene}$ bond lengths in the SCXRD. The ^{19}F-NMR spectra of **6–8** and **10** show three distinct resonances at approximately −133, −163.7, and −167.7 ppm, in a 2 : 1 : 2 ratio, which are assigned to the $[B(C_6F_5)_4]^-$ counterion. Compounds **6–8** and **10** in DCM solutions were further characterized by ESI-MS, which showed two distinct peaks: one corresponding to M^{2+} and another to $[M - 3(ZnX_2(cAAC)X)]^+$. Both the NMR and mass spectra clearly indicate that the tetrameric motif is also maintained in solution with no monomerization observed.

To further explore different coordination environments and their influence on the excited-state nature, we attempted halide exchange in $[Zn_2Cl_2(\mu\text{-}Cl)_2(^{Me}cAAC)_2]$ (**1**) with mono-anionic bidentate acetylacetonate (acac) or monodentate carbazolate (Cz) ligands. Both ligands are known to be promising donors that form ligand-to-ligand charge transfer (LLCT) states in Cu^I emitters, which have applications in OLEDs and NIR emitters.[11,48–51] The reaction of one equivalent of sodium acetylacetonate or potassium carbazolate with **1** in THF yields complexes **11** and **12** in 50–70% yield (Fig. 2).

The ^{1}H-NMR spectra of **11** and **12** show a 1 : 1 ratio of resonances for the carbene and acac or Cz, confirming the exchange of one halide with the ligand and complexation. In the ^{13}C-NMR spectrum of **11**, the most downfield signal appears at approximately 246.9 ppm for the carbene carbon, along with a downfield signal at 192.4 ppm for the carbonyl carbon of acac. We also note additional resonances at 3.58 ppm and 1.77 ppm in the ^{1}H-NMR spectrum of **12**, corresponding to a free THF molecule.

Recrystallization of complex **11** by gas-phase diffusion of pentane over a saturated THF solution yields colourless, block-shaped crystals, which were further characterized by X-ray diffraction. Complex **11** crystallizes in the monoclinic $P2_1/n$ space group and adopts a tetrahedral zinc(ii) geometry, coordinating one chloride ion in the coordination sphere (Fig. 3). The Zn–Cl and Zn–$C^{carbene}$ bond lengths in **11** of 2.2503(6) and 2.050(1) Å, respectively, are similar to those in the parent $[Zn_2Cl_2(\mu\text{-}Cl)_2(^{Me}cAAC)_2]$, [43] while the Zn–O bond length (1.998(1) Å) is consistent with known compounds featuring Zn–O bonds.

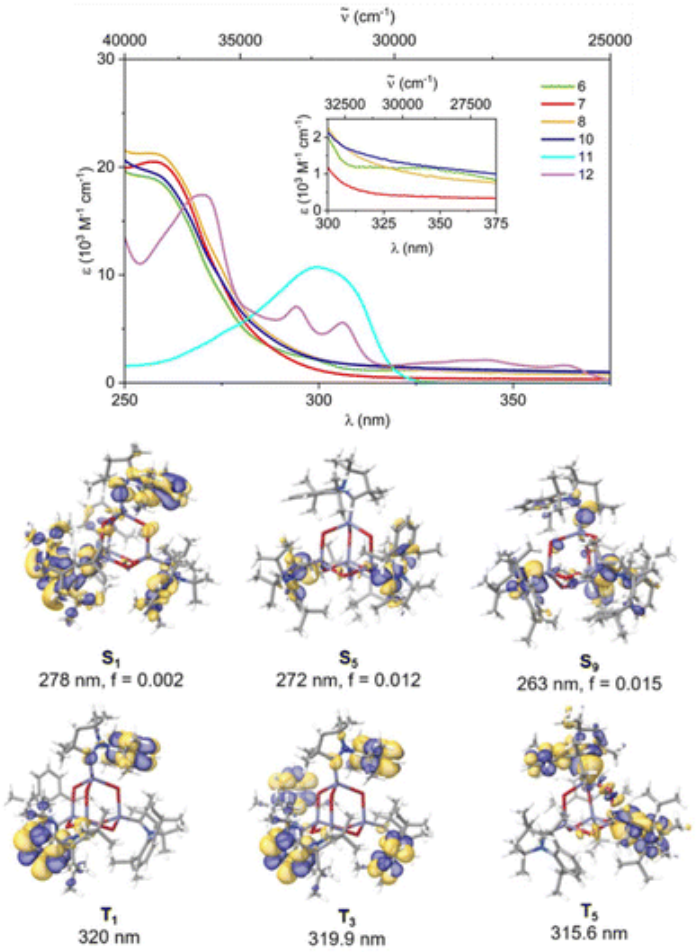
Recrystallization of complex **12** from a THF/pentane mixture yields light yellow, block-shaped crystals. These crystals are found to be coordinated to one molecule of THF, achieving tetrahedral geometry around the zinc(ii) centre, along with a carbazolate ligand and a terminal chloride ion (Fig. 3). Complex **12** crystallizes in the triclinic $P\bar{1}$ space group, with Zn–Cl and Zn–$C^{carbene}$ bond lengths of 2.2375(6) and 2.046(2) Å, respectively. The Zn–N bond length in **12** is approximately 1.975(1) Å, which is consistent with the Zn–N bond length in other zinc-carbazolate complexes, such as [ZnCl(Cz)(ITr)] (∼1.94 Å). [42] The THF coordination in **12** in solution is supported by the presence of a free THF peak in the ^{1}H-NMR spectrum, which may result from ligand exchange with THF-d_8.

Complexes **6–12** are extremely sensitive to oxygen and moisture, both in the solid and solution states. They gradually decompose to form protonated carbene salts in the presence of moisture. This sensitivity is also observed in the parent halides **1–5**, which we attribute to the absence of bulkier groups that

would protect the Zn–carbene bond. As a result, further handling and photophysical measurements of complexes **6–12** must be conducted under an inert atmosphere.

UV/Vis absorption studies

Complexes **3–5** undergo photo-decomposition under continuous irradiation with 300 nm light as also observed for **1** and **2**, [43] so further photophysical measurements were not continued for them (Fig. S31). The absorption spectra of the tetrameric compounds **6–8** and **10** in dichloromethane predominantly exhibit a high-energy band (Fig. 4, top), which is consistent with their colourless nature. This band has a broad feature with a maximum absorption at λ_{max} = 260 nm with an extinction coefficient of *ca.* 20 000 M^{-1} cm^{-1}. This absorption is primarily attributed to a mixture of $LC_{\pi-\pi^*}$ transitions, with minor contributions from halide-to-carbene (XLCT) transitions, as suggested by TD-DFT calculations (Fig. 4, bottom). Additionally, we observe some tailing of this band in the lower-energy region. TD-DFT analysis indicates that this region is associated with spin-forbidden triplet states. However, due to the insignificant SOC of the zinc(ii) ion, the observed high extinction coefficients of up to 1000 M^{-1} cm^{-1} must be the result of the structural fluxionality of the molecule in solution in combination with SOC mediated by the halides, leading to an increased transition probability for ISC in this region.



Complex [ZnCl(acac)(^{Me}cAAC)] (**11**) also exhibits only high-energy absorption (Fig. 4, top), as expected from its colourless appearance. The spectral shape of **11** is somewhat similar to that of [Cu(acac)(^{Me}cAAC)], [48] except for the visible energy bands that arise mainly from Cu/acac → π^*_{Dipp} (cAAC) charge transfer (MLCT and LLCT) transitions in the latter complex. The broad higher-energy absorption band of **11** with λ_{max} = 300 nm and ε = 10 000 M^{-1} cm^{-1} possibly results from a mixture of XLCT and LLCT transitions (acac → cAAC) as well as some LE states. The hypsochromic shift of the absorption band observed in comparison to the copper(i) complex is likely due to the absence of the MLCT contribution which contributes to the absorption of visible light.

Fig. 4 Top: UV-vis absorption spectra of **6–8** and **10–11** in CH_2Cl_2, and of **12** in THF at room temperature. Bottom: Electron density differences of selected vertical $S_0 \rightarrow S_n$ transitions relevant for the experimental absorption spectra of **7** in DCM and of selected triplet excited states calculated at the D3(BJ)-PBE0/ZORA/def2-SVP level of theory. Loss of electron density is indicated in blue and gain in yellow.

UV-Vis absorption of [ZnCl(Cz)(THF)(^{Me}cAAC)] (**12**) (Fig. 4) was measured in THF to retain its THF-coordinated structure, showing the lowest energy band at λ_{max} = 360 nm with ε = 1600 M^{-1} cm^{-1} along with an overlapping band at 345 nm (ε = 2100 M^{-1} cm^{-1}). These low energy bands are assigned to originate from an admixture of LLCT transition from the Cz to the ^{Me}cAAC acceptor unit and XLCT. A vibrationally resolved band at 295–305 nm (ε = 5 600–7000 M^{-1} cm^{-1}) is observed, which we attribute to $LC_{\pi-\pi^*}$ transitions of the Cz ligand. Additionally, higher energy bands (λ < 280 nm) are attributed to π–π* transitions of the cAAC ligands.

Luminescence properties

When irradiated with 265 nm light in DCM solution at room temperature, tetramers **6** and **7** exhibit structureless high energy emission with a maximum at *ca.* 375 nm, while [Zn_4(μ-Cl)$_6$(^{Cy}cAAC)$_4$] (**10**) shows well-resolved emission between 375 and 425 nm along with a weak and broad low energy band between 450–680 nm (Fig. 5). Since no significant change was observed when switching from chloride to bromide, we conclude that the high-energy emission is purely carbene-centred. We propose that different conformers present in the solution state contribute to significant broadening of the bands observed for compounds **6** and **7**. In contrast, the higher rigidity imparted by the steric constraints of the cyclohexyl group in **10** may result in a larger energy barrier between these conformations, leading to the more resolved emission observed in solution. The excitation-dependent emission spectra of [Zn_4(μ-Br)$_6$(^{Me}cAAC)$_4$] (**7**) produce structurally resolved high-energy emission, with a slight hypsochromic shift in the emission maximum (Fig. 5, bottom right). As the excitation energy decreases, a new lower-energy emission band becomes more prominent similar to that observed for **10**, indicating a shift in the relative population of excited states.

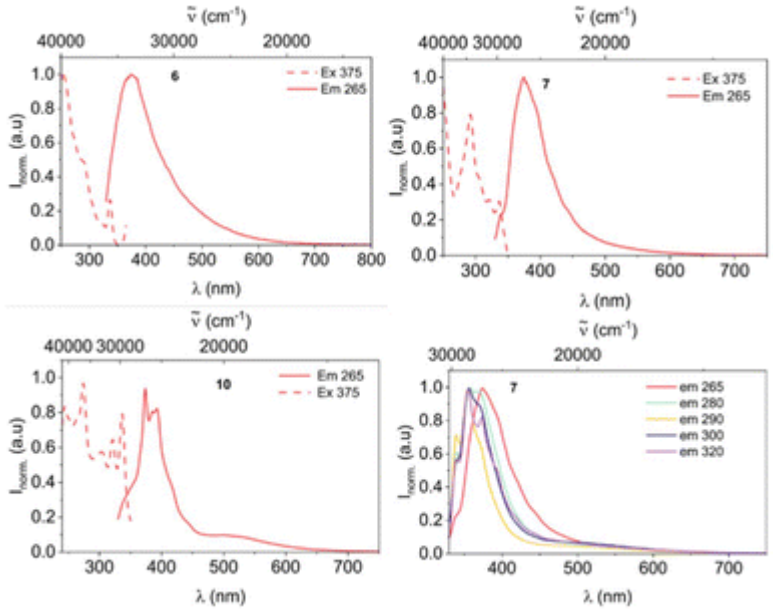


Fig. 5 Emission (λ_{ex} = 265 nm) and excitation (λ_{em} = 375 nm) spectra of **6, 7** (top) and **10** (bottom left) in DCM at 297 K, and excitation wavelength-dependent emission spectra of **7** in DCM at 297 K (bottom right).

In the solid state, upon excitation with 265 nm light, compounds **6–8** and **10** exhibit broad, structureless emission with a slight bathochromic shift in comparison to solution state, peaking around λ_{max} = 385–

390 nm (Fig. 6 and Table 1). Under continuous photo-irradiation, the luminescence intensity decreases, indicating photo-chemical transformations occurring in these compounds. The changes are most pronounced in $[Zn_4(\mu\text{-}Cl)_6(^{Me}cAAC)_4]$ (**6**) with a new low-energy emission band at 497 nm appearing (Fig. 7, left), while **7**, **8** and **10** show a similar decrease in emission intensity, but without the formation of additional bands within the 10 minutes timescale (Fig. S32).

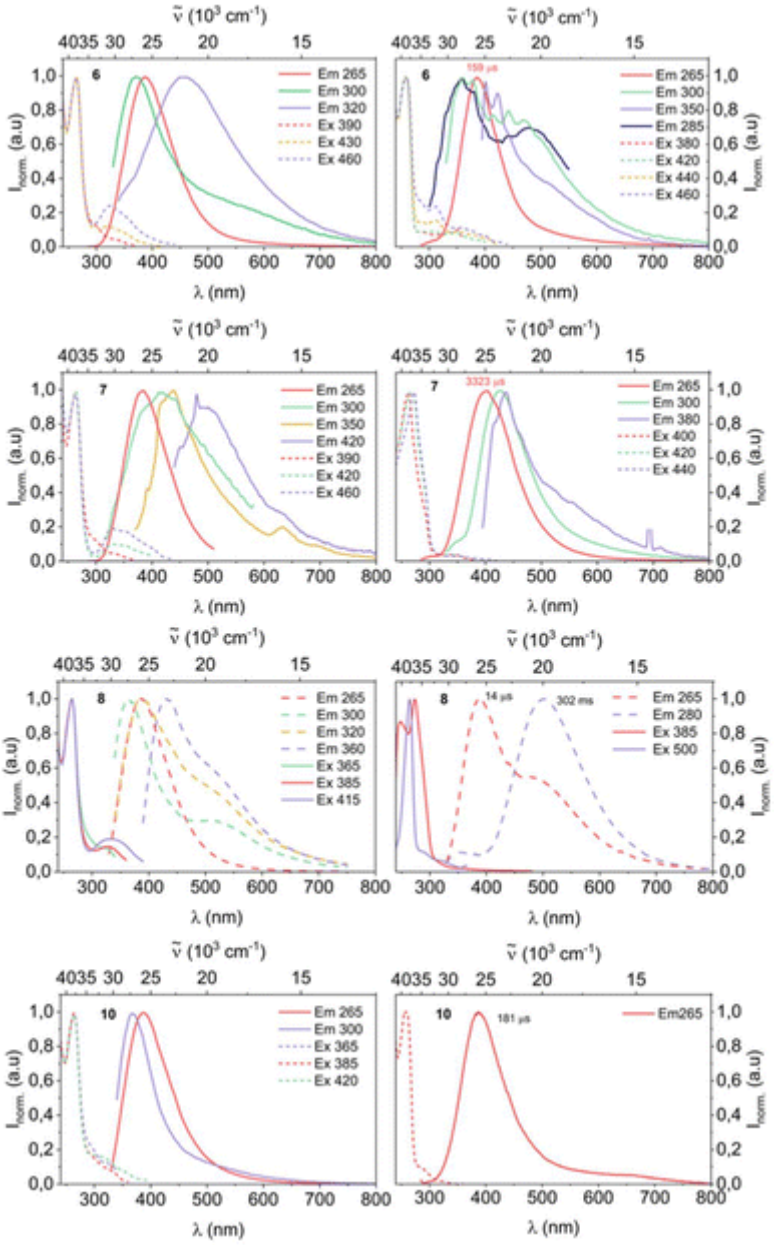


Fig. 6 Emission and excitation spectra of **6–8** and **10** in the solid state at 297 K (left) and 77 K (right).

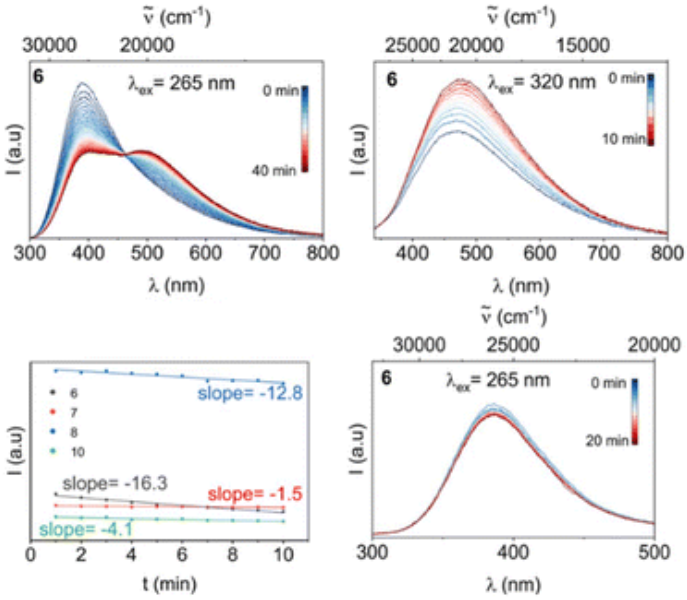


Fig. 7 Top: Temporal evolution of the emission spectrum of **6** in solid state at 297 K (λ_{ex} = 265 nm, left; λ_{ex} = 320 nm, right). Bottom: Temporal evolution of the emission intensity at λ_{max} = 385 nm of **6–8** and **10** in the solid state at 297 K (left), and of the emission spectrum of **6** in the solid state at 77 K (right).

Table 1 Selected photophysical data for 6–8 and 10–12 in the solid state.

Cpd.	λ_{ex} *(nm)*	*T (K)*	λ_{em} *(nm)*	*τ (μs)*	*Φ*
6	265	297	386	—	<0.01
		77	385	159	
7	265	297	390	—	<0.01
		77	400	3323	
8	265	297	385	—	<0.01
		77	385	14	
			500	302	
10	265	297	385	—	<0.01
		77	385	181	
11	320	297	422, 484, 507	—	0.03
		77	422, 480, 510	42×10^3	0.05
12	370	297	590	—	<0.01
		77	580	41	0.09

Importantly, the presence of an isosbestic point for **6** suggests that the spectral changes are not due to decomposition, but instead result from a specific conformational change in the excited state, leading to the formation of a single, new species that emits from the low energy state. A similar phenomenon has been observed in $[Zn_2Cl_2(\mu\text{-}Cl)_2(^{Me}cAAC)_2]$, where the intensity of a high-energy band at λ_{max} = 360 nm (associated with the ^{3}XLCT transition) diminishes, while the intensity of a broad low-energy band at λ_{max} = 451 nm (attributable to a $^3LE_{cAAC}$ transition) increases.[43] This transformation was linked to asymmetric distortion of the cAAC ligand along the Zn–carbene bond, along with other unidentified processes. However, due to the higher rigidity of the tetrameric clusters **6–8** and **10**, the rate of photo-transformation

is comparatively slower than in the previous dimer, where photo-chemical changes occur within just a few minutes.

Since the 265 nm excitation directly interacts with the Zn–carbene bond as indicated by TD-DFT calculations (Fig. S33), we propose that photo-irradiation causes compound 6 to undergo a geometry change involving that particular bond. The rate of this photo-transformation (**6** > **8** ≫ **10** > **7**) is influenced by the structural rigidity of the complexes (Fig. 7, bottom left), which varies depending on the substituents on the cAAC ligand. The much slower rate of decomposition in $[Zn_4(\mu\text{-}Br)_6(^{Me}cAAC)_4]$ (**7**) in comparison to the chloride analogue **6**, or the bulkier carbene bearing clusters **8** and **10**, is somewhat unexpected, as one might anticipate higher photo-conversion due to the presence of smaller methyl substituents and the weaker Zn–Br bond strength. This assumption holds true if the Zn–X bonds were involved in the conformational change. However, as the change mostly occurs at the carbene and/or $Zn–C^{carbene}$ bond, thus the halides may just influence the ISC pathways, which may alter the relative populations of excited states. Therefore, while the halide influence appears to play a role, the exact mechanism remains inconclusive and any further hypothesis is highly speculative as the available analytical methods to characterize the excited state kinetics further are not applicable to the solid state samples. However, the finding that the low energy band does not form when 6 is being excited at 77 K is in line with these conclusions (Fig. 7, bottom right).

Surprisingly, when excited with lower-energy light (λ_{ex} > 265 nm), compounds **6–8** exhibit different additional low-energy emission bands, a change that is much less pronounced for $[Zn_4(\mu\text{-}Cl)_6(^{Cy}cAAC)_4]$ (**10**) (Fig. 6). This suggests that structural rigidity plays an important role in determining the relative population of different states involved in the emission of the tetrameric clusters *via* excited-state geometry changes, giving rise to dual phosphorescence behaviour. The excitation spectra for the low-energy emission bands (λ_{max} > 385 nm) also significantly shift, intensifying in the lower energy region (300–390 nm). The time-dependent emission spectra, excited at 320 nm (corresponding to the triplet state energy region as determined by TD-DFT), reveal a continuous increase in the intensity of the lower-energy band at 490 nm for compound **6** (Fig. 7, top right). This behaviour suggests that direct excitation into the triplet state triggers an immediate conformational change, occurring more rapidly than the conformational transition pathway accessed through higher-lying excited states. These newly formed conformers appear to persist, at least partially, in the ground state, thereby contributing to increased absorptivity in the macroscopic sample and a corresponding growth in emission intensity. However, the low intensity of the emission bands prevents accurate determination of the emission lifetimes, making it difficult to ascertain the nature of the emissions at room temperature.

To resolve the emission mechanism and prevent photochemical transformation, further photophysical studies were carried out at 77 K in the solid state. A slight redshift to 400 nm is observed for compound **7**, while emissions for compounds **6** and **10** remain unchanged regardless of temperature under 265 nm irradiation (Fig. 6) and a new emission band at 500 nm is observed for compound **8** alongside the major 385 nm band. Time-resolved measurements reveal luminescence lifetimes in the micro-to-millisecond regime for the 385 nm emission in compounds **6–8** and **10**, with compound 8 showing a

comparatively short lifetime of 14 µs at the emission maximum, which indicates triplet states being involved in the emission (Table 1).

We attribute the observed luminescence to carbene-centred triplet states localized at the aromatic *N*-substituent, with some minor XLCT contribution. The significant overlap of emission and excitation spectra, as mentioned before, indicates that the low-energy excitation band (320–390 nm) is also triplet in nature. TD-DFT calculations for compound **7** show that several triplet states (λ = 320 nm, 319.9 nm, 315.6 nm) exist in this region (Fig. 4, bottom). While these states are mainly carbene-based, different contributions from the carbene and the halides lead to nearly degenerate triplet states. These states are also vibrationally resolved in the 77 K excitation spectra.

When excited with lower-energy light (*e.g.*, 300 or 320 nm), different triplet excited states can be populated depending on the excitation wavelength, the energy gap between these states, and the activation barrier for transitions between them, all of which are influenced by the molecular structure. The system can either be directly excited to a low-energy triplet state or repopulate from the initially populated high-energy state, which involves a geometry change upon excitation (Fig. 8). The radiative rates k_r and k_r' also play a crucial role in determining the possible emission outcomes. With high-energy excitations, where $k_r > k_r'$, the emission predominantly originates from the high-energy state. Thus, the equilibrium between high- and low-energy states leads to different emission behaviours for compounds **6–8** and **10** under varying excitation energies. This assumption is further supported by the different emission lifetimes observed at 77 K. For **6**, under 265 nm irradiation, only one emission at 385 nm is observed, corresponding to a long-lived triplet state with a lifetime of 159 µs, with no low-energy emission detected. This suggests a very fast equilibrium between the two conformers, with the emission predominantly coming from the higher-energy state. In contrast, for compound **10**, the rigid structure prevents significant geometry changes upon excitation, resulting in a major 385 nm emission with a similar lifetime. For compound **8**, two emissions are observed upon 265 nm excitation, the primary 385 nm emission is relatively short-lived, as it decays preferentially to a low-energy state, resulting in emission at 500 nm. The lifetime of this low-energy state is recorded at 302 ms, confirming its triplet origin. However, the relatively long lifetime observed for compound **8** cannot be fully explained by this mechanism, indicating that additional processes may be involved. The observed photophysical behaviour of the tetramers suggests that high-energy excitation leads to emission primarily from the high-energy state, likely due to a strong Franck–Condon overlap of the transition, while emission from the low-energy excited state is suppressed or ‘trapped’. On the other hand, low-energy excitation promotes direct triplet excitations and repopulation of the lower-energy triplet from higher-lying triplet states. This process is dependent on the structural properties of the molecule, which influence the energy gap and intersystem crossing rates. This rigidity-dependent excited state behaviour is driven by the equilibrium between the two excited states, which is regulated by geometry changes in the excited state, highlighting the importance of molecular structure in determining the emission profile.

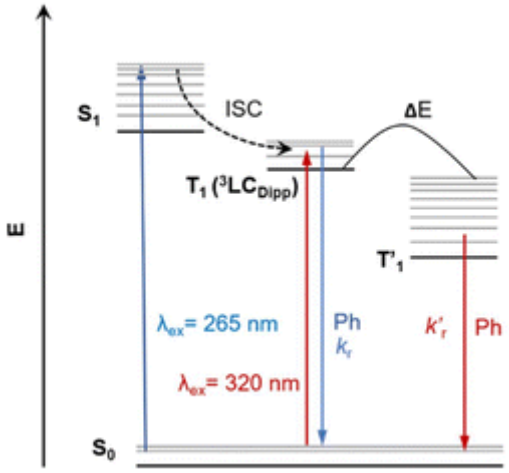


Fig. 8 Schematic diagram of the emission mechanism of tetrameric **6–8** and **10**.

Upon irradiation with 320 nm light, [ZnCl(acac)(^{Me}cAAC)] (**11**) shows two different emission maxima at 420 nm and 480 nm along with a shoulder at 507 nm (Fig. 9). We hypothesize that the emission of compound **11** arises simultaneously from LE, LLCT and XCT states. Although the complex does not exhibit any absorption beyond 325 nm, consistent with its colourless appearance, the excitation spectra of compound **11** at 420 nm reveal an intense low-energy band between 330 and 400 nm. This band is attributed to direct triplet absorption, likely enabled by the effectively infinite concentration of molecules in the solid state, which allows otherwise forbidden transitions to become observable.

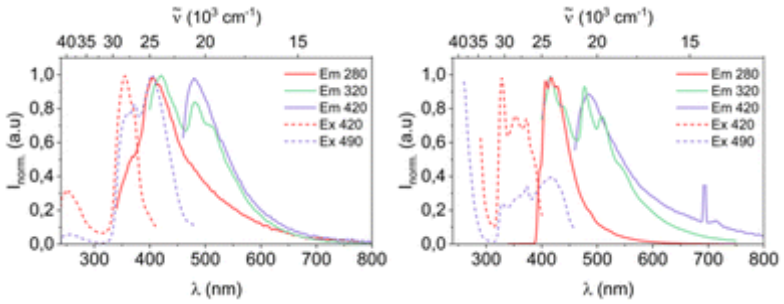


Fig. 9 Emission and excitation spectra of **11** in the solid state at 297 K (left) and 77 K (right).

Upon cooling to 77 K, a similar but structurally resolved emission spectrum is observed under 320 nm excitation. The photoluminescence lifetime at 480 nm emission maximum is 42.1 ms, with a quantum yield of 0.05, leading to a radiative rate constant of 1.2 s^{-1}. This supports the involvement of triplet states in the emission process and thus phosphorescence. Excitation with 280 nm light leads to only emission at high energy band at 420 nm at 297 K, which shows vibrational progression at 77 K, indicating involvement of LE states. When irradiated with 420 nm, structureless, broad emission at λ_{max} = 485 nm is observed at both temperatures. Presumably, this emission is of CT nature, which is exclusively getting populated with low energy excitation.

When excited with 370 nm light in the solid state, [ZnCl(Cz)(THF)(^{Me}cAAC)] (**12**) exhibits weak yellow photoluminescence with broad emission peaking at λ_{max} = 590 nm (Fig. 10). The broad nature of this emission band suggests a charge transfer (CT) character, likely a LLCT transition from the Cz to the

carbene moiety. Similar broad LLCT emissions have been documented in the literature for complexes such as [$Zn_2(bdt)_2(MecAAC)_2$] and [Zn(bdt)(MenthcAAC)], both of which display broad, featureless yellow-orange emission, with thermally activated delayed fluorescence (TADF) as the primary radiative pathway.[15,44] To further investigate the emission mechanism, compound **12** was cooled to 77 K, where it exhibited a slight hypsochromic shift in the emission, likely due to rigidification at lower temperature. This shift was accompanied by an enhanced emission lifetime of 41 µs, leading to a radiative rate constant of 2.1 × 10^3 s^{-1}, indicative of triplet-state emission. The 77 K emission spectrum also revealed a small shoulder at 450 nm, which may arise from a ^{3}Cz state, a feature also observed in the emission of [Cu(Cz)(^{Menth}cAAC)].[11]

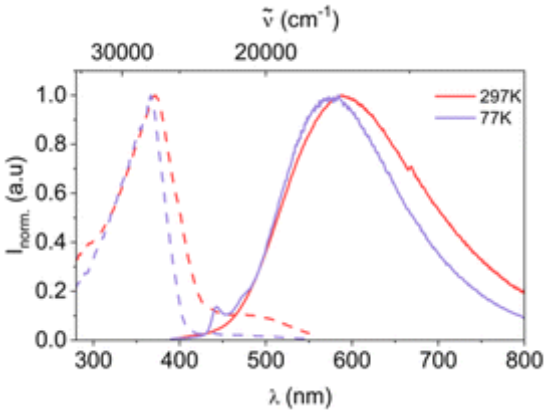


Fig. 10 Emission and excitation spectra of **12** in the solid state at 297 K and 77 K.

Conclusion

We have synthesized a series of adamantane-like tetrameric cationic zinc compounds based on cAAC with halides as bridging ligands (**6–10**). Additionally, we have prepared tetrahedral zinc(ii) complexes with acac or Cz ligands, with one chloride terminally attached. Halide abstraction or exchange from the parent halide dimer leads to the formation of entirely new zinc(ii) structural motifs. All of the synthesized complexes exhibit phosphorescence as their emission pathway, though the origin of the emission varies with the structural motif. The clusters **6–8** and **10** show emission in the high-energy range most likely from ^{3}LE states and, depending on the substituents, they appear to undergo conformation change to populate lower energy triplet states and emit from there. The experimental data suggest that the observed rigidity-dependent dual phosphorescence behaviour arises from an equilibrium between the two excited states, governed by geometry changes in the excited state. While acac coordination (**11**) results in very structured emission in the high-energy range, attributed to a localized excited state, the coordination of carbazolate leads to broad LLCT emission in the yellow region of the spectrum. Although these compounds are weakly emissive in the solid state, which limits their potential applications, they offer valuable insights into the photophysical properties of zinc(ii) compounds, particularly in relation to triplet emission and the rare observation of phosphorescence emission in zinc(ii) complexes.

References

1. M. Soleilhavoup and G. Bertrand, *Acc. Chem. Res.*, **2015**, 48, 256-266.

2. N. V. Tzouras, E. A. Martynova, X. Y. Ma, T. Scattolin, B. Hupp, H. Busen, M. Saab, Z. Y. Zhang, L. Falivene, G. Pisanò, K. Van Hecke, L. Cavallo, C. S. J. Cazin, A. Steffen and S. P. Nolan, *Chem. – Eur. J.*, **2021**, *27*, 11904-1191.

3. M. Melaimi, R. Jazzar, M. Soleilhavoup and G. Bertrand, *Angew. Chem., Int. Ed.*, **2017**, *56*, 10046-10068.

4. V. Lavallo, Y. Canac, C. Präsang, B. Donnadieu and G. Bertrand, *Angew. Chem., Int. Ed.*, **2005**, *44*, 5705-5709.

5. J. Chu, D. Munz, R. Jazzar, M. Melaimi and G. Bertrand, *J. Am. Chem. Soc.*, **2016**, *138*, 7884-7887.

6. U. S. D. Paul and U. Radius, *Eur. J. Inorg. Chem.*, **2017**, 3362-3375.

7. R. Jazzar, M. Soleilhavoup and G. Bertrand, *Chem. Rev.*, **2020**, *120*, 4141-4168.

8. P. Bellotti, M. Koy, M. N. Hopkinson and F. Glorius, *Nat. Rev. Chem.*, **2021**, *5*, 711-725.

9. S. K. Kushvaha, A. Mishra, H. Roesky and K. C. Mondal, *Chem. – Asian J.*, **2022**, *17*, e202101301.

10. M. Gernert, U. Müller, M. Haehnel, J. Pflaum and A. Steffen, *Chem. – Eur. J.*, **2017**, *23*, 2206-2216.

11. R. Hamze, J. L. Peltier, D. Sylvinson, M. Jung, J. Cardenas, R. Haiges, M. Soleilhavoup, R. Jazzar, P. I. Djurovich, G. Bertrand and M. E. Thompson, *Science*, **2019**, *363*, 601-606.

12. T. Y. Li, S. J. Zheng, P. I. Djurovich and M. E. Thompson, *Chem. Rev.*, **2024**, *12*, 4332-4392.

13. Y. Q. Ding, R. Goddard and K. R. Pörschke, *Organometallics*, **2005**, *24*, 439-445.

14. L. Q. Jin, D. S. Weinberger, M. Melaimi, C. E. Moore, A. L. Rheingold and G. Bertrand, *Angew. Chem., Int. Ed.*, **2014**, *53*, 9059-9063.

15. M. Mitra, O. Mrózek, M. Putscher, J. Guhl, B. Hupp, A. Belyaev, C. M. Marian and A. Steffen, *Angew. Chem., Int. Ed.*, **2024**, *63*, e202316300.

16. J. Hossain, R. Akhtar and S. Khan, *Polyhedron*, **2021**, *201*, 115151.

17. A. Ruduss, A. Jece, K. A. Stucere, K.-W. Chen, B. Turovska, S. Belyakov, A. Vembris, C.-H. Chang and K. Traskovskis, *J. Mater. Chem. C*, **2024**, *12*, 2968-2980.

18. A. Farokhi, S. Lipinski, L. M. Cavinato, H. Shahroosvand, B. Pashaei, S. Karimi, S. Bellani, F. Bonaccorso and R. D. Costa, *Chem. Soc. Rev.*, **2024**, *54*, 266-340.

19. G. Morselli, C. Reber and O. S. Wenger, *J. Am. Chem. Soc.*, **2025**, *147*, 11608-11624.

20. S. Bestgen, C. Schoo, B. L. Neumeier, T. J. Feuerstein, C. Zovko, R. Köppe, C. Feldmann and P. W. Roesky, *Angew. Chem., Int. Ed.*, **2018**, *57*, 14265-14269.

21. K. D. Oyler, F. J. Coughlin and S. Bernhard, *J. Am. Chem. Soc.*, **2007**, *129*, 210-217.

22. J. Kuhnt, M. Mitra, S. Maity, B. Hupp, C. M. Marian and A. Steffen, *J. Phys. Chem. Lett.*, **2024**, *15*, 6409-6414.

23. I. Y. Chan, W. G. van Dorp, T. J. Schaafsma and J. H. van der Waals, *Mol. Phys.*, **1971**, *22*, 753-760.

24. A. Harriman, *J. Chem. Soc., Faraday Trans.*, **1980**, *76*, 1978-1985.

25. P. J. Gronlund, J. A. Burt and W. F. Wacholtz, *Inorg. Chim. Acta*, **1995**, *234*, 13-18.

26. E. Kimura and T. Koike, *Chem. Soc. Rev.*, **1998**, *27*, 179-184.

27. V. Yam and K. K. Lo, *Chem. Soc. Rev.*, **1999**, *28*, 323-334.

28. A. Gusev, E. Braga, E. Zamnius, M. Kiskin, M. Kryukova, A. Baryshnikova, B. Minaev, G. Baryshnikov, H. Ågren and W. Linert, *RSC Adv.*, **2019**, *9*, 22143-22152.

29. R. Diana and B. Panunzi, *Molecules*, **2020**, *25*, 4984.

30. H. Deng, T. Wang, Y. Chen, K. Dou, X. Liu, C. Zhao, H. Zhan, C. Yang, C. Qin and Y. Cheng, *J. Phys. Chem. Lett.*, **2024**, *15*, 7003-7010.

31. S. A. Elgadi, S. Mikulin and Z. Hudson, *Adv. Opt. Mater.*, **2025**, *13*, 2500683.

32. D. A. Shariaty, P. I. Djurovich and M. E. Thompson, *J. Am. Chem. Soc.*, **2025**, *147*, 29065-29078.

33. D. A. Shariaty, J. Schaab, E. McClure, T. Nattikalungal, P. I. Djurovich, S. Bradforth and M. E. Thompson, *Inorg. Chem.*, **2025**, *64*, 1228-1240.

34. Y. Sakai, Y. Sagara, H. Nomura, N. Nakamura, Y. Suzuki, H. Miyazaki and C. Adachi, *Chem. Commun.*, **2015**, *51*, 3181-3184.

35. G. A. Crosby, R. G. Highland and K. A. Truesdell, *Coord. Chem. Rev.*, **1985**, *64*, 41-52.

36. R. G. Highland and G. A. Crosby, *Chem. Phys. Lett.*, **1985**, *119*, 454-458.

37. J. A. Burt and G. A. Crosby, *Chem. Phys. Lett.*, **1994**, *220*, 493-496.

38. V. W. W. Yam, Y. L. Pui and K. K. Cheung, *Inorg. Chim. Acta*, **2002**, *335*, 77-84.

39. V. W. W. Yam, Y. L. Pui, K. K. Cheung and N. Y. Zhu, *New J. Chem.*, **2002**, *26*, 536-542.

40. T. W. Ngan, C. C. Ko, N. Zhu and V. W. Yam, *Inorg. Chem.*, **2007**, *46*, 1144-1152.

41. N. Lüdtke, J. Kuhnt, T. Heil, A. Steffen and C. M. Marian, *ChemPhotoChem*, **2023**, *7*, e202200142.

42. S. Koop, O. Mrózek, L. Janiak, A. Belyaev, M. Putscher, C. M. Marian and A. Steffen, *Inorg. Chem.*, **2023**, *63,* 891-901.

43. O. Mrózek, M. Gernert, A. Belyaev, M. Mitra, L. Janiak, C. M. Marian and A. Steffen, *Chem. – Eur. J.*, **2022**, *28*, e202201114.

44. O. Mrózek, M. Mitra, B. Hupp, A. Belyaev, N. Lüdtke, D. Wagner, C. Wang, O. S. Wenger, C. M. Marian and A. Steffen, *Chem. – Eur. J.*, **2023**, *29,* e202203980.

45. J. B. Lambert, S. H. Zhang, C. L. Stern and J. C. Huffman, *Science*, **1993***, 260*, 1917-1918.

46. J. B. Lambert, S. Z. Zhang and S. M. Ciro, *Organometallics*, **1994**, *13*, 2430-2443.

47. N. Rinn, I. Rojas-León, B. Peerless, S. Gowrisankar, F. Ziese, N. W. Rosemann, W. C. Pilgrim, S. Sanna, P. R. Schreiner and S. Dehnen, *Chem. Sci.*, **2024**, *15*, 9438-9509.

48. A. M. T. Muthig, M. Krumrein, J. Wieland, M. Gernert, F. Kerner, J. Pflaum and A. Steffen, *Inorg. Chem.*, **2022**, *61*, 14833-14844.

49. S. Y. Shi, M. C. Jung, C. C. A. Tadle, M. R. D. Sylvinson, P. I. Djurovich, S. R. Forrest and M. E. Thompson, *J. Am. Chem. Soc.*, **2019**, *141*, 3576-3588.

50. A. M. T. Muthig, O. Mrózek, T. Ferschke, M. Rödel, B. Ewald, J. Kuhnt, C. Lenczyk, J. Pflaum and A. Steffen, *J. Am. Chem. Soc.*, **2023**, *145*, 4438-4449.

51. M. Gernert, L. Balles-Wolf, F. Kerner, U. Müller, A. Schmiedel, M. Holzapfel, C. M. Marian, J. Pflaum, C. Lambert and A. Steffen, *J. Am. Chem. Soc.*, **2020**, *142*, 8897-8909.

52. (*a*) CCDC 2404735: Experimental Crystal Structure Determination, 2026, 10.5517/ccdc.csd.cc2lqb3s. (*b*) CCDC 2404736: Experimental Crystal Structure Determination, 2026, 10.5517/ccdc.csd.cc2lqb4t. (*c*) CCDC 2404737: Experimental Crystal Structure Determination, 2026, 10.5517/ccdc.csd.cc2lqb5v. (*d*) CCDC 2404738: Experimental Crystal Structure Determination, 2026, 10.5517/ccdc.csd.cc2lqb6w. (*e*) CCDC 2404739: Experimental Crystal Structure Determination, 2026, 10.5517/ccdc.csd.cc2lqb7x. (*f*) CCDC 2404740: Experimental Crystal Structure Determination, 2026, 10.5517/ccdc.csd.cc2lqb8y. (*g*) CCDC 2404741: Experimental Crystal Structure Determination, 2026, 10.5517/ccdc.csd.cc2lqb9z. (*h*) CCDC 2404742: Experimental Crystal Structure Determination, 2026, 10.5517/ccdc.csd.

2.2 An Air- and Moisture-stable Zinc(II) Carbene Dithiolate Dimer Showing Fast Thermally Activated Delayed Fluorescence and Dexter Energy Transfer Catalysis

This subchapter as part of this dissertation work was published in collaboration with Wiley-VCH GmbH.[4] Reprinted with permission from *Chem. Eur. J.* **2023**, *29*, e202203980. copyright © 2023 Wiley-VCH GmbH.

Summary: A dimeric Zn^{II} carbene complex featuring bridging and chelating benzene-1,2-dithiolate ligands is highly stable towards air and water. The donor-Zn-acceptor structure leads to visible light emission in the solid state, solution and polymer matrices with λ_{max} between 577–657 nm and, for zinc(II) complexes, unusually high radiative rate constants for triplet exciton decay of up to k_r=1.5×105s 1 at room temperature. Variable temperature and DFT/MRCI studies show that a small energy gap between the $^{1/3}$LL/LMCT states of only 79 meV is responsible for efficient thermally activated delayed fluorescence (TADF). Time-resolved luminescence and transient absorption studies confirm the occurrence of long-lived, dominantly ligand-to-ligand charge transfer ex cited states in solution, allowing for application in Dexter energy transfer photocatalysis.

Contribution to experimental part: approx. 30%

Contribution to the written part: approx. 10%

An Air- and Moisture-stable Zinc(II) Carbene Dithiolate Dimer Showing Fast Thermally Activated Delayed Fluorescence and Dexter Energy Transfer Catalysis

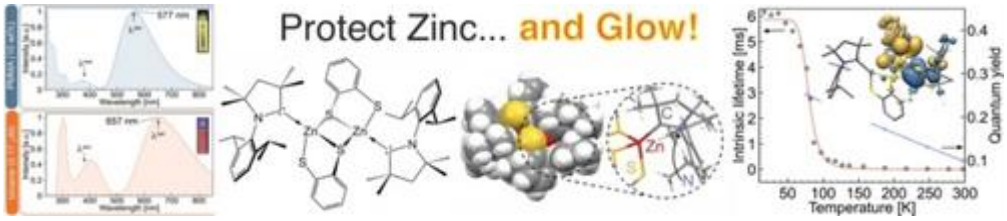
Ondřej Mrózek, Mousree Mitra, Bejamin Hupp, Andrey Belyaev, Nora Lüdtke, Dorothee Wagner, Cui Wang, Oliver S. Wenger, Christel M. Marian, and Andreas Steffen

Abstract

A dimeric Zn^{II} carbene complex featuring bridging and chelating benzene-1,2-dithiolate ligands is highly stable towards air and water. The donor-Zn-acceptor structure leads to visible light emission in the solid state, solution and polymer matrices with λ_{max} between 577–657 nm and, for zinc(II) complexes, unusually high radiative rate constants for triplet exciton decay of up to k_r=1.5×10^5 s^{-1} at room temperature. Variable temperature and DFT/MRCI studies show that a small energy gap between the $^{1/3}$LL/LMCT states of only 79 meV is responsible for efficient thermally activated delayed fluorescence (TADF). Time-resolved luminescence and transient absorption studies confirm the occurrence of long-lived, dominantly ligand-to-ligand charge transfer excited states in solution, allowing for application in Dexter energy transfer photocatalysis.

Graphical Abstract

Steric protection of the Zn-Carbene bond by a bridging coordination mode of 1,2-dithiolate ligands leads to air- and moisture-stable complexes. Efficient TADF with high radiative rate constants at room temperature is observed from $^{1/3}$LL/LMCT states according to variable temperature, transient absorption and DFT/MRCI studies. Application in Dexter energy transfer catalysis is demonstrated, exemplifying the potential of this new class of abundant 3d photoactive systems.



Introduction

Photoactive complexes of the 3d elements are currently being intensively investigated[1-6] with regard to their potential to either substitute or complement more precious 4d/5d transition metal complexes in photonic applications, where triplet excitons need to be harvested. The exploitation scenarios include, for example, sensors,[7] imaging,[8] organic light emitting devices (OLEDs),[9,10] stimuli-responsive materials,[11] as well as photocatalysis[5, 12-14] for high-value products. Besides the argument of relative costs of the metals, one of the major driving forces for this development is certainly also the desire to understand the spin dynamics and various luminescence phenomena, and to discover new photoreactions. Ultimately, the breadth of findings will lead to the formulation of structure-property

relationships, allowing for control of the photophysical and -chemical properties for a given application scenario. For many of the first-row transition metal complexes in their d^1 to d^9 electron configuration, an important intellectual challenge to realize room-temperature luminescence is the occurrence of metal-centred (MC) d–d* states,[15] which can be populated thermally from the initial excited states of charge transfer (CT) character and often lead to undesired non-radiative decay. Strategies to overcome this problem are to increase the ligand field splitting[16, 17] or manipulate the energy of CT states[18] by judicious choice of the ligand sphere.

An alternative is to employ metal centres in their d^0 or d^{10} electron configuration.[10, 18-23] This approach provides the additional advantage of various coordination spheres of the same metal centre being accessible, which greatly influences the nature, energy and reactivity of the excited states. Extensive work on trigonally and linearly coordinated Cu^I compounds, in particular, has shown that very efficient triplet state decay can be obtained either by phosphorescence,[20, 24-26] or thermally activated delayed fluorescence (TADF).[10, 21, 27-29] For this, the ideal molecular structure should allow for the formation of low-energy ligand-to-ligand charge transfer (LLCT) states with some metal-to-ligand (ML)CT admixture to mediate spin-orbit coupling (SOC). While Cu^I is beneficially redox-active, the high oxidation potential of Zn^{II} forbids the formation of MLCT states. In addition, the majority of photoactive zinc(II) complexes is homoleptically coordinated, and thus fluorescent from ligand-centred (^{1}LC) states.[30-32]

However, a class of heteroleptically coordinated [ZnX_2(phen)] (phen=1,10-phenanthroline; X=halides, thiolates) has been reported to exhibit rare, but very weak phosphorescence at room temperature from ^{3}LLCT/^{3}LC(phen) states.[33] We recently refined this analysis by extensive theoretical and experimental studies, showing that, in fact, TADF occurs from $^{1/3}$LLCT states with a very small energy gap $\Delta E(S_1\text{-}T_1)$, although non-radiative deactivation is dominant.[34] A similar behaviour was described for a zinc(II) iminophosphonamide complex by Roesky et al.[35] Adachi and co-workers reported TADF from a homoleptically coordinated Zn^{II} compound, albeit low radiative rate constants of only $k_r=2.6\times10^4$ s^{-1} from intra-ligand $^{1/3}$(IL)CT states were found.[36]

These rare examples show that there is indeed potential to exploit zinc(II) complexes for triplet exciton harvesting via TADF, and we thus followed the strategy of preparing donor-M-acceptor structures to enter $^{1/3}$LLCT states to ensure high k_r. As a first foray into this field, we recently employed an electrophilic cyclic alkyl(amino)carbene (cAAC) as acceptor site for Zn^{II} halides, with the latter acting as donors. The obtained dimers [$Zn_2Cl_2(\mu\text{-}Cl)_2(^{Me}cAAC)_2$] feature triplet ^{3}XCT/LE excited states with ultra-long lifetimes up to several milliseconds, but undesired photo-induced conformational transformation as well as further decomposition processes at room temperature involving the Zn−X bonds was observed.[37] In order to enhance the stability and foster the formation of low-energy LLCT excited states, we now focused on chelating benzene-1,2-dithiolate (bdt) as a redox-active donor for the {Zn(^{Me}cAAC)} acceptor motif.

Results and Discussion

The reaction of two equivalents disodium benzene-1,2-dithiolate (Na_2bdt) with [$Zn_2Cl_2(\mu\text{-}Cl)_2(^{Me}cAAC)_2$][37] in THF solution occurs with a fast color change from colorless to yellow and

simultaneous precipitation of NaCl (Figure 1). After work-up, crystallization using a CH_2Cl_2/*n*-pentane mixture afforded yellow single crystals of **Zn1** in 74 % isolated yield. X-ray diffraction analysis revealed a centrosymmetric, dimeric arrangement, in which the bdt units each bind with one sulfur solely to one zinc(II) ion and bridge the two {Zn(^{Me}cAAC)} fragments with the other (Figure 1).

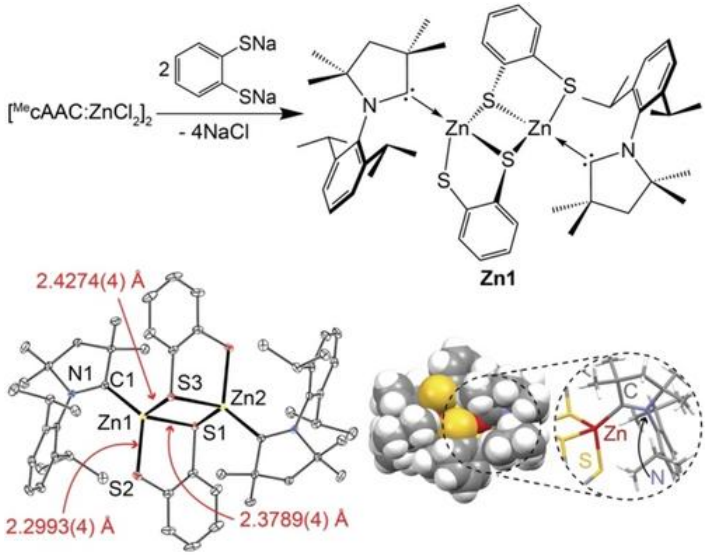


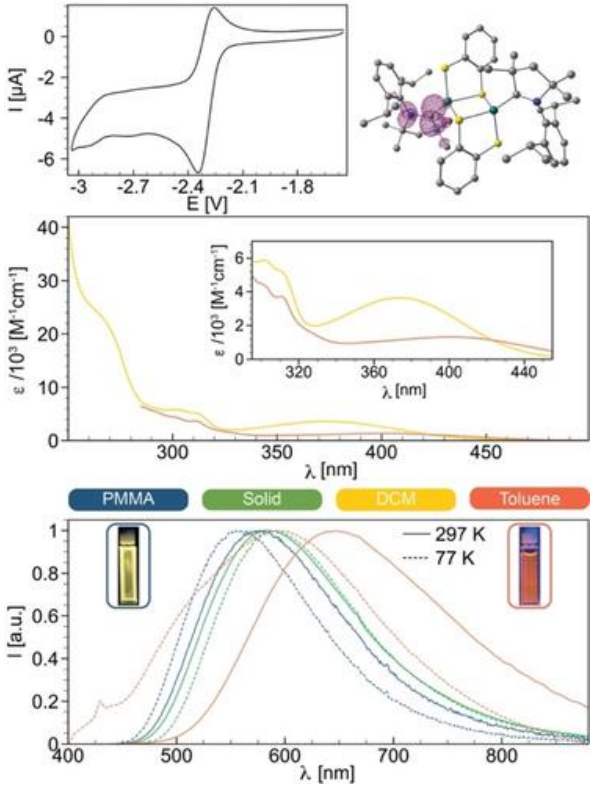
Figure 1. Synthesis and crystal structure of **Zn1**. Thermal ellipsoids are drawn at the 30 % probability level and hydrogens are omitted for clarity. Selected bond lengths (Å) and angles (°): Zn1-C1 2.0575(13); Zn1-S1 2.3789(4); Zn1-S2 2.2993(4); Zn1-S3 2.4274(4); C1-Zn1-S1 115.47(4); C1-Zn1-S2 125.36(4); C1-Zn1-S3 119.58(4); Zn1-S1-Zn2 80.83(1); S1-Zn1-S3 99.17(1).

Although a similar coordination mode of bdt was reported for electron-deficient Zn^{II} complexes bearing *N*,*N*-chelating ligands,[38, 39] it is unprecedented in the context of carbene compounds, and we find that the Zn-$S^{bridging}$ distances are slightly shorter by ~0.07 Å for **Zn1**. The Zn−$C^{carbene}$ bond length of 2.0575(13) Å is very similar to the value found for [$Zn_2Cl_2(\mu$-$Cl)_2$(^{Me}cAAC)$_2$] of 2.0547(17) Å. We note that the dimeric structure of **Zn1** is maintained in solution as the ^{1}H and ^{13}C{^{1}H} NMR spectra show only one set of sharp signals.

The μ_2,k^2-bonding mode of the bdt ligands is a key feature of the molecular structure and provides enhanced steric protection of the Zn−C(carbene) bond of **Zn1** in comparison to the chloride bridged congener[37], which is highly photolabile at room temperature even in the solid state, and highly sensitive towards oxygen and moisture. In contrast, **Zn1** is remarkably photostable not only in the solid state, but more importantly also in dry and de-oxygenated, or aerated and wet CD_2Cl_2 solution (Figure S6 in Supporting Information). Notably, no protonation of ^{Me}cAAC or bdt ligands was observed in the presence of water, which is surprising as carbene complexes are typically prone to hydrolysis even in the presence of traces of moisture in organic solvents. TGA/DSC measurements indicate good thermal stability as single-crystalline **Zn1** decomposes only above 210 °C by dissociation of one ^{Me}cAAC ligand after first liberating 2 equivalents of co-crystallized solvent (Figure S5).

Cyclic voltammetry (CV) on **Zn1** performed in acetonitrile using the ferrocene/ferrocenium couple as a reference revealed a series of irreversible oxidation events within the potential range of 0.2–1.5 V (Figure S7) that we assign to consecutive oxidations of the thiolate moieties. As a consequence, thiyl

radicals can be formed that have a strong tendency to dimerize to give disulfide species,[40] which can easily dissociate from the zinc(II) centers and thus explain the irreversible character of the oxidative events. In addition, we observed a fully reversible reduction wave at −2.35 V associated with the reduction of the ^{Me}cAAC ligand as shown by DFT calculations (Figure 2).



The UV/vis absorption spectra of **Zn1** in CH_2Cl_2 solution display a broad low-energy band with λ_{max}=374 nm (ϵ=3,600 M^{-1} cm^{-1}), which stems from bdt(π)→^{Me}cAAC(π*$_{CN}$) LLCT excitations with LMCT admixture according to our DFT/MRCI calculations (Figures 2 and 3). In the inversion-symmetric minimum nuclear arrangement of the electronic ground state, only the S_0→S_2 and S_0→S_3 transitions, both of ^1A_g→^1A_u type, carry nonvanishing but small electric dipole oscillator strengths of 0.02 and 0.05, respectively, which are in line with the observed weak absorption. Vibronic interactions, which lift the symmetry selection rules, are expected to lend intensity to the S_0→S_1 and S_0→S_4 transitions as well, thus broadening the band in the low-energy regime. The high-energy region of the spectrum shows a series of additional

Figure 2. Top: CV vs. Fc/Fc^+ in CH_3CN using an Ag reference electrode (left) and calculated spin density (right) of the radical anion Zn1$^-$. Middle: absorption spectra of **Zn1** in CH_2Cl_2 (yellow) and toluene (orange). Bottom: emission spectra of **Zn1** in PMMA, solid state, CH_2Cl_2 and toluene at 297 (solid lines) and 77 K (dashed lines).

absorptions including rather broad bands centred at 306 (structured, ϵ~5,500 M^{-1} cm^{-1}), 267 (ϵ=23,000 M^{-1} cm^{-1}) and 243 nm (ϵ=37,600 M^{-1} cm^{-1}), respectively. The first transition, calculated at 301 nm in THF, originates from an intra-ligand (IL)CT on bdt involving sulfur lone-pair orbitals as donors and the benzene π system as acceptor (Figure S25). The band with λ_{max}=267 nm consists of several strong transitions with varying LLCT and ILCT contributions. Here, charge is transferred from sulfur lone pairs to π* orbitals of the ^{Me}cAAC ligand or of the benzene unit of btd. At the blue edge of this band, the first bdt→Rydberg transition, involving 3d shells of the sulfur atoms, is encountered in the DFT/MRCI spectrum. Complex **Zn1** further features additional strong and high-energy absorptions shown as two narrow bands at 248 and 236 nm (ϵ~53,000 M^{-1} cm^{-1}) that can be assigned to LC transitions of π→π* character localized at the bdt unit (Figure S26). The absorption features in toluene solution are very similar, but λ_{max} of the lowest energy band shifts bathochromically by 27 nm (1,800 cm^{-1}) due to the lower solvent polarity in comparison to CH_2Cl_2 (see below), which is beneficial for utilization of **Zn1** in photocatalysis.

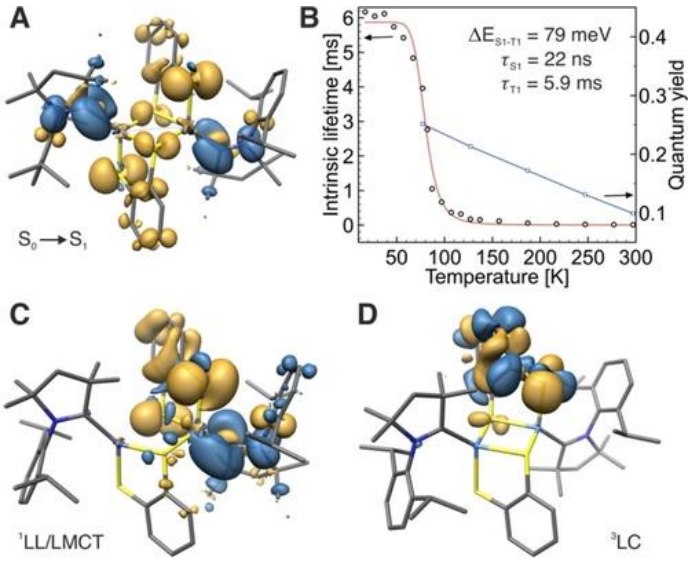


Figure 3. DFT/MRCI difference densities (isovalue ±0.0015) of the $S_0 \rightarrow S_1$ absorption (A), and of the optimized ^{1}LL/LMCT (C) and ^{3}LC (D) states of **Zn1** in THF. Areas losing electron density upon electronic excitation from the ground state are shown in gold, areas gaining electron density in blue. Experimental TADF fit of Zn1 in PMMA (B).

Upon photoexcitation (λ_{ex}=360–480 nm), broad luminescence with λ_{max}=648 nm is observed in de-aerated CH_2Cl_2 at room temperature, albeit with low quantum yield ϕ_{PL}=0.02 (Figure 2 and Table 1). The observed emission lifetime of 135 ns gives rise to k_r=1.5×10^5 s^{-1}, indicative of triplet states being involved.[6, 20-26] However, k_r is too fast for phosphorescence as SOC mediated by the zinc and sulfur atoms would be too small, and thus we assign the emission to TADF. We note a minor negative solvatochromic shift in toluene by 164 cm^{-1}, that might be related to the centrosymmetric nature of **Zn1** in its ground state. In both solvents, large Stokes shifts of 9,700–11,300 cm^{-1} are caused by unhindered geometry relaxation in the S_1 and T_1 state accompanied by substantial nuclear displacements and localization of the CT excitation on one side of the complex according to our calculations (Figure 3C). Consequently, facile vibrational relaxation $S_1/T_1 \rightsquigarrow S_0$ is possible, explaining the low ϕ_{PL} and short τ. This structural distortion is hindered in the solid state or in polystyrene (PS) matrix, and thus the emission shifts hypsochromically to λ_{max}=585 nm (Table 1). Interestingly, **Zn1** in PMMA matrix (10 wt-%) shows an even larger hypsochromic shift of 1,946 cm^{-1} compared to CH_2Cl_2 solution to λ_{max}=577 nm. In addition to the enhanced rigidity (see above), the polar environment stabilizes the polar ground state of **Zn1** with negatively charged bdt ligands and positively charged Zn$^{II/Me}$cAAC, further increasing the energy gap $\Delta E_{(S1-S0)}$. These effects lead to greatly enhanced ϕ_{PL}=0.10 while maintaining the high k_r. In order to shed light on the assumed TADF mechanism, we performed detailed variable-temperature (VT) measurements in PMMA, in which **Zn1** exhibits the most efficient luminescence (Figures 2 and 3). Upon lowering the temperature to 77 K, the yellow emission shifts hypsochromically by ca. 20 nm due to further rigidification, with a concomitant increase of τ to 987 µs. The intrinsic radiative lifetimes τ_{rad}=1/k_r between 7–297 K can be fitted to a three-states kinetic model (Figure 3B) according to Equation 1:

$$\tau_{rad} = \frac{3 + \exp\left[-\frac{\Delta E(S_1 - T_1)}{k_B T}\right]}{3k_{fl} + k_{ph} \cdot \exp\left[-\frac{\Delta E(S_1 - T_1)}{k_B T}\right]} \quad (1)$$

Table 1. Photophysical data for Zn1 in solid state, solutions, and polymeric matrices.

Medium	*T [K]*	λ_{max} *[nm]*	τ *[ns][a]*	Φ_{PL}	k_r *[s^{-1}][b]*	k_{nr} *[s^{-1}][c]*
solid	297	585	472	0.02	4.2×10^4	2.1×10^6
	77	587	170×10^3	0.06	35.2	552
crystals	297	644	97	>0.01	–	–
	77	639	260×10^3	0.01	38.5	3810
DCM	297	650	135	0.02	1.5×10^5	7.3×10^6
	77	551	316×10^3	–	–	–
Toluene	297	657	194	0.02	1.0×10^5	5.1×10^6
	77	596	641×10^3	–	–	–
PS	297	585	444	0.02	4.5×10^4	2.2×10^6
	77	580	927×10^3	0.08	86.3	993
PMMA	297	577	741	0.10	1.4×10^5	1.2×10^6
	77	558	987×10^3	0.25	253.0	760

[a] amplitude average lifetime, [b] $k_r=\phi_{PL}/\tau$, [c] $k_{nr}=(1-\phi_{PL})/\tau$.

providing an estimated $\Delta E_{(S1\text{-}T1)}$=79 meV (637 cm^{-1}), which is in excellent agreement with the DFT/MRCI energy difference at the S_1 minimum in THF of 90 meV (726 cm^{-1}). The small energy gap and long lifetime of the T_1 state of ca. 6 ms (calc. 32 ms) are beneficial for efficient rISC, and in combination with the estimated short $\tau(S_1)$=22 ns, efficient TADF is enabled.

An anomalous hypsochromic shift of the emission in CH_2Cl_2 by ca. 100 nm upon cooling to 77 K is observed (Table 1), which appears to originate from a population of a different excited state. In addition to the ^{3}LLCT state, we find a higher-lying minimum on the T_1 potential energy surface that is of ^{3}LC(dbt) nature (Figure 3D and Figure S31). The involvement of the sulfur atoms in the excitation mediates SOC (64 cm^{-1}, Table S9), resulting in phosphorescence with τ_{rad}=22 ms according to the calculations.

Transient absorption (TA) studies of Zn1 in toluene (Figure 4) confirm that internal conversion and ISC leading to the formation of the final ^{3}LL/LMCT state, that is involved in the TADF process, occur on a timescale faster than our instrument response of 10 ns. The TA spectrum shows in general a positive absorbance change over the whole spectral range with a drop in optical density at λ_{abs}=390 and 320 nm, which coincides with overlapping ground state absorption. The decays of the excited state absorption (ESA) at λ_{abs}=348 and 440 nm were fitted monoexponentially and yielded lifetimes of 370 and 354 ns, respectively, which is in the range of the recorded luminescence lifetimes.

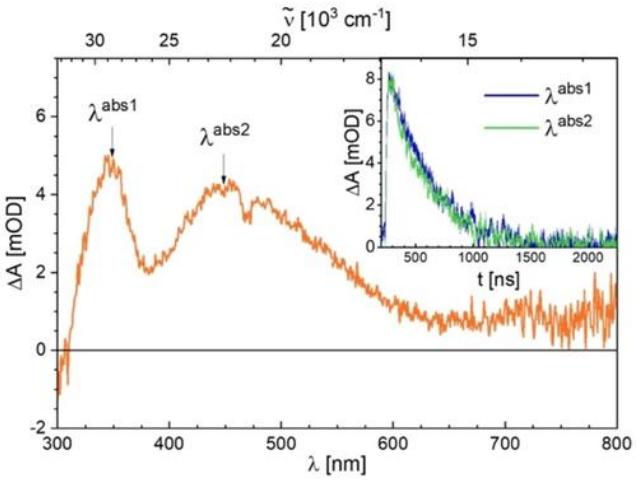


Figure 4. Transient absorption spectrum of **Zn1** in de-aerated toluene at 293 K, recorded at 10 ns time delay upon excitation at 420 nm with laser pulse energy of 15 mJ. The spectrum was recorded with an integration time of 100 ns after the indicated delay time. The inset shows the decays of the excited state absorption (ESA) signals at 348 nm (blue trace) and 440 nm (green trace).

The population of triplet excited states, of which the broad emission covers an energy range from 2.48-1.60 eV, with associated long lifetimes of hundreds of nanoseconds in solution suggests that **Zn1** may be employed in photocatalytic transformations as triplet sensitizer, similar to two recently reported Zn(II) complexes with dark (non-emissive) triplet excited states.[41] Fulfilling another important prerequisite for photocatalysis, the continuous irradiation of Zn1 for one hour with high-power 450 nm LEDs revealed excellent photostability by maintaining 96 % and 99 % of the original absorbance in toluene and THF, respectively (Figure S24). The photo-isomerization (*E*)-stilbene→(*Z*)-stilbene requires the population of the organic T_1 state at 2.2 eV, of which sensitization with our zinc(II) complex appears feasible. Indeed, 2 mol-% of Zn1 in degassed toluene give 93 % conversion after four hours of irradiation, which is faster than found for the standard $[Ru(bpy)_3]^{3+}$ that requires 5 mol-% and 8 h.[42] Control experiments under identical conditions but without Zn1 showed no formation of (*Z*)-stilbene (Figure S25), highlighting the suitability of our zinc(II) complex for photocatalytic transformations.

Conclusions

In conclusion, a new type of dimeric Zn^{II}-based emitter in the yellow to orange region of the electromagnetic spectrum, with a donor-M-acceptor motif by employing an electron-rich thiolate ligand in combination with an electrophilic carbene ligand, exhibits $^{1/3}$LLCT states suitable for efficient TADF with high k_r. The visible light absorption, for carbene complexes astonishing stability towards air and water, in combination with the observation of long-lived triplet states in solution renders the complex suitable for Dexter energy transfer photocatalysis. Overall, these promising first results clearly show that Zn^{II}-based photoactive complexes bear great potential as serious alternatives to traditional 4d and 5d transition metal compounds employed in devices and photochemistry.

Experimental Section

General considerations: All operations were performed under an argon atmosphere by using conventional Schlenk-line techniques or glovebox. The solvents were dried using Technology Inc. Pure-

Solv system or standard methods, and were degassed and stored over activated 4 Å molecular sieves. Dimeric $[Zn_2(\mu\text{-}Cl)_2(Cl)_2(^{Me}cAAC)_2]$[37] and benzene-1,2-dithiol[43, 44] (for details see below) were prepared according to established procedures. All other starting materials were available commercially and were used without further purification. ^1H, $^{13}C\{^1H\}$ APT, $^1H-^{13}C$ HSQC, $^1H-^{13}C$ HSMB, $^1H-^1H$ COSY and $^1H-^{15}N$ HMBC NMR spectra were measured at 300 K on Bruker 500 Avance or Bruker 600 Avance spectrometers. The chemical shifts are given in ppm relative to residual signals of the respective solvent [^1H, ^{13}C: CD_2Cl_2 (5.32, 53.84 ppm); C_6D_6 (7.16, 128.06)]. Cyclic voltammetry measurements were performed on a Gamry Instruments Reference [600] potentiostat with three electrodes cell configuration (working electrode: Pt-disk, counter electrode: Pt-wire, reference electrode: silver wire separated by Vycor tip). Redox potentials are referenced to the ferrocene/ferrocenium couple and $^nBu_4NBF_4$ was used (100 mM solution) as supporting electrolyte. TGA/DSC data were recorded using a STA650 instrument (TA instruments, USA) with a heat rate of 10 °C/min and under constant flow of nitrogen gas.

All photophysical measurements were performed in dry and de-aerated solutions. In the case of polymeric matrices, the respective polymer (PMMA or PS) was weighted into a vial together with 10 wt% of Zn1. Subsequently, the mixture was dissolved in DCM, the solution was added to a spectroscopic cuvette, and the solvent was slowly evaporated to form a thin layer (film) of Zn1 in the matrix. The remaining solvent molecules were evaporated by keeping the film under a low vacuum for 12 h. The solid-state measurements were performed either in single-crystalline form (sample denoted as ′crystals′) or, to remove co-crystallized molecules of solvent, single-crystals were ground and dried under vacuum for 24 h (sample denoted as ′solid′). Optical absorption spectroscopy was performed using an Agilent Cary 5000 spectrophotometer using standard 1 cm path length quartz cells. Excitation and emission spectra were recorded on an Edinburgh Instrument FLS1000 spectrometer, equipped with a 450 W Xenon arc lamp, double monochromators for the excitation and emission pathways, and a red-sensitive photomultiplier (PMT-980) as a detector. The excitation and emission spectra were corrected using the standard corrections supplied by the manufacturer for the excitation source‘s spectral power and the detector‘s sensitivity. Quantum yields in solution were measured using an FLS1000 spectrometer equipped with an integrating sphere (N-M01), and the quantum yield of solid samples and polymeric matrices were measured using an integrating cryosphere (Microstat N2) from Oxford Instruments. The luminescence lifetimes were measured using a µF2 pulsed 60 W Xenon microsecond flashlamp, with a repetition rate of 100 Hz and a multichannel scaling (MCS) module or with VPLEDs (383.8 nm with 1.1 mW or 449.6 nm with 37 mW), with 100 ns pulse width and an MCS module, depending on the time range. The emission was collected at a right angle to the excitation source. The low-temperature experiments were performed using liquid nitrogen-cooled OptistatDN-V cryostat from Oxford Instruments or 4 K cryostat (CS204SI-FMX-1SS) from Advanced Research System equipped with a closed cycle water-cooled helium compressor.

An LP920-KS apparatus from Edinburgh Instruments was employed for nanosecond transient absorption spectroscopy. Excitation was performed by a frequency-tripled Nd:YAG laser (Quantel Brilliant b, ca. 10 ns pulse width and ca. 10 mJ output) equipped with an OPO from Opotek (excitation wavelength set to 420 nm with ca. 15 mJ output). A beam expander (GBE02-A from Thorlabs) was used

to ensure homogeneous excitation. Detection of transient absorption spectra occurred on an iCCD camera (Andor), whereas kinetics at a single wavelength were recorded using a photomultiplier tube. Samples were prepared in toluene (50 µM), degassed by rigorous bubbling with dry Ar, and checked for photodegradation via UV/VIS in regular intervals over the course of the measurements.

Preliminary picosecond transient absorption studies with sub-nanosecond time resolution were performed using a TRASS instrument from Hamamatsu and a mode-locked picosecond Nd:YAG laser (model PL2251B-10-SH-TH with PRETRIG option) as an excitation source. The laser pulse duration was ~30 ps and the pulse frequency was 10 Hz. The third harmonic (355 nm) was used for excitation of the sample, however, significant decomposition was observed over the course of the measurement, presumably due to the high energy (both pulse energy and wavelength) of the excitation source.

Computational Methods: For all geometry optimizations the Gaussian 16 program was used.[45] The ground state geometries were optimized with Kohn–Sham density functional theory (DFT).[46] For the optimization of the singlet excited state geometries the time dependent DFT (TDDFT)[47] was used and for the excited triplet state geometries the Tamm-Dancoff approximation (TDA)[48] to TDDFT was chosen. The 10-mdf 6 s5p3d basis set with defpp-ecp was used for the zinc atoms[49] and for sulfur the def2-SVPD basis was chosen.[50] For all other atoms the def-SV(P) basis set was used.[50] As functional BH-LYP functional was chosen for all calculations.[51, 52] A THF environment was mimicked via the polarizable continuum model (PCM).[53, 54] To examine the excitation energies and oscillator strengths of the spin allowed transitions, DFT/MRCI calculations were carried out.[55, 56] As Hamiltonian, the redesigned R2018 was selected and 30 singlet and 30 triplet roots were calculated. For the DFT/MRCI calculations, the point charges of the Gaussian 16 calculations were extracted. With the SPOCK program, the spin-orbit coupling matrix elements (SOCMEs) were obtained.[57, 58]

Synthetic Procedures

$C_6H_4S_2H_2$ (H_2bdt): 5 mL of benzenethiol (49 mmol) were added dropwise to a mixture of *n*-BuLi (103 mmol, 2.5 M, 41 mL) and TMEDA (54 mmol, 8.1 mL) in 40 mL of *n*-pentane at −78 °C. The mixture was allowed to slowly warm to room temperature and stirred overnight. Then the solution was again cooled to −78 °C and octasulfur (49 mmol) was added dropwise. The mixture was stirred at −78 °C for two hours and overnight at room temperature, followed by slow addition of 10 mL of water. The quenched mixture was poured into diluted hydrochloric acid and extracted with Et_2O (3×50 mL). Organic layers were combined, dried over anhydrous $MgSO_4$ and evaporated to dryness using rotavapor. The crude product was vacuum distilled (55 °C, 0.2 mbar) to give 1.4 mL (24 %) of colorless liquid. ^{1}H NMR (500 MHz, C_6D_6): 7.96 (m, 2H), 6.65 (m, 2H), 3.35 (s, 2H). ^{13}C NMR (125 MHz, C_6D_6): 131.4 (s, 2 C), 130.9 (s, 2 C), 126.4 (s, 2 C).

$C_6H_4S_2Na_2$ (bdt): 337 mg (14 mmol) of NaH was dispersed in 20 mL of THF and 1.1 g (7.7 mmol) of benzene-1,2-dithiol in 10 mL of THF was added dropwise. After complete addition, the mixture was stirred for one hour at 60 °C and then overnight at room temperature. After filtration, the remaining white solid was washed with additional portion of THF (2×15 mL) and the product was vacuum-dried for 4 h at 60 °C. Yield: 942 mg (5.0 mmol, 72 %) of white powder.

[(^{Me}cAAC)Zn(k*S*:μ^2*S*-PhS$_2$)$_2$Zn(^{Me}cAAC)] (**Zn1**): 47 mg of (250 mmol) disodium benzene-1,2-dithiolate (bdt) was mixed with 100 mg (119 mmol) of [(^{Me}cAAC)(Cl)Zn(μ-Cl)$_2$Zn(Cl)(^{Me}cAAC)] in 7 mL of THF and the resulting mixture was stirred overnight at room temperature. After that, the solvents were vacuum-evaporated, and the solid residue was extracted with DCM (3x5 mL). The combined organic fractions were concentrated by vacuum evaporation to a final volume of 3 mL and crystallization was induced by gas phase diffusion of n-pentane. The obtained single-crystals were collected, washed with cold THF (2 mL), *n*-pentane (2×5 mL) and vacuum dried. Yield: 86 mg (73.5 %, 86 mmol) of yellow crystalline material. CHNS analysis calcd for $C_{53}H_{72}N_2S_4ZnCl_2$: C, 59.7; H, 6.8; N, 2.6. Found: C, 59.8; H, 7.1; N, 2.62. ^{1}H NMR (600 MHz, CD_2Cl_2): δ [ppm]=7.53 (t, $^3J(^1H,^1H)$=7.8 Hz, 2H, H^4, C$_6$*H*$_3$^{i}Pr$_2$), 7.39 (m, 4H, C$_6$*H*$_4$S$_2$), 7.35 (d, $^3J(^1H,^1H)$=7.8 Hz, 4H, H^{3,5}, C$_6$*H*$_3$^{i}Pr$_2$), 6.69 (m, 4H, C$_6$*H*$_4$S$_2$), 2.77 (sept, $^3J(^1H,1H)$=6.7 Hz, 4H, C*H*^{iPr}), 2.17 (s, 4H, −C*H*$_2$−), 1.57 (s, 12H, (C*H*$_3$)$_2$), 1.48 (s, 12H, (C*H*$_3$)$_2$), 1.32 (d, $^3J(^1H,1H)$=6.7 Hz, 12H, C*H*$_3$^{iPr}), 1.23 d, $^3J(^1H,^1H)$=6.7 Hz, 12H, C*H*$_3$^{iPr}). ^{13}C NMR (125 MHz, CD_2Cl_2): δ [ppm]=243.8 (s, 2 C, *C*^{carbene}), 145.2 (s, 4 C, C^{2,6}, *Dipp*), 144.4 (s, 4 C, C^{1,2}, *Ph*S$_2$), 133.9 (s, 2 C, C^1, *Dipp*), 130.9 (s, 2 C, C^4, *Dipp*), 130.6 (s, 4 C, *Ph*S$_2$), 126.1 (s, 4 C, C^{3,5}, *Dipp*), 122.3 (s, 4 C, *Ph*S$_2$), 84.5 (s, 2 C, N*C*C^{carbene}), 55.2 (s, 2 C, N*C*(CH$_3$)$_2$), 49.9 (s, 2 C, -*C*H$_2$−), 29.5 (s, 4 C, C(*C*H$_3$)$_2$), 29.4 (s, 4 C, *C*H(CH$_3$)$_2$, Dipp), 28.1 (s, 4 C, C(*C*H$_3$)$_2$), 27.3 (s, 4 C, CH(*C*H$_3$)$_2$, Dipp), 23.9 (s, 4 C, CH(*C*H$_3$)$_2$, Dipp). ^{15}N (60 MHz, CD_2Cl_2): δ [ppm]=-141.86 ppm.

Deposition Number 2189606 (for Zn1) contains the supplementary crystallographic data for this paper. These data are provided free of charge by the joint Cambridge Crystallographic Data Centre and Fachinformationszentrum Karlsruhe Access Structures service.

References

[1] C. Förster, K. Heinze, *Chem. Soc. Rev.* **2020**, *49*, 1057–1070.

[2] O. S. Wenger, *J. Am. Chem. Soc.* **2018**, *140*, 13522–13533.

[3] C. B. Larsen, O. S. Wenger, *Chem. Eur. J.* **2018**, *24*, 2039–2058.

[4] C. Wegeberg, O. S. Wenger, *JACS Au* **2021**, *1*, 1860–1876.

[5] B. M. Hockin, C. Li, N. Robertson, E. Zysman-Colman, *Catal. Sci. Technol.* **2019**, *9*, 889–915. [6] A. Steffen, B. Hupp, in Comprehensive Coordination Chemistry III (Eds.: E. C. Constable, G. Parkin, L. Que Jr), Elsevier, Oxford, **2021**, pp. 466–502.

[7] O. S. Wenger, *Chem. Rev.* **2013**, *113*, 3686–3733.

[8] Q. Zhao, C. Huang, F. Li, *Chem. Soc. Rev.* **2011**, *40*, 2508–2524.

[9] C. Bizzarri, E. Spuling, D. M. Knoll, D. Volz, S. Bräse, *Coord. Chem. Rev.* **2018**, *373*, 49–82.

[10] R. Hamze, J. L. Peltier, D. Sylvinson, M. Jung, J. Cardenas, R. Haiges, M. Soleilhavoup, R. Jazzar, P. I. Djurovich, G. Bertrand, M. E. Thompson, *Science* **2019**, *363*, 601–606.

[11] J. X. Wang, C. Li, H. Tian, *Coord. Chem. Rev.* **2021**, *427*, 213579.

[12] J.-H. Shon, D. Kim, M. D. Rathnayake, S. Sittel, J. Weaver, T. S. Teets, *Chem. Sci.* **2021**, *12*, 4069–4078.

[13] C. K. Prier, D. A. Rankic, D. W. C. MacMillan, *Chem. Rev.* **2013**, *113*, 5322–5363.

[14] D. M. Arias-Rotondo, J. K. McCusker, *Chem. Soc. Rev.* **2016**, *45*, 5803–5820.

[15] J. K. McCusker, *Science* **2019**, *363*, 484–488.

[16] P. Chábera, Y. Liu, O. Prakash, E. Thyrhaug, A. El Nahhas, A. Honarfar, S. Essén, L. A. Fredin, T. C. B. Harlang, K. S. Kjær, K. Handrup, F. Ericson, H. Tatsuno, K. Morgan, J. Schnadt, L. Häggström, T. Ericsson, A. Sobkowiak, S. Lidin, P. Huang, S. Styring, J. Uhlig, J. Bendix, R. Lomoth, V. Sundström, P. Persson, K. Wärnmark, *Nature* **2017**, *543*, 695–699.

[17] S. Otto, M. Grabolle, C. Förster, C. Kreitner, U. Resch-Genger, K. Heinze, *Angew. Chem. Int. Ed.* **2015**, *54*, 11572–11576.

[18] S. B. Vittardi, R. T. Magar, B. R. Schrage, C. J. Ziegler, E. Jakubikova, J. J. Rack, *Chem. Commun.* **2021**, *57*, 4658–4661.

[19] Y. Zhang, T. S. Lee, J. M. Favale, D. C. Leary, J. L. Petersen, G. D. Scholes, F. N. Castellano, C. Milsmann, *Nat. Chem.* **2020**, *12*, 345–352.

[20] M. Gernert, U. Müller, M. Haehnel, J. Pflaum, A. Steffen, *Chem. Eur. J.* **2017**, *23*, 2206–2216.

[21] M. Gernert, L. Balles-Wolf, F. Kerner, U. Müller, A. Schmiedel, M. Holzapfel, C. M. Marian, J. Pflaum, C. Lambert, A. Steffen, *J. Am. Chem. Soc.* **2020**, *142*, 8897–8909.

[22] R. Hamze, S. Shi, S. C. Kapper, D. S. Muthiah Ravinson, L. Estergreen, M.-C. Jung, A. C. Tadle, R. Haiges, P. I. Djurovich, J. L. Peltier, R. Jazzar, G. Bertrand, S. E. Bradforth, M. E. Thompson, *J. Am. Chem. Soc.* **2019**, *141*, 8616–8626.

[23] A. M. T. Muthig, M. Krumrein, J. Wieland, M. Gernert, F. Kerner, J. Pflaum, A. Steffen, *Inorg. Chem.* **2022**, *61*, 14833–14844.

[24] V. A. Krylova, P. I. Djurovich, B. L. Conley, R. Haiges, M. T. Whited, T. J. Williams, M. E. Thompson, *Chem. Commun.* **2014**, *50*, 7176–7179.

[25] B. Hupp, C. Schiller, C. Lenczyk, M. Stanoppi, K. Edkins, A. Lorbach, A. Steffen, *Inorg. Chem.* **2017**, *56*, 8996–9008.

[26] B. Hupp, J. Nitsch, T. Schmitt, R. Bertermann, K. Edkins, F. Hirsch, I. Fischer, M. Auth, A. Sperlich, A. Steffen, *Angew. Chem. Int. Ed.* **2018**, *57*, 13671–13675;

[27] J. Nitsch, F. Lacemon, A. Lorbach, A. Eichhorn, F. Cisnetti, A. Steffen, *Chem. Commun.* **2016**, *52*, 2932–2935.

[28] A. Ruduss, B. Turovska, S. Belyakov, K. A. Stucere, A. Vembris, K. Traskovskis, *Inorg. Chem.* **2022**, *61*, 2174–2185.

[29] R. Tang, S. Xu, T.-L. Lam, G. Cheng, L. Du, Q. Wan, J. Yang, F.-F. Hung, K.-H. Low, D. L. Phillips, C.-M. Che, *Angew. Chem. Int. Ed.* **2022**, *61*, e202203982.

[30] S. Bestgen, C. Schoo, B. L. Neumeier, T. J. Feuerstein, C. Zovko, R. Köppe, C. Feldmann, P. W. Roesky, *Angew. Chem. Int. Ed.* **2018**, *57*, 14265–14269;

[31] R. Sakamoto, T. Iwashima, J. F. Kögel, S. Kusaka, M. Tsuchiya, Y. Kitagawa, H. Nishihara, *J. Am. Chem. Soc.* **2016**, *138*, 5666–5677.

[32] J. F. Kögel, S. Kusaka, R. Sakamoto, T. Iwashima, M. Tsuchiya, R. Toyoda, R. Matsuoka, T. Tsukamoto, J. Yuasa, Y. Kitagawa, T. Kawai, H. Nishihara, *Angew. Chem. Int. Ed.* **2016**, *55*, 1377–1381;

[33] K. A. Truesdell, G. A. Crosby, *J. Am. Chem. Soc.* **1985**, *107*, 1787–1788.

[34] N. Lüdtke, J. Kuhnt, T. Heil, A. Steffen, C. M. Marian, *ChemPhotoChem* **2022**, *7*, e202200142.

[35] B. Goswami, T. J. Feuerstein, R. Yadav, S. Lebedkin, P. J. Boden, S. T. Steiger, G. Niedner-Schatteburg, M. Gerhards, M. M. Kappes, P. W. Roesky, *Chem. Eur. J.* **2021**, *27*, 15110–15119.

[36] Y. Sakai, Y. Sagara, H. Nomura, N. Nakamura, Y. Suzuki, H. Miyazaki, C. Adachi, *Chem. Commun.* **2015**, *51*, 3181–3184.

[37] O. Mrózek, M. Gernert, A. Belyaev, M. Mitra, L. Janiak, C. M. Marian, A. Steffen, *Chem. Eur. J.* **2022**, *28*, e202201114.

[38] K. Halvorsen, G. A. Crosby, W. F. Wacholtz, *Inorg. Chim. Acta* **1995**, *228*, 81–88.

[39] D. M. Hatch, W. F. Wacholtz, J. T. Mague, *Acta Crystallogr. Sect. C* **2003**, *59*, m452-m453.

[40] M. Borsari, M. Cannio, G. Gavioli, *Electroanalysis* **2003**, *15*, 1192–1197.

[41] J. A. Kübler, B. Pfund, O. S. Wenger, *JACS Au* **2022**, *2*, 2367–2380.

[42] M. M. Floes-Leonar, C. R. Azpilcueta, C. Amador-Bedolla, S. S. Rozenel, *J. Photochem. Photobiol. A* **2021**, *414*, 113224.

[43] P. S. Nejman, B. Morton-Fernandez, N. Black, D. B. Cordes, A. M. Slawin, P. Kilian, J. D. Woollins, *J. Organomet. Chem.* **2015**, *776*, 7–16.

[44] D. M. Giolando, K. Kirschbaum, *Synthesis* **1992**, 451–452.

[45] Gaussian 16, Revision A.03, M. J. Frisch, G. W. Trucks, H. B. Schlegel, G. E. Scuseria, M. A. Robb, J. R. Cheeseman, G. Scalmani, V. Barone, G. A. Petersson, H. Nakatsuji et al., **2016**; Gaussian Inc. Wallingford CT.

[46] M. Von Arnim, R. Ahlrichs, *J. Comput. Chem.* **1998**, *19*, 1746–1757.

[47] F. Furche, R. Ahlrichs, *J. Chem. Phys.* **2002**, *117*, 7433–7447.

[48] S. Hirata, M. Head-Gordon, *Chem. Phys. Lett.* **1999**, *314*, 291–299.

[49] D. Figgen, G. Rauhut, M. Dolg, H. Stoll, *Chem. Phys.* **2005**, *311*, 227–244.

[50] A. Schäfer, H. Horn, R. Ahlrichs, *J. Chem. Phys.* **1992**, *97*, 2571–2577.

[51] C. Lee, W. Yang, R. G. Parr, *Phys. Rev. B* **1988**, *37*, 785–789.

[52] A. D. Becke, *J. Chem. Phys.* **1993**, *98*, 1372–1377.

[53] E. Cancès, B. Mennucci, J. Tomasi, *J. Chem. Phys.* **1997**, *107*, 3032.

[54] B. Mennucci, E. Cancès, J. Tomasi, *J. Phys. Chem. B* **1997**, *101*, 10506.

[55] S. Grimme, M. Waletzke, *J. Chem. Phys.* **1999**, *111*, 5645–5655.

[56] C. M. Marian, A. Heil, M. Kleinschmidt, *WIREs Comput. Mol. Sci.* **2019**, *9*, e1394.

[57] M. Kleinschmidt, J. Tatchen, C. M. Marian, *J. Comput. Chem.* **2002**, *23*, 824–833.

[58] M. Kleinschmidt, C. M. Marian, *Chem. Phys.* **2005**, *311*, 71–79.

2.3 Structural Control of Highly Efficient Thermally Activated Delayed Fluorescence in Carbene Zinc(II) Dithiolates

This subchapter as part of this dissertation work was published in collaboration with Wiley-VCHGmbH.[5] Reprinted with permission from *Angew. Chemie Int. Ed.* **2024**, *63*, e202316300. copyright ©2023 The Authors. Angewandte Chemie International Edition published by Wiley-VCH GmbH.

Summary: Luminescent metal complexes based on earth abundant elements are a valuable target to substitute 4d/5d transition metal complexes as triplet emitters in advanced photonic applications. Whereas Cu^{I} complexes have been thoroughly investigated in the last two decades for this purpose, no structure-property-relationships for efficient luminescence involving triplet excited states from Zn^{II} complexes are established. Herein, we report on the design of monomeric carbene zinc(II) dithiolates (CZT) featuring a donor-acceptor-motif that leads to highly efficient thermally activated delayed fluorescence (TADF) with for Zn^{II} compounds unprecedented radiative rate constants k_{TADF} = 1.2×10^{6} s^{-1} at 297K. Our high-level DFT/MRCI calculations revealed that the relative orientation of the ligands involved in the ligand-to-ligand charge transfer ($^{1/3}$LLCT) states is paramount to control theTADFprocess. Specifically, a Dihedral angle of 36–40° leads to very efficient reverse intersystem-crossing(rISC) on the order of10^{9} s^{-1} due to spin-orbit coupling (SOC) mediated by the sulfur atoms in combination with a small $\Delta E_{S1\text{-}T1}$ of ca. 56meV.

Contribution to experimental part: approx. 70%

Contribution to the written part: approx. 20%

Structural Control of Highly Efficient Thermally Activated Delayed Fluorescence in Carbene Zinc(II) Dithiolates

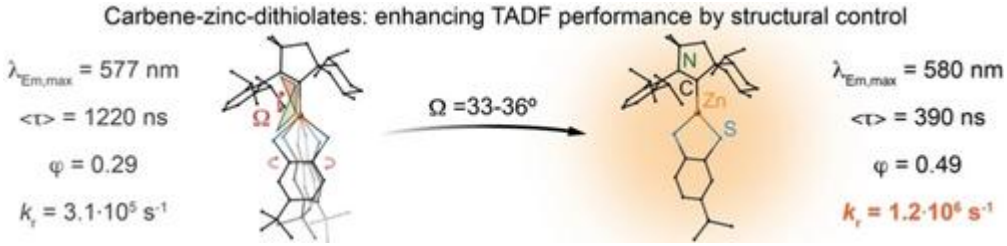
Mousree Mitra, Ondřej Mrózek, Markus Putscher, Jasper Guhl, Benjamin Hupp, Andrey Belyaev, Christel M. Marian, Andreas Steffen

Abstract

Luminescent metal complexes based on earth abundant elements are a valuable target to substitute 4d/5d transition metal complexes as triplet emitters in advanced photonic applications. Whereas Cu^{I} complexes have been thoroughly investigated in the last two decades for this purpose, no structure-property-relationships for efficient luminescence involving triplet excited states from Zn^{II} complexes are established. Herein, we report on the design of monomeric carbene zinc(II) dithiolates (CZT) featuring a donor-acceptor-motif that leads to highly efficient thermally activated delayed fluorescence (TADF) with for Zn^{II} compounds unprecedented radiative rate constants k_{TADF}=1.2×10^6 s^{-1} at 297 K. Our high-level DFT/MRCI calculations revealed that the relative orientation of the ligands involved in the ligand-to-ligand charge transfer ($^{1/3}$LLCT) states is paramount to control the TADF process. Specifically, a dihedral angle of 36–40° leads to very efficient reverse intersystem-crossing (rISC) on the order of 10^9 s^{-1} due to spin-orbit coupling (SOC) mediated by the sulfur atoms in combination with a small $\Delta E_{S1\text{-}T1}$ of ca. 56 meV.

Graphical Abstract

Zinc - the new iridium. Structural control of the dihedral angle between the ligands in trigonal-planar carbene-Zn^{II}-dithiolates leads to highly efficient thermally activated delayed fluorescence (TADF) with unprecedented radiative rate constants k_{TADF}=1.2×10^6 s^{-1} at 297 K, which surpass the efficiency of commercial Ir^{III}- and Pt^{II}-based triplet emitters.



Introduction

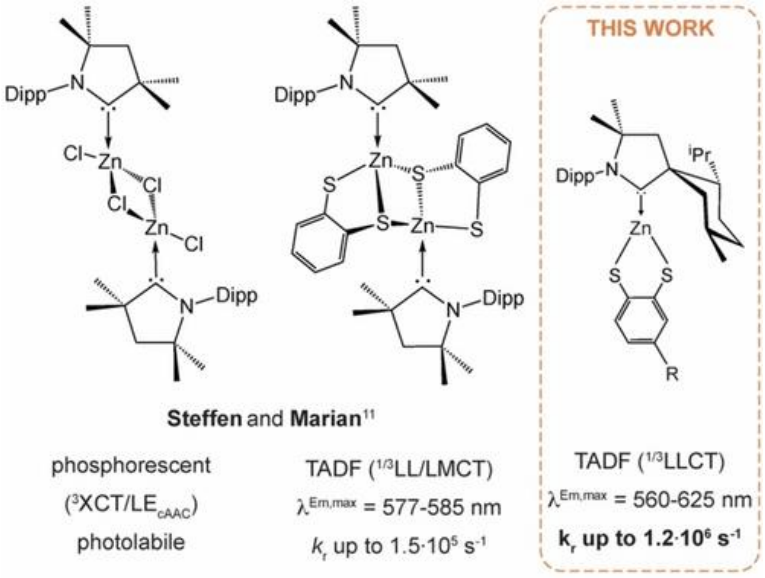
The investigation of 3d transition metal compounds as substitutes for precious metal complexes in photonic applications is a very timely topic.[1] One of the reasons is the comparably costly and energy-intensive production of 4d and 5d elements that are typically employed to facilitate and make use of photoinduced spin-forbidden processes due to their strong SOC, including phosphorescence as a radiative decay channel of triplet excited states. Another motivation is the search for new combinations of photophysical and photochemical properties and modes to control them. The last decade has seen a phoenix-like rise of the lighter and weaker SOC-mediating congeners of the d element complexes,

with manifold applications of Zr^{IV},[2] $Cr^{0/III/VI}$,[3] Mn^{I},[4] $Fe^{II/III}$,[5] Co^{III},[6] Ni^{II}[7] and Cu^{I}[8] compounds in photo-induced energy (EnT) and electron transfer (ET), up-conversion, sensing, light-emitting devices, and as responsive smart materials. However, when it comes to efficient luminescence involving triplet excited states for device applications, copper(I) complexes in their d^{10} electron configuration are undoubtedly the prime choice among the 3d elements.[1a, 8a-8c, 9] They do not feature detrimental metal-centered (MC) dd* states as potential non-radiative decay channels, and the weak SOC is sufficient for (r)ISC processes necessary for TADF, by which inefficient phosphorescence from the triplet excited states is bypassed and emission can occur from the singlet manifold. It is important to note the general photophysical differences between organic and transition metal TADF emitters. The latter usually exhibit a higher density of states (DOS) due to additional metal-to-ligand charge transfer (MLCT) or ligand-to-metal (LM)CT states promoting SOC, which influence the excited state kinetics. Consequently, the radiative lifetimes τ_{TADF} of organometallic TADF emitters at room temperature are typically shorter than observed for organics and can even surpass those of established Ir^{III} or Pt^{II} emitters.[8g, 10] Although luminescent Cu^{I} complexes are well established, one of the limitations of their widespread usage is the high redox activity of the copper center, which can lead to premature degradation in electroluminescent devices.

An alternative that could resolve this issue are Zn^{II} complexes, where the metal ion features a considerably higher redox stability and a d^{10} electron configuration, hindering undesired non-radiative decay via MC states and allowing for modification of the coordination geometry to tune the photophysical properties. Only few Zn^{II} compounds with emission involving triplet excited states have been reported, most of which undergo facile non-radiative decay at room temperature and phosphoresce only at low temperatures.[11] Wenger and co-workers showed that the dark but long-lived ligand-centred (^{3}LC) states in zinc(II) complexes can be useful for application in photocatalysis, photoinduced ET and upconversion.[12] However, Bernhard and co-workers found indications that a hemi-cage analogue of fluorescent $[Zn(bpy)_3]^{2+}$ bearing a hexadentate bipyridyl-based ligand shows phosphorescence from a ^{3}LC state with τ=70 ns in solution at room temperature, albeit with low quantum yields of Φ=0.07.[11g] Heteroleptic zinc(II) 1,10-phenanthroline bis(thiophenolates) exhibit excited states of LLCT character and have been studied in detail by Crosby et al.[11h, 11i] Although the emission is very weak at room temperature, very recently we were able to show that the dominant radiative path is TADF.[13] Adachi and co-workers found in $[Zn(PX\text{-}BOX\text{-}O)_2]$ (PX-BOX-O=bis(2-(benzo[d]oxazol-2-yl)-5-(10H-phenoxazin-10-yl)phenolate) a delayed component with Φ_{TADF}=0.48–0.66 beside prompt fluorescence (Φ_{Fl}=0.10–0.12) from intra-ligand ($^{1/3}$IL)CT states. The rISC is moderately efficient with k_{rISC}=1.4–16.9×10^4 s^{-1}, but proof-of-concept application in OLEDs demonstrates the potential of Zn^{II} complexes.[11j]

In contrast to Cu^{I} complexes featuring MLCT states that can mediate SOC for spin-forbidden processes, the d orbitals of the Zn^{II} ion do not participate in the excited states in the above-mentioned examples, which explains the low to moderate triplet emission performance. In order to improve the TADF process by enhancing the DOS,[14] we have started to develop a fundamentally different class of Zn^{II} emitters bearing cyclic(alkyl)(amino) carbenes (cAAC) as potent excited-state π-acceptors, which can provide

access to LLCT states with an admixture of unusual LMCT.[15] Following our initial report on phosphorescent $[ZnX_2(^{Me}cAAC)_2]_2$ with ultra-long lifetimes,[15a] we developed the first dimeric carbene-zinc-thiolate (CZT) $[Zn(bdt)(^{Me}cAAC)]_2$ (bdt=benzene-1,2-dithiolate) with a suitable donor-acceptor motif for this purpose (Scheme 1).[15b]

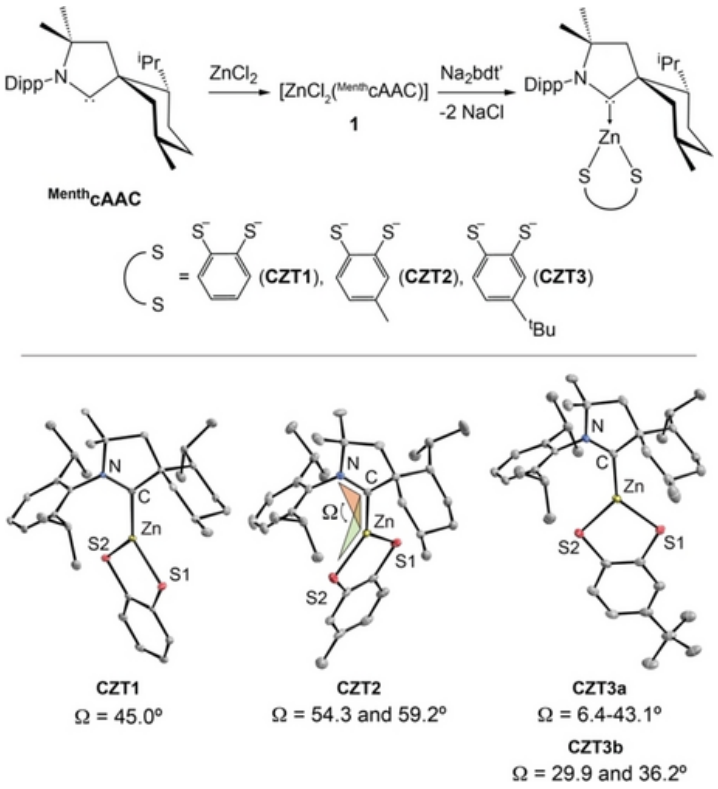


Scheme 1. Development of luminescent Zn^{II} carbene complexes. Left: phosphorescent Zn^{II} halide carbenes. Middle: first example of a carbene-zinc-thiolate (CZT) showing TADF. Right: latest generation of CZT-TADF emitters.

Indeed, the resulting small energy gap $\Delta E_{S1\text{-}T1}$ of 79 meV allows for efficient rISC and TADF with good k_{TADF} of up to 1.5×10^5 s^{-1} in dichloromethane solution at room temperature. Although these results clearly demonstrate the potential of our approach, and the compound is even stable in oxygen-saturated wet organic solvents under UV irradiation, the main drawback remains the moderate Φ=0.1 in PMMA matrix.[15b] Herein, we report on a new generation of monomeric **CZT** complexes composed of sterically demanding menthyl-substituted cAAC (^{Menth}cAAC) and various bdt derivatives, giving highly efficient TADF for Zn^{II} complexes with unprecedented k_{TADF} of up to 1.2×10^6 s^{-1} at 297 K.

Results and Discussion

The target compounds $[Zn(^{R}bdt)(^{Menth}cAAC)]$ (R=4-H (**CZT1**), 4-Me (**CZT2**), 4-^{t}Bu (**CZT3**)) were prepared by a two-step protocol (Scheme 2, top), starting with addition of ^{Menth}cAAC to $ZnCl_2$ to afford the synthon $[ZnCl_2(^{Menth}cAAC)]$ (**1**). We found **1** to be highly reactive and unstable, leading to contamination with protonated carbene independent of the purification methods. Although this prevented its full characterization, single crystals were obtained by gas phase diffusion of *n*-pentane into a THF solution of **1** (Figure S9). However, in situ generation of **1** and subsequent halide exchange with the disodium salt of the respective 4-R-benzene-1,2-dithiolate provides facile access to monomeric **CZT1–3**. The compounds are highly soluble and stable in THF, dichloromethane and toluene, which we attribute to the chelating coordination of the bdt ligands and the steric protection of the Zn−C(cAAC) bond. Remarkably, the ^{t}Bu moiety in **CZT3** not only leads to additional solubility in *n*-pentane, but greatly enhances the stability in solution even in the presence of water (Figure S7).



Scheme 2. Top: Synthesis of **1** and **CZT1–3**. Bottom: Molecular structures of **CZT1–3** and their dihedral angles Ω. Hydrogen atoms are omitted for clarity.

The $^{13}C\{^{1}H\}$ NMR resonance of the carbene carbon in **CZT1–3** at ≈245 ppm shows a significant upfield shift in comparison to the free ligand (319 ppm)[16] and thus clearly proves successful coordination of ^{Menth}cAAC to the Zn^{II} ion. In addition, the ^{1}H and ^{13}C NMR spectroscopic measurements of **CZT1–3** also show only one set of sharp signals, arguing for barrier-free rotation of the carbene and/or dithiolate ligands at room temperature. Indeed, our DFT calculations confirm a very low rotational energy barrier of only 4 kJ/mol for **CZT1** (Figure S16). Single crystal X-ray diffraction studies reveal a trigonal planar coordination of the zinc(II) center in **1** and **CZT1–3** (Scheme 2, bottom).[17] For all complexes the Zn−$C^{CARBENE}$ interatomic distances have comparable values in the range of 2.015–2.045 pm. The Zn−Cl and Zn−S distances of ≈2.2 pm found in **1**, and **CZT1**/**CZT2**, respectively, are in the range typically found for related Zn^{II} halide and aromatic dithiolate complexes.[15b, 18] The molecular packing in the solid state is influenced by the bdt substituents in the 4-position, leading to different dihedral angles Ω between the S−Zn−S plane and the carbene plane of 45° and 59° for **CZT1** and **CZT2**, respectively. Interestingly, we were able to isolate different ligand conformations upon recrystallization of **CZT3** from either THF/*n*-pentane (**CZT3a**) or toluene/cyclohexane (**CZT3b**) mixtures (Scheme 2), which greatly affect the excited state behavior (see below). In the case of **CZT3a**, the unit cell comprises eight independent molecules with values of Ω between 6.4–43.1°, whereas for **CZT3b** only two independent molecules with Ω of 29.9 and 36.2° were found (Table S1).

The electronic UV/Vis absorption spectra of **CZT1–3** in dichloromethane show a very broad low intensity band between 350–480 nm that we assign to a π(bdt)→π*(C−N, cAAC) transition of LLCT character according to our DFT/MRCI studies, which is sensitive to the dihedral angle Ω between the ligands

(Figure 1). A tilted conformation (calc. Ω_{S0}=40°) is the most stable one in the electronic ground state, and a scan of the torsional potential shows that nearly planar (Ω_{S0}=10°) and orthogonal (Ω_{S0}=76°) conformers are separated by only small energy barriers, which are easily surmounted at ambient temperatures (Figure S16).

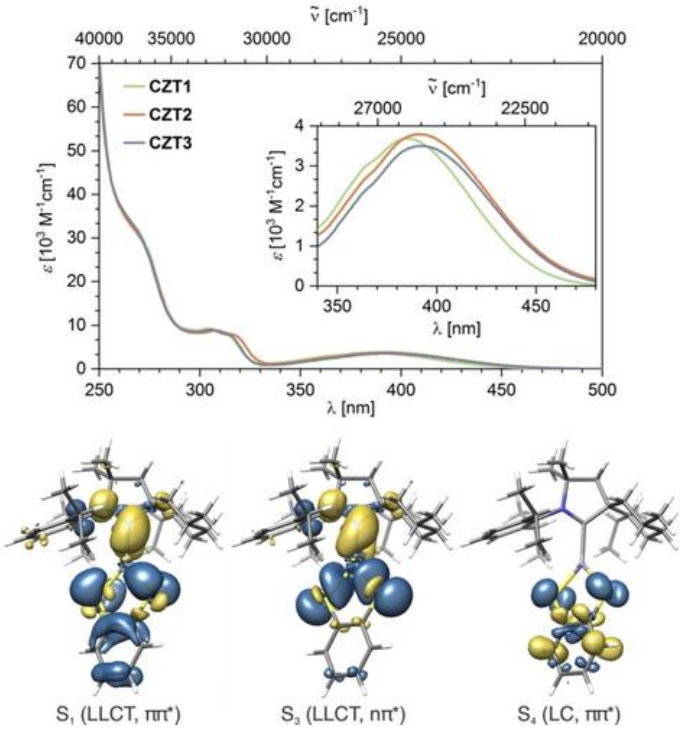


Figure 1. Experimental UV/Vis absorption spectra of **CZT1–3** in CH_2Cl_2 solution at room temperature and electron density differences of the transitions from the ground state S_0 to the S_1 (^{1}LLCT, ππ*), S_3 (^{1}LLCT, nπ*) and S_4 (^{1}LC, ππ*) excited states (calculated at the DFT/MRCI level of theory; loss of electron density is indicated in blue and gain in yellow; isosurface values ±0.002; see also ESI).

Consequently, the extinction coefficients ϵ=3,500–3,800 M^{-1} cm^{-1} represent averages over all conformers in solution due to the high fluxionality of the complexes. Substitution of the bdt ligand in the 4-position in **CZT2** and **CZT3** gives rise to only a very minor bathochromic shift of this band. The more intense (ϵ ≈8,900–9,300 M^{-1} cm^{-1}) band between 290–330 nm shows two maxima and originates from an LLCT transition related to an excitation from the sulfur lone pairs (n) to the C−N π* orbital of the cAAC, and an LC ππ*(bdt) state (see also Tables S9–S11). The high energy region (below 280 nm) is dominated by allowed, high intensity bands of ^{1}LC (ππ*) character.

Upon irradiation of powder samples of **CZT1–3** with λ_{ex}<450 nm, bright yellow-to-orange photoluminescence with large Stokes shift (λ_{max}=560–583 nm) apparently from an LLCT state is observed at room temperature (Figure 2, Table 1). In comparison to previously reported dimeric [Zn(bdt)(^{Me}cAAC)]$_2$, which displays a small photoluminescence quantum yield Φ=0.02,[15b] the efficiency of the monomers is 6–15 times enhanced to reach values of up to 0.29 for **CZT3**. The observed averaged luminescence lifetimes of τ_{av}=170–630 ns suggest radiative rate constants of k_r=4.5 (**CZT1**), 7.5 (**CZT2**) and 7.4×10^5 (**CZT3**) s^{-1}, that are higher by more than one order of magnitude than found for the dimer[15b] and indicative of triplet excited states being involved. Although the luminescence

quantum yields are decreased in PMMA or polystyrene films for **CZT2** and **CZT3,** the k_r are still in the range of 10^5 s^{-1} (Table 1). The broad LLCT emission is also observed in CH_2Cl_2 solution at room temperature (Figure S11), but the high fluxionality of the complexes in solution (see above) leads to very facile non-radiative decay and prevents further analysis.

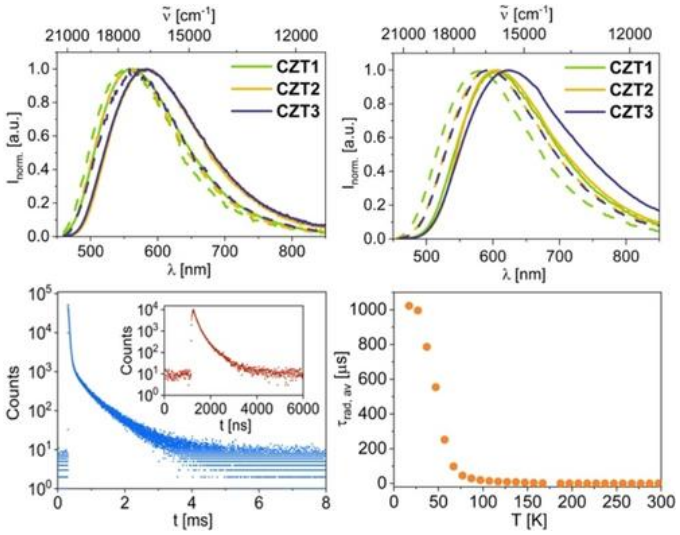


Figure 2. Top left: Photoluminescence of **CZT1–3** in the solid state at room temperature (dashed lines) and at 77 K (solid lines). Top right: Photoluminescence of **CZT1–3** in 1 wt % PS (solid lines) and PMMA (dashed lines). Bottom left: Photoluminescence decay of **CZT2** at 77 K and 297 K (inset) in the solid state. Bottom right: temperature-dependence of the averaged radiative lifetimes $\tau_{av,rad}$ of **CZT2**.

Table 1. Photophysical data of **CTZ1–3** in the solid state and doped in polymer matrices (1 wt-%).

	medium	T / K	λ_{max} / nm	$^a\tau_{av}$ / µs	Φ	^bk_r / s^{-1}		medium	T / K	λ_{max} / nm	$^a\tau_{av}$ / µs	Φ	^bk_r / s^{-1}
CZT1	Powder	297	560	0.63	0.28	4.5×10^5	**CZT3**	Powder	297	580	0.45	0.33	7.3×10^5
		77	556	1940	0.49	2.5×10^2			77	570	1149	0.76	6.6×10^2
	PMMA	297	570	0.28	0.02	7.2×10^4		PMMA	297	592	0.30	0.16	5.3×10^5
	PS	297	605	0.19	0.01	5.2×10^4		PS	297	625	0.21	0.12	5.7×10^5
CZT2	Powder	297	583	0.17	0.13	7.5×10^5	**CTZ3a**	Crystals	297	577	0.95	0.29	3.1×10^5
		77	568	46	0.31	6.7×10^3		(Ω = 6-43°)	77	561	1220	0.48	3.9×10^2
	PMMA	297	590	0.22	0.06	2.7×10^5	**CTZ3b**	Crystals	297	580	0.39	0.49	1.2×10^6
	PS	297	607	0.21	0.03	1.4×10^5		(Ω = 30/36°)	77	553	346	0.97	2.8×10^3

[a] For multiexponential decays, the amplitude averaged lifetimes are given (see also Supporting Information). [b] $k_r=\Phi/\tau$.

Bearing in mind that Zn^{II} does not mediate strong SOC for fast phosphorescence,[13, 15] we were curious whether the zinc dithiolate complexes emit via TADF and thus we carried out time-resolved variable temperature (tr-VT) luminescence studies. Indeed, the luminescence lifetimes τ_{av} of **CZT1–3** in the solid state increase by several orders of magnitude at 77 K, where we were able to experimentally determine Φ_{77K}, giving rise to much smaller $k_r=2.5\times10^2$–6.7×10^3 s^{-1} (Table 1). Upon further cooling compound **CZT2** to <50 K, a luminescence lifetime plateau is observed in the millisecond regime (Figure 2, and Table S7).

Such a photophysical behavior is typical for a temperature-dependent Boltzmann equilibrium between states of very different oscillator strength and cannot be explained by regular phosphorescence, but rather by TADF involving states of different spin multiplicity.

Noteworthy, the transient luminescence decays are biexponential at 297 K, but at lower temperatures become multiexponential with 3–4 lifetime components (Figure 2). Presumably this is due to the structural flexibility of the Zn^{II} complexes, i.e., several conformers with different dihedral angles Ω between the ligands being present in the powder samples, which give rise to different emitting excited state geometries with different Franck–Condon factors. Indeed, upon isolating larger amounts of polymorph **CTZ3a** containing eight independent molecules with different Ω we observed very complex transient luminescence decays of the single crystals. Under such conditions, k_r obtained from the average lifetime τ_{av} is not an appropriate descriptor for an in-depth analysis because the observed luminescence properties are not related to a single species or may be due to different excited state geometries. However, the modelling of the kinetic processes for population of the emitting excited states involved in the TADF process assumes a three-state-scenario between S_0, S_1 and T_1, with each of them exhibiting only one geometry that is dominantly responsible for the respective transition.

We were able to isolate larger quantities of single-crystalline material of polymorph **CZT3b** that contains two independent molecules in the unit cell with very similar dihedrals Ω of 29.9° and 36.2°, respectively, and which exhibits only biexponential lifetime decays, allowing for a more detailed analysis. Both decay channels contribute to the TADF process as indicated by their VT behavior in Figure 3. At 27 K, we observed long lifetimes of 2.9 and 7.7 ms, which suggests that the involved triplet excited states experience very weak SOC and that they differ in their geometry or character. Upon increasing the temperature, the excited states responsible for the two emission paths interconvert as the relative contributions of τ_1 and τ_2 change (see below). Between 257–297 K, they appear to be in thermal equilibrium (see Table S8) because the contributions remain constant and thus τ_{av} is an appropriate approximation to evaluate k_r of **CTZ3b**, giving a record value for Zn^{II}-based emitters of 1.2×10^6 s^{-1} and high Φ=0.49 at room temperature (Table 1).

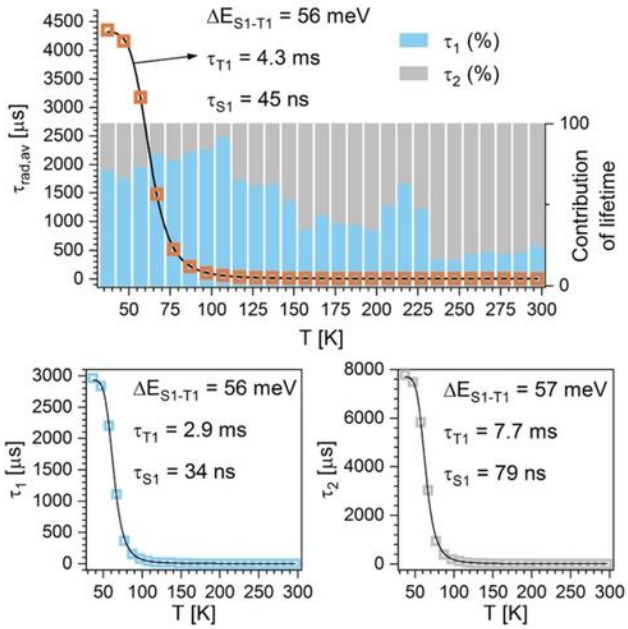


Figure 3. Top: Temperature-dependence of the averaged radiative lifetime $\tau_{rad,av}$ of **CZT3b** and relative contributions of τ_1 and τ_2. Bottom: Temperature-dependence of τ_1 and τ_2. The black lines represent the fit of the experimental data according to eq 1, and the obtained fitting parameters of the TADF are given in the graphs.

Fitting the VT lifetime data of either the single lifetime components of **CZT3b** or their average according to eq. 1 in the temperature range between 27–297 K using an established three-state kinetic model provides deeper insight into the TADF parameters. The obtained energy gap $\Delta E_{S1\text{-}T1}$ appears to be as low as 56 meV (452 cm^{-1}), which is sufficiently small to allow for efficient rISC $T_1 \rightarrow S_1$, and in combination with a short τ_{S1}=34–79 ns (k_F=1.2–2.9×10^7 s^{-1}) for fast TADF (Figure 3).

$$\frac{1}{k_r} = \tau_{rad} = \frac{3 + \exp\left[-\frac{\Delta E^{S1-T1}}{k_B T}\right]}{3k_P + k_F \cdot \exp\left[-\frac{\Delta E^{S1-T1}}{k_B T}\right]} \quad (1)$$

As mentioned above, our DFT/MRCI calculations of the model compound **CZT1** show that tilted, near-planar and orthogonal conformations of the ligands are very close in energy in the electronic ground state S_0. A similar situation is found for the singlet and triplet excited states S_1 and T_1, which are responsible for the TADF mechanism. On the ^{1}LLCT(ππ*) potential energy surface, a slight preference for the planar conformer is observed, with the tilted (ΔE_{S1}=160 cm^{-1}) and orthogonal (ΔE_{S1}=260 cm^{-1}) being marginally higher in energy. Despite their small energy differences, the minima exhibit considerably different photophysical properties and thus may explain the observed multiexponential lifetime decays as well as the different T_1 lifetimes at very low temperatures (Table 2). The variation of the fluorescence rate constant follows the expectation that the oscillator strength of a ^{1}LLCT(ππ*) transition is highest for a coplanar orientation of the donor and acceptor moieties, giving k_F=1.0×10^7 s^{-1}. Even the increase of the phosphorescence rates with increasing twist angle can be explained by a simple model based on El-Sayed's rules. Because SOC preferentially couples ^{3}ππ* states with ^{1}nπ* states, the ^{3}LLCT(ππ*) phosphorescence primarily borrows intensity from an energetically higher lying,

spin-allowed ^{1}LLCT(nπ*)→S_0 transition (Figure 4 and Tables S10–S13), which is strongest for the orthogonal conformer and leads to k_P=939 s^{-1} (Table 2). Here, the highest occupied nonbonding sulfur n MO and the C−N antibonding π* MO of the carbene exhibit similar symmetry properties (Figure S17), thus facilitating the electric dipole transition.

Table 2. DFT/MRCI calculated parameters of the model complex **CZT1** relevant for the TADF process of this general class of emitters.

Conformer	Dihedral angle Ω[a]	ΔE(S_1–T_1)[b] / cm^{-1}	Σ SOCME^2 / cm^{-2}		k_{ISC}[c] / s^{-1}		k_{rISC}[c] / s^{-1}		k_F / s^{-1}	k_P / s^{-1}	k_{TADF}[d] / s^{-1}
			S_1	T_1	298 K	77 K	298 K	77 K			
Planar	10/17/13°	195/281	3.1	1.8	2×10^9	1×10^9	6×10^7	9×10^5	1.0×10^7	2	3.3×10^5
Tilted	40/38/36°	223/153	21.6	20.1	3×10^{10}	3×10^{10}	5×10^9	7×10^8	7.8×10^6	31	1.2×10^6
Ortho	76/76/80°	157/594	8.9	7.2	5×10^9	6×10^9	9×10^6	1×10^4	1.3×10^6	939	3.5×10^3
Kinked	–/29/31°	133/155	2.2	3.4	2×10^9	4×10^8	4×10^8	1×10^7	7.4×10^4	1570	3.5×10^3

[a] For the definition of Ω, see Scheme 2. Values are displayed for S_0/S_1/T_1. [b] Adiabatic energy gap excluding/including zero-point vibrational energy corrections. [c] k_{ISC} and k_{rISC} have been calculated independently. [d] $k_{TADF}=k_F$ (k_{rISC}/k_{ISC})

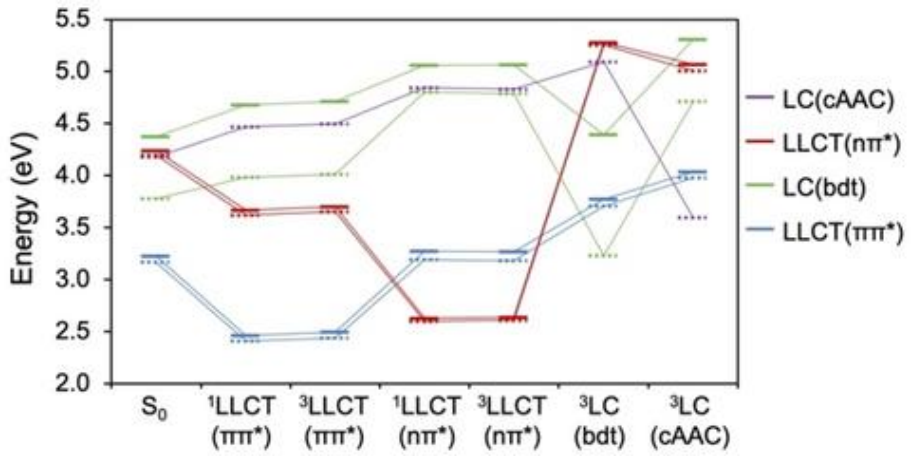


Figure 4. DFT/MRCI excitation energies of the relevant states at different geometries for model compound **CZT1** (tilted conformer). All energies are calculated relative to the ground state energy at the S_0 geometry.

Highly important for the TADF efficiency and evaluation of structure–property relationships is the finding that ISC and rISC become ultrafast in the tilted conformation of the S_1 and T_1 states (Table 2). At 298 K, these formally spin-forbidden processes occur with calculated rate constants of $k_{ISC}=3\times10^{10}$ and $k_{rISC}=5\times10^9$ s^{-1} due to the unusually large mutual $^{1/3}$LLCT(ππ*) SOC in combination with a small energy gap $\Delta E_{S1\text{-}T1}$ of only 153 cm^{-1}. Typically, singlet and triplet states with similar electronic structures exhibit tiny SOC matrix elements. However, the bdt ligand in the tilted conformer is slightly kinked at the sulfur atoms, which leads to a small admixture of LLCT(nπ*) character into the LLCT(ππ*) wavefunction, sufficient to increase the SOC because the π and n orbitals both exhibit large amplitudes at the sulfur centers (Figure S18). In addition, the relative excited state kinetics k_{ISC}/k_{rISC} provide the most favorable steady-state equilibrium $T_1\leftrightarrow S_1$ for the tilted conformation with Ω values as observed for polymorph CZT3b, giving a theoretically calculated rate constant for delayed fluorescence of $k_{TADF}=1.2\times10^6$ s^{-1} at

298 K (Table 2). This is fully consistent with the obtained experimental value and thus provides a structural design criterium for exceptionally fast TADF in Zn^{II} complexes.

Although the global minima of the S_1 and T_1 states are of $^{1/3}$LLCT(ππ*) character, local minima arise from the $^{1/3}$LLCT(nπ*) excitation with a conformation, which does not have a counterpart in the electronic ground state (Figure 4 and Table S13). Characteristic of the nuclear arrangements are bdt kink angles (S−Zn−S−C) close to 50°, which are unfavorable for the LLCT(ππ*) electronic structure, resulting in a conical intersection of their potential energy surfaces (Figure 5).

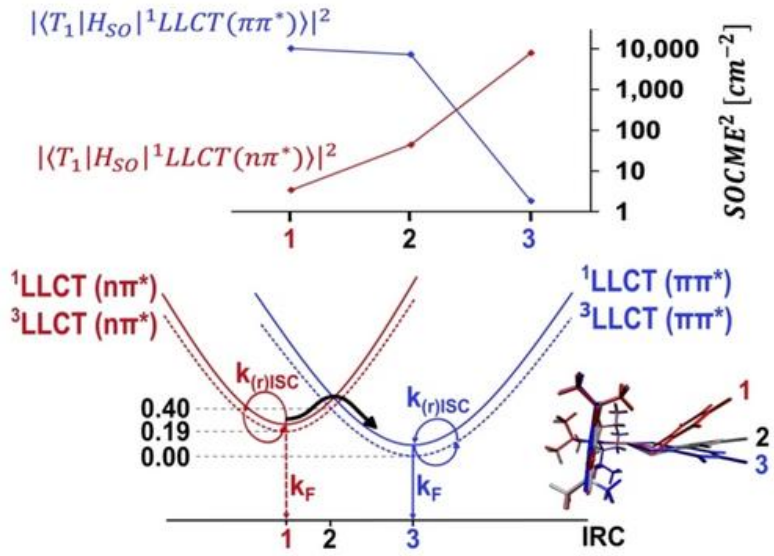


Figure 5. Bottom left: Schematic energy profiles of the ^{1}LLCT (solid lines) and ^{3}LLCT states (dashed lines) of **CZT1** along an intrinsic reaction coordinate (IRC) connecting the minima of the ^{3}LLCT(nπ*) (1) and ^{3}LLCT(ππ*) (3) states. The crossing point (2) of the ^{3}LLCT(nπ*) and ^{3}LLCT(ππ*) potential energy surfaces is located energetically 0.21 eV above the ^{3}LLCT(nπ*) minimum and 0.40 eV above the ^{3}LLCT(ππ*) minimum at the DFT/MRCI level of theory. Molecules populating initially the LLCT(nπ*) states decay preferentially to the LLCT(ππ*) state which emit prompt and delayed fluorescence. Bottom right: Nuclear arrangements of CTZ1 at the geometry points 1–3. The bdt ligand is strongly kinked in the ^{3}LLCT(nπ*) state whereas the benzene and S−Zn−S plane exhibit an angle close to 180° in the ^{3}LLCT(ππ*) state. Top: Spin-orbit strength of the T_1 state at the geometry points 1–3. T_1 exhibits ^{3}LLCT(nπ*) at points 1 and 2 and ^{3}LLCT(ππ*) character at point 3.

Adiabatically, the $^{1/3}$LLCT(nπ*) minima are located ca. 1500 cm^{-1} above the planar $^{1/3}$LLCT(ππ*) structures. Due to the large geometry displacements between the initial and final states, (r)ISC rate constants cannot be determined with high confidence. However, based on values of ≈10^4 cm^{-2} for the component-averaged squared $^{1/3}$LLCT(nπ*)-$^{3/1}$LLCT(ππ*) SOC, downhill ISC processes are estimated to proceed on the (sub)nanosecond timescale, despite the moderate vibrational overlap. Uphill $^{3/1}$LLCT(ππ*)-$^{1/3}$LLCT(nπ*) transitions are not expected to occur. Considering the comparably low k_F (Table 2), ^{1}LLCT(nπ*) fluorescence cannot compete against nonradiative deactivation. Noteworthy, the weaker SOC and smaller k_{rISC} of the non-tilted conformations results in diminished calculated k_{TADF} values of 3.5×10^3–3.5×10^5 s^{-1}, which explains the different experimental radiative rate constants found in dependence of the aggregation state or medium at room temperature in these geometrically fluxional emitters (Table 1).

Conclusion

The monomeric Zn^{II} TADF emitters **CZT1–3** reported herein exhibit greatly increased k_r by up to one order of magnitude and 25-fold enhancement of ϕ in comparison to previously reported dimeric $[Zn(bdt)(^{Me}cAAC)]_2$, although the electronic properties of the ^{Menth}cAAC ligand generally resemble those of the less bulky derivate ^{Me}cAAC. Time-resolved variable temperature luminescence studies on polymorphs of $[Zn(bdt^{tBu})(^{Menth}cAAC)]$ (**CZT3**) in conjunction with high-level DFT/MRCI calculations revealed that the relative orientation of the ligands involved in the $^{1/3}$LLCT states is paramount to control the TADF properties. The inefficient TADF dimers $[Zn(bdt)(^{Me}cAAC)]_2$ feature bdt ligands lying entirely out of the plane of the carbene ligand (Scheme 1). In contrast, the dihedral angle of 33–36° in **CZT3b** leads to very efficient rISC on the order of 10^9 s^{-1} due to SOC mediated by the sulfur atoms in combination with a small $\Delta E_{S1\text{-}T1}$ of ca. 56 meV. Consequently, a high k_{TADF}=1.2×10^6 s^{-1} is obtained at room temperature, which is exceptional for Zn^{II} based emitters involving triplet excited states.

A comparison with other Zn^{II} complexes emitting via TADF is imperative and highlights our design strategy using $^{1/3}$LLCT states that can be sterically controlled for achieving high k_r. Adachi and co-workers demonstrated that Zn^{II} complexes emitting via TADF from $^{1/3}$ILCT states can achieve k_{TADF} of ca. 2×10^4 s^{-1}.[11j] Luminescent Schiff-base Zn^{II} complexes have also been reported to show TADF from an equilibrium of $^{1/3}$ILCT states, albeit with low quantum yields as the major decay path is prompt fluorescence and ISC/rISC processes are inefficient.[19] Clearly, the construction of nearly degenerate $^{1/3}$LLCT/LMCT states with SOC contribution from the heteroatoms of the ligands is superior and leads to the fastest Zn^{II} based triplet emitters to date, of which the k_{TADF} of up to 1.2×10^6 s^{-1} are even competitive to well-established triplet emitters applied in commercial devices based on rare 4d/5d transition metals.

References

[1a] A. Steffen, B. Hupp, in Comprehensive Coordination Chemistry III (Eds.: E. C. Constable, G. Parkin, L. Que, Jr.), Elsevier, Oxford, **2021**, pp. 466–502; [1b] O. S. Wenger, *J. Am. Chem. Soc.* **2018**, *140*, 13522–13533; [1c] C. Förster, K. Heinze, *Chem. Soc. Rev.* **2020**, *49*, 1057–1070; [1d] C. Wegeberg, O. S. Wenger, *JACS Au* **2021**, *1*, 1860–1876; [1e] N. Sinha, O. S. Wenger, *J. Am. Chem. Soc.* **2023**, *145*, 4903–4920.

[2a] Y. Zhang, T. S. Lee, J. L. Petersen, C. Milsmann, *J. Am. Chem. Soc.* **2018**, *140*, 5934–5947; [2b] Y. Zhang, T. S. Lee, J. M. Favale, D. C. Leary, J. L. Petersen, G. D. Scholes, F. N. Castellano, C. Milsmann, *Nat. Chem.* **2020**, *12*, 345–352; [2c] M. Yang, S. Sheykhi, Y. Zhang, C. Milsmann, F. N. Castellano, *Chem. Sci.* **2021**, *12*, 9069–9077.

[3a] C. Wang, F. Reichenauer, W. R. Kitzmann, C. Kerzig, K. Heinze, U. Resch-Genger, *Angew. Chem. Int. Ed.* **2022**, *61*, e202202238; [3b] N. Sinha, C. Wegeberg, D. Häussinger, A. Prescimone, O. S. Wenger, *Nat. Chem.* **2023**, *15*, 1730–736; [3c] T. H. Bürgin, F. Glaser, O. S. Wenger, *J. Am. Chem. Soc.* **2022**, *144*, 14181–14194; [3d] F. Reichenauer, C. Wang, C. Förster, P. Boden, N. Ugur, R. Báez-Cruz, J. Kalmbach, L. M. Carrella, E. Rentschler, C. Ramanan, G. Niedner-Schatteburg, M. Gerhards, M. Seitz, U. Resch-Genger, K. Heinze, *J. Am. Chem. Soc.* **2021**, *143*, 11843–11855.

[4] P. Herr, C. Kerzig, C. B. Larsen, D. Häussinger, O. S. Wenger, *Nat. Chem.* **2021**, *13*, 956–962.

[5a] J. Steube, A. Kruse, O. S. Bokareva, T. Reuter, S. Demeshko, R. Schoch, M. A. Argüello Cordero, A. Krishna, S. Hohloch, F. Meyer, K. Heinze, O. Kühn, S. Lochbrunner, M. Bauer, *Nat. Chem.* **2023**, *15*, 468–474; [5b] W. Leis, M. A. Argüello Cordero, S. Lochbrunner, H. Schubert, A. Berkefeld, *J. Am. Chem. Soc.* **2022**, *144*, 1169–1173; [5c] K. S. Kjær, N. Kaul, O. Prakash, P. Chábera, N. W. Rosemann, A. Honarfar, O. Gordivska, L. A. Fredin, K.-E. Bergquist, L. Häggström, T. Ericsson, L. Lindh, A. Yartsev, S. Styring, P. Huang, J. Uhlig, J. Bendix, D. Strand, V. Sundström, P. Persson, R. Lomoth, K. Wärnmark, *Science* **2019**, *363*, 249–253.

[6a] M. M. Alowakennu, A. Ghosh, J. K. McCusker, *J. Am. Chem. Soc.* **2023**, *145*, 20786–20791; [6b] N. Sinha, B. Pfund, C. Wegeberg, A. Prescimone, O. S. Wenger, *J. Am. Chem. Soc.* **2022**, *144*, 9859–9873; [6c] A. Y. Chan, A. Ghosh, J. T. Yarranton, J. Twilton, J. Jin, D. M. Arias-Rotondo, H. A. Sakai, J. K. McCusker, D. W. C. MacMillan, *Science* **2023**, *382*, 191–197.

[7] T. Ogawa, O. S. Wenger, *Angew. Chem. Int. Ed.* **2023**, *62*, e202312851.

[8a] R. Hamze, J. L. Peltier, D. Sylvinson, M. Jung, J. Cardenas, R. Haiges, M. Soleilhavoup, R. Jazzar, P. I. Djurovich, G. Bertrand, M. E. Thompson, *Science* **2019**, *363*, 601–606; [8b] M. Gernert, L. Balles-Wolf, F. Kerner, U. Müller, A. Schmiedel, M. Holzapfel, C. M. Marian, J. Pflaum, C. Lambert, A. Steffen, *J. Am. Chem. Soc.* **2020**, *142*, 8897–8909; [8c] A. M. T. Muthig, O. Mrózek, T. Ferschke, M. Rödel, B. Ewald, J. Kuhnt, C. Lenczyk, J. Pflaum, A. Steffen, *J. Am. Chem. Soc.* **2023**, *145*, 4438–4449; [8d] A. M. T. Muthig, J. Wieland, S. Koop, C. Lenczyk, F. Kerner, B. Hupp, A. Steffen, *Inorg. Chem.* **2022**, *61*, 17427–17437; [8e] A. Hossain, A. Bhattacharyya, O. Reiser, *Science* **2019**, *364*, eaav9713; [8f] A. M. T. Muthig, M. Krumrein, J. Wieland, M. Gernert, F. Kerner, J. Pflaum, A. Steffen, *Inorg. Chem.* **2022**, *61*, 14833–14844; [8g] C. N. Muniz, J. Schaab, A. Razgoniaev, P. I. Djurovich, M. E. Thompson, *J. Am. Chem. Soc.* **2022**, *144*, 17916–17928; [8h] C. N. Muniz, C. A. Archer, J. S. Applebaum, A. Alagaratnam, J. Schaab, P. I. Djurovich, M. E. Thompson, *J. Am. Chem. Soc.* **2023**, *145*, 13846–13857.

[9a] J. Nitsch, F. Lacemon, A. Lorbach, A. Eichhorn, F. Cisnetti, A. Steffen, *Chem. Commun.* **2016**, *52*, 2932–2935; [9b] B. Hupp, J. Nitsch, T. Schmitt, R. Bertermann, K. Edkins, F. Hirsch, I. Fischer, M. Auth, A. Sperlich, A. Steffen, *Angew. Chem. Int. Ed.* **2018**, *57*, 13671–13675; [9c] L. Bergmann, J. Friedrichs, M. Mydlak, T. Baumann, M. Nieger, S. Bräse, *Chem. Commun.* **2013**, *49*, 6501–6503.

[10a] R. Hamze, S. Shi, S. C. Kapper, D. S. Muthiah Ravinson, L. Estergreen, M.-C. Jung, A. C. Tadle, R. Haiges, P. I. Djurovich, J. L. Peltier, R. Jazzar, G. Bertrand, S. E. Bradforth, M. E. Thompson, *J. Am. Chem. Soc.* **2019**, *141*, 8616–8626; [10b] H. Yersin, D. Donges, in Transition Metal and Rare Earth Compounds: Excited States, Transitions, Interactions II (Ed.: H. Yersin), Springer Berlin Heidelberg, Berlin, **2001**, pp. 81–186; [10c] A. M. T. Muthig, B. Ewald, T. H. Ferschke, J. Pflaum, A. Steffen, PCT/EP2022/073938, **2022**; [10d] J. Ma, J. Schaab, S. Paul, S. R. Forrest, P. I. Djurovich, M. E. Thompson, *J. Am. Chem. Soc.* **2023**, *145*, 20097–20108.

[11a] I. B. Lozada, J. D. Braun, J. A. G. Williams, D. E. Herbert, *Inorg. Chem.* **2022**, *61*, 17568–17578; [11b] V. Ferraro, F. Baggio, J. Castro, M. Bortoluzzi, *Eur. J. Inorg. Chem.* **2022**, e202200119; [11c] D. Temerova, K. S. Kisel, T. Eskelinen, A. S. Melnikov, N. Kinnunen, P. Hirva, J. R. Shakirova, S. P. Tunik,

E. V. Grachova, I. O. Koshevoy, *Inorg. Chem. Front.* **2021**, *8*, 2549–2560; [11d] Z. Mahmood, N. Rehmat, S. Ji, J. Zhao, S. Sun, M. Di Donato, M. Li, M. Teddei, Y. Huo, *Chem. Eur. J.* **2020**, *26*, 14912–14918; [11e] B. Goswami, T. J. Feuerstein, R. Yadav, S. Lebedkin, P. J. Boden, S. T. Steiger, G. Niedner-Schatteburg, M. Gerhards, M. M. Kappes, P. W. Roesky, *Chem. Eur. J.* **2021**, *27*, 15110–15119; [11f] J. Xiong, K. Li, T. Teng, X. Chang, Y. Wei, C. Wu, C. Yang, *Chem. Eur. J.* **2020**, *26*, 6887–6893; [11g] K. D. Oyler, F. J. Coughlin, S. Bernhard, *J. Am. Chem. Soc.* **2007**, *129*, 210–217; [11h] R. G. Highland, G. A. Crosby, *Chem. Phys. Lett.* **1985**, *119*, 454–458; [11i] K. A. Truesdell, G. A. Crosby, *J. Am. Chem. Soc.* **1985**, *107*, 1787–1788; [11j] Y. Sakai, Y. Sagara, H. Nomura, N. Nakamura, Y. Suzuki, H. Miyazaki, C. Adachi, *Chem. Commun.* **2015**, **51**, 3181–3184.

[12] J. A. Kübler, B. Pfund, O. S. Wenger, *JACS Au* **2022**, *2*, 2367–2380.

[13] N. Lüdtke, J. Kuhnt, T. Heil, A. Steffen, C. M. Marian, *ChemPhotoChem* **2023**, *7*, e202200142.

[14] H. Noda, H. Nakanotani, C. Adachi, *Sci. Adv.* **2018**, *4*, eaao6910.

[15a] O. Mrózek, M. Gernert, A. Belyaev, M. Mitra, L. Janiak, C. M. Marian, A. Steffen, *Chem. Eur. J.* **2022**, *28*, e202201114; [15b] O. Mrózek, M. Mitra, B. Hupp, A. Belyaev, N. Lüdtke, D. Wagner, C. Wang, O. S. Wenger, C. M. Marian, A. Steffen, *Chem. Eur. J.* **2023**, *29*, e202203980.

[16] V. Lavallo, Y. Canac, C. Präsang, B. Donnadieu, G. Bertrand, *Angew. Chem. Int. Ed.* **2005**, *44*, 5705–5709.

[17] Deposition numbers 2290921 (for **1**), 2290922 (for **CZT1**), 2290923 (for **CZT2**), 2290925 (for **CZT3a**) and 2290924 (for **CZT3b**) contain the supplementary crystallographic data for this paper. These data are provided free of charge by the joint Cambridge Crystallographic Data Centre and Fachinformationszentrum Karlsruhe Access Structures service.

[18a] M. Tesmer, H. Vahrenkamp, *Eur. J. Inorg. Chem.* **2001**, 1183–1188; [18b] K. Halvorsen, G. A. Crosby, W. F. Wacholtz, *Inorg. Chim. Acta* **1995**, *228*, 81–88.

[19] A. Steinegger, S. M. Borisov, *ACS Omega* **2020**, *5*, 7729–7737.

[20] W. L. F. Armarego, Purification of laboratory Chemicals, Butterworth Heinemann, Oxford, **1996**.

[21] R. Jazzar, J. Bourg, R. D. Dewhurst, B. Donnadieu, G. Bertrand, *J. Org. Chem.* **2007**, *72*, 3492–3499.

[22] M. Deng, N. F. M. Mukhtar, N. D. Schley, G. Ung, *Angew. Chem. Int. Ed.* **2020**, *59*, 1228–1231.

[23] Gaussian 16, revision A.03, M. J. Frisch, G. W. Trucks, H. B. Schlegel, G. E. Scuseria, M. A. Robb, J. R. Cheeseman, G. Scalmani, V. Barone, G. A. Petersson, H. Nakatsuji, et al., Gaussian Inc.: Wallingford CT, **2016**.

[24] E. Cancès, B. Mennucc, J. Tomasi, *J. Chem. Phys.* **1997**, *107*, 3032–3041.

[25] B. Mennucci, E. Cancès, J. Tomasi, *J. Phys. Chem. B* **1997**, *101*, 10506–10517.

[26] C. Lee, W. Yang, R. G. Parr, *Phys. Rev. B* **1988**, *37*, 785–789.

[27] A. D. Becke, *J. Chem. Phys.* **1993**, *98*, 1372–1377.

[28] A. Schäfer, H. Horn, R. Ahlrichs, *J. Chem. Phys.* **1992**, *97*, 2571–2577.

[29] D. Figgen, G. Rauhut, M. Dolg, H. Stoll, *Data. Chem. Phys.* **2005**, *311*, 227–244.

[30] S. Grimme, M. Waletzke, *J. Chem. Phys.* **1999**, *111,* 5645–5655.

[31] C. M. Marian, A. Heil, M. Kleinschmidt, *Wiley Interdiscip. Rev.: Comput. Mol. Sci.* **2019**, *9*, e1394.

[32] A. Heil, M. Kleinschmidt, C. M. Marian, *J. Chem. Phys.* **2018**, *149*, 164106.

[33] R. Ahlrichs, M. Bär, M. Häser, H. Horn, C. Kölmel, *Chem. Phys. Lett.* **1989**, *162*, 165–169.

[34] TURBOMOLE V6.6 2014, a development of University of Karlsruhe and Forschungszentrum Karlsruhe GmbH, 1989–2007, TURBOMOLE GmbH, since 2007.

[35] M. Kleinschmidt, J. Tatchen, C. M. Marian, *J. Comput. Chem.* **2002**, *23*, 824–833.

[36] M. Kleinschmidt, C. M. Marian, *Chem. Phys.* **2005**, *311*, 71–79.

[37] B. A. Heß, C. M. Marian, U. Wahlgren, O. Gropen, *Chem. Phys. Lett.* **1996**, *251*, 365–371.

[38] AMFI is an atomic spin-orbit integral program written by B. Schimmelpfennig, University of Stockholm, **1996**.

[39] M. Kleinschmidt, J. Tatchen, C. M. Marian, *J. Chem. Phys.* **2006**, *124*, 124101.

[40] M. Etinski, J. Tatchen, C. M. Marian *J. Chem. Phys.* **2011**, *134*, 154105.

[41] M. Etinski, J. Tatchen, C. M. Marian, *Phys. Chem. Chem. Phys.* **2014**, *16*, 4740–4751.

[42] P. S. Nejman, B. Morton-Fernandez, N. Black, D. B. Cordes, A. M. Slawin, P. Kilian, J. D. Woollins, *J. Organomet. Chem.* **2015**, *776*, 7–16.

[43] S. I. Etkind, J. Lopez, Y. G. Zhu, J. Fang, W. J. Ong, Y. Shao-Horn, T. M. Swager, *ACS Sustainable Chem. Eng.* **2022**, *10*, 11739–11750.

[44] G. M. Sheldrick, *Acta Crystallogr. Sect. C* **2015**, *71*, 3–8.

[45] G. M. Sheldrick, *Acta Crystallogr. Sect. A* **2015**, *71*, 3–8.

[46] O. V. Dolomanov, L. J. Bourhis, R. J. Gildea, J. A. K. Howard, H. Puschmann, *J. Appl. Crystallogr.* **2009**, *42*, 339–341.

2.4 TADF Zn(II) Bicyclic(Alkyl)(Amino)Carbene Thiolate Complexes with Near-Unity Quantum Yield

The development of highly efficient luminescent materials based on earth-abundant metals has emerged as a central objective in modern photochemistry and materials science, particularly in the context of optoelectronic applications such as organic light-emitting diodes (OLEDs), sensing, and bioimaging. While noble-metal complexes (e.g., Ir(III), Pt(II))[42-46] dominate the field due to their strong spin–orbit coupling (SOC) and efficient phosphorescence, their high cost and limited availability motivate the search for sustainable alternatives. In this regard, thermally activated delayed fluorescence (TADF) has gained significant attention as a strategy to achieve high emission efficiencies without relying on heavy metals. TADF materials utilize reverse intersystem crossing (rISC) from triplet (T_1) to singlet (S_1) states, enabled by a small singlet–triplet energy gap ($\Delta E_{(S_1-T_1)}$), thereby harvesting both singlet and triplet excitons for light emission.

Among earth-abundant metals, Zn(II) complexes represent an attractive yet underexplored class of emitters. Owing to their d^{10} electronic configuration, Zn(II) complexes lack low-lying metal-centered (MC) states, which often act as non-radiative decay pathways in first-row transition metal systems. However, the absence of strong SOC in Zn(II) also limits conventional phosphorescence, making the design of efficient emissive systems particularly challenging. To overcome this limitation, ligand-centered and ligand-to-ligand charge transfer (LLCT) excited states have been exploited to promote TADF behavior in Zn(II) complexes. Nevertheless, achieving high photoluminescence quantum yields (Φ_{PL}) in such systems remains difficult due to competing non-radiative decay processes, often associated with structural flexibility and excited-state distortion.

Recent advances have demonstrated that carbene ligands, particularly cyclic (alkyl)(amino)carbenes (cAACs), can effectively modulate the electronic structure of Zn(II) complexes by providing strong σ-donation and π-acceptance, thereby stabilizing charge-transfer excited states.[3,4] However, cAAC-based systems frequently suffer from conformational flexibility and limited stability, which can adversely affect their photophysical performance. In this context, bicyclic (alkyl)(amino)carbenes (BicAACs) offer a promising alternative, combining enhanced rigidity with superior electronic tunability. The rigid bicyclic framework is expected to suppress non-radiative decay by limiting excited-state geometric relaxation, while the strong donor–acceptor characteristics can facilitate LLCT transitions and reduce $\Delta E_{(S_1-T_1)}$.

Herein, we report the synthesis, structural characterization, and comprehensive photophysical investigation of a new class of carbene–zinc thiolate (CZT) complexes supported by BicAAC ligands. By systematically varying the ligand environment and nuclearity, we demonstrate how steric and electronic factors govern the formation of mono- and dimeric species and influence their excited-state properties. In particular, incorporation of benzene-1,2-dithiolate (bdt) ligands enables the formation of robust complexes exhibiting strong LLCT character. Detailed spectroscopic studies, including steady-state and time-resolved measurements across different environments and temperatures, reveal efficient TADF behavior with exceptionally high solid-state quantum yields. The role of ligand rigidity, dihedral

angle, and environmental effects in modulating radiative and non-radiative decay pathways is elucidated, providing key design principles for the development of next-generation, earth-abundant luminescent materials.

Synthesis and characterization

We prepared the starting zinc halides (**1** and **2**) according to literature-reported synthetic protocols, involving the reaction of equimolar quantities of two differently substituted bicyclic (alkyl)(amino)carbenes (BicAACs), namely ^{Me}BicAAC and $^{i\text{Pr}}$BicAAC, with $ZnCl_2$ in THF under inert conditions (**Fig 1**).[3,76] As previously documented, the reaction between ^{Me}BicAAC and $ZnCl_2$ leads to the formation of the dimeric complex $(^{Me}BicAAC)_2Zn_2Cl_4$(**1**). In contrast, when $^{i\text{Pr}}$BicAAC was employed under analogous reaction conditions, we observed the formation of a monometallic complex, ($^{i\text{Pr}}$BicAAC)$ZnCl_2$ (**2**), which adopts a trigonal planar coordination geometry around the zinc center, as unequivocally established by single-crystal X-ray diffraction (SCXRD) analysis.

The divergence in nuclearity and coordination geometry between complexes **1** and **2** can be rationalized on the basis of steric effects imparted by the substituents on the carbene ligand. Specifically, the increased steric bulk associated with the isopropyl group in $^{i\text{Pr}}$BicAAC likely inhibits dimerization and favors the formation of a lower-coordinated monomeric species. This steric congestion restricts the approach of additional ligands or metal centers, thereby stabilizing the trigonal planar geometry observed in **2**.

Both complexes **1** and **2** exhibit markedly reduced reactivity toward protonated carbene formation when compared to their five-membered cyclic (alkyl)(amino)carbene (cAAC) counterparts.[3] This behavior is particularly noteworthy, as cAAC-based zinc complexes are often challenging to isolate in analytically pure form due to their higher reactivity. The diminished reactivity of the BicAAC-based systems can be attributed to their distinct electronic properties, as revealed by density functional theory (DFT) calculations.[77] BicAAC ligands display enhanced π-accepting capability alongside strong σ-donating character, arising from a combination of LUMO stabilization and HOMO destabilization. These electronic features result in stronger metal–ligand bonding interactions, which in turn reduce the propensity for protonation or ligand dissociation.

This interpretation is further corroborated by structural metrics obtained from SCXRD studies. The Zn–$C_{carbene}$ bond lengths in complexes **1** and **2** (2.046 and 2.021 Å, respectively) are significantly shorter than those reported for analogous cAAC-based complexes such as $(^{Me}cAAC)_2Zn_2Cl_4$ and (^{Menth}cAAC)$ZnCl_2$ (2.055 and 2.046 Å, respectively). The contraction of the Zn–C bond distance is indicative of stronger metal–carbene interactions in the BicAAC systems, consistent with their enhanced donor–acceptor characteristics.

Although complexes **1** and **2** were successfully synthesized and structurally characterized, further photophysical investigations were not pursued. This decision was based on prior reports highlighting the inherent photolability of zinc halide carbene complexes, including species such as $(^{Me}cAAC)_2Zn_2X_4$

and (ITr)ZnX_2, which tend to undergo decomposition or structural rearrangement upon light exposure.[xx] Consequently, efforts were directed toward the development of more robust derivatives.

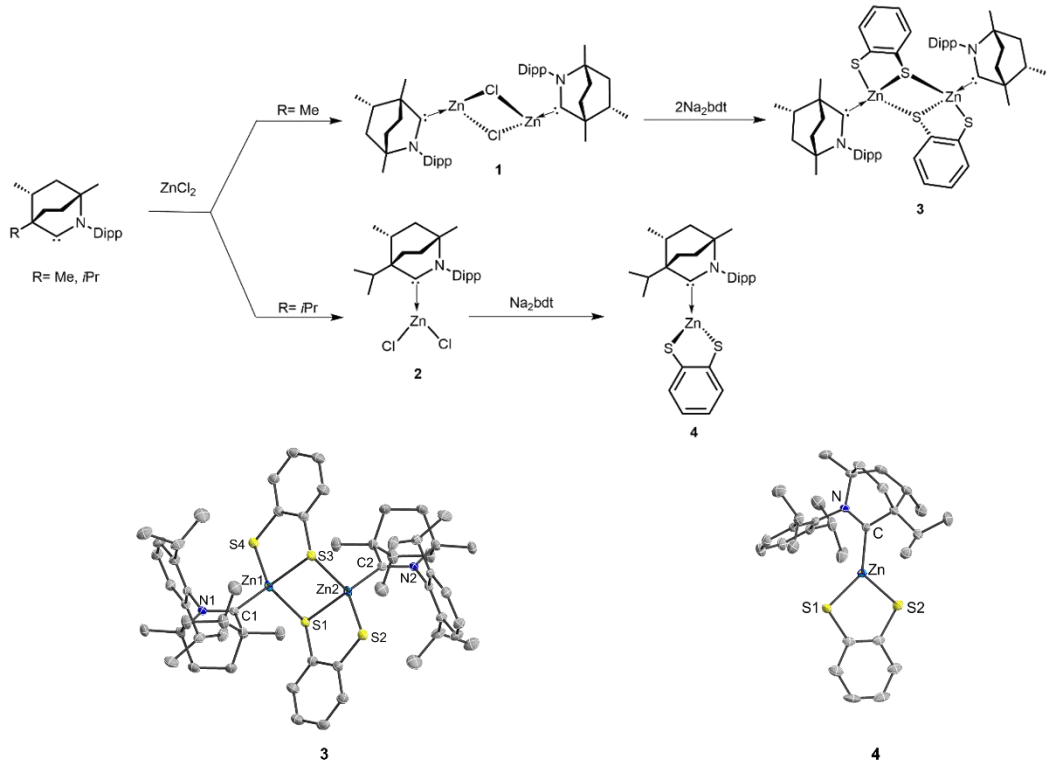


Fig 1. Synthesis and molecular structures of **1**-**4**.

Treatment of complexes **1** and **2** with a stoichiometric amount of disodium benzene-1,2-dithiolate (Na_2bdt) in THF, followed by standard work-up procedures and recrystallization from a dichloromethane (DCM)/n-pentane solvent system, afforded the target thiolate complexes **3** and **4** as yellow crystalline solids in good yields (70–85%) (**Fig 1**). Both compounds exhibit excellent solubility and stability in DCM. Compound **3** displays only partial solubility in THF and toluene, whereas compound **4** is readily soluble in these solvents, reflecting subtle differences in molecular structure and intermolecular interactions.

A particularly notable feature of compound **3** is its exceptional stability under ambient conditions. It remains stable in both the solid state and in solution, even upon prolonged exposure to oxygen and moisture. This robustness is comparable to that observed for (Me-cAAC)$_2$Zn$_2$(bdt)$_2$ and can be attributed to the chelating, multidentate nature of the benzene-1,2-dithiolate ligand.[4] The bdt ligand effectively encapsulates the zinc center, providing significant steric shielding of the Zn–$C_{carbene}$ bond and thereby suppressing decomposition pathways involving hydrolysis or oxidation.

Thermal stability studies conducted using thermogravimetric analysis (TGA) and differential scanning calorimetry (DSC) further underscore the robustness of these complexes. Compound **3** exhibits thermal stability up to approximately 250 °C, while compound **4** remains stable up to around 200 °C before undergoing decomposition (**Fig S8**). The combination of high thermal stability and resistance to

environmental degradation renders compound **3** particularly attractive for potential applications in materials science and related technological domains.

Single-crystal X-ray diffraction studies reveal that compounds **3** and **4** crystallize in the triclinic $P\bar{1}$ and monoclinic $P2_1/c$ space groups, respectively, with each structure incorporating one co-crystallized molecule of DCM. Structurally, compound 3 adopts a centrosymmetric dimeric arrangement, in which each zinc center is coordinated in a pseudo-tetrahedral geometry. In contrast, compound **4** exists as a monomeric species with a trigonal planar coordination environment around the zinc atom.

The Zn–S bond distances in compound **3** fall within the range of approximately 2.28–2.47 Å, while those in compound 4 are slightly shorter, averaging around 2.22 Å. Similarly, the Zn–$C_{carbene}$ bond lengths are measured to be 2.0584 Å for compound **3** and 1.995 Å for compound **4**. These values are consistent with those reported for other carbene–zinc thiolate (CZT) complexes.[4,5]

An important structural parameter in these systems is the dihedral angle (Ω) between the plane of the dithiophenolate ligand and that of the carbene (defined by the C–N–C fragment). In compound 3, this angle is approximately 49°, which is notably smaller than that observed in (^{Me}cAAC)$_2$Zn$_2$(bdt)$_2$ (~67°).[4]This parameter is known to play a crucial role in governing the excited-state properties of CZT complexes, as it influences orbital overlap and electronic communication between the ligand and metal center.

Interestingly, compound **4** crystallizes exclusively as a single conformer with a dihedral angle of approximately 46°, in contrast to related systems such as (^{Menth}cAAC)Zn(R-bdt), where multiple conformers with varying Ω values coexist within the crystal lattice.[5] The absence of conformational diversity in compound 4 is likely a consequence of the rigid bicyclic framework of the BicAAC ligand, which imposes conformational constraints not present in more flexible five-membered cAAC systems.

Finally, both compounds **3** and **4** were thoroughly characterized using multinuclear NMR spectroscopy. In CD_2Cl_2 solution, the ^{1}H NMR spectra of both compounds display a single set of well-resolved, sharp resonances, indicating that the solid-state structures are retained in solution and that no significant dynamic processes or equilibria are present on the NMR timescale. Furthermore, the carbene carbon resonance in the ^{13}C NMR spectrum exhibits a pronounced upfield shift to approximately 253 ppm, compared to around 335 ppm for the free carbene. This substantial shift provides clear evidence for successful coordination of the carbene to the zinc center and reflects the strong electronic interaction between the ligand and the metal.

Photophysical studies

The UV–Vis absorption spectra of compounds **3** and **4**, recorded in dichloromethane solutions, exhibit very similar overall profiles, each displaying three distinct absorption bands (**Fig 2a**). Despite this close resemblance in spectral features, a notable difference is observed in the magnitude of the molar extinction coefficients (ε) associated with these bands. In particular, the extinction coefficients for compound **3** are approximately more than twice those of compound **4**. This enhancement can be

reasonably attributed to the presence of a greater number of chromophoric units in **3**, consistent with its dimeric structure, which allows for increased light absorption.

The lowest-energy absorption band appears as a broad feature spanning the 350–450 nm region, which is responsible for the characteristic yellow color of both compounds. This band exhibits relatively low intensity, with extinction coefficients in the range of ε ≈ 1000–2500 M^{-1} cm^{-1}. Time-dependent density functional theory (TD-DFT) calculations suggest that this transition predominantly arises from a ligand-to-ligand charge transfer (LLCT) process, specifically involving π(bdt) → π*(BicAAC) excitation. The relatively low intensity and broad nature of this band are consistent with the partially allowed character of such charge-transfer transitions.

At higher energies, a more intense and structured absorption band is observed, with extinction coefficients in the range of ε ≈ 3500–8000 M^{-1} cm^{-1}. This feature is assigned to a combination of LLCT and ligand-centered (LC) transitions. More specifically, it is attributed to n(bdt) → π*(BicAAC) charge transfer, along with π → π* transitions localized on the benzene-1,2-dithiolate (bdt) ligand. The increased intensity of this band reflects the more allowed nature of these electronic excitations and the involvement of multiple contributing transitions.

In the high-energy region, a strong absorption band is observed around 267 nm, characterized by a significantly higher extinction coefficient. This band is dominated by an allowed ligand-centered (^{1}LC) π → π* transition, primarily localized on the aromatic framework of the ligand system. The high intensity of this transition is consistent with its fully allowed character and strong oscillator strength.

Overall, the absorption behavior of compounds **3** and **4** highlights the important role of ligand-based electronic transitions and ligand-to-ligand charge transfer processes in governing their photophysical properties. The differences in extinction coefficients, despite similar spectral shapes, further emphasize the influence of molecular structure—particularly nuclearity and chromophore count-on light-harvesting efficiency in these carbene–zinc thiolate systems.

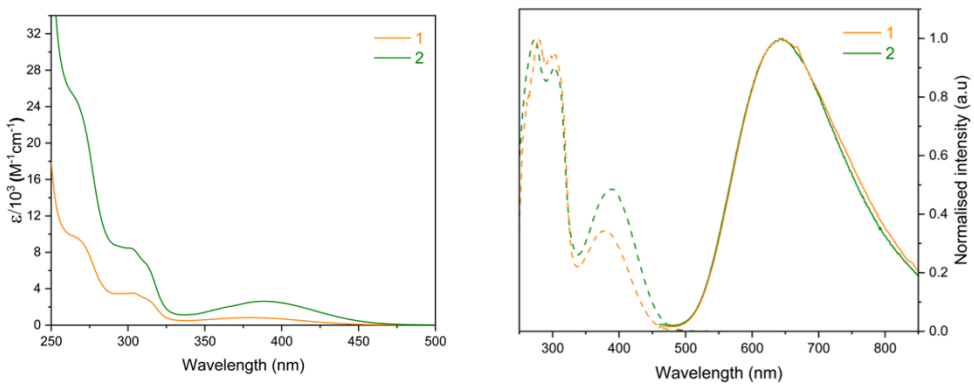


Fig 2. UV-Vis absorption spectra (left, a) and emission-excitation spectra (right, b) of **3** and **4** in DCM solution at RT.

Upon irradiation with 400 nm light in deaerated dichloromethane solution, both compounds **3** and **4** exhibit broad emission bands characteristic of ligand-to-ligand charge transfer (LLCT) excited states

(**Fig 2b**). The emission maxima are centered at approximately 645 nm, extending toward the near-infrared (NIR) region, and are associated with very low photoluminescence quantum yields ($\Phi_{PL} \approx 0.01$). Time-resolved measurements reveal luminescence lifetimes of 105 ns for **3** and 160 ns for **4**, which correspond to radiative rate constants (k_r) on the order of ~1 × 10^5 s^{-1}. These relatively long lifetimes, combined with modest radiative rates, are indicative of emission originating from a triplet excited state.

However, conventional spin–orbit coupling (SOC)-mediated phosphorescence is unlikely to be efficient in these systems due to the weak heavy-atom effect associated with zinc(II) and sulfur donors. Instead, the observed emission is more plausibly attributed to thermally activated delayed fluorescence (TADF), where reverse intersystem crossing (RISC) from the triplet to the singlet excited state enables radiative decay. The charge-transfer character of the excited state is expected to reduce the singlet–triplet energy gap,nthereby facilitating efficient RISC despite the intrinsically weak SOC.

A striking feature of the solution-state emission is the very large Stokes shift (~10,000 cm^{-1} for both **3** and **4**). This can be rationalized by significant geometric and electronic relaxation in the excited state. In LLCT systems, excitation typically leads to substantial redistribution of electron density from the donor (bdt) to the acceptor (BicAAC), resulting in a more polarized excited state with a different equilibrium geometry compared to the ground state. In fluid solution, the absence of structural constraints allows for extensive conformational relaxation, including changes in dihedral angles (Ω), bond lengths, and planarity between ligands. This large reorganization energy leads to pronounced red-shifted emission and consequently a large Stokes shift. Solvent reorganization in polarizable media such as DCM may further stabilize the excited state, contributing to the observed shift.

In contrast, upon excitation at 400 nm in the solid state at RT, compounds **3** and **4** exhibit intense green to yellow photoluminescence with emission maxima at 538 nm and 560 nm, respectively (**Fig 3**). These emissions are hypsochromically shifted by approximately 2353–3083 cm^{-1} relative to their solution-state counterparts. The emission bands remain broad, consistent with their charge-transfer origin; however, a significant narrowing of the full width at half maximum (FWHM) is observed (4510–6000 cm^{-1} in the solid state versus 11,660–12,010 cm^{-1} in solution). This narrowing can be attributed to reduced vibrational and conformational freedom in the solid state, which limits excited-state distortion and suppresses inhomogeneous broadening.

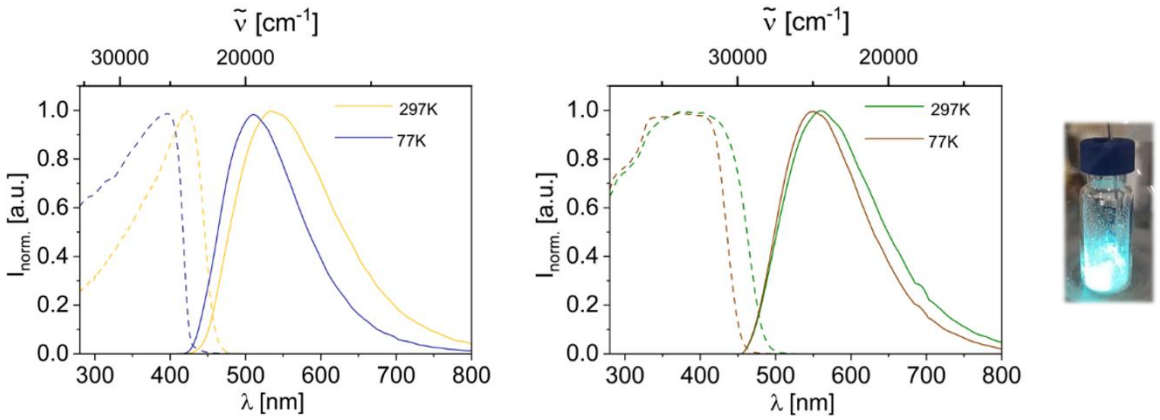


Fig 3. Emission and excitation spectra of **3** (left) and **4** (right) at RT and 77K in solid state, picture of emission of **3** in solid state at RT.

Most notably, both complexes display dramatically enhanced photoluminescence efficiencies in the solid state. Compound **3**, in particular, exhibits an exceptionally high quantum yield of $\Phi_{PL} \approx 0.9$ at room temperature (**Table 1**), representing an approximately 45-fold increase compared to the previously reported dimeric $(Me\text{-}cAAC)_2Zn_2(bdt)_2$ (Φ_PL = 0.02).[3] This value ranks among the highest reported for Zn(II)-based TADF emitters and approaches the efficiencies observed in highly luminescent Cu(I) carbene–metal–amide (CMA) complexes that are widely investigated for OLED applications.[62b]

Such high efficiencies are particularly remarkable in the context of earth-abundant metal complexes, which often suffer from significant non-radiative decay pathways. These include rapid deactivation via low-lying metal-centered (MC) states (commonly observed in Cr, Fe, Ni, Co, and Mn systems)[12-16], structural flexibility leading to vibrational dissipation (e.g., Zr(IV) complexes)[78], or distortions such as Jahn–Teller or Renner–Teller effects (notably in Cu(I) systems)[62]. Even Zn(II) complexes, despite their closed-shell d^{10} configuration, typically exhibit low quantum yields due to facile non-radiative decay. Only a few notable exceptions exist in the literature, such as homoleptic Zn(II) TADF complexes reported by Adachi and co-workers ($\Phi_{PL} \approx 0.8$)[xx], Cu(I) CMA complexes with near-unity efficiency[62b], and Zr-based LMCT emitters with moderate quantum yields (~0.5)[78].

	media	T [K]	λ_{em}^{max} [nm]	τ [ns] [a]	Φ_{PL}	k_r [s^{-1}] [b]	k_{nr} [s^{-1}] [c]
1	Powder	297	538	1310	0.9	6.9×10^5	7.6×10^4
		77	512	35×10^3	0.95	3.7×10^4	1428
	PMMA	297	570	779	0.17	2.2×10^5	1.1×10^6
	PS	297	590	538	0.10	1.9×10^5	1.7×10^6
	mCP	297	553	818	0.21	2.6×10^5	9.6×10^5
2	Powder	297	560	933	0.62	6.7×10^5	4.1×10^5
		77	550	1120×10^3	0.95	848	45
	PMMA	297	565	450	0.21	4.7×10^5	1.7×10^6
	PS	297	590	276	0.16	5.8×10^5	3.0×10^6
	mCP	297	568	410	0.13	3.2×10^5	2.1×10^6

Table 1. Selected photophysical data of **3** and **4** in different media.

For compound **3**, the high quantum yield, combined with a measured luminescence lifetime of 1.31 µs in the solid state, corresponds to a remarkably large radiative rate constant ($k_r \approx 6.9 \times 10^5\ s^{-1}$) for a transition-metal-based emitter, especially considering the weak SOC of zinc. Compared to $(Me\text{-}cAAC)_2Zn_2(bdt)_2$, this represents an approximately 16-fold increase in k_r and a nearly 30-fold reduction in the non-radiative rate constant (k_{nr}), which decreases from $2.1 \times 10^6\ s^{-1}$ to $7.6 \times 10^4\ s^{-1}$. This dramatic suppression of non-radiative decay is the primary factor responsible for the enhanced photoluminescence efficiency.

To probe the origin of this improvement, steric parameters such as buried volume ($\%V_{bur}$) of the carbene ligands were analyzed. Interestingly, both systems exhibit very similar buried volumes (43.1% for **3** vs.

42.0% for (^{Me}cAAC)$_2$Zn$_2$(bdt)$_2$), suggesting that steric protection alone does not account for the observed differences in photophysical behavior (**Fig S9**). Instead, the rigid bicyclic framework of the BicAAC ligand appears to play a crucial role by reducing conformational flexibility and limiting excited-state geometric distortion. This rigidity suppresses non-radiative decay pathways associated with structural reorganization, consistent with observations in related systems such as linear ($^{i\text{Pr}}$BicAAC)Cu(cz) complexes[79].

Furthermore, the relative orientation of the ligands, quantified by the dihedral angle Ω (S–Zn–S vs. carbene plane), emerges as a key factor in determining luminescence efficiency. In compound **3**, Ω is approximately 49°, compared to ~67° in (^{Me}cAAC)$_2$Zn$_2$(bdt)$_2$.[4] Previous studies have shown that intermediate dihedral angles (~40–50°) promote optimal mixing of ππ* and nπ* LLCT states, enhancing spin–orbit coupling and facilitating efficient TADF. In contrast, more orthogonal arrangements (Ω ≈ 67–76°) reduce orbital overlap and hinder this mixing, leading to lower emission efficiencies. This effect is further supported by studies on (^{Menth}cAAC)Zn(bdt), where a tilted conformer (Ω ≈ 40°) exhibits enhanced TADF compared to planar (Ω ≈ 10°) or highly twisted conformations[5].

Thus, the superior photophysical performance of compound **3** can be attributed to a synergistic combination of factors: rigid ligand architecture, reduced excited-state distortion, favorable ligand orientation, and efficient LLCT-mediated TADF. These findings highlight the importance of geometric and electronic fine-tuning in the design of highly emissive, earth-abundant metal complexes.

Compound **4** exhibits comparatively weaker photoluminescence (Φ_{PL} = 0.62) at RT than the dimeric complex **3**, although its emission efficiency remains significantly high in the context of Zn(II)-based emitters. The reduced quantum yield of **4** can be rationalized in terms of its higher structural flexibility relative to **3**, which allows for greater geometric distortion in the excited state and consequently enhances non-radiative decay pathways. In contrast, the dimeric architecture of 3, combined with the rigid coordination environment, effectively suppresses such distortions, thereby favoring radiative decay.

Despite its lower efficiency compared to **3**, compound **4** still outperforms previously reported systems such as (^{Menth}cAAC)Zn(bdt).[5] This improvement can be attributed to a combination of structural and electronic factors. Notably, compound **4** adopts a tilted geometry with a dihedral angle Ω (S–Zn–S vs. carbene plane) of 45.8°, which lies within the optimal range for facilitating mixing between ππ* and nπ* LLCT states. Such mixing enhances spin–orbit coupling and promotes efficient thermally activated delayed fluorescence (TADF). Additionally, the rigid bicyclic framework of the BicAAC ligand reduces conformational flexibility compared to conventional cAAC systems, thereby lowering the non-radiative decay rate constant (k_{nr}) to 4.1 × 10^5 s^{-1}, a significant decrease from 1.1 × 10^6 s^{-1} observed in (^{Menth}cAAC)Zn(bdt).

Time-resolved photophysical measurements reveal a luminescence lifetime of 933 ns for compound **4** in the solid state (**Table 1**). This relatively long lifetime, in conjunction with the high quantum yield, corresponds to an appreciable radiative rate constant (k_r ≈ 6.7 × 10^5 s^{-1}), which is notable for a zinc-

based emitter with inherently weak spin–orbit coupling. These results further support the assignment of an efficient TADF mechanism operating in this system.

To substantiate the TADF nature of the emission, temperature-dependent photophysical measurements were carried out. Upon cooling to 77 K and further to 17 K, compound **3** exhibits a hypsochromic shift in the emission maximum to $\lambda^{max} \approx 512$ nm, accompanied by a blue shift in the emission onset (924–944 cm^{-1}) and in the excitation onset (~1420 cm^{-1}) (**Fig 3**). These shifts can be attributed to increased rigidification of the molecular framework at low temperatures, which limits structural relaxation in the excited state and stabilizes higher-energy emissive states.

In addition, the emission decay profile undergoes a notable change with temperature. While biexponential decay behavior is observed at room temperature, cooling leads to the emergence of a three-exponential decay profile, with significantly prolonged lifetimes reaching up to 35 μs at 77 K. The presence of multiexponential decay components suggests the involvement of multiple emissive states, potentially arising from different conformations or from contributions of both monomeric and dimeric subunits within the structure.

Variable-temperature (VT) lifetime data were analyzed using an established three-state kinetic model (as described in Eq. 1) over the temperature range of 17–297 K to extract key TADF parameters (**Fig 4**). Although a characteristic sigmoidal trend—indicative of thermally activated delayed fluorescence—was observed, quantitative fitting for compound **3** deviated beyond acceptable error margins. This discrepancy likely arises from limitations in the estimation of the radiative rate constant (k_r), as values derived from average lifetimes may not adequately capture the complexity of multicomponent decay processes present in the system. Consequently, while the qualitative features strongly support a TADF mechanism, precise quantitative analysis remains challenging for this compound.

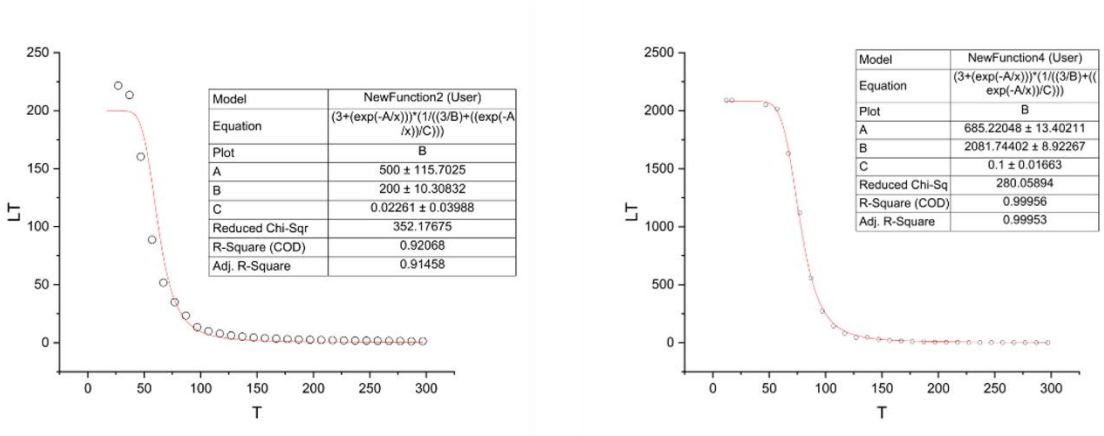


Fig 4. VT-LT plot for **3** (left) and **4** (right).

In contrast to compound **3**, compound **4** exhibits a significantly smaller hypsochromic shift of approximately 324 cm^{-1} upon cooling to 77 K or 17 K. This relatively modest blue shift suggests that the excited-state geometry of 4 undergoes less structural reorganization upon cooling, indicating a comparatively more rigid excited-state landscape or a smaller difference between ground- and excited-state geometries than in 3. Concomitantly, a substantial increase in the emission lifetime is observed,

reaching the millisecond regime at low temperatures. Such long-lived emission is characteristic of triplet-state dominated processes, where thermally activated reverse intersystem crossing (rISC) becomes inefficient at reduced temperatures, leading to accumulation of population in the triplet state.

Fitting of the variable-temperature lifetime (VT-LT) data using the previously described kinetic model yields a singlet–triplet energy gap ($\Delta E_{(S_1-T_1)}$) of approximately 685 cm^{-1} for compound **4**. This relatively small energy gap is well within the range required to enable efficient thermally activated delayed fluorescence (TADF), as it facilitates reverse intersystem crossing ($T_1 \rightarrow S_1$) at ambient temperatures. Furthermore, the short singlet excited-state lifetime (τ_{S1} ≈ 100 ns) supports rapid radiative decay from the S_1 state once repopulated via rISC, contributing to the overall high emission efficiency.

To further investigate the environment-dependent photophysical behavior, spectroscopic measurements were carried out in different host matrices relevant to technological applications. In a nonpolar matrix such as polystyrene (PS) film, both compounds **3** and **4** exhibit a noticeable hypsochromic (blue) shift in their emission maxima at ≈ 590 nm (**Fig 5**) compared to their solution-state emission. This shift is accompanied by radiative rate constants (k_r) in the range of 2.2–5.8 × 10^5 s^{-1}, consistent with efficient thermally activated delayed fluorescence (TADF). The observed blue shift can be attributed primarily to the restriction of structural relaxation in the rigid polymer matrix, which limits excited-state distortion. As a result, the emissive state is less stabilized relative to solution, leading to higher-energy emission. This rigidification effect is further reflected in the narrowing of the emission bandwidth, with the full width at half maximum (FWHM) decreasing to approximately 5000 cm^{-1}.

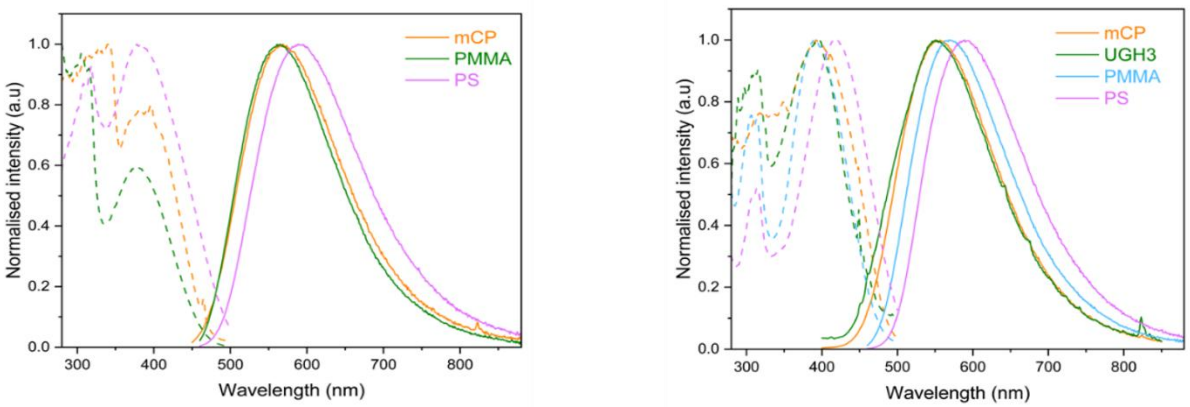


Fig 5. Emission and excitation profiles of **3** (left) and **4** (right) in different matrices (2 wt%) at RT.

In more polar matrices such as poly(methyl methacrylate) (PMMA) and mCP (1,3-bis(N-carbazolyl)benzene), an additional hypsochromic shift is observed. For compound **3**, the emission maxima shift to λ^{max} ≈ 570 nm (PMMA) and 553 nm (mCP), while for compound **4**, the corresponding values are λ^{max} ≈ 568 nm and 565 nm (**Fig 28**). This further blue shift arises from a combination of matrix-induced rigidification and differential stabilization of the ground and excited states. In particular, polar environments tend to stabilize the more polar ground state of these LLCT systems more effectively than the excited state, thereby increasing the effective energy gap and leading to higher-energy emission.

Despite these favorable shifts, a somewhat counterintuitive decrease in photoluminescence efficiency is observed for both compounds in these matrices compared to their pristine solid-state forms. Nevertheless, TADF remains the dominant emission mechanism, as evidenced by the retention of relatively high radiative rate constants ($k_r > 10^5\ s^{-1}$). The reduction in quantum yield is therefore primarily attributed to an increase in non-radiative decay pathways.

This enhancement of non-radiative decay in polymer matrices can be rationalized by considering the microenvironmental differences relative to the crystalline solid state. In the crystalline phase, strong intermolecular interactions and tight packing effectively rigidify the molecular framework, minimizing vibrational and conformational degrees of freedom. In contrast, even though polymer matrices impose some degree of rigidity, they still allow for local segmental motion and free volume around the emitter molecules. This residual flexibility enables excited-state structural distortion and vibrational relaxation, thereby increasing non-radiative decay rates. Additionally, weak host–guest interactions and possible heterogeneity in local environments within the matrix may further contribute to energy dissipation.

Overall, these results highlight the delicate balance between rigidity, polarity, and local environment in governing the emission properties of these carbene–zinc thiolate systems. While rigid matrices promote blue-shifted and spectrally narrower emission, achieving high photoluminescence efficiency requires suppression of non-radiative decay through optimal structural confinement, as best realized in the crystalline solid state.

The BicAAC-supported zinc thiolate complexes are readily accessible via straightforward, high-yielding synthetic routes under mild conditions, highlighting their synthetic practicality. Incorporation of the benzene-1,2-dithiolate ligand further enhances robustness, particularly in compound 3, which exhibits exceptional thermal and ambient stability due to strong chelation and effective steric protection of the Zn–carbene bond.

Photophysically, both complexes operate via ligand-to-ligand charge transfer (LLCT) excited states and display thermally activated delayed fluorescence (TADF). In solution, significant structural relaxation leads to large Stokes shifts and pronounced non-radiative decay. In contrast, the solid state enforces geometric rigidity, substantially suppressing non-radiative pathways such as vibrational dissipation and excited-state distortion. This effect is most prominent in compound 3, where the rigid bicyclic ligand framework and favorable ligand orientation minimize energy loss, resulting in near-unity photoluminescence efficiency.

In summary, we have developed a series of carbene–zinc thiolate complexes supported by rigid bicyclic (alkyl)(amino)carbene (BicAAC) ligands and demonstrated their potential as highly efficient TADF emitters. The synthetic strategy enabled the formation of structurally distinct mono- and dimeric precursors, which upon incorporation of benzene-1,2-dithiolate ligands yielded target complexes with well-defined geometries and strong ligand-to-ligand charge transfer (LLCT) character.

Comprehensive photophysical investigations reveal that both complexes exhibit LLCT-based emission with small singlet–triplet energy gaps, enabling efficient thermally activated delayed fluorescence. While

solution-state emission is weak due to significant excited-state relaxation and non-radiative decay, a dramatic enhancement in photoluminescence efficiency is observed in the solid state. Notably, the dimeric complex **3** displays an exceptional quantum yield of $\Phi_{PL} \approx 0.9$, among the highest reported for Zn(II)-based TADF systems, accompanied by a high radiative rate constant despite the intrinsically weak spin–orbit coupling of zinc.

The superior performance of **3** is attributed to a combination of factors, including the rigid bicyclic carbene framework, reduced structural flexibility, and an optimal dihedral angle that promotes effective mixing of excited states and facilitates reverse intersystem crossing. In contrast, the monomeric complex 4, although still highly emissive ($\Phi_{PL} \approx 0.62$), exhibits increased non-radiative decay due to greater conformational freedom. Temperature-dependent studies further confirm the TADF mechanism, highlighting the role of small $\Delta E_{(S_1-T_1)}$ and thermally activated processes in governing emission.

Additionally, matrix-dependent studies underscore the importance of environmental effects, demonstrating that rigid media suppress excited-state distortion and modulate emission energy, while polymer matrices introduce competing non-radiative pathways despite maintaining TADF characteristics. These findings emphasize that both molecular design and external environment are critical in achieving optimal photophysical performance.

Overall, this work establishes BicAAC-supported Zn(II) thiolate complexes as a promising platform for efficient, earth-abundant TADF emitters. The insights gained into the interplay between ligand rigidity, geometric parameters, and excited-state dynamics provide valuable guidelines for the rational design of next-generation luminescent materials for optoelectronic applications.

2.5 Discussion

The exploration of Zn^{II} compounds, particularly those involving triplet excitons, remains comparatively underdeveloped. We address this gap by investigating the photophysical properties of luminescent Zn^{II} complexes and their potential for future technological applications. By examining the interplay between structural design, excited-state dynamics, and emission behaviour, this work demonstrates the versatility of Zn(II) complexes as sustainable and earth-abundant alternatives to precious metal-based materials in optoelectronic and catalytic applications.

Chapter 2.1 (Synthesis, structural characterization and rigidity dependent dual phosphorescence behavior of high-energy phosphorescent zinc(ii) cyclic (alkyl)(amino)carbene complexes)[75] explores how careful ligand design and structural control can enable efficient phosphorescence in zinc-based systems, focusing on developing zinc(II) complexes supported by cyclic (alkyl)(amino)carbene (cAAC) ligands and understanding how molecular rigidity governs their excited-state behavior, particularly the emergence of dual phosphorescence from distinct triplet states.

The central design principle of this work is based on overcoming the intrinsic limitations of Zn(II) by shifting the locus of photophysical activity from the metal center to the ligand framework. cAAC ligands are chosen because they are stronger σ-donors and better π-acceptors than conventional N-heterocyclic carbenes (NHCs), enabling stabilization of unusual electronic configurations and promoting charge-transfer interactions. By coordinating CAAC ligands to zinc(II) along with appropriate co-ligands, we construct a system in which the frontier molecular orbitals are largely ligand-centered. This allows access to excited states with significant charge-transfer character, even in the absence of metal-centered redox activity.

A second key aspect of the design is the deliberate tuning of molecular rigidity. We synthesize a series of zinc(II) complexes with varying degrees of conformational constraint, achieved through ligand substitution patterns and coordination geometries that either restrict or permit intramolecular motion. This variation in rigidity is critical because nonradiative decay pathways in excited states are often facilitated by structural relaxation and vibrational freedom. By increasing rigidity, these pathways can be suppressed, allowing radiative decay processes such as phosphorescence to compete more effectively.

The synthesis of the complexes involves standard coordination strategies for Zn(II), where the parent $(^{Me}Caac)_2Zn_2X_4$ was treated with one equivalent of the in situ prepared strongly halophilic silylium reagent $[(Et_3Si)(toluene)][B(C_6F_5)_4]$ to yield Zn_4X_6 cluster-type tetramers **45a-e**. Structural characterization, primarily through single-crystal X-ray diffraction, confirms the tetrahedral motif around zinc(II) with all halides in coordinated via bridging mode.

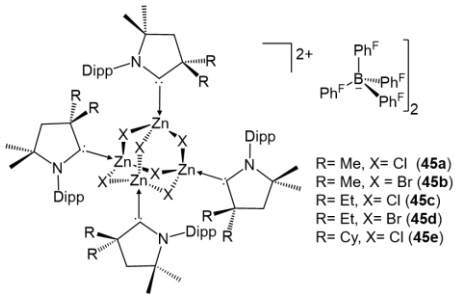


Figure 19. Molecular structures of tetramers.[75]

Photophysical studies show that these complexes display high-energy phosphorescence together with dual emission, indicating the presence of two distinct emissive triplet states. The higher-energy band is attributed to a ligand-centered (^{3}LE) excited state, while the second, lower-energy emission arises from an alternative triplet state that becomes accessible upon structural relaxation. The ability to access this lower-energy state depends strongly on the substituents, which influence the extent of conformational flexibility in the excited state. Consequently, the observed dual phosphorescence is governed by a rigidity-dependent equilibrium between two emissive triplet states, where excited-state geometric reorganization controls the balance between the high- and low-energy emission pathways.

This rigidity-dependent behavior highlights the importance of controlling excited-state landscapes through molecular design. By restricting conformational freedom, we effectively slow down nonradiative decay processes and stabilize higher-energy emissive states that would otherwise be inaccessible.

Mechanistically, the phosphorescence observed in these zinc complexes arises despite the absence of strong spin–orbit coupling typically provided by heavy metals. Instead, the system relies on ligand-centered electronic transitions and subtle spin–orbit coupling contributions from the coordination environment. The presence of charge-transfer character in the excited states can also enhance intersystem crossing by increasing spin–orbit coupling through orbital mixing, enabling population of triplet states even in a first-row metal system. Once populated, these triplet states can decay radiatively if nonradiative pathways are sufficiently suppressed, which is achieved here through rigidity.

The study also emphasizes the role of electronic structure in determining the energy and nature of the emitting states. By tuning the donor and acceptor properties of the ligands, the relative energies of LE and CT states can be adjusted, which in turn influences which triplet states are populated and how they contribute to emission. This provides an additional design handle beyond structural rigidity, allowing fine control over emission color and efficiency.

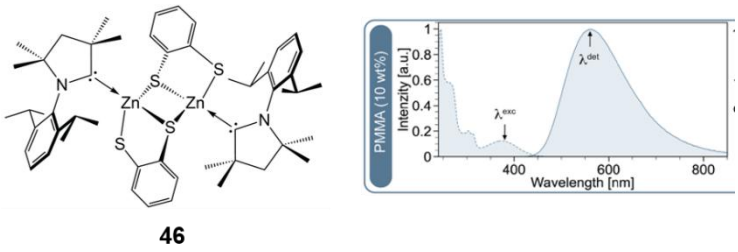
In conclusion, this work establishes a clear relationship between molecular rigidity, ligand design, and excited-state dynamics in zinc(II) CAAC complexes. By employing strongly donating carbene ligands and enforcing structural rigidity, we create a system in which ligand-centered excited states enable the observation of high-energy and dual phosphorescence, phenomena that are rarely accessible in complexes of earth-abundant metals. However, the low luminescence efficiency limits their suitability for practical applications and motivates further structural modifications to improve its photophysical performance.

Building on these insights, the second study introduces a significant modification in ligand design and nuclearity to move from fundamental understanding toward practical functionality. Instead of relying solely on cAAC ligands, the system incorporates dithiolate ligands, introducing sulfur atoms into the coordination sphere and forming a dimeric zinc(II) structure bridged by dithiolate groups.

Chapter 2.2 (An Air- and Moisture-stable Zinc(II) Carbene Dithiolate Dimer Showing Fast Thermally Activated Delayed Fluorescence and Dexter Energy Transfer Catalysis)[4] presents the rational design, synthesis, and detailed photophysical investigation of a zinc(II) carbene dithiolate complex that combines air and moisture stability with efficient light emission and photocatalytic activity.

The central design principle of the reported complex relies on constructing a donor–metal–acceptor (D–M–A) framework in which the metal center acts primarily as a structural and electronic mediator rather than as the main participant in frontier orbital transitions. Specifically, we employ cyclic(alkyl)(amino)carbene ligands as strong σ-donating units and benzene-1,2-dithiolate ligands as π- accepting components. The resulting coordination environment around Zn(II) enforces a geometry that electronically decouples donor and acceptor fragments while still enabling controlled charge transfer between them. This ligand-centered design is essential because Zn(II), being a d^{10} ion, does not readily engage in metal-to-ligand charge transfer (MLCT) processes typical of d^6 metals such as iridium(III) or ruthenium(II). Instead, the system is engineered to promote ligand-to-ligand charge transfer (LLCT), which becomes the dominant excited-state motif.

Structurally, the complex **46** forms a dimeric arrangement in which two zinc centers are bridged by dithiolate ligands. This dimerization contributes to both the rigidity and stability of the system, suppressing nonradiative decay pathways that often plague flexible organic chromophores. The air- and moisture-stable nature of the compound is a notable practical advantage for practical applications.



46

Figure 20. Molecular structure and emission profile of first prepared dithiolate dimer of ^{Me}cAAC.[4]

Photophysically, the complex exhibits strong luminescence in the orange-to-red spectral region across multiple environments, including solution, solid state, and polymer matrices. The emission behavior is governed by thermally activated delayed fluorescence (TADF), a mechanism that enables efficient harvesting of both singlet and triplet excitons. The key requirement for TADF is a small energy gap between the lowest singlet excited state (S_1) and the triplet state (T_1). In this system, the singlet–triplet energy splitting is sufficiently small (on the order of tens of meV) to allow thermal upconversion from T_1 back to S_1 via reverse intersystem crossing (RISC). This process effectively converts non-emissive triplet excitations into emissive singlet states, thereby enhancing overall luminescence efficiency.

A significant outcome of the molecular design is the unusually fast radiative decay associated with the emissive states. Despite the involvement of triplet states, which are typically characterized by slow phosphorescence in first-row transition metal complexes, the compound displays comparatively high radiative rate constants ($1.5 \cdot 10^5\ s^{-1}$in DCM).This behavior arises from the partial singlet character mixed into the emitting state through the TADF mechanism, allowing faster emission than would be expected for purely triplet-derived phosphorescence. The efficient emission observed in this zinc complex demonstrates that heavy-atom effects are not strictly necessary to achieve rapid radiative decay, provided that the electronic structure is appropriately engineered.

The nature of the excited states plays a crucial role in both emission and catalytic function. Spectroscopic and computational analyses indicate that the lowest excited states are dominated by LLCT character, involving electron density redistribution between the carbene and dithiolate ligands. These charge-transfer states are spatially separated, which reduces exchange interaction and thus contributes to the small singlet–triplet energy gap required for TADF. Also, the relatively long-lived triplet states of the zinc complex make it an effective sensitizer for transferring energy to suitable substrates, thereby promoting their excitation into reactive triplet states. This capability enables the complex to mediate photochemical transformations that rely on triplet activation pathways.

The integration of TADF behavior with Dexter energy transfer catalysis represents a particularly important aspect of the study. The TADF mechanism ensures efficient population of the emissive singlet state while maintaining access to triplet excitations, effectively balancing radiative output and reactive excited-state availability. Here, zinc(II) carbene dithiolate dimer exemplifies how careful molecular design can overcome intrinsic limitations of d^{10} metal centers. Through the deliberate construction of a donor–acceptor ligand framework, the system achieves a small singlet–triplet gap, enabling thermally activated delayed fluorescence, while also providing long-lived excited states suitable for Dexter energy transfer catalysis.

Thus, the transition from the first to the second system can be viewed as a deliberate evolution: from rigid CAAC-supported complexes that exhibit dual phosphorescence due to distinct triplet states, to a more electronically engineered, sulfur-containing dimer that promotes rapid reverse intersystem crossing and delayed fluorescence. In addition to improved photophysical efficiency, the second system also achieves air and moisture stability, addressing a practical limitation often associated with carbene complexes. Furthermore, the long-lived excited states in the dithiolate dimer enable Dexter energy transfer catalysis, extending its utility beyond light emission into photochemical applications.

Now, the goal is to modify the carbene dithiolate framework by focusing on structural control to maximize TADF efficiency. While retaining the same fundamental ligand motif introduced in the second work, this study systematically varies ligand structure, steric environment, and coordination geometry to precisely tune the electronic properties. The primary goal here is not just to demonstrate TADF, but to optimize it—achieving higher photoluminescence quantum yields, faster RISC, and minimized nonradiative losses.

Chapter 2.3 (Structural Control of Highly Efficient Thermally Activated Delayed Fluorescence in Carbene Zinc(II) Dithiolates)[5] investigates how deliberate molecular and structural engineering of zinc(II) carbene–dithiolate complexes can be used to achieve highly efficient thermally activated delayed fluorescence (TADF). The central design principle of this work is similar to **46**, but with bulkier menthyl substituted cAAC and differently substituted thiophenolate ligands to achieve trigonal planar **CZT1-3**.

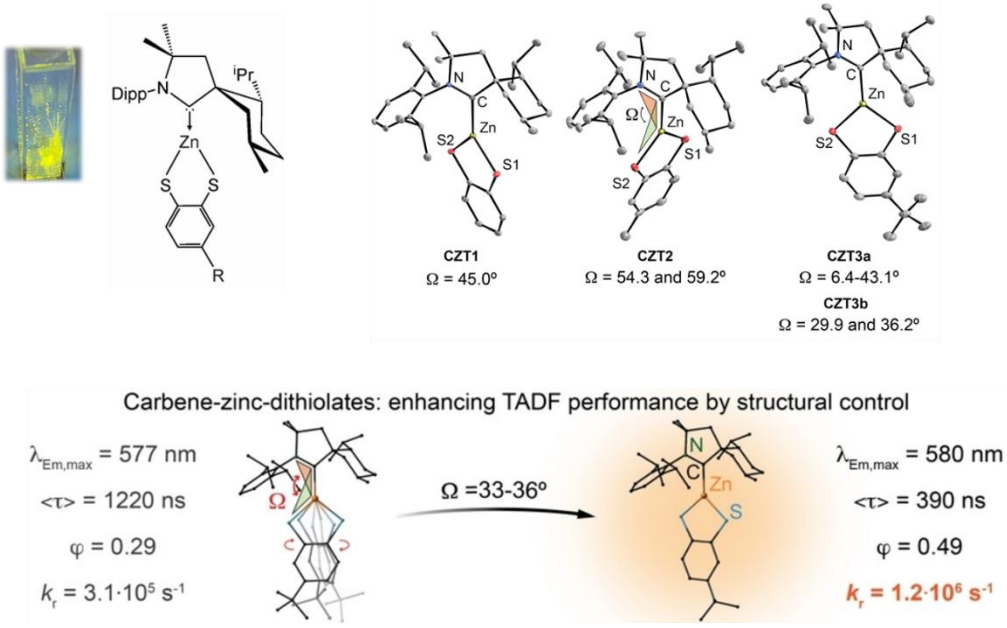


Figure 21. molecular structure of trigonal planar CZTs and Structural control of TADF in CZTs.[5]

In the solid state, **CZT1-3** show bright yellow–orange emission with enhanced quantum yields (up to 0.29) and relatively high radiative rate constants (10^5–10^6 s^{-1}), consistent with efficient triplet harvesting.

Temperature-dependent studies confirm a TADF mechanism, supported by small singlet–triplet energy gaps (~56 meV) that enable efficient reverse intersystem crossing. However, the coexistence of multiple conformers leads to complex, multiexponential decay profiles, demonstrating that emission arises from a distribution of geometries rather than a single well-defined structure. The CZT3b polymorph, with a narrower range of dihedral angles, exhibits more controlled photophysics and achieves record radiative rates (~10^6 s^{-1}) and high quantum yield (~0.49), underscoring the importance of geometric control.

Theoretical calculations reveal that subtle structural changes, particularly the dihedral angle between ligands and distortion at the sulfur atoms, modulate the balance between LLCT(ππ*) and LLCT(nπ*) states. These changes enhance spin–orbit coupling through orbital mixing, enabling unusually fast ISC and rISC despite the Zn(II) center. The tilted conformation is identified as optimal for TADF, providing the best balance between small singlet-triplet gapand strong coupling between singlet and triplet states.

Overall, this study demonstrates that not only ligand choice but also conformational control is critical for maximizing TADF efficiency. It establishes that fine-tuning geometry, restricting conformational freedom,

and stabilizing specific orientations are key design principles for developing high-performance Zn(II)-based TADF emitters.

Chapter 2.4 (TADF Zn(II) Bicyclic(Alkyl)(Amino)Carbene Thiolate Complexes with Near-Unity Quantum Yield) presents a systematic investigation into how ligand design, metal coordination geometry, and structural rigidity collectively govern the photophysical behavior of zinc(II) carbene–dithiolate complexes. The modified structural element of the design is the deliberate modulation of nuclearity and rigidity through steric control of the BicAAC substituents. The use of two ligands—^{Me}BicAAC and ^{iPr}BicAAC—leads to divergent structural outcomes at the Zn(II) center even under identical synthetic conditions. The less bulky ^{Me}BicAAC favors dimerization, forming a centrosymmetric Zn_2Cl_4 core like **46**, whereas the sterically demanding ^{iPr}BicAAC enforces monomer formation with trigonal planar coordination similar to **CZT**s. This demonstrates that steric hindrance is a primary control element for dictating nuclearity, coordination geometry, and ultimately electronic communication between ligands.

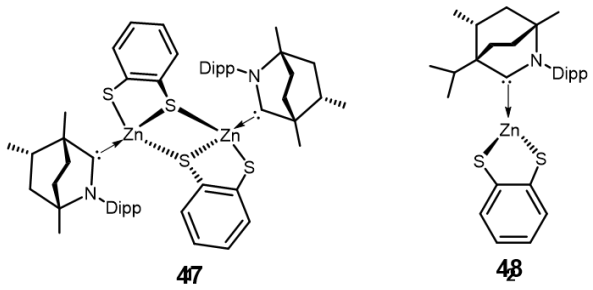


Figure 22. molecular structure of biCZTs.

Structurally, the final Zn–carbene–bdt complexes exhibit either monomeric or dimeric arrangements depending on ligand identity. A key geometric parameter is the dihedral angle (Ω) between the bdt plane and the carbene coordination plane. This angle governs orbital overlap between donor and acceptor ligands and thereby directly tunes the electronic coupling responsible for charge-transfer transitions. The dimeric complex exhibits Ω ≈ 49°, while the monomeric analogue is slightly more constrained (~46°).

The most striking result is observed for the dimeric complex, which achieves an exceptional solid-state quantum yield of Φ_{PL} ≈ 0.9, placing it among the most efficient Zn(II)-based TADF emitters reported. This efficiency arises from a synergistic combination of factors: increased chromophore density in the dimer, rigid BicAAC framework, optimal dihedral angle promoting electronic mixing, and strong suppression of nonradiative decay pathways. Quantitatively, this corresponds to a very high radiative rate (k_r ≈ 10^5–10^6 s^{-1}) and a drastically reduced nonradiative rate, demonstrating that structural confinement is more important than intrinsic spin–orbit coupling in determining efficiency.

The monomeric analogue also shows high emission efficiency, but significantly lower than the dimer due to increased conformational flexibility. This difference highlights a key structure–property relationship: nuclearity and rigidity directly control excited-state distortion, which in turn governs nonradiative decay rates. Steric analysis confirms that simple buried volume considerations are

insufficient to explain these differences; instead, the rigidity of the BicAAC scaffold and the resulting suppression of excited-state geometric relaxation are decisive.

Temperature-dependent studies further confirm the TADF mechanism. At low temperatures, emission shifts to higher energy and lifetimes increase dramatically, reaching microsecond to millisecond regimes, consistent with frozen-out RISC and triplet-state accumulation. Kinetic analysis yields small singlet–triplet gaps (~685 cm^{-1}), well within the range required for thermally activated upconversion. These results provide direct experimental support for the LLCT-driven TADF mechanism.

In summary, this work establishes a clear and transferable design principle for achieving highly efficient TADF in zinc(II) complexes: construct a ligand-centered donor–acceptor system that generates LLCT states, enforce structural rigidity through bicyclic carbene ligands and chelating dithiolate coordination, and tune dihedral angles to optimize orbital mixing while suppressing nonradiative decay. The zinc center functions primarily as a geometric scaffold that organizes the ligands rather than as an electronically active participant. Through this strategy, we demonstrate that earth-abundant metal complexes can achieve photophysical performances comparable to noble-metal systems, provided that excited-state structure, rigidity, and charge-transfer character are precisely controlled.

The development of luminescent zinc(II) carbene complexes across these studies (Chapter 2.1 to 2.4) reflects a systematic evolution from fundamental photophysics to highly optimized, application-ready TADF materials, where each successive work introduces targeted structural modifications to overcome limitations of the previous systems.

The first study on cyclic (alkyl)(amino)carbene (CAAC) zinc(II) complexes (**45a-e**) establishes the foundational understanding of excited-state behavior in d^{10} systems. The key insight here is that molecular rigidity governs nonradiative decay and triplet-state accessibility, with more rigid structures stabilizing higher-energy triplet states and enhancing emission. At this stage, the system is tetrameric or monomeric, and focused on phosphorescence, with no emphasis on efficiency or practical stability.

Building on this, the second study introduces a major structural and electronic modification: replacement of the halide framework with dithiolate ligand system and formation of dimeric CZT (**46**). This change serves multiple purposes. First, incorporation of sulfur atoms increases spin–orbit coupling relative to the CAAC system, facilitating more efficient intersystem crossing. Second, dimerization enhances rigidity and electronic communication, addressing the rigidity requirement identified in the first study. Most importantly, the excited-state mechanism shifts from phosphorescence to thermally activated delayed fluorescence (TADF) by reducing the singlet–triplet energy gap. This represents a conceptual transition: instead of relying on direct triplet emission, the system now recycles triplet excitons via reverse intersystem crossing (RISC). Additionally, this system achieves air and moisture stability and introduces Dexter energy transfer catalysis, marking a move toward functional applications.

The third study further refines this carbene–dithiolate platform by focusing on systematic structural control to optimize TADF efficiency. By employing ^{Menth}cAAC, this work fine-tunes steric environment, coordination geometry, and dihedral angle (Ω) to precisely control $\Delta E_{(S_1-T_1)}$and excited-state dynamics.

A key outcome is the identification of an optimal dihedral angle (~40–50°) that enables effective mixing of ππ* and nπ* states, enhancing spin–orbit coupling and RISC efficiency. Compared to the second study, where TADF is demonstrated as a feature of the system, this work represents a shift toward quantitative optimization, improving photoluminescence quantum yields and reducing nonradiative decay. However, despite these improvements, some limitations remain due to residual conformational flexibility, which still allows excited-state distortion.

The fourth study, based on bicyclic (alkyl)(amino)carbene (BicAAC)-supported Zn(II) thiolate complexes, represents the most advanced stage in this progression by addressing the remaining limitation—structural flexibility at the ligand backbone level. The key modification here is the transition from flexible CAAC-type ligands to rigid BicAAC frameworks, which intrinsically restrict geometric relaxation. This change directly builds on the insights of the third study: while earlier work optimized dihedral angles and local geometry, the BicAAC system enforces these optimal geometries through backbone rigidity. As a result, nonradiative decay is dramatically suppressed, leading to near-unity photoluminescence quantum yield ($\Phi_{PL} \approx 0.9$).

It is also noteworthy that the development of zinc(II) carbene-based luminophores represents a distinct and increasingly sophisticated approach within the broader landscape of d-block photophysics, particularly when compared with classical d^{10} emitters such as Copper(I), Silver(I), and Gold(I), as well as low-spin–orbit coupling (SO) first-row transition-metal systems including Iron(II), Cobalt(II), Nickel(II), and Manganese(II).[12-16, 62, 80] Across these classes, emissive behavior is fundamentally governed by the interplay between SOC, excited-state structure, and nonradiative decay pathways, with zinc(II) occupying a unique position due to its closed-shell d^{10} configuration, absence of low-lying metal-centered states, and intrinsically weak SOC.

In classical Cu(I), Ag(I), and Au(I) systems, photoluminescence is predominantly dictated by metal-to-ligand or ligand-to-ligand charge transfer (MLCT/LLCT) excited states, where SOC plays a central role in enabling efficient intersystem crossing (ISC). In Cu(I) systems, particularly carbene–metal–amide (CMA) and diimine complexes, emission typically arises from metal-to-ligand charge transfer (MLCT) or ligand-to-ligand charge transfer (LLCT) states, where SOC from Cu(I) enables rapid ISC and efficient population of triplet states.[62] However, these systems often suffer from structural reorganization in the excited state, leading to nonradiative decay and aggregation-induced quenching in some cases. Silver(I) analogues exhibit similar electronic structures but significantly weaker SOC compared to Cu(I), resulting in less efficient TADF and more pronounced sensitivity to structural relaxation. In contrast, Gold(I) complexes benefit from very strong relativistic SOC effects, enabling highly efficient room-temperature phosphorescence even from ligand-centered or cluster-centered excited states; however, their high cost and limited tunability restrict practical scalability. In contrast, first-row transition-metal complexes such as Fe(II), Co(II), Ni(II), and Mn(II) are strongly influenced by low-lying metal-centered (MC) states, which provide ultrafast nonradiative decay channels that effectively quench emission. Even when charge-transfer states are accessible, as in some Fe(II) polypyridyl or Mn(II) halide systems, excited-state lifetimes remain extremely short due to spin crossover, Jahn–Teller distortions, or vibrational relaxation. Similarly, high-valent d^0–d^{10} systems such as Zr(IV) LMCT emitters can exhibit

luminescence, but typically with moderate efficiency due to structural flexibility and insufficient radiative stabilization.[78]

Within this broader context, Zn(II) complexes are uniquely positioned: while they avoid MC-state quenching due to their d^{10} configuration, they lack the SOC necessary for efficient triplet harvesting. The series of zinc(II) carbene systems discussed here demonstrates how this limitation can be systematically overcome through ligand engineering and structural design.

Overall, comparison with both classical d^{10} systems and broader low-SOC transition-metal complexes highlights a fundamental shift in design philosophy. Whereas Cu(I), Ag(I), and Au(I) systems derive emissive properties from intrinsic relativistic effects, and Fe/Co/Ni/Mn complexes are limited by metal-centered nonradiative decay, Zn(II) carbene systems operate through a purely ligand-engineered framework. Across the four studies, a clear progression emerges—from rigidity-controlled phosphorescence, to sulfur-assisted TADF, to geometric optimization, and finally to backbone rigidification—culminating in a system where high-efficiency emission is achieved not by enhancing SOC, but by eliminating all competing nonradiative pathways through structural control. This establishes Zn(II) as a unique platform for sustainable luminescent materials, demonstrating that near-unity emission can be realized in low-SOC metals through rational molecular engineering alone.

3 Summary and Outlook

Taken together, this thesis outlines a coherent evolution in the design of Zn(II)-based emitters. Initial cAAC-supported Zn(II) systems established the fundamental role of structural rigidity in enabling long-lived triplet emission. Incorporation of dithiolate donors and dimeric architectures introduced stronger electronic coupling and sulfur-based contributions, shifting the emission mechanism toward TADF while improving functionality. Subsequent tuning of dithiolate systems demonstrated that precise geometric control—particularly dihedral angle (Ω) and steric effects—directly governs excited-state dynamics and TADF efficiency. Finally, the development of bicyclic (alkyl)(amino)carbene (bicAAC) thiolate complexes enforces intrinsic rigidity and optimal orbital alignment, enabling near-unity quantum yields.

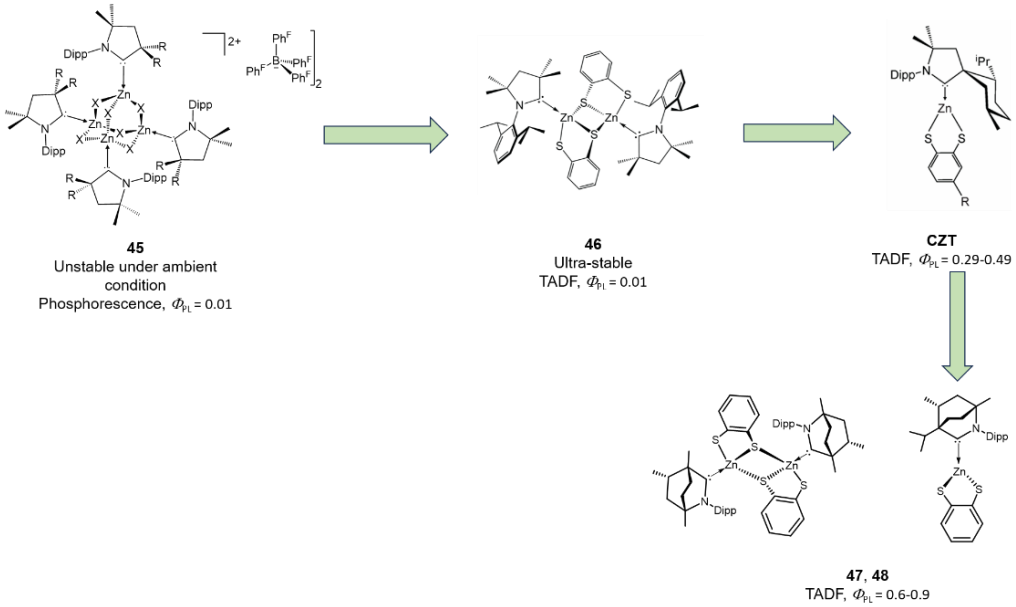


Figure 23. progression of Zn(II) emitters.

Overall, this progression moves systematically from fundamental understanding to practical optimization, where each step introduces a targeted design element: rigidity, donor strength and dimerization, geometric fine-tuning, and backbone rigidification. This results in highly efficient, stable, and application-relevant Zn(II)-based TADF luminophores.

However, there is still significant scope for further improvement and expansion of these systems. In terms of circularly polarized luminescence (CPL), both the **CZT** series and complexes **47–48** exhibit

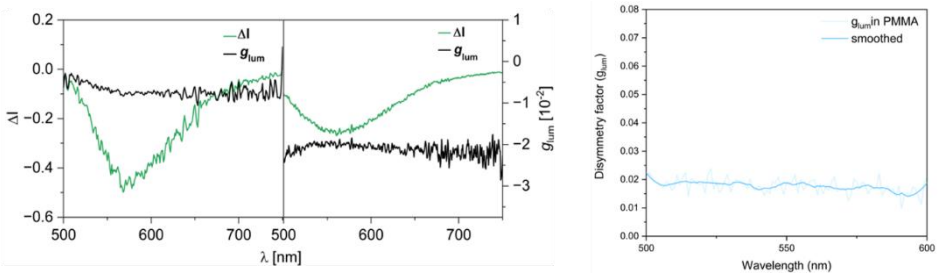


Figure 24. CPL properties of CZTs and 47.

CPL activity with appreciable g_{lum} values in different matrices, highlighting their potential for applications in chiroptical devices and advanced display technologies (**Figure 24**).

Beyond emissive properties, preliminary photocatalysis studies within the EZC group show that the CZT complexes are active in reactions such as oxidative quenching and photoredox processes (**Figure 25**), highlighting their potential dual role as luminophores and photocatalysts. However, the current reaction yields are modest, indicating that further optimization of reaction conditions and substrate design is required.

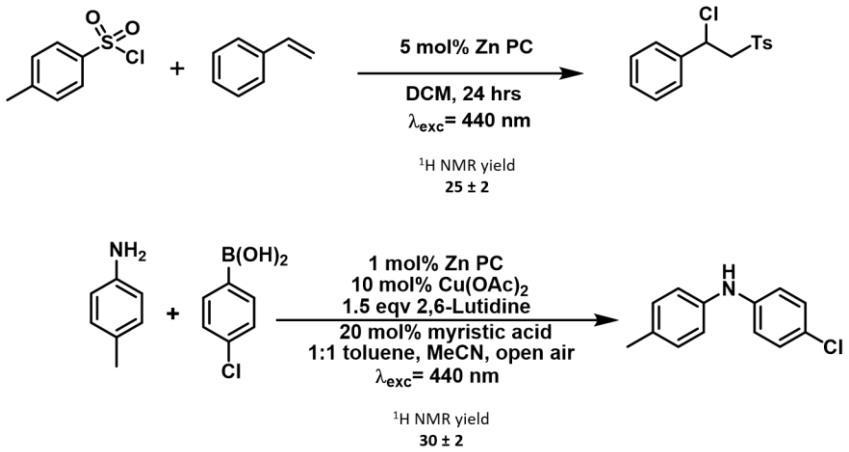


Figure 25. Catalysis with CZT3.

Further tuning of the ligand environment offers additional opportunities. For instance, replacing dithiolate donors with diphenolate ligands has been shown to shift emission toward the near-infrared (NIR) region (**Figure 26**), an area currently under active investigation.

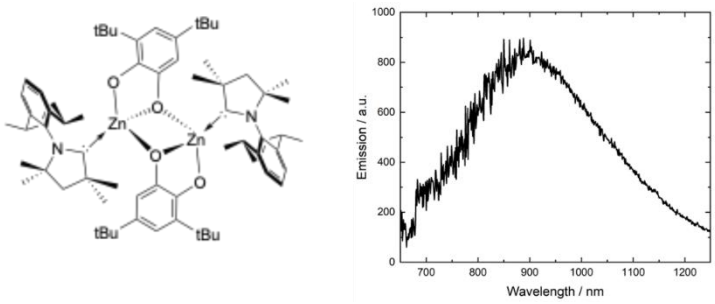


Figure 26. Molecular structure of CZP (carbene-zinc-diphenolate) and NIR-emission in solid state at room temperature.

Efforts to enhance rigidity through chelating systems such as tetrathiophenolate—also of interest for potential exciton coupling—and hexathiophenolate ligands have been explored. While the tetrathiophenolate approach was unsuccessful, the hexathiophenolate system led to the formation of an unusual dimeric motif, where two carbene undergoes C–S bond formation to generate a thioether-linked species (**Figure 27**). This indicates alternative coordination pathways and highlights the non-innocent behavior of the carbene under these conditions. Such a new type of structure opens up an intriguing direction for understanding carbene reactivity and its role in Zn(II) photophysics.

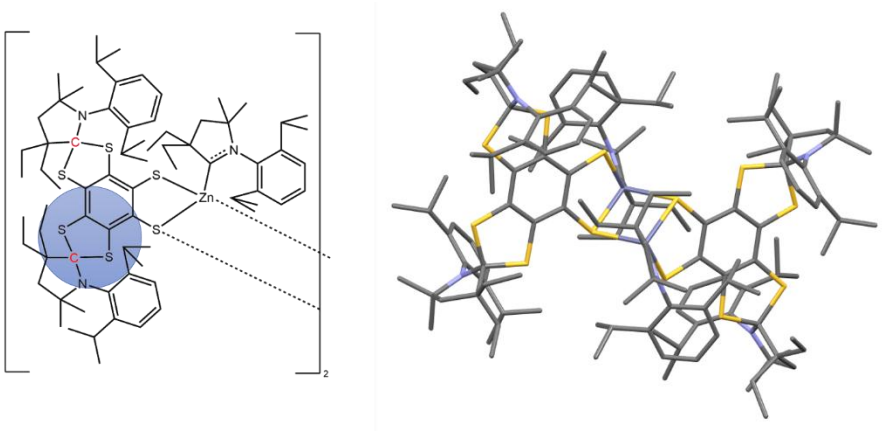


Figure 27. Molecular structure and crystal structure of hexathiophenolate based zinc(II) carbene complex.

Collectively, this thesis establishes a comprehensive framework for the rational design of Zn(II) complexes for advanced photonic and catalytic applications. It demonstrates how systematic structural and electronic modifications can profoundly tune photophysical behavior, enabling improved emission efficiency, controlled excited-state dynamics, and multifunctional performance. In doing so, the work provides a clear design strategy for developing sustainable, cost-effective luminophores and photocatalysts based on earth-abundant zinc, offering viable alternatives to traditional rare- and precious-metal systems. At the same time, it opens several promising directions for future research in ligand design, excited-state engineering, CPL-active materials, NIR emission, and photocatalytic functionality.

4 References

[1]. B. Goswami, T. J. Feuerstein, R. Yadav, S. Lebedkin, P. J. Boden, S. T. Steiger, G. Niedner-Schatteburg, M. Gerhards, M. M. Kappes, P. W. Roesky, *Chem. Eur. J.* **2021**, *27*, 15110-15119.

[2]. Y. Sakai, Y. Sagara, H. Nomura, N. Nakamura, Y. Suzuki, H. Miyazaki, C. Adachi, *Chem. Commun.* **2015**, *51*, 3181-3184.

[3]. O. Mrózek, M. Gernert, A. Belyaev, M. Mitra, L. Janiak, C. M. Marian, A. Steffen, *Chem. Eur. J.* **2022**, *28*, e202201114.

[4]. O. Mrózek, M. Mitra, B. Hupp, A. Belyaev, N. Lüdtke, D. Wagner, C. Wang, O. S. Wenger, C. M. Marian, A. Steffen, *Chem. Eur. J.* **2023**, *29*, e202203980.

[5]. M. Mitra, O. Mrózek, M. Putscher, J. Guhl, B. Hupp, A. Belyaev, C. M. Marian, A. Steffen, *Angew. Chemie Int. Ed.* **2024**, *63*, e202316300.

[6] C. Bizzarri, E. Spuling, D. M. Knoll, D. Volz, S. Bräse, *Coord. Chem. Rev.* **2018**, *373*, 49-82.

[7]. D. M. Arias-Rotondo, J. K. McCusker, *Chem. Soc. Rev.* **2016**, *45*, 5803-5820.

[8]. A. B. Muñoz-Garcí, I. Benesperi, G. Boschloo, J. J. Concepcion, J. H. Delcamp, E. A. Gibson, G. J. Meyer, M. Pavone, H. Pettersson, A. Hagfeldt, M. Freitag, *Chem. Soc. Rev.*, **2021**, 50 , 12450-12550.

[9]. Q. Zhao, C. Huang, F. Li, *Chem. Soc. Rev.* **2011**, *40*, 2508–2524.

[10]. J. H. Correia, J. A. Rodrigues, S. Pimenta, T. Dong, Z. Yang, *Pharmaceutics*, **2021**, *13*, 1332.

[11]. M. A. Baldo, D. F. O'Brien, Y. You, A. Shoustikov, S. Sibley, M. E. Thompson, S. R. Forrest, *Nature,* **1998**, *395*, 151-154.

[12]. a) S. Otto, M. Grabolle, C. Förster, C. Kreitner, U. Resch-Genger, K. Heinze, *Angew. Chem. Int. Ed.* **2015**, *54*, 11572–11576; *Angew. Chem.* **2015**, *127*, 11735–11739. b) F. Reichenauer, C. Wang, C. Förster, P. Boden, N. Ugur, R. Báez-Cruz, J. Kalmbach, L. Carrella, E. Rentschler, C. Ramanan, G. Niedner-Schatteburg, M. Gerhards, M. Seitz, U. Resch-Genger, K. Heinze, *J. Am. Chem. Soc.* **2021**, *143*, 11843-11855. c) L. A. Büldt, X. W. Guo, R. Vogel, A. Prescimone, O. S. Wenger, *J. Am. Chem. Soc.* **2017**, *139*, 985– 992. d)N. Sinha, C. Wegeberg, D. Häussinger, A. Prescimone, O. S. Wenger, *Nat. Chem.* **2023**, *15*, 1730–1736.

[13]. a) J. P. Harris, C. Reber, H. E. Colmer, T. A. Jackson, A. P. Forshaw, J. M. Smith, R. A. Kinney, R. J. Telser, *Can. J. Chem*. **2017**, *95*, 547-552. b) N. R. East, R. Naumann, C. Förster, C. Ramanam, G. Diezemann, K. Heinze, *Nat. Chem.* **2024**, *16*, 827-834. c) P. Herr, C. Kerzig, C. B. Larsen, D. Häussinger, O. S. Wenger, *Nat. Chem.* **2021**, *13*, 956-962.

[14]. a) P. Chábera, Y. Z. Liu, O. Prakash, E. Thyrhaug, A. El Nahhas, A. Honarfar, S. Essén, L. A. Fredin, T. C. B. Harlang, K. S. Kjær, K. Handrup, F. Ericson, H. Tatsuno, K. Morgan, J. Schnadt, L.

Häggström, T. Ericsson, A. Sobkowiak, S. Lidin, P. Huang, S. Styring, J. Uhlig, J. Bendix, R. Lomoth, V. Sundström, P. Persson, K. Wärnmark, *Nature* **2017**, *543*, 695-699. b) K. S. Kjær, N. Kaul, O. Prakash, P. Chábera, N. W. Rosemann, A. Honarfar, O. Gordivska, L. A. Fredin, K.-E. Bergquist, L. Häggström, T. Ericsson, L. Lindh, A. Yartsev, S. Styring, P. Huang, J. Uhlig, J. Bendix, D. Strand, V. Sundström, P. Persson, R. Lomoth, K. Wärnmark, *Science* **2019**, *363*, 249-253. c) J. Steube, A. Kruse, O. S. Bokareva, T. Reuter, S. Demeshko, R. Schoch, M. A. Argüello Cordero, A. Krishna, S. Hohloch, F. Meyer, K. Heinze, O. Kühn, S. Lochbrunner, M. Bauer, *Nat. Chem.* **2023**, *15*, 468. d) J. D. Braun, B. Lozada, I. C. Kolodziej, C. Burda, K. M. Newman, J. van Lierop, R. L. Davis, D. Herbert, *Nat. Chem.* **2019**, *11*, 1144-1150. e) W. Leis, M. A. Argüello Cordero, S. Lochbrunner, H. Schubert, A. Berkefeld, *J. Am. Chem. Soc.* **2022**, *144*, 1169-1173.

[15]. a) A. K. Pal, C. F. Li, G. S. Hanan, E. Zysman-Colman, *Angew. Chem. Int. Ed.* **2018**, *57*, 8027–8031; *Angew. Chem.* **2018**, *130*, 8159-8163. b) S. Kaufhold, N. W. Rosemann, P. Chábera, L. Lindh, I. B. Losada, J. Uhlig, T. Pascher, D. Strand, K. Wärnmark, A. Yartsev, P. Persson, *J. Am. Chem. Soc.* **2021**, *143*, 1307-1312. c) N. Sinha, B. Pfund, C. Wegeberg, A. Prescimone, O. S. Wenger, *J. Am. Chem. Soc.* **2022**, *144*, 9859-9873.

[16]. a) Y. S. Wong, M. C. Tang, M. G. Ng, V. W. W. Yam, *J. Am. Chem. Soc.* **2020**, *142*, 7638-7646. b) T. Ogawa, N. Sinha, B. Pfund, A. Prescimone, O. S. Wenger, *J. Am. Chem. Soc.* **2022**, *144*, 48, 21948–21960. c) L. A. Büldt, C. B. Larsen, O. S. Wenger, *Chem. - Eur. J.* **2017**, *23*, 8577-8580.

[17]. M. Montalti, A. Credi, L. Prodi, M. T. Gandolfi, *Handbook of Photochemistry*, CRC Press, **2006**.

[18]. M. Klessinger, J. Michl, *Excited States and Photochemistry of Organic Molecules*, VCH Publishers, Inc., New York, **1995**.

[19]. T. J. Penfold, E. Gindensperger, C. Daniel, C.M. Marian, *Chem. Rev*., **2018**, *118*, 6975-7025.

[20]. M. A. El-Sayed, *J. Chem. Phys*., **1963**, *38*, 2834–2838.

[21]. C. W. Hsu, C. C. Lin, M. W. Chung, Y. Chi, G. H. Lee, P. T. Chou, C. H. Chang, P. Y. Chen, *J. Am. Chem. Soc.* **2011**, *133*, 12085– 12099.

[22]. M. Born, R. Oppenheimer, *Ann. Phys.* **1927**, *389*, 457–484.

[23]. A. C. Albrecht, *J. Chem. Phys.* **1963**, *38*, 354–365.

[24]. N. J. Turro, V. Ramamurthy, J. C. Scaiano, *Modern Molecular Photochemistry of Organic Molecules*, University Science Books, Sausalito, **2010**.

[25]. A. Steffen, B. Hupp*, Design of Efficient Emissive Materials* in *Comprehensive Coordination Chemistry III*, *Vol. 373* (Eds.: E. Constable, G. Parkin, L. Que Jr), Elsevier, San Diego, **2021**, PP. 466-502.

[26]. G. Baryshnikov, B. Minaev, H. Ågren, *Chem. Rev.* **2017**, *117*, 6500-6537.

[27]. A. Heil, C. M. Marian, *Inorg. Chem.* **2019**, *58*, 6123-6136.

[28]. H. Yersin, A.F. Rausch, R. Czerwieniec, T. Hofbeck, T. Fischer, *Coord. Chem. Rev*., **2011**, *255*, 2622-2652.

[29]. H. Yersin, *Triplet Emitters for OLED Applications. Mechanisms of Exciton Trapping and Control of Emission Properties, In: Transition Metal and Rare Earth Compounds*. Topics in Current Chemistry, Vol. 241, Springer, Berlin, Heidelberg, **2004**.

[30]. D. Volz, M. Wallesch, C. Fléchon, M. Danz, A. Verma, J. M. Navarro, D. M. Zink, S. Bräse, T. Baumann, *Green Chem*. **2015**, *17*, 1988.

[31]. C.A. Parker, C.G. Hatchard, *Trans. Faraday Soc.*, **1961**, *57*, 1894-1904.

[32]. A. Endo, M. Ogasawara, A. Takahashi, D. Yokoyama, Y. Kato, C. Adachi, *Adv. Mater.* **2009**, *21*, 4802-4806.

[33]. M. J. Leitl, D. M. Zink, A. Schinabeck, T. Baumann, D. Volz, H. Yersin*, Copper(I) Complexes for Thermally Activated Delayed Fluorescence: From Photophysical to Device Properties* in *Photoluminescent Materials and Electroluminescent Devices* (Eds.: N. Armaroli, H. J. Bolink), Springer International Publishing, Cham, **2017**, pp. 141-174.

[34]. M.Y. Wong, E. Zysman-Colman, *Adv. Mater*., **2017**, *29*, p. 1605444.

[35]. P. W. Atkins, J. de Paula, *Physical Chemistry*. 9th ed., W.H Freeman and Company, New York, **2010**.

[36]. R. Englman, J. Jortner, *Mol. Phys*. **1970**, *18*, 145-164.

[37]. J. R. Lakowicz, *Principles of fluorescence spectroscopy*. 3rd ed., Springer, New York, **2006**.

[38]. M. Dorn, N. R. East, C. Förster, W. R. Kitzmann, J. Moll, F. Reichenauer, T. Reuter, L. Stein, K. Heinze, *d-d and Charge Transfer Photochemistry of 3d Metal Complexes* in *Comprehensive Inorganic Chemistry III* (Section Ed. V. W.-W. Yam) **2023**, 707-788.

[39]. R. Englman, *J. Lumin*. **1970**, *1, 2*, 134-142.

[40]. L. Flamigni, A. Barbieri, C. Sabatini, B. Ventura, F. Barigelletti, Photochemistry and Photophysics of Coordination Compounds: Iridium. In: *Photochemistry and Photophysics of Coordination Compounds II. Topics in Current Chemistry*, *Vol. 281*, V. Balzani, S. Campagna (Eds), Springer Berlin, Heidelberg, **2007**.

[41]. S. Campagna, F. Puntoriero, F. Nastasi, G. Bergamini, V. Balzani, Photochemistry and Photophysics of Coordination Compounds: Ruthenium. In: *Photochemistry and Photophysics of Coordination Compounds I. Topics in Current Chemistry*, *Vol. 280*, V. Balzani, S. Campagna (Eds), Springer Berlin, Heidelberg, **2007**.

[42]. K. W. Lo, G. S. M. Tong, G. Cheng, K. H. Low and C. M. Che, *Angew. Chem., Int. Ed.*, **2022**, *61*, e202115515.

[43]. K. K. W. Lo, K. H. K. Tsang, W. K. Hui, N. Zhu, *Inorg. Chem.* **2005**, *44*, 6100-6110.

[44]. a) M.A. Baldo, S. Lamansky, P.E. Burrows, M.E. Thompson, S. R. Forrest, *Appl. Phys. Lett.* **1999**, *75*, 4. b) A.B. Tamayo, B.D. Alleyne, P.I. Djurovich, S. Lamansky, I. Tsyba, R. Bau, M.E. Thompson, *J. Am. Chem. Soc.* **2003**, *125*, 7377.

[45]. A. F. Rausch, M. E. Thompson, H. Yersin, *J. Phys. Chem. A* **2009**, *113*, 5927-5932.

[46]. Z. Chen, H. Zhang, D. Wen, W. Wu, Q. Zeng, S. Chen, W. Y. Wong, *Chem. Sci.*, **2020**, *11*, 2342-2349.

[47]. S. Campagna, F. Puntoriero, F. Nastasi, G. Bergamini, V. Balzani, *Top. Curr. Chem*. **2007**, *280*, 1-36.

[48]. T. M. Rodriguez, M. Deegbey, C.H. Chen, E. Jakubikova, J.L Dempsey, *Inorg. Chem.* **2023**, *62* (17), 6576-6585.

[49]. Y. M. Dikova, D.S. Yufit, J. A. G. Williams, *Inorg. Chem.* **2023**, *62*, 1306-1322.

[50]. B. W. Pfennig, M. E. Thompson, A. B. Bocarsly, *Organometallics*, **1993**, *12*, 649-655.

[51]. H. C. London, T. J. Whittemore, A. G. Gale, C. D. McMillen, D. Y. Pritchett, A. R. Myers, H. D. Thomas, G. C. Shields, P. S. Wagenknecht, *Inorg. Chem.* **2021**, *60*, 14399-14409.

[52]. H. C. London, D. Y. Pritchett, J. A. Pienkos, C. D. McMillen, T. J. Whittemore, C. J. Bready, A. R. Myers, N. C. Vieira, S. Harold, G. C. Shields, P. S. Wagenknecht, *Inorg. Chem.* **2022**, *61* (28), 10986-10998.

[53]. M. Dorn, J. Kalmbach, P. Boden, A. Päpcke, S. Gómez, C. Förster, F. Kuczelinis, L. M. Carrella, L. A. Büldt, N. H. Bings, E. Rentschler, S. Lochbrunner, L. González, M. Gerhards, M. Seitz, K. Heinze, *J. Am. Chem. Soc*, **2020**, *142*(17), 7947-7955.

[54]. R. D. Dill, R. I. Portillo, S. G. Shepard, M. P. Shores, A. K. Rappé, N. H. Damrauer, *Inorg. Chem.* **2020**, *59*, 14706-14715.

[55]. A. Juris, V. Balzani, F. Barigelletti, S. Campagna, P. Belser, A. V. Zelewsky, *Coord. Chem. Rev.* **1988**, *84*, 85-277.

[56]. J. R. Jiménez, B. Doistau, C. M. Cruz, C. Besnard, J.G. Cuerva, A.G. Campagna, C. Piguet, *J. Am. Chem. Soc.* **2019**, *141*, 13244-13252.

[57]. N. Sinha, J.R. Jiménez, B. Pfund, A. Prescimone, C. Piguet, O.S. Wenger, *Angew. Chem., Int. Ed.* **2021**, *60*, 23722 – 23728.

[58]. N. Kaul, E. Asempa, J. A. Valdez-Moreira, J. M. Smith, E. Jakuikova, L. Hammarström, *J. Am. Chem. Soc.* **2024**, *146*, 35, 24619-24629.

[59]. O. S. Wenger, *Chem. Eur J.*, **2019**, *25*, 24, 6043-6052.

[60]. a) S. G. Shepard, S. M. Fatur, A. K. Rappe, N. H. Damrauer, *J. Am. Chem. Soc.* **2016**, *138*, 2949-2952. b) T. C. B. Harlang, Y. Z. Liu, O. Gordivska, L. A. Fredin, C. S. Ponseca Jr., P. Huang, P. Chábera, K. S. Kjær, H. Mateos, J. Uhlig, R. Lomoth, R. Wallenberg, S. Styring, P. Persson, V. Sundström, K. Wärnmark, *Nat. Chem.* **2015**, *7*, 883-889.

[61]. C. Wegeberg and O. S. Wenger, *JACS Au,* **2021,** *1* (11), 1860-1876.

[62]. a) M. Gernert, U. Müller, M. Haehnel, J. Pflaum, A. Steffen, *Chem. - Eur. J.* **2017**, *23*, 2206-2216. b) R. Hamze, J. L. Peltier, D. Sylvinson, M. Jung, J. Cardenas, R. Haiges, M. Soleilhavoup, R. Jazzar, P. I. Djurovich, G. Bertrand, M. E. Thompson, *Science* **2019**, *363*, 601-606. c) S. Shi, M. C. Jung, C. Coburn, A. Tadle, D. Sylvinson M. R, P. I. Djurovich, S. R. Forrest, M. E. Thompson, *J. Am. Chem. Soc.* **2019**, *141*, 3576-3588. d) M. Gernert, L. Balles-Wolf, F. Kerner, U. Müller, A. Schmiedel, M. Holzapfel, C. M. Marian, J. Pflaum, C. Lambert, A. Steffen, *J. Am. Chem. Soc.* **2020**, *142*, 8897-8909. e) A. M. T. Muthig, O. Mrózek, T. Ferschke, M. Rödel, B. Ewald, J. Kuhnt, C. Lenczyk, J. Pflaum, A. Steffen, *J. Am. Chem. Soc.* **2023**, *145*, 4438-4449.

[63]. C. E. Housecroft, E. C. Constable, *Chem. Soc. Rev.* **2015**, *44*, 8386-8398.

[64]. M. S. Lazorski, F. N. Castellano, *Polyhedron* **2014**, *82*, 57-70.

[65]. A. F. Holleman, E. Wiberg*, Lehrbuch der Anorganischen Chemie,* 102. Aufl., de Gruyter, Berlin, **2008**.

[66]. C. Bizzarri, E. Spuling, D. M. Knoll, D. Volz, S. Bräse, *Coord. Chem. Rev.* **2018**, *373*, 49-82.

[67]. a) S. Hofmann, M. Hummert, R. Scholz, R. Luschtinetz, C. Murawski, P.-A. Will, S. I. Hintschich, J. Alex, V. Jankus, A. P. Monkman, B. Lüssem, K. Leo, M. C. Gather, *Chem. Mater.* **2014**, *26*, 2414-2426; b) V. K. Rai, R. Srivastava, M. N. Kamalasanan, *Synth. Met.* **2009**, *159*, 234-237; c) S. Reineke, M. Thomschke, B. Lüssem, K. Leo, *Rev. Mod. Phys.* **2013**, *85*, 1245-1293; d) A. Werner, M. Burghart, S. Murano, O. Schneider, T. Stübinger, M. Limmert, J. Blochwitz-Nimoth, *Dig. Tech. Pap.* **2006**, *37*, 1099.

[68]. I. B. Lozada, J. D. Braun, J. A. G. Williams, D. E. Herbert, *Inorg. Chem.* **2022**, *61*, 17568-17578.

[69]. G. A. Crosby, R. G. Highland, K. A. Truesdell, *Coord. Chem. Rev.* **1985**, *64*, 41-52. b) R. G. Highland, G. A. Crosby, *Chem. Phys. Lett.* **1985**, *119*, 454-458. c) K. A. Truesdell, G. A. Crosby, *J. Am. Chem. Soc.* **1985**, *107*, 1787-1788. d) R. G. Highland, J. G. Brummer, G. A. Crosby, *J. Phys. Chem.* **1986**, *90*, 1593-1598.

[70]. N. Lüdtke, J. Kuhnt, T. Heil, A. Steffen, C. M. Marian, *ChemPhotoChem* **2023**, *7*, e202200142.

[71]. S. Koop, O. Mrózek, L. Janiak, A. Belyaev, M. Putscher, C. M. Marian, A. Steffen, *Inorg. Chem.* **2024**, *63*, 891-901.

[72] J. Xiong, K. Li, T. Teng, X. Chang, Y. Wei, C. Wu, C. Yang, *Chem. Eur. J.* **2020**, *26*, 6887–6893.

[73a] K. D. Oyler, F. J. Coughlin, S. Bernhard, *J. Am. Chem. Soc.* **2007**, *129*, 210-217. [73b] J. Kuhnt, M. Mitra, S. Maity, B. Hupp, C. M. Marian, A. Steffen, *J. Phys. Chem. Lett.* **2024**, *15*, 6409-6414.

[74] D. A. Shariaty, P. I. Djurovich and M. E. Thompson, *J. Am. Chem. Soc.*, **2025**, *147*, 29065-29078.

[75] M. Mitra, O. Mrózek, A. Belyaev, L. Janiak, C. M. Marian, A. Steffen, *Dalton Trans.*, **2026**, *55*, 5519.

[76] N. M. Rajendran, N. Gautam, P. Sarkar,[b] J. Ahmed, A. Das, S. Das, S. K. Pati and S. K. Mandal, *Chem. Commun.*, **2021**,*57*, 5282-5285.

[77] E. Tomás-Mendivil, M. M. Hansmann, C. M. Weinstein, R. Jazzar, M. Melaimi, G. Bertrand, *J. Am. Chem. Soc.* **2017**, *139*, 23, 7753–7756.

[78] Yu Zhang, Tia S. Lee, Joseph M. Favale, Dylan C. Leary, Jeffrey L. Petersen, Gregory D. Scholes, Felix N. Castellano, and Carsten Milsmann, *Nature Chemistry* **2020**, *12*, 4, 345–352.

[79] F. Chotard, V. Sivchik, M. Linnolaht, M. Bochmann**,** A. S. Romanov**,** *Chem. Mater.* **2020**, *32*, 14, 6114–6122.

[80] T-Yi Li**,** S-Jia Zheng, P. I. Djurovich, M. E. Thompson, *Chem. Rev.* **2024**, *124*, 7, 4332–4392.

5 Appendix

5.1 Supporting information for chapter 2.1 (Synthesis, structural characterization and rigidity dependent dual phosphorescence behavior of high-energy phosphorescent zinc(ii) cyclic (alkyl)(amino)carbene complexes)

Supporting Information

Synthesis, Structural Characterization and Rigidity Dependent Anti-Kasha Behavior of High-Energy Phosphorescent Zinc(II) Cyclic (Alkyl)(Amino)carbene Complexes

Mousree Mitra, Ondřej Mrózek, Andrey Belyaev, Lars Janiak, Christel M. Marian and Andreas Steffen*

Table of Contents

1 METHODS AND MATERIALS 2

2 PHOTOPHYSICAL MEASUREMENTS 2

3 COMPUTATIONAL METHODS 3

4 SYNTHETIC PROCEDURES 4

5 NMR SPECTRA 11

6 MASS SPECTROMETRY 22

7 X-RAY CRYSTALLOGRAPHY 26

8 PHOTOPHYSICAL MEASUREMENTS 29

9 COMPUTATIONAL STUDIES 30

10 REFERENCES 44

1 Methods and materials

All operations were performed under an argon atmosphere by using conventional Schlenk-line techniques or glovebox. The solvents were dried using Technology Inc. Pure-Solv system or standard methods[1] and degassed prior to use. Carbenes ^{Me}cAAC, ^{Et}Caac and ^{Cy}cAAC and their zinc complexes [(^{R}cAAC)$_2$Zn$_2$(X)$_4$] (X = Cl, Br, R= Me, Et, Cy) (**1**-**5**) were prepared according to procedure reported in the literature.[2, 3] Zinc halides were dried by heating (up to 100 °C) under high vacuum. All other starting materials were available commercially and were used without further purification. ^{1}H, ^{13}C{^{1}H} APT, ^{1}H-^{13}C HSQC, ^{1}H-^{13}C HSMB, ^{1}H-^{1}H COSY and ^{1}H-^{15}N HMBC were measured at 300 K on Bruker 500 Avance and Bruker 600 Avance spectrometer. The chemical shifts are given in ppm relatively to residual signals of the solvent. [^{1}H,^{13}C: $CDCl_3$ (7.26, 77.16 ppm), (CD_2Cl_2 (5.32, 53.84 ppm), CD_3CN (1.94, 118.26 ppm), THF-d_8 (1.72, 3.58; 25.31, 67.21 ppm)]. MALDI-HRMS MS spectra were recorded on a Thermo Scientific Q Exactive in a positive ion mode connected with a TransMIT AP-SMALDI containing a laser with a wavelength of 343 nm. Best results were achieved with an attenuator of 35°.

2 Photophysical Measurements

All photophysical measurements were performed in dry and de-aerated solutions. UV-visible absorption spectroscopy was performed on an Agilent Cary 5000 spectrophotometer using standard 1 cm path length quartz cells. Excitation and emission spectra were recorded on an Edinburgh Instrument FLS1000 spectrometer, equipped with a 450 W Xenon arc lamp, double monochromators for the excitation and emission pathways, and a red-sensitive photomultiplier (PMT-980) as a detector. The excitation and emission spectra were corrected using the standard corrections supplied by the manufacturer for the excitation source's spectral power and the

detector's sensitivity. Quantum yields in solution were measured using Quantauras-QY, absolute PL quantum yield spectrometer and the quantum yield of solid samples was measured using an integrating cryosphere (Microstat N2) from Oxford Instruments. The luminescence lifetimes were measured using a µF2 pulsed 60 W Xenon microsecond flashlamp, with a repetition rate of 10-100 Hz and a multichannel scaling (MCS) module or with VPLEDs (449.6 nm with 37 mW), with 100 ns pulse width and an MCS module, depending on the time range. The emission was collected at a right angle to the excitation source. The low-temperature experiments were performed using 4 K cryostat (CS204SI-FMX-1SS) from Advanced Research System equipped with a closed cycle water-cooled helium compressor.

3 Computational Methods

Calculations were performed with the ORCA 4.2.1 program suite [4, 5] and the PBE0[6] hybrid functional, using density functional theory (DFT) by KOHN und SHAM[7] on the Linux-HPC-Cluster of TU Dortmund University. For geometry optimisations and calculations of molecular orbitals the split-valence basis set def2-TZVP with zero-order regular approximation of relativistic effects (ZORA) and BECKE-JOHNSON damping (D3-Cp*J) were used.[8,9] Frequency analysis was used to confirm convergence into a global minimum structure. For time-dependent DFT calculations the single-valence base set ZORA-def2-SVP was used as implemented in ORCA 5.0.1. All calculations were performed with tight SCF convergence (DE = 1·10-8 au).

4 Synthetic Procedures

[(^{Et}cAAC)$_2$Zn$_2$Cl$_4$] (**3**)

Solutions of 43 mg (315 µmol) of $ZnCl_2$ and 100 mg (315 µmol) of ^{Et}cAAC each in 5 ml of THF were cooled to -40°C, mixed and stirred 30 minutes at low temperature. After that, the mixture was allowed to slowly warm to room temperature for overnight, during which single-crystals suitable for X-ray diffraction analysis of **3** were formed. The supernatant was removed and the crystals were washed twice with 2 ml of THF and once with 2mLof *n*-pentane, and then vacuum dried to give white crystalline **3**. Yield: 125 mg (139 µmol, 71%).

^{1}H NMR (400 MHz, $CDCl_3$): δ [ppm] = 7.42 (t, $^3J(^1H,^1H)$ = 7.8 Hz, 2H, H^4, $C_6H_3{}^iPr_2$), 7.27 (d, $^3J(^1H,^1H)$ = 7.8 Hz, 4H, H^{3,5}, $C_6H_3{}^iPr_2$), 2.75 (sept, $^3J(^1H,1H)$ = 6.7 Hz), 4H, CH^{iPr}), 2.18 (m, 8H, -CH_2-), 1.99 (s, 4H), 1.41 (s, 12H, (CH_3)$_2$), 1.32 (d, $^3J(^1H,1H)$ = 6.7 Hz, 12H, C$H_3{}^{iPr}$), 1.26 (d, $^3J(^1H,1H)$ = 6.4 Hz, 12H, C$H_3{}^{iPr}$), 0.96 (t, $^3J(^1H,^1H)$ = 7.4 Hz, 12H).

^{13}C NMR (100 MHz, $CDCl_3$): δ [ppm] = 144.7, 133.7, 129.8, 125.3, 82.4, 65.2, 41.1, 30.4, 29.4, 29.0, 28.5, 26.5, 25.5, 24.1, 9.9.

[(^{Cy}cAAC)$_2$Zn$_2$Cl$_4$] (**4**)

Solutions of 41 mg (300 µmol) of $ZnCl_2$ and 100 mg (306 µmol) of ^{Cy}cAAC each in 5 ml of THF were cooled to -40°C, mixed and stirred 30 minutes at low temperature. After that, crystallization was induced by slow diffusion of *n*-pentane as anti-solvent leading to single-crystals suitable for X ray diffraction analysis. Precipitated product was collected, washed with 3 ml of *n*-pentane and vacuum dried to afford white crystals of **4**.

Yield: 100 mg (108 µmol, 70%).

^{1}H NMR (400 MHz, CD_3CN): δ [ppm] = 7.47 (t, $^{3}J(^{1}H,^{1}H)$ = 7.8 Hz, 1H, H^4, $C_6H_3{}^{i}Pr_2$), 7.39 (d, $^{3}J(^{1}H,^{1}H)$ = 7.8 Hz, 2H, $H^{3,5}$, $C_6H_3{}^{i}Pr_2$), 2.85 (sept, $^{3}J(^{1}H,1H)$ = 6.7 Hz), 2H, CH^{iPr}), 2.54 (m, 4H), 2.17 (s, 4H), 1.81-1.70 (m, 14H), 1.40 (s, 14H), 1.30 (d, $^{3}J(^{1}H,1H)$ = 6.7 Hz, 12H, $CH_3{}^{iPr}$), 1.29 (d, $^{3}J(^{1}H,1H)$ = 6.6 Hz, 12H, $CH_3{}^{iPr}$).

^{13}C NMR (100 MHz, CD_3CN): δ [ppm] = 146.6, 135.0, 131.0, 126.1, 83.6, 68.1, 66.2, 45.0, 35.4, 31.9, 29.8, 29.4, 26.6, 26.1, 26.0, 24.3, 22.3.

[(^{Et}cAAC)$ZnBr_2$(THF)] (**5**)

Compound 5 was prepared in a similar way as described for 4 but with 66 mg (293 µmol) of $ZnBr_2$ and 93 mg (293 µmol) of ^{Et}cAAC.

Yield: 91 mg (201 µmol, 68%).

^{1}H NMR (400 MHz, CD_3CN): δ [ppm] = 7.50 (t, $^{3}J(^{1}H,^{1}H)$ = 7.8 Hz, 1H, H^4, $C_6H_3{}^{i}Pr_2$), 7.41 (d, $^{3}J(^{1}H,^{1}H)$ = 7.8 Hz, 2H, $H^{3,5}$, $C_6H_3{}^{i}Pr_2$), 2.89 (sept, $^{3}J(^{1}H,1H)$ = 6.7 Hz), 2H, CH^{iPr}), 2.18-2.09 (m, 2H, -CH_2-), 2.06 (s, 2H), 2.0-1.97 (m, 2H), 1.41 (s, 6H, $(CH_3)_2$), 1.35 (d, $^{3}J(^{1}H,1H)$ = 6.7 Hz, 6H, $CH_3{}^{iPr}$), 1.31 (d, $^{3}J(^{1}H,1H)$ = 6.6 Hz, 6H, $CH_3{}^{iPr}$), 1.05 (t, $^{3}J(^{1}H,^{1}H)$ = 7.4 Hz, 6H).

^{13}C NMR (100 MHz, CD_3CN): δ [ppm] = 146.7, 135.3, 131.2, 126.3, 84.6, 66.3, 40.8, 31.9, 29.7, 27.2, 24.4, 10.7.

[(^{Me}cAAC)$_4Zn_4$(µ-Cl)$_6$] [BPh^{F}_4]$_2$ (**6**)

110 mg (120 µmol) of $Ph_3C[B(C_6F_5)_4]$ were dissolved in 3 ml of toluene and 0.2 ml of Et_3SiH was added and the mixture was stirred one hour at room temperature. After that, toluene and unreacted Et_3SiH were vacuum evaporated to dryness. The obtained solid residue was mixed with stochiometric amount of compound [(^{Me}cAAC)(Cl)Zn(µ-Cl)$_2$Zn(Cl)(^{Me}cAAC)] (**1**) (102 mg, 120 µmol) and 5 mL of toluene and stirred for 18

hours at room temperature. After that, solvent and Et_3SiCl were vacuum evaporated and off-white solid was dissolved in 5 mL of CH_2Cl_2 and the solution was filtered through celite. Slow gas phase diffusion of *n*-pentane into CH_2Cl_2 solution afforded colorless crystals, which were subsequently collected and washed two times with 5 mL of *n*-pentane. Yield: 126 mg (42 µmol, 70 %) of crystalline **6**.

CHNS analysis calcd for $C_{128}H_{124}N_4Zn_4Cl_6B_2F_{40}$ ·CH_2Cl_2: C, 50.6; H, 4.1; N, 1.8. Found: C, 51.0; H, 4.3; N, 2.0.

^{1}H NMR (400 MHz, CD_2Cl_2): δ [ppm] = 7.34 (t, $^{3}J(^{1}H,^{1}H)$ = 7.8 Hz, 4H, CH^{iPr}, 4H, H^4, $C_6H_3{}^{i}Pr_2$), 7.21 (d, $^{3}J(^{1}H,^{1}H)$ = 7.8 Hz, 8H, $H^{3,5}$, $C_6H_3{}^{i}Pr_2$), 2.52 (sept, $^{3}J(^{1}H,1H)$ = 6.7 Hz), 8H, CH^{iPr}), 2.06 (s, 8H, -CH_2-), 1.41 (s, 24H, $(CH_3)_2$), 1.29 (s, 24H, $(CH_3)_2$), 1.26 (d, $^{3}J(^{1}H,1H)$ = 6.7 Hz, 24H, $CH_3{}^{iPr}$), 1.03 (d, $^{3}J(^{1}H,1H)$ = 6.7 Hz, 24H, $CH_3{}^{iPr}$).

^{13}C NMR (100 MHz, CD_2Cl_2): δ [ppm] = 238.7 (s, 4C, $C^{carbene}$), 145.06 (s, 8C, $C^{2,6}$, Dipp), 133.44 (s, 4C, C^1, Dipp), 130.83 (s, 4C, C^4, Dipp), 126.13 (s, 8C, $C^{3,5}$, Dipp), 84.5 (s, 4C, $NC(CH_3)_2$), 55.7 (s, 4C, $C(CH_3)_2C^{carbene}$), 50.02 (s, 4C, -CH_2-), 29.31 (s, 8C, *C*H, Dipp), 29.14 (s, 8C, $C(CH_3)_2C^{carbene}$), 28.04 (s, 8C, $NC(CH_3)_2$), 26.35(s, 8C, CH_3, Dipp), 24.36(s, 8,C, CH_3, Dipp).

^{19}F (376 MHz, CD_2Cl_2): δ [ppm] = -132.9 (m, 16F, $F^{2,6}$), -163.7 (m, 8H, F^4), -167.5 (m, 16F, $F^{3,5}$).

[(^{Me}cAAC)$_4Zn_4$(µ-Br)$_6$] [BPh^{F}_4]$_2$ (**7**)

Compound **7** was prepared in similar manner as described for **6** but with 123 mg (120 µmol) of compound [(^{Me}cAAC)(Br)Zn(µ-Br)$_2$Zn(Cl)(^{Me}cAAC)] (**2**). Yield: 351 mg (290 µmol, 79 %). Yield: 149 mg (46 µmol, 77 %) of colorless crystalline **7**. Single crystals suitable for X-ray diffraction analysis were prepared by gas-phase diffusion of *n*-pentane into solution of **7** in DCM.

CHNS analysis calcd for $C_{128}H_{124}N_4Zn_4Br_8B_2F_{40}$: C, 47.4; H, 3.9; N, 1.7. Found: C, 47.3; H, 3.9; N, 1.6.

^{1}H NMR (400 MHz, CD_2Cl_2): δ [ppm] = 7.37 (t, $^3J(^1H,^1H)$ = 7.8 Hz, 4H, C*H*^{iPr}, 4H, H^4, $C_6H_3{}^iPr_2$), 7.22 (d, $^3J(^1H,^1H)$ = 7.8 Hz, 8H, H^{3,5}, $C_6H_3{}^iPr_2$), 2.54 (sept, $^3J(^1H,1H)$ = 6.7 Hz), 8H, C*H*^{iPr}), 2.07 (s, 8H, -CH_2-), 1.42 (s, 24H, (CH_3)$_2$), 1.30 (s, 24H, (CH_3)$_2$), 1.28 (d, $^3J(^1H,1H)$ = 6.7 Hz, 24H, C$H_3{}^{iPr}$), 1.04 (d, $^3J(^1H,1H)$ = 6.7 Hz, 24H, C$H_3{}^{iPr}$).

^{13}C NMR (100 MHz, CD_2Cl_2): δ [ppm] = 238.7 (s, 4C, $C^{carbene}$), 145.0 (s, 8C, C^{2,6}, Dipp), 133.4 (s, 4C, C^1, Dipp), 130.8 (s, 4C, C^4, Dipp), 126.1 (s, 8C, C^{3,5}, Dipp), 84.4 (s, 4C, NC(CH$_3$)$_2$), 55.6 (s, 4C, C(CH$_3$)$_2$C^{carbene}), 50.0 (s, 4C, -CH_2-), 29.2 (s, 8C, CH, Dipp), 29.1 (s, 8C, C(CH$_3$)$_2$C^{carbene}), 28.0 (s, 8C, NC(CH$_3$)$_2$), 26.3 (s, 8C, CH$_3$, Dipp), 24.3 (s, 8,C, CH$_3$, Dipp).

^{19}F (376 MHz, CD_2Cl_2): δ [ppm] = -132.9 (m, 16F, F^{2,6}), -163.7 (m, 8H, F^4), -167.5 (m, 16F, F^{3,5}).

[(^{Et}cAAC)$_4$Zn$_2$(μ-Cl)$_6$] [BPh$^F{}_4$]$_2$ **(8)**

Compound **8** was prepared in similar way as described for **6** but with 100 mg (111 μmol) of compound [(^{Et}cAAC)(Cl)Zn(μ-Cl)$_2$Zn(Cl)(^{Et}cAAC)] (**3**) .

Yield: 101 mg (32 μmol, 59 %) of colourless microcrystalline **8**.

CHNS analysis calcd for $C_{136}H_{140}N_4Zn_4Cl_6B_2F_{40}$: C, 52.9; H ,4.6; N, 1.8. Found: C, 52.8; H, 4.8; N, 1.9.

^{1}H NMR (400 MHz, CD_2Cl_2): δ [ppm] = 7.39 (t, $^3J(^1H,^1H)$ = 7.8 Hz, 4H, C*H*^{iPr}, 4H, H^4, $C_6H_3{}^iPr_2$), 7.24 (d, $^3J(^1H,^1H)$ = 7.8 Hz, 8H, H^{3,5}, $C_6H_3{}^iPr_2$), 2.59 (sept, $^3J(^1H,1H)$ = 6.7 Hz), 8H, C*H*^{iPr}), 2.05 (s, 8H, -CH_2-), 1.76 (m, 8H) , 1.42 (d, $^3J(^1H,1H)$ = 2.51 Hz, 32H), 1.28 (d, $^3J(^1H,1H)$ = 6.61 Hz, 24H), 1.04 (d, $^3J(^1H,1H)$ = 6.45 Hz, 24H, C$H_3{}^{iPr}$), 0.93 (t, $^3J(^1H,1H)$ = 7.35 Hz, 24H, CH_2CH_3).

^{13}C NMR (100 MHz, CD_2Cl_2): δ [ppm] = 239.74 (s, $C^{carbene}$), 145.03 (s, C^{2,6}, Dipp), 133.69 (s, C^1, Dipp), 130.89 (s, C^4, Dipp), 126.02 (s, C^{3,5}, Dipp), 85.04 (s, NC(CH$_3$)$_2$),65.28 (s), 40.23 (s), 30.66, 29.71 (s), 29.32 (s, 8C), 27.29, 26.48 (s, CH$_3$, Dipp), 24.20 (s, CH$_3$, Dipp), 10.44(s).

^{19}F (376 MHz, CD_2Cl_2): δ [ppm] = -132.9 (m, 16F, F^{2,6}), -163.7 (m, 8H, F^4), -167.5 (m, 16F, F^{3,5}).

[(^{Et}cAAC)$_4$Zn$_2$(μ-Cl)$_6$] [BPh$^F{}_4$]$_2$ **(9)**

Compound **9** was prepared in similar way as described for **6** but with 60 mg (133 μmol) of compound [(^{Et}cAAC)ZnBr$_2$(THF)] (**5**). Slow gas phase diffusion of *n*-pentane into CH_2Cl_2 solution afforded colorless crystals of **9**, suitable for X-ray diffraction. However, very low yield of **9** hindered any further chracterisation.

[(^{Cy}cAAC)$_4$Zn$_4$(μ-Cl)$_6$] [BPh$^F{}_4$]$_2$ **(10)**

Compound **10** was prepared in similar way as described for **6** but with 100 mg (128 μmol) of compound [(^{Cy}cAAC)(Cl)Zn(μ-Cl)$_2$Zn(Cl)(^{Cy}cAAC)]**.**

Yield: 139 mg (44 μmol, 82 %) of colorless microcrystalline **10**.

CHNS analysis calcd for $C_{140}H_{140}N_4Zn_4Cl_6B_2F_{40}$: C, 53.65; H ,4.50; N, 1.79. Found: C, 53.9; H, 4.7; N, 1.8.

^{1}H NMR (400 MHz, CD2Cl2): δ [ppm] = 7.37 (t, $^3J(^1H,^1H)$ = 7.8 Hz, 4H, C*H*^{iPr}, 4H, H^4, $C_6H_3{}^iPr_2$), 7.21 (d, $^3J(^1H,^1H)$ = 7.8 Hz, 8H, H^{3,5}, $C_6H_3{}^iPr_2$), 2.56 (sept, $^3J(^1H,^1H)$ = 6.7 Hz), 8H, C*H*^{iPr}), 2.15 (s, 8H, -CH_2-), 1.81 (m, 18H), 1.43 (s, 34H), 1.28 (d, 32H, $^3J(^1H,^1H)$= 6.6 Hz), 1.06 (d, $^3J(^1H,^1H)$ = 5.07 Hz, 20H), 0.87 (t, $^3J(^1H,^1H)$ = 7.08 Hz, 8H).

^{13}C NMR (100 MHz, CD_2Cl_2): δ [ppm] = 238.7 (s, 4C, $C^{carbene}$), 145.1 (s, 8C, $C^{2,6}$, Dipp), 133.71 (s, 4C, C^1, Dipp), 130.63 (s, 4C, C^4, Dipp), 126.10 (s, 8C, $C^{3,5}$, Dipp), 84.08 (s, 4C, $NC(CH_3)_2$), 61.34 (s), 44.87, 34.51, , 29.11 (s), 26.42 (s), 25.44, 22.73 (s), 22.7 (s), 21.87 (s), 14.21(s).

^{19}F (376 MHz, CD_2Cl_2): δ [ppm] = -133.07 (m, 16F, $F^{2,6}$), -163.80 (m, 8H, F^4), -167.60(m, 16F, $F^{3,5}$).

[(^{Me}cAAC)Zn(acac')(Cl)] (**11**)

185 mg (0.22 mmol) of [(^{Me}cAAC)$_2$Zn$_2$(Cl)$_4$] (**1**) and 55 mg (0.45 mmol) of sodium acetylacetonate were taken in a vial in the glovebox. 5 ml of THF was added and stirred overnight. The reaction mixture was filtered using celite and was recrystallized from gas phase diffusion of n-Pentane into THF solution to obtain white crystals of **11**. The crystals were collected and washed with 3 ml of *n*-pentane and vacuum dried. Yield: 112mg (230 mmol, 52%).

CHNS analysis calcd for **5**: C, 61.9; H ,7.9; N, 2.9. Found: C, 61.7; H, 8.1; N, 3.0. ^{1}H NMR (400 MHz, CD_3CN): δ [ppm] = 7.41 (t, $^3J(^1H,^1H)$ = 7.8 Hz, 1H, H^4, $C_6H_3{}^iPr_2$), 7.31 (d, $^3J(^1H,^1H)$ = 7.8 Hz, 2H, $H^{3,5}$, $C_6H_3{}^iPr_2$), 5.14 (s, 1H, $CH(COMe)_2$), 2.80 (sept, $^3J(^1H,1H)$ = 6.7 Hz), 2H, CH^{iPr}), 2.11 (s, 2H, -CH_2-), 1.61 (s, 6H, $COCH_3$), 1.55 (s, 6H, $(CH_3)_2$), 1.41 (s, 6H, $(CH_3)_2$), 1.29 (d, $^3J(^1H,1H)$ = 6.7 Hz, 6H, $CH_3{}^{iPr}$), 1.14 (d, $^3J(^1H,1H)$ = 6.7 Hz, 6H, $CH_3{}^{iPr}$).

^{13}C NMR (100 MHz, CD_3CN): δ [ppm] = 246.9 (s, $C^{carbene}$), 192.36 (s, $COCH_3$), 146.11 (s, $C^{2,6}$, Dipp), 134.92 (s, C^1, Dipp), 130.57 (s, C^4, Dipp), 125.92 (s, $C^{3,5}$, Dipp), 99.75 (s,1H, $CH(COMe)_2$), 84.59 (s, $NC(CH_3)_2$), 56.13 (s, $C(CH_3)_2C^{carbene}$), 50.06 (s, -CH_2-), 29.61 (s, CH, Dipp), 29.37 (s, $C(CH_3)_2C^{carbene}$), 27.92 (s, $NC(CH_3)_2$), 27.85 (s, $COCH_3$) 25.96 (s, CH_3, Dipp), 24.09 (s, CH_3, Dipp).

[(^{Me}cAAC)Zn(cbz)(THF)(Cl)] (**12**)

Compound **12** was prepared in similar way as described for **11** but with 100 mg (119 µmol) of compound [(^{Me}cAAC)$_2$Zn$_2$(Cl)$_4$] with 52 mg (255 µmol) of Potassium carbazolate.. Single crystals suitable for X-ray diffraction analysis were prepared by gas-phase diffusion of *n*-pentane into solution of **12** in THF.

Yield: 112 mg (179 µmol, 75%)

CHNS analysis calcd for $C_{36}H_{47}N_2OZnCl$: C, 69.2; H ,7.6; N, 4.5. Found: C, 68.9; H, 7.8; N, 4.0.

^{1}H NMR (400 MHz, THF-d_8): δ [ppm] = 7.90 (t, $^3J(^1H,^1H)$ = 8.6 Hz, 4H), 7.46 (m, 3H), 7.11 (t, $^3J(^1H,^1H$= 7.5Hz, 2H) 6.86 (t, $^3J(^1H,^1H)$ = 7.2 Hz, 2H), 3.13 (sept, $^3J(^1H,^1H)$ = 6.7 Hz), 2H, CH^{iPr}), 2.07 (s, 2H, -CH_2-), 1.51 (d, $^3J(^1H,1H)$ = 6.9 Hz, 12H), 1.42 (d, $^3J(^1H,^1H)$ = 6.53 Hz, 6H), 1.35 (s, 6H).

^{13}C NMR (100 MHz, THF-d_8): δ [ppm] = 150.17, 146.93, 130.58, 126.60, 125.69, 123.37, 119.38, 115.86, 115.51, 84.72, 57.83, 50.98, 29.70, 28.58, 27.38, 26.19, 25.62.

5 NMR Spectra

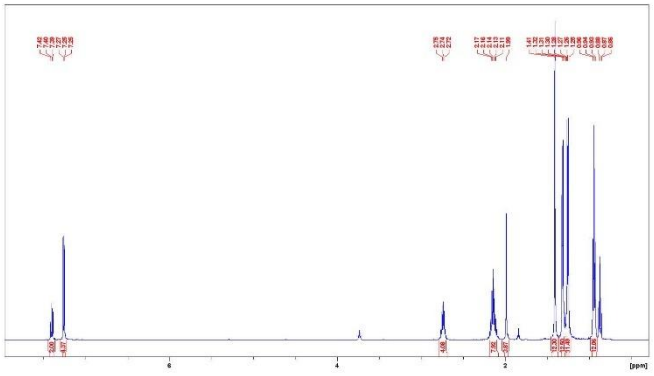


Figure S1. ^{1}H NMR spectrum of **3** in $CDCl_3$.

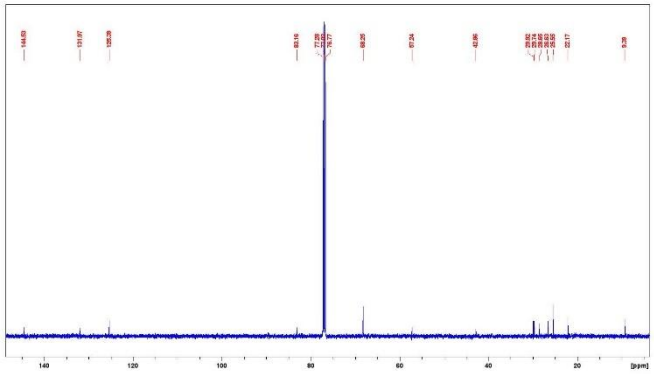


Figure S2. ^{13}C NMR spectrum of **3** in $CDCl_3$.

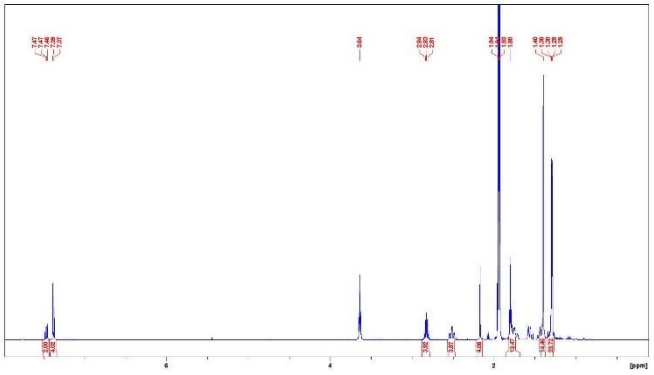


Figure S3. ^{1}H NMR spectrum of **4** in CD_3CN.

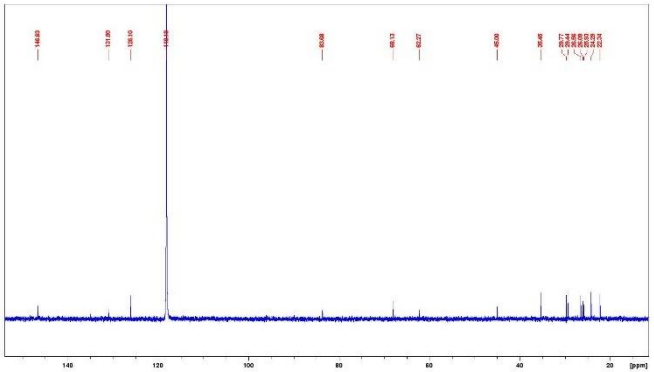


Figure S4. ^{13}C NMR spectrum of **4** in CD_3CN.

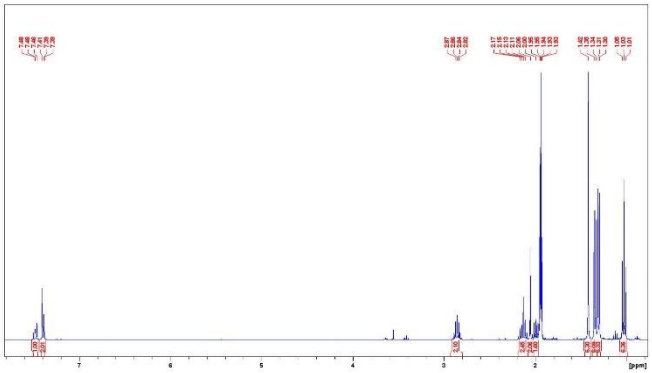


Figure S5. ^{1}H NMR spectrum of **5** in CD_3CN.

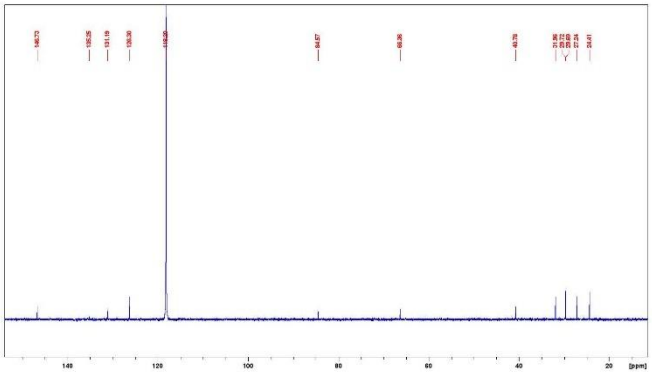


Figure S6. ^{13}C NMR spectrum of **5** in CD_3CN.

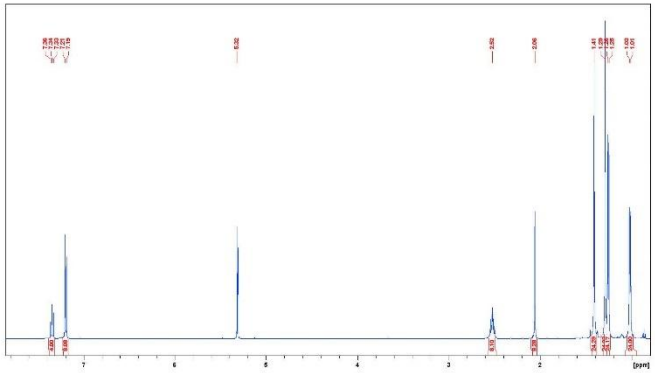


Figure S7. ^{1}H NMR spectrum of **6** in DCM-d_2.

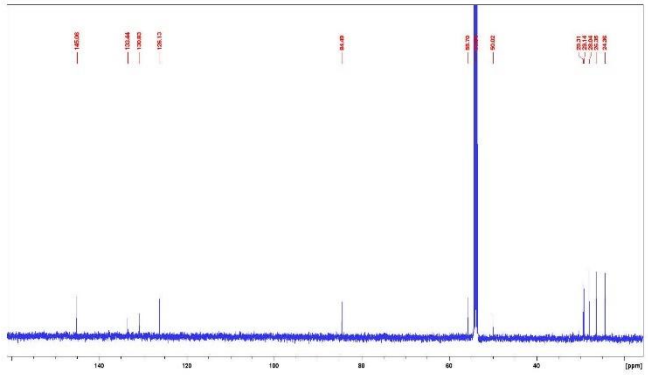


Figure S8. ^{13}C NMR spectrum of **6** in DCM-d_2.

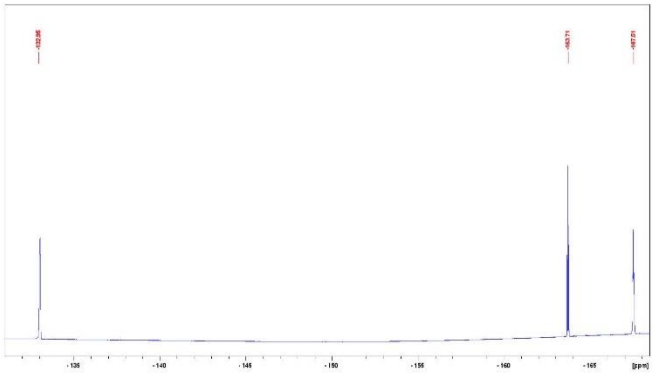


Figure S9. ^{19}F NMR spectrum of **6** in DCM-d_2.

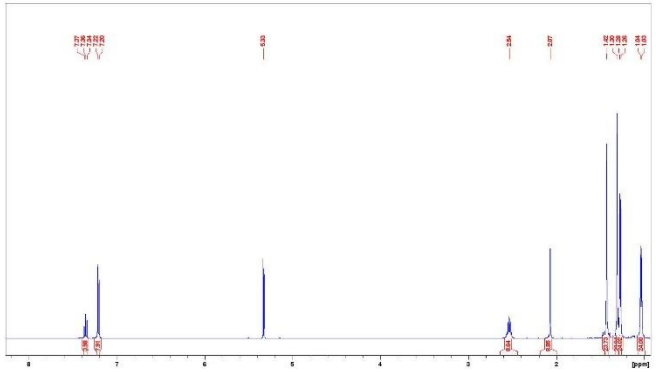


Figure S10. ^{1}H NMR spectrum of **7** in DCM-d_2.

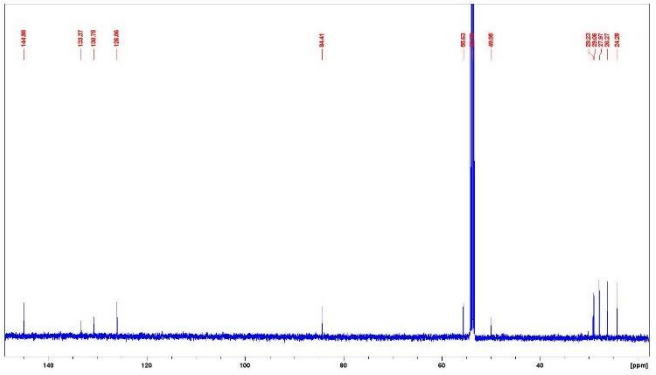


Figure S11. ^{13}C NMR spectrum of **7** in DCM-d_2.

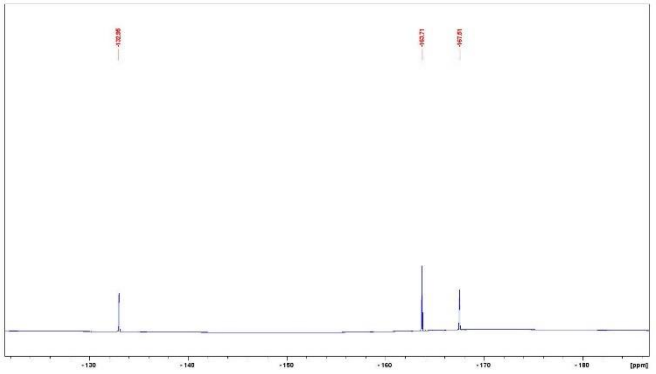


Figure S12. ^{19}F NMR spectrum of **7** in DCM-d_2.

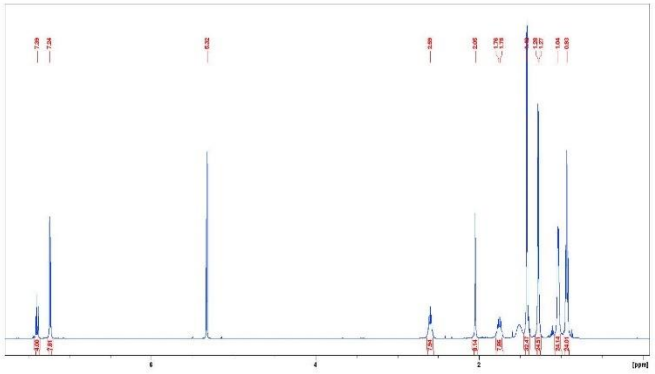


Figure S13. ^{1}H NMR spectrum of **8** in DCM-d_2.

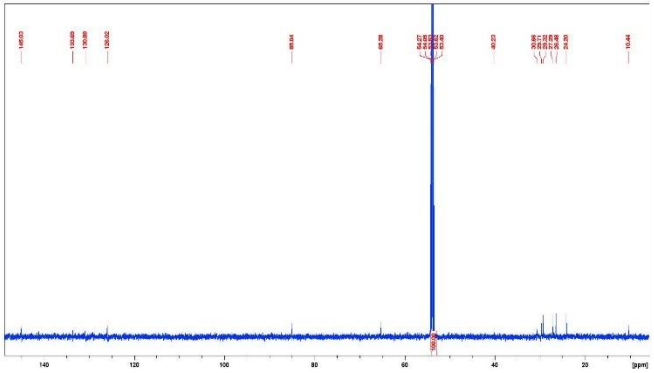


Figure S14. ^{13}C NMR spectrum of **8** in DCM-d_2.

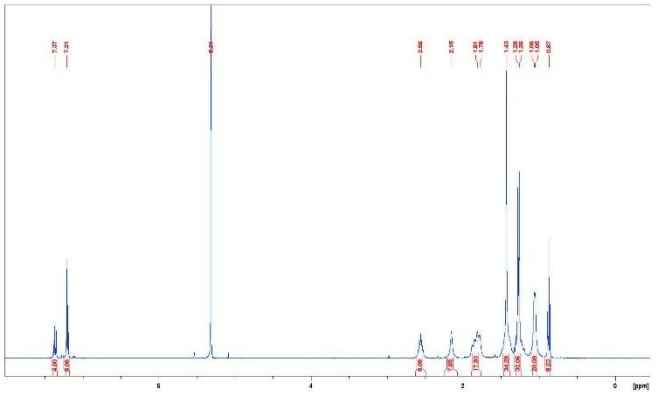


Figure S15. ^{19}F NMR spectrum of **8** in DCM-d_2.

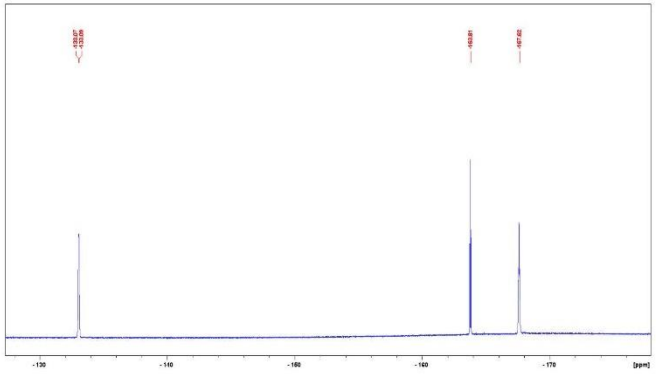


Figure S16. ^{1}H NMR spectrum of **10** in DCM-d_2.

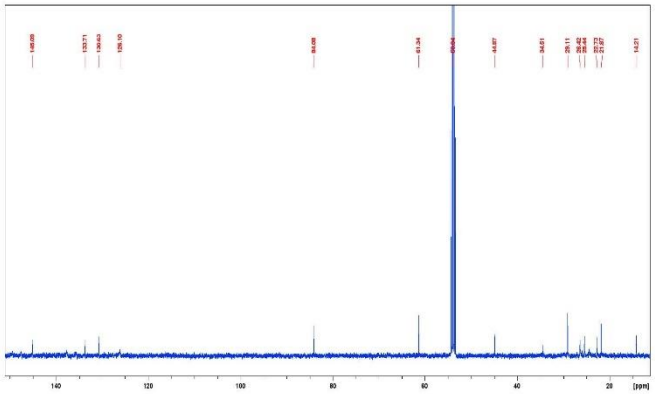


Figure S17. ^{13}C NMR spectrum of **10** in DCM-d_2.

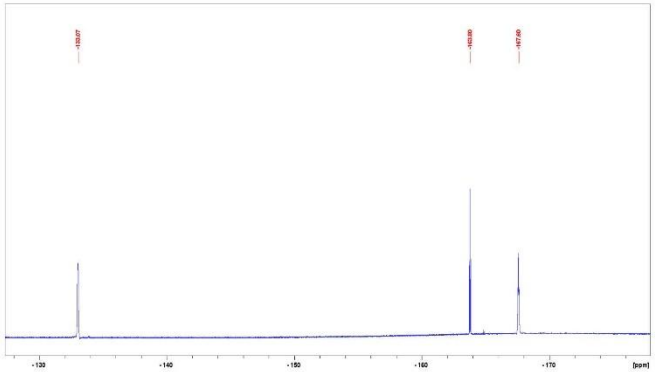


Figure S18. ^{19}F NMR spectrum of **10** in DCM-d_2.

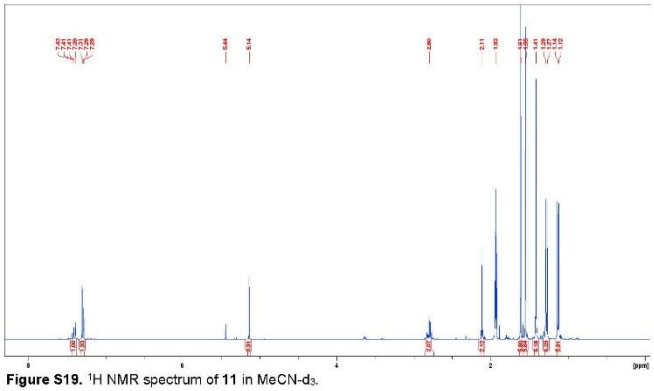


Figure S19. ^{1}H NMR spectrum of **11** in MeCN-d_3.

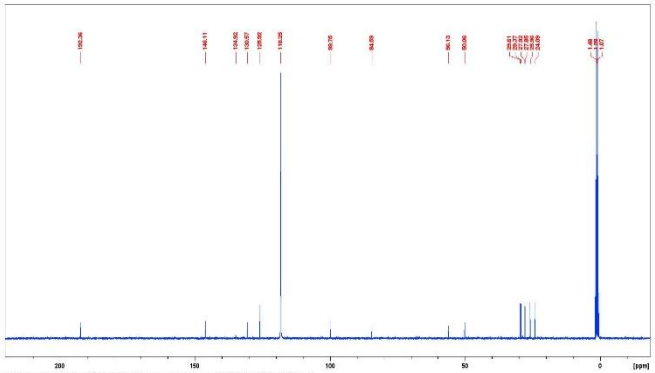


Figure S20. ^{13}C NMR spectrum of **11** in MeCN-d_3.

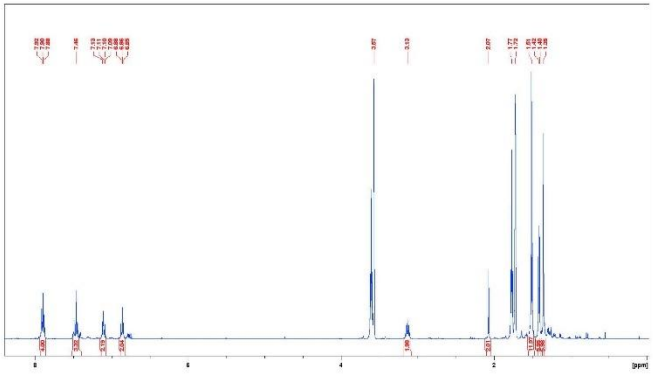


Figure S21. ^{1}H NMR spectrum of **12** in THF-d_8.

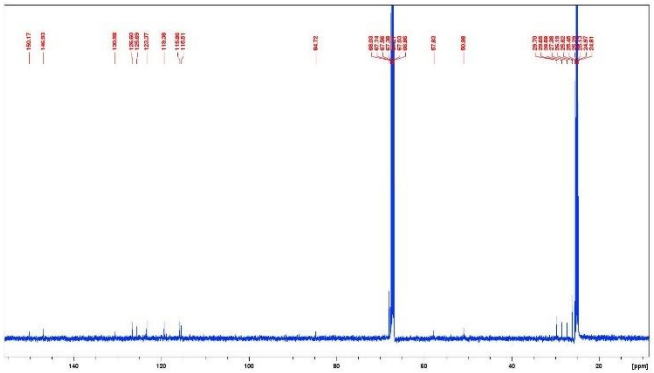


Figure S22. ^{13}C NMR spectrum of **12** in THF-d_8.

6 Mass Spectrometry

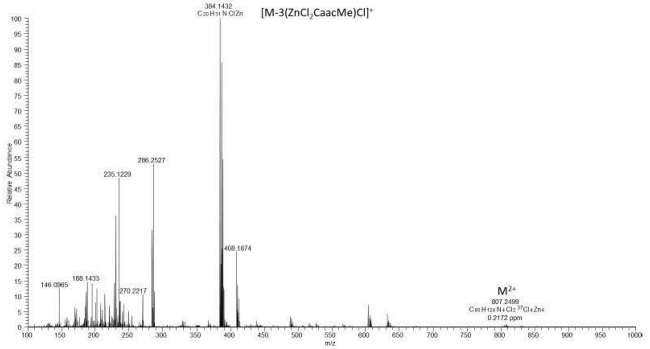


Figure S23. MS spectrum of **6**.

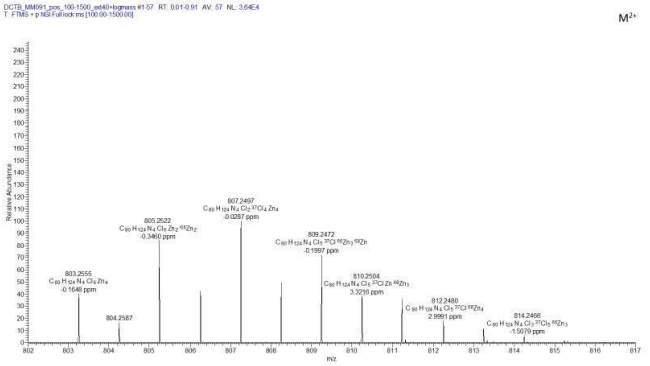


Figure S24. Details of MS spectrum of **6**.

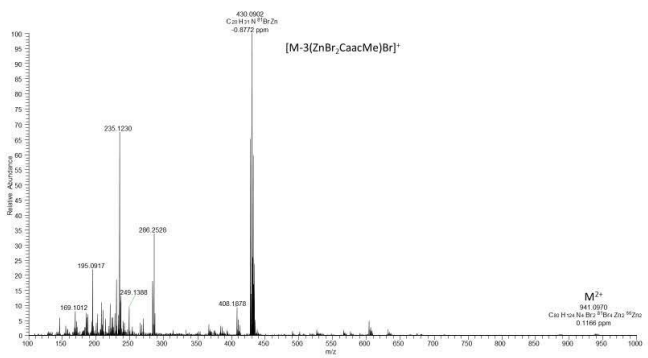


Figure S25. MS spectrum of **7**.

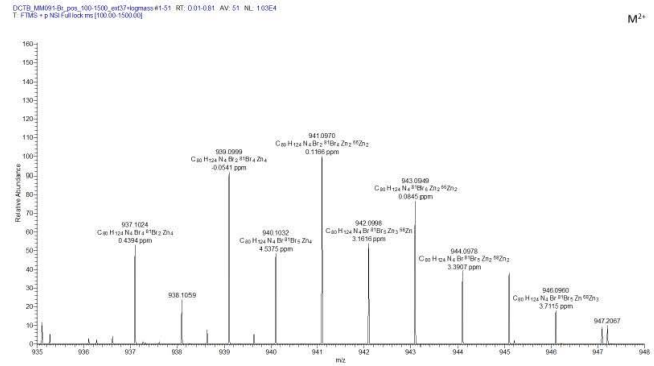


Figure S26. Details of MS spectrum of **7**.

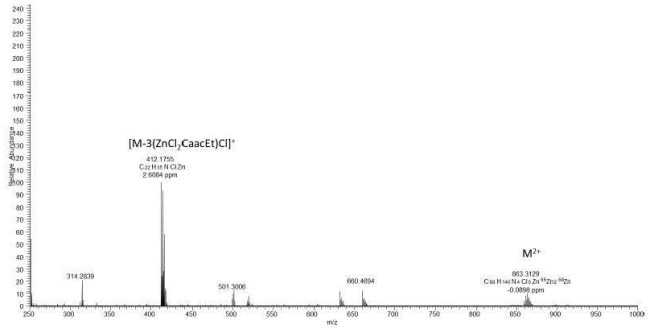


Figure S27. MS spectrum of **8**.

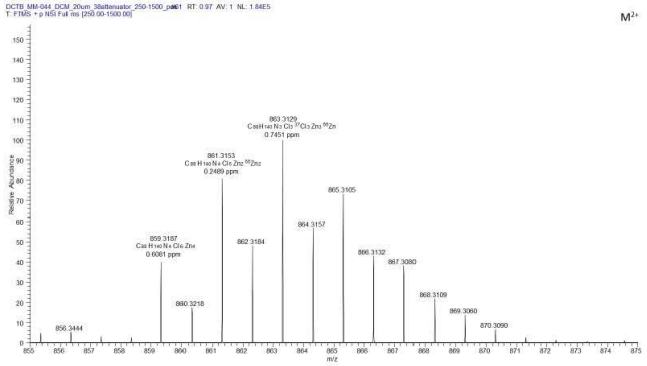


Figure S28. Details of MS spectrum of **8**.

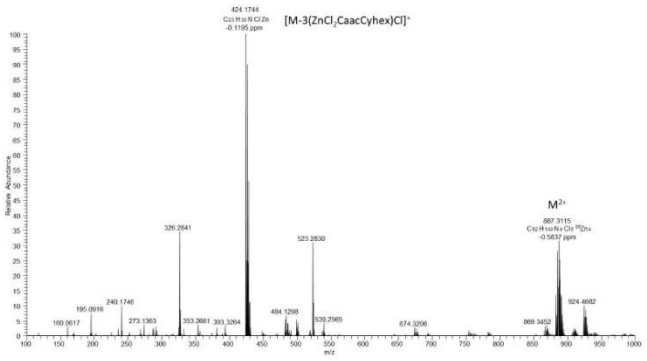


Figure S29. MS spectrum of **10**.

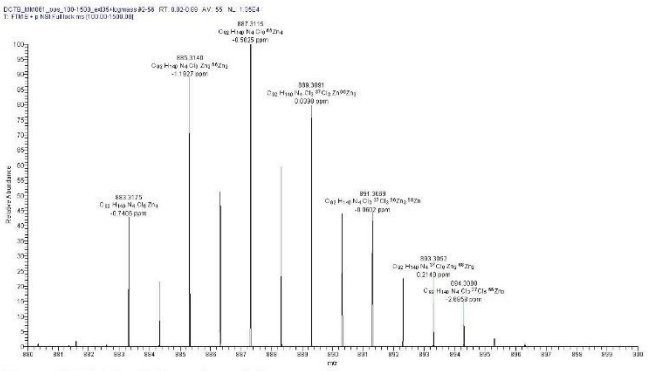


Figure S30. Details of MS spectrum of **10**.

7 X-Ray Crystallography

The crystals of **3–12** were immersed in a film of NVH or perfluoropolyether oil, mounted on a polyimide microloop (MiTeGen) and transferred to a stream of cold nitrogen (Bruker Kryoflex2), and measured at a temperature of 100 K. The X-ray diffraction data were collected on a Bruker D8 diffractometer with a CMOS Photon 100 and multilayer optics monochromated MoKα (0.71073Å) radiation (INCOATEC microfocus sealed tube). The frames were integrated with the Bruker SAINT software package using a narrow-frame algorithm. The APEX3 v2018.7-0 program package was used for cell refinements and data reductions. The structure was solved using the intrinsic phasing method,[10, 11] refined and visualized with the OLEX2-1.5 program.[12] A semiempirical absorption correction (SADABS) was applied to all data. All non-hydrogen atoms were refined anisotropically. Hydrogen atoms were included in structure factors calculations. All Hydrogen atoms were assigned to idealized geometric positions. The unit cells of the **6, 7, 9**, and **12** contain disordered solvent molecules which have been treated as a diffuse contribution to the overall scattering without specific atom positions by SQUEEZE/PLATON.[13] The crystallographic details are summarized in Tables 1 and 2. CCDC **XXXXXXX–XXXXXXX** numbers contain the supplementary crystallographic data for this paper.

Table S1. Crystal data and structure refinement for **3–7**.

Identification code	**3**	**4**	**5**	**6**	**7**
CCDC number					
Empirical formula	$C_{44}H_{70}Cl_4N_2Zn_2$	$C_{23}H_{35}Cl_2NZn$	$C_{26}H_{43}Br_2NOZn$	$C_{128}H_{124}B_2Cl_6F_{40}N_4Zn_4$	$C_{128}H_{124}B_2Br_6F_{40}N_4Zn_4$
Formula weight	899.56	461.79	610.80	2974.10	3240.86
Temperature [K]	100.00	100.00	100.00	100.00	100.00
Crystal system	triclinic	triclinic	monoclinic	monoclinic	monoclinic
Space group	P-1	P-1	$P2_1/n$	C2/c	C2/c
a [Å] b [Å] c [Å] α [°] β [°] γ [°]	9.6079(2) 10.8332(3) 11.6499(3) 85.6490(10) 71.7360(10) 74.3470(10)	9.2141(15) 9.3711(18) 13.198(2) 98.071(7) 90.623(7) 91.769(7)	14.6733(9) 11.6822(7) 16.1462(8) 90 102.661(2) 90	32.9419(8) 14.0164(3) 31.9005(8) 90 112.7360(10) 90	32.9862(12) 14.0098(6) 32.2452(13) 90 112.3930(10) 90
Volume [Å³]	1108.73(5)	1127.6(3)	2700.4(3)	13584.8(6)	13777.8(10)
Z	1	2	4	4	4
ρ_{calc} [g/cm³]	1.347	1.360	1.502	1.454	1.562
μ [mm⁻¹]	1.355	1.334	3.886	0.919	2.530
F(000)	476.0	488.0	1256.0	6048.0	6480.0
Crystal size [mm³]	0.08 × 0.06 × 0.03	0.12 × 0.055 × 0.037	0.29 × 0.27 × 0.2	0.111 × 0.067 × 0.034	0.247 × 0.242 × 0.191
Radiation type	MoKα (λ = 0.71073)	MoKα (λ = 0.71073)	MoKα (λ = 0.71073)	MoKα (λ = 0.71073)	MoKα (λ = 0.71073)
2Θ range for data collection [°]	5.394 to 54.994	4.392 to 54	5.492 to 57.06	4.716 to 52	4.526 to 55
Index ranges	-12 ≤ h ≤ 12, -14 ≤ k ≤ 13, -15 ≤ l ≤ 14	-11 ≤ h ≤ 11, -11 ≤ k ≤ 11, -16 ≤ l ≤ 16	-19 ≤ h ≤ 19, -15 ≤ k ≤ 15, -20 ≤ l ≤ 21	-40 ≤ h ≤ 40, -17 ≤ k ≤ 17, -39 ≤ l ≤ 39	-42 ≤ h ≤ 42, -18 ≤ k ≤ 18, -41 ≤ l ≤ 41
Reflections collected	25546	24504	49516	55038	80860
Independent reflections	5073 [R_{int} = 0.0198, R_{sigma} = 0.0148]	4852 [R_{int} = 0.1125, R_{sigma} = 0.0771]	6818 [R_{int} = 0.0708, R_{sigma} = 0.0377]	13304 [R_{int} = 0.0331, R_{sigma} = 0.0294]	15811 [R_{int} = 0.0401, R_{sigma} = 0.0313]
Data/restraints/parameters	5073/0/243	4852/0/250	6818/0/288	13304/0/846	15811/0/840
Goodness-of-fit on F² [a]	1.045	1.165	1.046	1.038	1.039
Final R indexes [I>=2σ (I)] [b]	R_1 = 0.0181, wR_2 = 0.0463	R_1 = 0.1056, wR_2 = 0.2858	R_1 = 0.0229, wR_2 = 0.0563	R_1 = 0.0335, wR_2 = 0.0882	R_1 = 0.0307, wR_2 = 0.0775
Final R indexes [all data] [b]	R_1 = 0.0188, wR_2 = 0.0467	R_1 = 0.1192, wR_2 = 0.2940	R_1 = 0.0282, wR_2 = 0.0577	R_1 = 0.0403, wR_2 = 0.0918	R_1 = 0.0391, wR_2 = 0.0812
Largest diff. peak/hole [e/Å⁻³]	0.40/-0.19	3.10/-1.23	0.89/-0.51	0.93/-0.43	1.61/-0.73

[a] GooF = S = $[[\sum w(F_o^2-F_c^2)^2]/(m-n)]^{1/2}$, where m = number of reflexes and n = number of parameters; [b] $R_1 = \sum||F_o|-|F_c||/\sum|F_o|$; $wR_2 = [\sum[w(F_o^2-F_c^2)^2/\sum[(wF_o^2)^2]]^{1/2}$; $w = 1/[\sigma^2(F_o^2)+(aP)^2+bP]$, where $P = (F_o^2+2F_c^2)/3$

Table S2. Crystal data and structure refinement for **9**, **11** and **12**.

Identification code	**9**	**11**	**12**
CCDC number			
Empirical formula	$C_{272}H_{278}B_4Br_{12}F_{80}N_8Zn_8$	$C_{25}H_{38}ClNO_2Zn$	$C_{36}H_{47}ClN_2OZn$
Formula weight	6704.13	485.38	624.57
Temperature [K]	100.00	100.00	100.00
Crystal system	orthorhombic	monoclinic	triclinic
Space group	Pbca	$P2_1/n$	P-1
a [Å] b [Å] c [Å] α [°] β [°] γ [°]	20.4042(6) 29.9585(6) 47.0638(12) 90 90 90	9.1146(3) 16.5666(6) 16.9064(6) 90 102.219(2) 90	9.7009(3) 11.0231(4) 17.5518(6) 90.0220(10) 98.1470(10) 95.8310(10)
Volume [Å³]	28769.1(13)	2495.00(15)	1848.12(11)
Z	4	4	2
ρ_{calc} [g/cm³]	1.548	1.292	1.122
μ [mm⁻¹]	2.426	1.112	0.763
F(000)	13464.0	1032.0	664.0
Crystal size [mm³]	0.078 × 0.032 × 0.011	0.101 × 0.089 × 0.077	0.22 × 0.14 × 0.12
Radiation type	MoKα (λ = 0.71073)	MoKα (λ = 0.71073)	MoKα (λ = 0.71073)
2Θ range for data collection [°]	3.992 to 55	4.93 to 52.998	5.626 to 53
Index ranges	-26 ≤ h ≤ 15, -38 ≤ k ≤ 38, -61 ≤ l ≤ 61	-11 ≤ h ≤ 11, -20 ≤ k ≤ 20, -21 ≤ l ≤ 21	-12 ≤ h ≤ 11, -13 ≤ k ≤ 13, -22 ≤ l ≤ 22
Reflections collected	240405	35283	41882
Independent reflections	33012 [R_{int} = 0.0777, R_{sigma} = 0.0518]	5166 [R_{int} = 0.0513, R_{sigma} = 0.0318]	7650 [R_{int} = 0.0460, R_{sigma} = 0.0307]
Data/restraints/parameters	33012/24/1755	5166/0/281	7650/0/378
Goodness-of-fit on F² [a]	1.034	1.045	1.058
Final R indexes [I>=2σ (I)] [b]	R_1 = 0.0551, wR_2 = 0.1417	R_1 = 0.0272, wR_2 = 0.0635	R_1 = 0.0313, wR_2 = 0.0776
Final R indexes [all data] [b]	R_1 = 0.0858, wR_2 = 0.1577	R_1 = 0.0334, wR_2 = 0.0662	R_1 = 0.0372, wR_2 = 0.0802
Largest diff. peak/hole [e/Å⁻³]	2.69/-1.63	0.33/-0.25	0.47/-0.34

[a] GooF = S = $[[\sum w(F_o^2-F_c^2)^2]/(m-n)]^{1/2}$, where m = number of reflexes and n = number of parameters; [b] $R_1 = \sum||F_o|-|F_c||/\sum|F_o|$; $wR_2 = [\sum[w(F_o^2-F_c^2)^2/\sum[(wF_o^2)^2]]^{1/2}$; $w = 1/[\sigma^2(F_o^2)+(aP)^2+bP]$, where $P = (F_o^2+2F_c^2)/3$

8 Photophysical Measurements

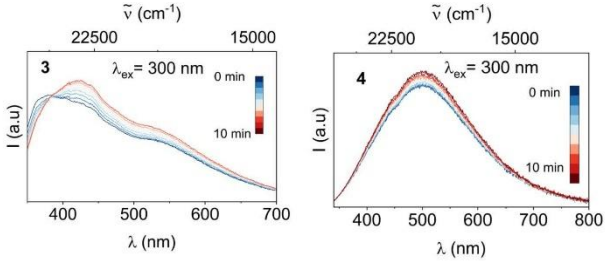


Figure S31. Multiple emission spectra of **3** and **4** in solid state at 297 K.

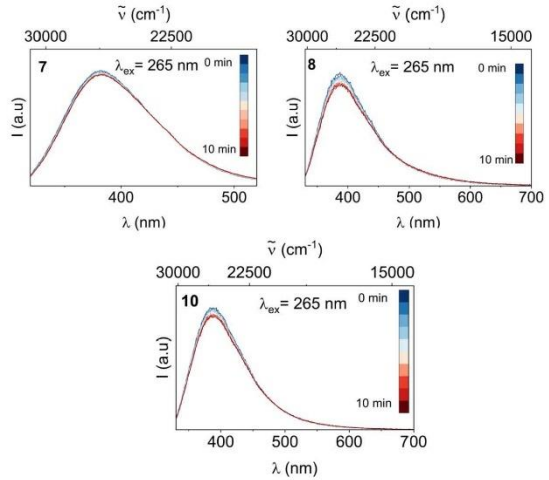


Figure S32. Multiple emission spectra of **7-10** in solid state at 297 K.

Table S3: Lifetimes of the decay channels with the significance of their respective contribution to the decay of emission of 6-10 in solid state at 77K.

Sample	λ_{max}/ nm	t_1[µs]	B_1	t_2[µs]	B_2	t_3[µs]	B_3	t_4[µs]	B_4	[χ^2]	t_{exp}[µs]
6	385	55.1	0.7	394.8	0.3	-	-	-	-	1.105	155.7
7	400	1146.2	0.38	3015.2	0.47	10038	0.15	-	-	1.102	3323
8	385	10.0	0.97	95.7	0.03	-	-	-	-	1.079	14.4
	500	29.8	0.14	223.7	0.49	507.5	0.37	-	-	1.143	301.8
10	385	13.28	0.36	61.5	0.38	243.8	0.18	1317.3	0.08	1.076	180.7
11	480	$5.05 \cdot 10^3$	0.03	$22.30 \cdot 10^3$	0.18	$79.47 \cdot 10^3$	0.79	-	-	1.087	$42.1 \cdot 10^3$
12	580	9.7	0.86	109.1	0.12	972.0	0.02	-	-	1.220	41.47

9 Computational studies

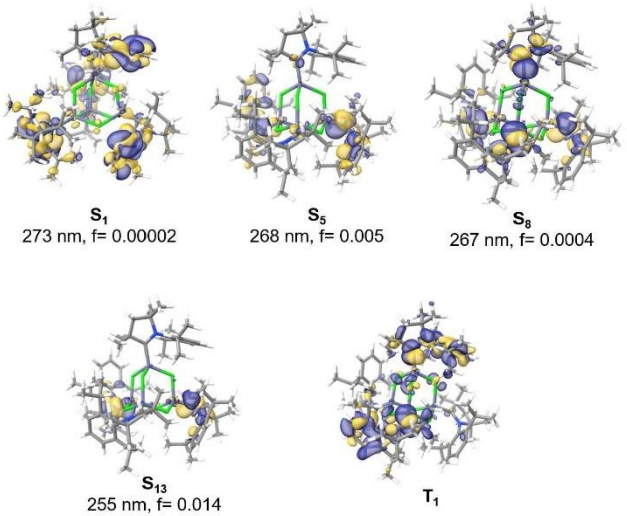


Figure S33: selected electron density differences in triplet states of **6** in DCM calculated at the D3(BJ)-PBE0/ZORA/def2-SVP level of theory. Loss of electron density is indicated in blue and gain in yellow.

Table S4: XYZ coordinates of optimized molecule **6**.

Zn	5.251649	10.321224	22.185194
Zn	7.343400	13.096063	24.038917
Cl	7.223596	9.060743	22.065811
Cl	5.424924	11.802170	23.967671
Cl	5.322526	11.615479	20.266998
Cl	7.224413	14.355422	22.066009
N	2.767603	8.816151	21.664398
N	6.822515	14.601242	26.522784
C	3.712609	9.081977	22.517279
C	5.539665	13.928133	26.642204
C	7.296510	15.647517	27.552873
C	7.675293	14.335633	25.577639
C	2.647954	9.489587	20.381753
C	5.481345	12.694499	27.326581
C	4.229352	12.075601	27.437766
H	4.157330	11.119529	27.957238
C	1.737629	7.769718	22.138270
C	6.700973	11.964399	27.867652
H	7.574754	12.616893	27.761241
C	1.963604	10.723277	20.324092
C	7.581482	14.973381	28.894936
H	6.675964	14.500096	29.294492
H	7.897249	15.749827	29.604388
H	8.380175	14.225412	28.832277
C	6.240244	16.727496	27.752344
H	6.032799	17.268146	26.822626
H	6.625399	17.448216	28.486563
H	5.306355	16.307804	28.149806
C	4.409035	14.499591	26.020431
C	3.088574	12.641435	26.876378
H	2.125159	12.138553	26.972917
C	3.269432	8.918552	19.250753
C	6.553320	11.604906	29.354300
H	6.330576	12.485566	29.971221
H	7.485080	11.152531	29.723115
H	5.745543	10.874117	29.504729
C	8.558709	16.172570	26.845742
H	9.368232	16.358337	27.562364

H	8.326584	17.122064	26.343257
C	8.951933	15.115831	25.784177
C	3.185139	13.832553	26.163068
H	2.297138	14.248659	25.685619
C	1.539086	6.689297	21.082281
H	1.141636	7.108487	20.148162
H	0.805160	5.968291	21.467461
H	2.469166	6.149105	20.875260
C	2.444335	7.245341	23.400986
H	2.947207	6.295908	23.169434
H	1.727418	7.059658	24.210270
C	4.461849	15.738051	25.138799
H	5.485088	16.136137	25.155769
C	1.422758	11.452889	21.544122
H	1.529531	10.800172	22.417715
C	4.150993	7.680006	19.302857
H	4.134447	7.281704	20.326019
C	6.990063	10.696406	27.047152
H	6.150797	9.987346	27.103315
H	7.887283	10.197811	27.440314
H	7.161750	10.927615	25.989926
C	0.395117	8.443417	22.422210
H	0.456910	9.191580	23.220774
H	-0.314275	7.666790	22.737662
H	-0.003971	8.916370	21.516311
C	1.851966	11.342568	19.072337
H	1.332360	12.298602	19.000759
C	5.609814	8.044563	18.980053
H	5.702993	8.397656	17.943435
H	6.252438	7.160023	19.098215
H	5.985328	8.831370	19.643927
C	3.505439	8.302508	23.794262
C	3.503270	16.837339	25.624799
H	2.457443	16.510016	25.532770
H	3.625754	17.740531	25.009601
H	3.681844	17.107042	26.673265
C	3.126368	9.585989	18.027123
H	3.603361	9.170079	17.138785
C	4.139636	15.373449	23.679859
H	4.803587	14.586553	23.304652

H	4.258151	16.257945	23.037237
H	3.103028	15.020437	23.586245
C	2.243126	12.720923	21.833383
H	3.300408	12.489798	22.004840
H	1.850053	13.219224	22.730802
H	2.186722	13.430186	20.994307
C	10.027935	14.130211	26.300438
H	9.735547	13.656638	27.246181
H	10.959238	14.689497	26.468477
H	10.223932	13.339274	25.565746
C	3.664492	6.580996	18.344216
H	2.616102	6.311279	18.523201
H	4.279710	5.677745	18.466167
H	3.756047	6.908605	17.298435
C	9.444440	15.751750	24.478045
H	9.708063	14.979260	23.742878
H	10.340821	16.354792	24.682024
H	8.678350	16.403216	24.036310
C	2.412838	10.777027	17.931159
H	2.316231	11.280382	16.967999
C	2.988023	9.288981	24.868994
H	3.722662	10.079870	25.065336
H	2.818652	8.730373	25.800461
H	2.042787	9.762592	24.575053
C	-0.063987	11.812200	21.396995
H	-0.214731	12.543309	20.589566
H	-0.432624	12.264142	22.329037
H	-0.680833	10.931542	21.174057
C	4.811249	7.667287	24.288398
H	5.253847	7.015337	23.523221
H	4.606682	7.064890	25.185081
H	5.545983	8.440169	24.552089
Zn	9.196217	10.320414	21.947055
Zn	7.105249	13.096074	20.093162
Cl	9.023114	11.801254	20.164408
Cl	9.125181	11.614580	23.865326
N	11.680351	8.815440	22.468547
N	7.626481	14.601111	17.609232
C	10.735347	9.081016	21.615590
C	8.909182	13.927690	17.489795

S33

C	7.152737	15.647520	16.579152
C	6.773613	14.335692	18.554360
C	11.799729	9.488618	23.751370
C	8.967196	12.694144	16.805236
C	10.219021	12.074928	16.693965
H	10.290784	11.118883	16.174408
C	12.710489	7.769080	21.994793
C	7.747362	11.964419	16.264148
H	6.873765	12.617120	16.370722
C	12.484318	10.722139	23.809635
C	6.867576	14.973510	15.237067
H	7.772938	14.499932	14.837501
H	6.552077	15.750084	14.527634
H	6.068619	14.225816	15.299700
C	8.209256	16.727257	16.379729
H	8.416855	17.267780	17.309485
H	7.824241	17.448121	15.645578
H	9.143038	16.307384	15.982206
C	10.039983	14.498799	18.111594
C	11.359951	12.640394	17.255409
H	12.323234	12.137271	17.158809
C	11.177889	8.917306	24.882043
C	7.894812	11.605206	14.777413
H	8.117760	12.485959	14.160693
H	6.962890	11.153192	14.408562
H	8.702362	10.874217	14.626738
C	5.890646	16.172855	17.286266
H	5.081190	16.358800	16.569614
H	6.122962	17.122295	17.788763
C	5.497149	15.116175	18.347782
C	11.263708	13.831470	17.968830
H	12.151821	14.247291	18.446317
C	12.909606	6.689123	23.051144
H	13.306738	7.108839	23.985161
H	13.643960	5.968398	22.666260
H	11.979812	6.148481	23.258278
C	12.003633	7.244054	20.732439
H	11.501051	6.294583	20.964451
H	12.720435	7.058245	19.923084
C	9.987613	15.737309	18.993177

S34

H	8.964492	16.135703	18.976279
C	13.025381	11.452152	22.589955
H	12.918844	10.799639	21.716206
C	10.296119	7.678940	24.829377
H	10.313134	7.280646	23.806219
C	7.458033	10.696357	17.084445
H	8.297194	9.987175	17.028227
H	6.560750	10.197960	16.691181
H	7.286329	10.927446	18.141697
C	14.052684	8.443090	21.710126
H	13.990292	9.190982	20.911342
H	14.762159	7.666562	21.394611
H	14.452043	8.916431	22.615703
C	12.595863	11.340940	25.061641
H	13.115552	12.296896	25.133630
C	8.837195	8.043767	25.151393
H	8.743512	8.396969	26.187932
H	8.194474	7.159333	25.032959
H	8.462133	8.830583	24.487273
C	10.942221	8.300843	20.338970
C	10.946506	16.836270	18.507046
H	11.992238	16.508641	18.599080
H	10.824306	17.739557	19.122161
H	10.767988	17.105924	17.458561
C	11.320845	9.584274	26.105940
H	10.843527	9.168181	26.994019
C	10.309857	15.372673	20.452094
H	9.645739	14.585957	20.827377
H	10.191604	16.257210	21.094706
H	11.346387	15.019412	20.545639
C	12.205012	12.720230	22.300882
H	11.147779	12.489122	22.129116
H	12.598273	13.218829	21.403710
H	12.261186	13.429243	23.140192
C	4.420855	14.130890	17.831472
H	4.713017	13.657406	16.885612
H	3.489677	14.690443	17.663633
H	4.224733	13.339891	18.566063
C	10.781877	6.579802	25.788255
H	11.830334	6.309945	25.609880

H	10.166595	5.676651	25.665887
H	10.689748	6.907365	26.833999
C	5.004835	15.752213	19.653941
H	4.741219	14.979782	20.389167
H	4.108502	16.355340	19.450010
H	5.771046	16.403614	20.095559
C	12.034565	10.775147	26.202482
H	12.131341	11.277969	27.165904
C	11.458831	9.286470	19.263132
H	10.724212	10.077423	19.066944
H	11.627124	8.727193	18.331870
H	12.404500	9.760010	19.555805
C	14.512090	11.811436	22.737489
H	14.662708	12.542218	23.545238
H	14.880897	12.263736	21.805688
H	15.128882	10.930674	22.960188
C	9.636201	7.664981	19.846088
H	9.194300	7.013416	20.611997
H	9.840372	7.062053	18.949674
H	8.901104	8.437515	19.582404

Table S5: XYZ coordinates of optimized molecule **7**.

Br	5.270186	11.619085	20.460564
Br	7.279676	8.858086	22.363066
Br	7.280387	14.537360	22.362599
Br	5.380467	11.775994	24.370466
Zn	5.214148	10.229956	22.478577
Zn	7.399003	13.164699	24.427461
N	6.837110	14.675632	26.912179
N	2.730178	8.717354	21.918865
C	5.547878	12.751759	27.752511
C	4.311341	12.107168	27.889073
H	4.266447	11.158285	28.424695
C	6.789380	12.060572	28.297317
H	7.646386	12.732414	28.174358
C	7.701617	14.412711	25.976172
C	5.570274	13.975605	27.046628
C	2.595618	9.415796	20.651152
C	3.212676	13.819160	26.599195

H	2.310057	14.207148	26.125729
C	3.151233	12.639110	27.334163
H	2.200350	12.117259	27.451798
C	3.665952	8.981776	22.783217
C	3.214723	8.879950	19.501061
C	7.106911	10.785395	27.498108
H	6.284310	10.058548	27.568240
H	8.016818	10.314187	27.896566
H	7.271432	11.003519	26.436767
C	4.419329	14.510760	26.428516
C	7.553605	15.100107	29.291839
H	6.648881	14.615978	29.679936
H	7.839855	15.894485	29.993881
H	8.366990	14.366613	29.259906
C	8.971271	15.203886	26.198718
C	1.888411	10.638841	20.627046
C	7.284175	15.744688	27.932193
C	10.032606	14.227836	26.763767
H	9.708075	13.762889	27.703032
H	10.954959	14.793182	26.958264
H	10.257167	13.430588	26.044263
C	1.710974	7.647897	22.366735
C	5.565973	8.054660	19.160910
H	5.623296	8.443371	18.134297
H	6.224604	7.177069	19.232834
H	5.948593	8.825230	19.839091
C	6.659501	11.723098	29.790958
H	6.402764	12.604905	30.392655
H	7.609575	11.315266	30.164940
H	5.882611	10.962745	29.957078
C	3.043533	9.569826	18.293491
H	3.517803	9.181329	17.391509
C	6.212542	16.815160	28.094199
H	6.001678	17.323687	27.147301
H	6.585579	17.562515	28.807715
H	5.283218	16.394648	28.501090
C	1.343021	11.331154	21.867647
H	1.466609	10.660527	22.725501
C	4.122191	7.658295	19.514045
H	4.136858	7.245929	20.531879

C	4.430512	15.733664	25.522693
H	5.447744	16.147532	25.508587
C	9.504788	15.824281	24.902393
H	9.786854	15.044555	24.181673
H	10.396973	16.426213	25.127084
H	8.754608	16.474259	24.432297
C	0.350522	8.291279	22.635009
H	0.381327	9.025467	23.447802
H	-0.350793	7.496387	22.921623
H	-0.037706	8.774233	21.729717
C	1.751506	11.281780	19.389693
H	1.214968	12.230083	19.343513
C	2.307310	10.748999	18.230392
H	2.189391	11.269558	17.278837
C	8.549834	16.273159	27.235730
H	9.346627	16.479363	27.961007
H	8.315108	17.211685	26.714138
C	2.407486	7.121401	23.633176
H	1.682150	6.915498	24.429996
H	2.929902	6.183032	23.399653
C	2.141252	12.607328	22.183571
H	3.202748	12.390166	22.348390
H	1.742445	13.079380	23.092884
H	2.070612	13.333089	21.360053
C	-0.150888	11.667227	21.737415
H	-0.317685	12.426433	20.959552
H	-0.525157	12.075982	22.686979
H	-0.751874	10.784589	21.481856
C	1.550452	6.576174	21.296112
H	1.143232	6.995299	20.366302
H	0.837771	5.828325	21.669755
H	2.497991	6.068572	21.085903
C	4.077983	15.338659	24.078388
H	4.757312	14.569584	23.694810
H	4.148591	16.217206	23.420888
H	3.051942	14.948515	24.020596
C	3.443552	8.191946	24.053734
C	3.463432	16.825045	26.010691
H	2.421479	16.480328	25.940411
H	3.561724	17.721148	25.381017

H	3.654388	17.112408	27.052020
C	3.635543	6.564883	18.548578
H	2.594601	6.276456	18.740054
H	4.266385	5.669736	18.648102
H	3.705275	6.908206	17.506127
C	2.877500	9.168865	25.113740
H	3.596363	9.966899	25.337559
H	2.683147	8.604487	26.036721
H	1.937991	9.632771	24.788449
C	4.740102	7.573089	24.588441
H	5.211120	6.922850	23.839065
H	4.515405	6.971712	25.481001
H	5.460039	8.353619	24.870257
Br	9.291292	11.618668	24.262164
Br	9.178907	11.776988	20.353025
Zn	9.344887	10.229439	22.243735
Zn	7.161153	13.166490	20.296890
N	7.721860	14.677576	17.812191
N	11.830161	8.717434	22.797798
C	9.011080	12.753868	16.971440
C	10.247623	12.109304	16.834790
H	10.292528	11.160462	16.299097
C	7.769527	12.062613	16.426834
H	6.912322	12.734004	16.550893
C	6.857725	14.414627	18.748537
C	8.988706	13.977648	17.677416
C	11.967364	9.416358	24.064925
C	11.346306	13.821199	18.124789
H	12.248871	14.209006	18.598507
C	11.407735	12.641185	17.389757
H	12.358535	12.119118	17.272415
C	10.892569	8.981617	21.935361
C	11.350958	8.880878	25.216635
C	7.453041	10.786681	17.225222
H	8.275739	10.060080	17.153704
H	6.542851	10.315583	16.827273
H	7.289451	11.003854	18.286901
C	10.139623	14.512702	18.295636
C	7.005107	15.103007	15.432733
H	7.909902	14.619281	15.044300

H	6.718606	15.897657	14.731102
H	6.191906	14.369297	15.464381
C	5.587903	15.205583	18.526383
C	12.674330	10.639581	24.086892
C	7.274594	15.747002	16.792652
C	4.526524	14.229497	17.961461
H	4.850583	13.765201	17.021715
H	3.603871	14.794666	17.767857
H	4.302633	13.431737	18.680608
C	12.848541	7.648066	22.348020
C	9.000923	8.054624	25.562600
H	8.945981	8.444106	26.589052
H	8.342543	7.176656	25.493022
H	8.616264	8.824513	24.884796
C	7.898578	11.726413	14.932840
H	8.154423	12.608826	14.331644
H	6.948474	11.318351	14.559186
H	8.675765	10.966611	14.765601
C	11.524734	9.571307	26.423514
H	11.052749	9.182998	27.326769
C	8.346131	16.817641	16.630969
H	8.557124	17.325750	17.578061
H	7.972905	17.565303	15.917873
H	9.275427	16.397414	16.223708
C	13.217036	11.331293	22.844765
H	13.091753	10.660208	21.987485
C	10.444082	7.658732	25.206332
H	10.427366	7.245859	24.188729
C	10.128209	15.735074	19.202163
H	9.110691	16.148197	19.217176
C	5.054703	15.825572	19.823032
H	4.772900	15.045599	20.543590
H	4.162413	16.427511	19.598781
H	5.804978	16.475447	20.293122
C	14.208303	8.291722	22.076996
H	14.175681	9.026389	21.264698
H	14.909095	7.497059	21.788479
H	14.598436	8.774241	22.981702
C	12.813875	11.283090	25.323653
H	13.350442	12.231455	25.368281

C	12.260959	10.750598	26.484466
H	12.380922	11.271599	27.435526
C	6.008948	16.275109	17.489476
H	5.211985	16.481286	16.764379
H	6.243600	17.213596	18.011174
C	12.149407	7.121256	21.083130
H	12.873110	6.915266	20.284852
H	11.627589	6.182876	21.317957
C	12.417864	12.607116	22.529837
H	11.355969	12.389697	22.367942
H	12.814220	13.078342	21.619030
H	12.490542	13.333644	23.352497
C	14.711132	11.667820	22.971621
H	14.879452	12.427091	23.749093
H	15.083068	12.076738	22.021208
H	15.313040	10.785406	23.225771
C	13.011404	6.576425	23.418372
H	13.421524	6.995349	24.347003
H	13.722538	5.828057	23.042809
H	12.064139	6.069461	23.631284
C	10.482008	15.339549	20.646009
H	9.803689	14.569544	21.029532
H	10.410934	16.217619	21.304097
H	11.508470	14.950395	20.702934
C	11.112335	8.191582	20.664515
C	11.094089	16.827435	18.713999
H	12.136352	16.483453	18.783233
H	10.995647	17.723119	19.344246
H	10.902057	17.115231	17.672980
C	10.933415	6.566077	26.171301
H	11.974068	6.278041	25.977692
H	10.302786	5.670573	26.073673
H	10.865829	6.909935	27.213719
C	11.676066	9.168000	19.602812
H	10.957257	9.966611	19.380897
H	11.867301	8.603315	18.679365
H	12.616927	9.631144	19.925266
C	9.814632	7.572486	20.132914
H	9.345306	6.922433	20.883506
H	10.037353	6.970921	19.239985

H	9.094002	8.352896	19.852541

Table S6: Calculated absorption data of **6**.

State	Energy (cm-1)	Wavelength (nm)	fosc (au**2)	T2 (au)	TX (au)	TY (au)	TZ
1	36563.4	273.5	0.000029408	0.00026	0.01286	0.00997	0.00021
2	36567.3	273.5	0.003689355	0.03321	-0.14734	-0.00589	0.10710
3	36568.3	273.5	0.003701819	0.03333	-0.10735	0.00913	-0.14738
4	36573.3	273.4	0.004109307	0.03699	-0.00046	0.19206	0.01017
5	37311.5	268.0	0.005239793	0.04623	0.17512	-0.00044	0.12476
6	37311.8	268.0	0.005206310	0.04594	0.12408	0.00005	-0.17476
7	37444.8	267.1	0.000000016	0.00000	0.00023	-0.00029	-0.00003
8	37457.7	267.0	0.000470805	0.00414	0.00023	0.06433	0.00006
9	39166.3	255.3	0.000008292	0.00007	0.00550	-0.00412	0.00474
10	39169.8	255.3	0.000219612	0.00185	-0.00883	-0.02559	0.03336
11	39170.3	255.3	0.000394786	0.00332	-0.01682	-0.01469	-0.05310
12	39171.4	255.3	0.000473962	0.00398	0.06138	-0.00793	-0.01237
13	39240.0	254.8	0.014447024	0.12121	-0.29743	-0.00002	0.18094
14	39241.8	254.8	0.014469976	0.12139	-0.18080	-0.00011	-0.29783
15	39540.7	252.9	0.010991788	0.09152	-0.00018	-0.30252	0.00004
16	39569.6	252.7	0.000009015	0.00008	-0.00021	0.00866	-0.00008
17	40855.3	244.8	0.000264834	0.00213	0.00772	0.00092	0.04554
18	40856.4	244.8	0.000262918	0.00212	-0.04538	-0.00069	0.00765
19	40876.7	244.6	0.000241388	0.00194	-0.00034	0.04408	-0.00103
20	40878.0	244.6	0.000075484	0.00061	-0.00068	0.02464	0.00054
21	31338.8	319.1	spin forbidden (mult=3)				
22	31338.9	319.1	spin forbidden (mult=3)				
23	31339.3	319.1	spin forbidden (mult=3)				
24	31340.8	319.1	spin forbidden (mult=3)				
25	32262.0	310.0	spin forbidden (mult=3)				
26	32265.6	309.9	spin forbidden (mult=3)				
27	32443.4	308.2	spin forbidden (mult=3)				
28	32461.9	308.1	spin forbidden (mult=3)				
29	35696.6	280.1	spin forbidden (mult=3)				
30	35704.6	280.1	spin forbidden (mult=3)				
31	35706.2	280.1	spin forbidden (mult=3)				
32	35709.5	280.0	spin forbidden (mult=3)				
33	36336.7	275.2	spin forbidden (mult=3)				
34	36337.3	275.2	spin forbidden (mult=3)				

35	36339.4	275.2	spin forbidden (mult=3)
36	36347.0	275.1	spin forbidden (mult=3)
37	37427.7	267.2	spin forbidden (mult=3)
38	37431.7	267.2	spin forbidden (mult=3)
39	37441.7	267.1	spin forbidden (mult=3)
40	37441.8	267.1	spin forbidden (mult=3)

Table S7: Calculated absorption data of **7**.

state	Energy (cm-1)	Wavelength (nm)	fosc (au**2)	T2 (au)	TX (au)	TY (au)	TZ
1	35931.8	278.3	0.002279396	0.02088	0.10860	-0.01043	-0.09477
2	35933.4	278.3	0.001069161	0.00980	0.08738	0.00529	0.04617
3	35934.9	278.3	0.001721313	0.01577	-0.05741	0.02572	-0.10868
4	35944.3	278.2	0.003451260	0.03161	0.01265	0.17713	0.00871
5	36828.6	271.5	0.011682563	0.10443	0.30470	0.00070	0.10764
6	36832.6	271.5	0.011669040	0.10430	-0.10873	0.00040	0.30410
7	37114.0	269.4	0.000003878	0.00003	-0.00079	0.00581	0.00012
8	37138.8	269.3	0.001444711	0.01281	-0.00020	-0.11316	0.00124
9	38076.1	262.6	0.014998475	0.12968	-0.27372	-0.00014	-0.23400
10	38076.7	262.6	0.015048317	0.13011	-0.23441	0.00058	0.27415
11	38197.4	261.8	0.000641177	0.00553	-0.00071	-0.07433	0.00097
12	38205.5	261.7	0.001675863	0.01444	0.00121	-0.12016	0.00057
13	38369.1	260.6	0.002032569	0.01744	0.06634	-0.00042	0.11419
14	38380.1	260.6	0.002001054	0.01716	-0.11396	-0.00131	0.06462
15	38616.4	259.0	0.006714706	0.05724	-0.00025	0.23926	-0.00041
16	38644.2	258.8	0.000026103	0.00022	-0.00050	-0.01490	-0.00051
17	40289.0	248.2	0.000468692	0.00383	-0.00923	0.00043	-0.06119
18	40292.4	248.2	0.000462679	0.00378	0.06082	-0.00000	-0.00900
19	40328.2	248.0	0.001240098	0.01012	0.00013	0.10061	0.00021
20	40332.6	247.9	0.000342596	0.00280	0.00025	0.05288	-0.00030
21	31253.8	320.0	spin forbidden (mult=3)				
22	31254.7	320.0	spin forbidden (mult=3)				
23	31258.0	319.9	spin forbidden (mult=3)				
24	31260.4	319.9	spin forbidden (mult=3)				
25	31690.5	315.6	spin forbidden (mult=3)				
26	31695.3	315.5	spin forbidden (mult=3)				
27	31972.9	312.8	spin forbidden (mult=3)				
28	31990.5	312.6	spin forbidden (mult=3)				
29	35329.6	283.0	spin forbidden (mult=3)				
30	35335.3	283.0	spin forbidden (mult=3)				
31	35338.0	283.0	spin forbidden (mult=3)				
32	35344.4	282.9	spin forbidden (mult=3)				
33	36054.3	277.4	spin forbidden (mult=3)				
34	36054.9	277.4	spin forbidden (mult=3)				
35	36065.4	277.3	spin forbidden (mult=3)				
36	36080.1	277.2	spin forbidden (mult=3)				
37	37064.9	269.8	spin forbidden (mult=3)				
38	37072.6	269.7	spin forbidden (mult=3)				
39	37091.1	269.6	spin forbidden (mult=3)				
40	37093.6	269.6	spin forbidden (mult=3)				

10 References

[1]. W. L. F. Armarego, *Purification of laboratory Chemicals*, Butterworth Heinemann, Oxford; Boston, **1996**.

[2]. R. Jazzar, J. Bourg, R. D. Dewhurst, B. Donnadieu, G. Bertrand, *J. Org. Chem.* **2007**, *72*, 9, 3492–3499.

[3]. O. Mrózek, M. Gernert, A. Belyaev, M. Mitra, L. Janiak, C. M. Marian, A. Steffen, *Chem. Eur. J.* **2022**, *28*, e202201114.

[4]. F. Neese, The ORCA program system. *WIREs Comput. Mol. Sci.* **2012**, *2* (1), 73–78.

[5]. F. Neese, Software update: the ORCA program system, version 4.0. *WIREs Comput. Mol. Sci.* **2018**, *8* (1), e1327.

[6]. J. P. Perdew, M. Ernzerhof, K. Burke, Rationale for mixing exact exchange with density functional approximations. *J. Chem. Phys.* **1996**, *105* (22), 9982-9985.

[7]. W. Kohn, L. J. Sham, L. J. Self-Consistent Equations Including Exchange and Correlation Effects. *Phys. Rev.* **1965**, *140* (4A), A1133-A1138.

[8]. F. Weigend, R. Ahlrichs, Balanced basis sets of split valence, triple zeta valence and quadruple zeta valence quality for H to Rn: Design and assessment of accuracy. *Phys. Chem. Chem. Phys.* **2005**, *7* (18), 3297–3305.

[9]. S. Grimme, J. Antony, S. Ehrlich, H. Krieg. A consistent and accurate ab initio parametrization of density functional dispersion correction (DFT-D) for the 94 elements H-Pu. *J. Chem. Phys.* **2010**, *132* (15), 154104.

[10]. G. M. Sheldrick, Acta Crystallogr. C 2015, 71, 3-8.

[11]. G. M. Sheldrick, Acta Crystallogr. A 2015, 71, 3-8.

[12]. O. V. Dolomanov, L. J. Bourhis, R. J. Gildea, J. A. K. Howard, H. Puschmann, J. Appl. Crystallogr. 2009, 42, 339.

[13]. A. L. Spek, *Acta. Cryst.* **2015**. *C71*, 9-18.

5.2 Supporting information for chapter 2.2 (An Air- and Moisture-stable Zinc(II) Carbene Dithiolate Dimer Showing Fast Thermally Activated Delayed Fluorescence and Dexter Energy Trans fer Catalysis)

An Air- and Moisture-stable Zinc(II) Carbene Dithiolate Dimer Showing Fast Thermally Activated Delayed Fluorescence and Dexter Energy Transfer Catalysis

Ondřej Mrózek, Mousree Mitra, Bejamin Hupp, Andrey Belyaev, Nora Lüdtke, Dorothee Wagner, Cui Wang, Oliver S. Wenger, Christel M. Marian,* and Andreas Steffen*

Table of Contents

NMR Spectra *S1*
Thermogravimetry analysis *S5*
Stability Towards Water and Oxygen *S6*
X-ray Crystallography *S7*
Cyclic Voltammetry *S10*
Photophysical Measurements *S11*
Emission and Excitation Spectra at 297 and 77 K. S12
Lifetime Measurements at room temperature S16
Lifetime Measurements at 77K S19
Photostability *S22*
Photo-isomerization of (E)-stilbene *S23*
Computational Methods and Technical details *S24*
References *S53*

NMR Spectra

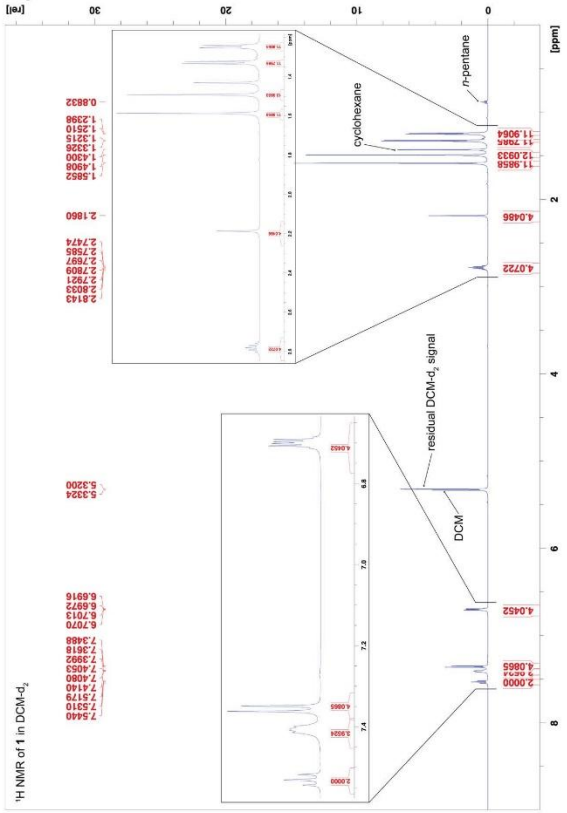


Figure S1. ^{1}H NMR spectrum of **Zn1** in DCM-d_2. The residual molecules of cyclohexane and *n*-pentane are impurities presented in deuterated solvents while DCM is a crystal solvent presented in crystal lattice, which was evidenced by X-ray diffraction analysis and elemental analysis.

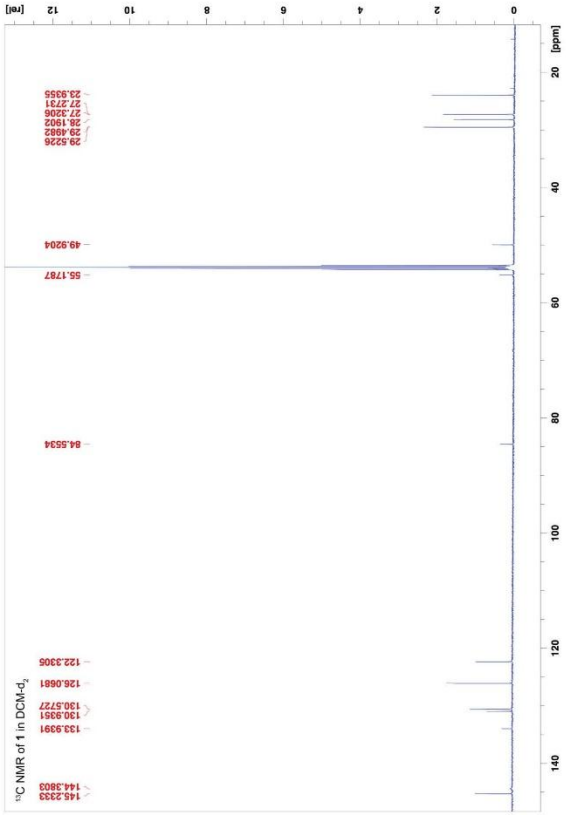


Figure S2. ^{13}C NMR spectrum of **Zn1** in DCM-d_2.

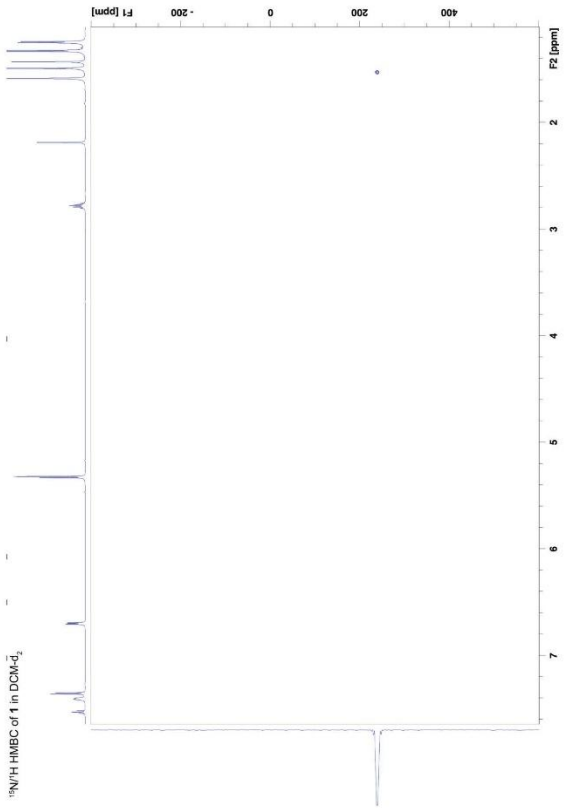


Figure S3. ^{15}N/^{1}H HMBC spectrum of **Zn1** in DCM-d_2. δ = 239.9 ppm (NH_3 reference scale) = -141.86 ppm (CH_3NO_2 reference scale).

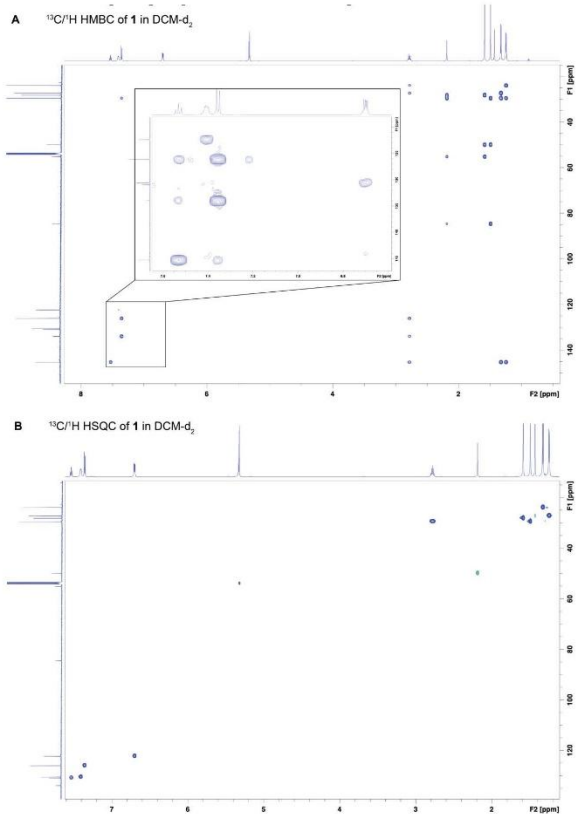


Figure S4. ^{13}C/^{1}H HMBC (**A**) and ^{13}C/^{1}H HSQC (**B**) spectra of **Zn1** in DCM-d_2.

Thermogravimetry analysis

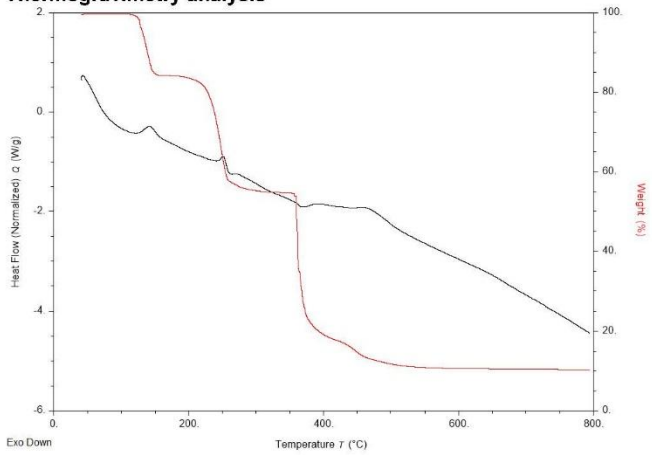


Figure S5. TGA/DSC data for compound **Zn1** in single crystalline form.

Stability Towards Water and Oxygen

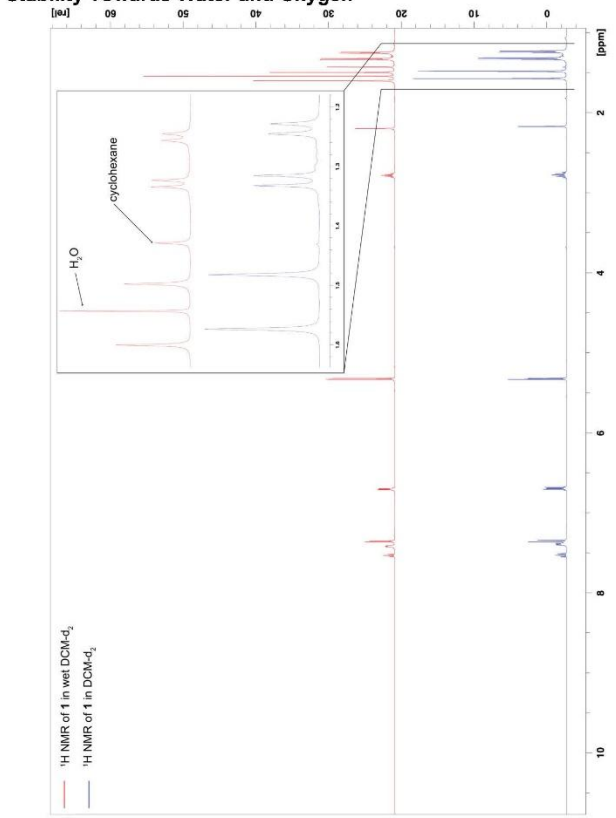


Figure S6. ^{1}H NMR spectra of **Zn1** in wet (red) and dry/degassed (blue) DCM-d_2. Spectra, showing no formation of protonated ^{Me}cAAC or bdt species, were recorded after four hours of dissolution of complex in wet, air-saturated solvent.

X-ray Crystallography

The crystals of **Zn1** were immersed in a film of NVH or perfluoropolyether oil, mounted on a polyimide microloop (MicroMounts of MiTeGen) and transferred to stream of cold nitrogen (Bruker Kryoflex2), and measured at a temperature of 100 K. The X-ray diffraction data was collected on a Bruker D8 diffractometer with a CMOS Photon 100 and multilayer optics monochromated MoKα (0.71073Å) radiation (INCOATEC microfocus sealed tube). The frames were integrated with the Bruker SAINT software package using a narrow-frame algorithm. The APEX3 v2018.7-0 program package was used for cell refinements and data reductions. The structure was solved using intrinsic phasing methods,[1,2] refined and visualized with the OLEX2-1.3 program.[3] A semiempirical absorption correction (SADABS) was applied to all data. All non-hydrogen atoms were refined anisotropically. Hydrogen atoms were included in structure factors calculations. All Hydrogen atoms were assigned to idealised geometric positions. The unit cell of the 1 contains disordered solvent molecules of dichloromethane which has been treated as a diffuse contribution to the overall scattering without specific atom positions by SQUEEZE/PLATON.[4] The crystallographic details are summarized in Table 1. CCDC 2189606 contain the supplementary crystallographic data for this paper.

Table S1. Crystal data and structure refinement for **Zn1**.

Identification code	**Zn1**
CCDC number	**2189606**
Empirical formula	$C_{52}H_{70}N_2S_4Zn_2$
Formula weight	982.08
Temperature/K	100.0
Crystal system	triclinic
Space group	P-1
a/Å b/Å c/Å α/° β/° γ/°	10.4251(2) 11.4928(3) 12.4597(3) 104.1850(10) 91.9470(10) 96.1930(10)
Volume/Å^3	1436.05(6)
Z	1
ρ_{calc}g/cm^3	1.136
μ/mm^{-1}	1.012
F(000)	520.0
Crystal size/mm^3	0.307 × 0.156 × 0.14
Radiation	MoKα (λ = 0.71073)
2Θ range for data collection/°	5.058 to 51.998
Index ranges	-12 ≤ h ≤ 12, -14 ≤ k ≤ 14, -14 ≤ l ≤ 15
Reflections collected	29910
Independent reflections	5624 [R_{int} = 0.0234, R_{sigma} = 0.0168]
Data/restraints/parameters	5624/0/279
Goodness-of-fit on F^2	1.059
Final R indexes [I>=2σ (I)]	R_1 = 0.0235, wR_2 = 0.0642
Final R indexes [all data]	R_1 = 0.0246, wR_2 = 0.0650
Largest diff. peak/hole / e Å^{-3}	0.33/-0.42

[a] $R_1 = \sum||F_o|-|F_c||/\sum|F_o|$; $wR_2 = [\sum[w(F_o^2-F_c^2)^2]/\sum[(wF_o^2)^2]]^{1/2}$; $w = 1/[\sigma^2(F_o^2)+(aP)^2+bP]$, where $P = (F_o^2+2F_c^2)/3$
[b] GooF = $S = [[\sum w(F_o^2-F_c^2)^2]/(m-n)]^{1/2}$, where m = number of reflexes and n = number of parameters

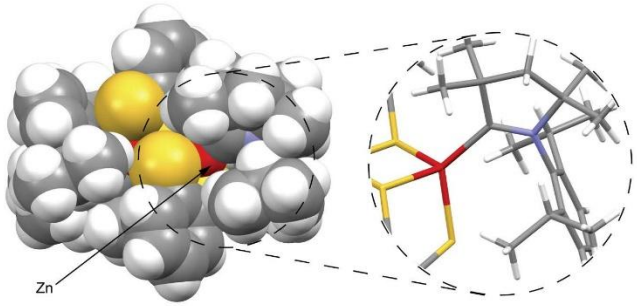


Figure S7. Space-filling showing steric protection of Zn–$C^{carbene}$ bond.

Cyclic Voltammetry

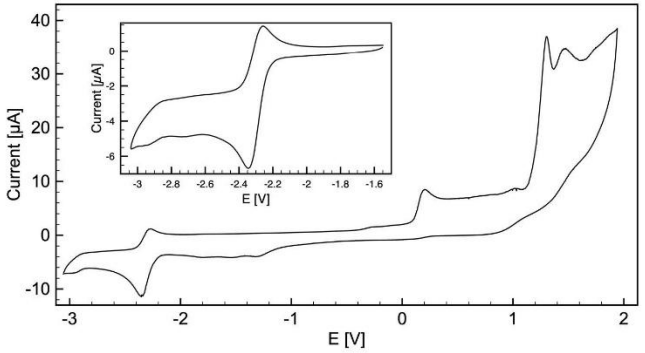


Figure S8. Cyclic voltammetry of **Zn1** in CH_3CN using ferrocene/ferrocenium couple as a reference (scan rate 100 mV/s, 100 mM $^nBu_4NBF_4$, Pt-disk working electrode). Inset: detail of reversible reduction.

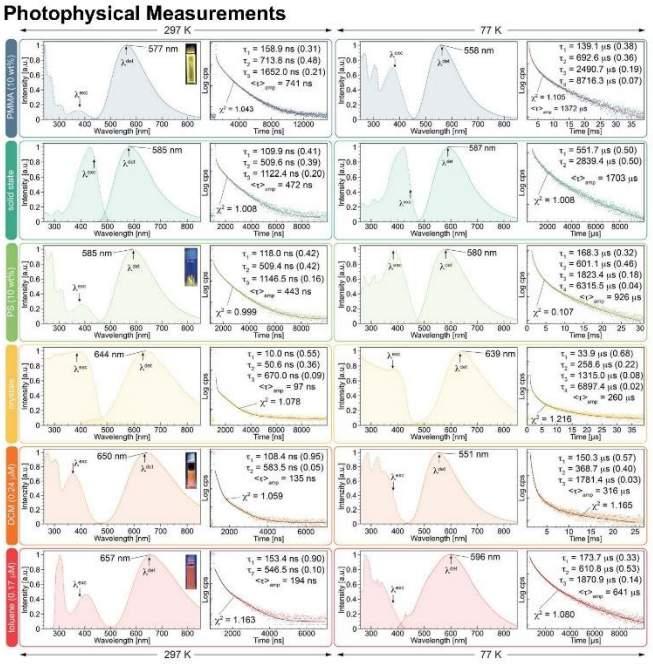


Figure S9. Summary of photophysical data of **Zn1** in different media.

Emission and Excitation Spectra at 297 and 77 K.

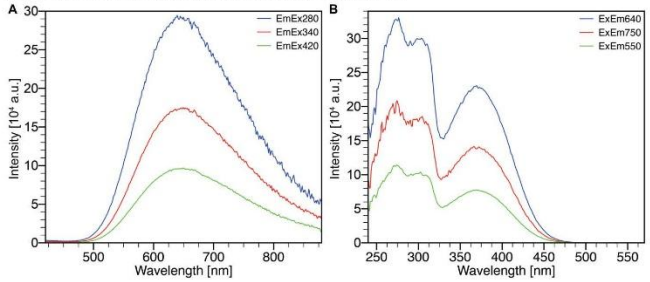


Figure S10. Emission (**A**) and excitation maps (**B**) of **Zn1** in DCM (2.4×10^{-5} M) at 297K.

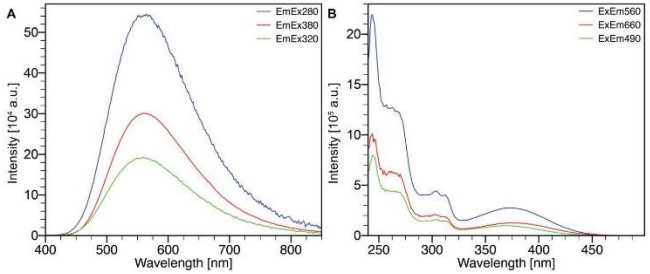


Figure S11. Emission (**A**) and excitation map (**B**) of **Zn1** in PMMA matrix (10wt%) at 297K.

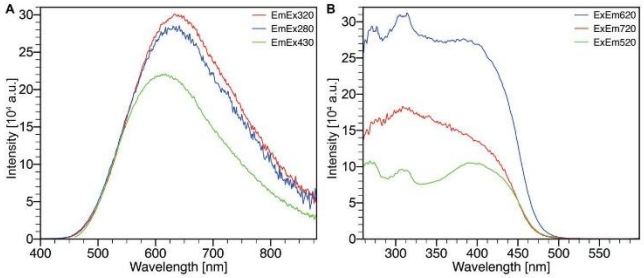


Figure S12. Emission (**A**) and excitation map (**B**) of **Zn1** in solid state at 297K.

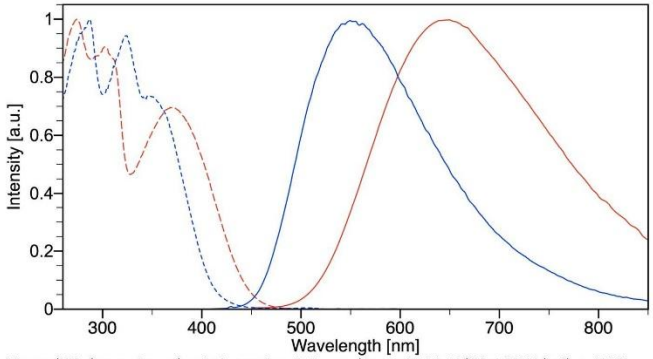


Figure S13. Comparison of emission and excitation profiles on **Zn1** in DCM at 297K (red) and 77K (blue).

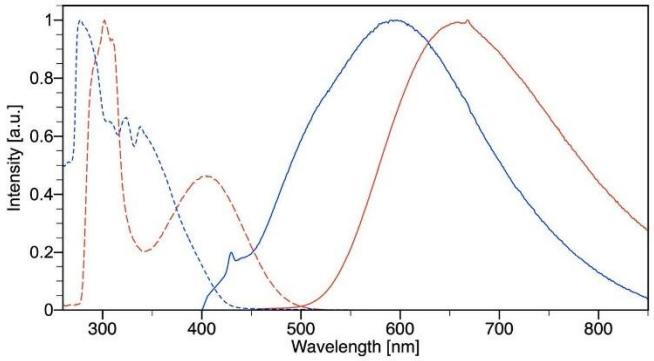


Figure S14. Comparison of emission and excitation profiles on **Zn1** in toluene at 297K (red) and 77K (blue).

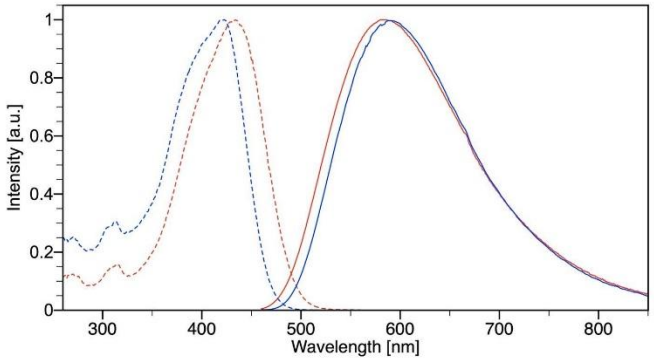


Figure S15. Comparison of emission and excitation profiles on **Zn1** in solid-state at 297K (red) and 77K (blue).

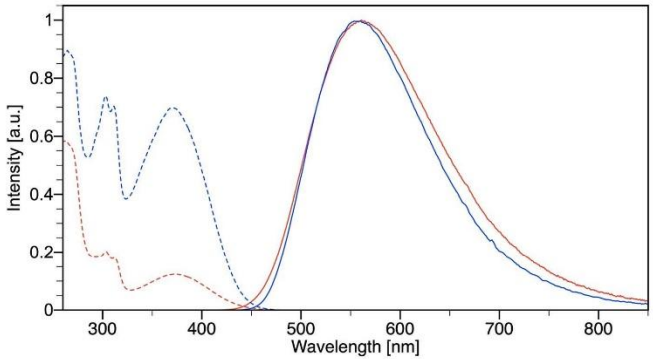


Figure S16. Comparison of emission and excitation profiles on **Zn1** in PMMA (10 wt%) at 297K (red) and 77K (blue).

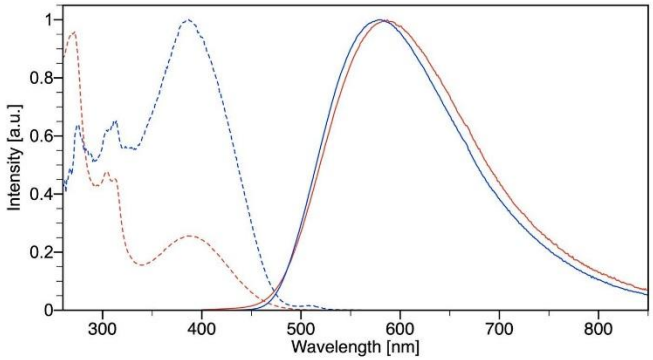


Figure S17. Comparison of emission and excitation profiles on **Zn1** in PS (10 wt%) at 297K (red) and 77K (blue).

Lifetime Measurements at room temperature

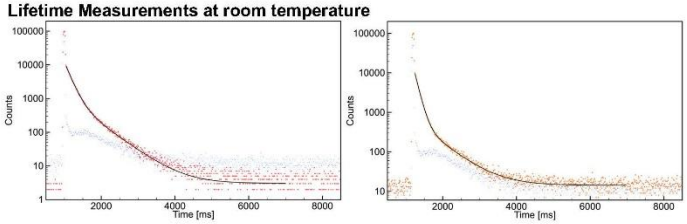


Figure S18. Luminescence decay and IRF (blue dots) obtained for **Zn1** in DCM (blue dots, 2.4×10^{-5} M) and toluene (orange dots, 1.7×10^{-5} M) solution at room temperature after 450 nm excitation (VPL) and biexponential fits (DCM: red curve, $\chi^2 = 1.059$; toluene: black curve, $\chi^2 = 1.163$) of the data.

Table S2 Parameters of biexponential fit of photoluminescence decay of **Zn1** in DCM.

	LT [ns]	pre-exponential factors	Rel. %	$\langle\tau\rangle_{amp}$ [ns]	$\langle\tau\rangle_{int}$ [ns]
		DCM solution			
τ_1	108.4±0.7	9726.4	76.01	134.8±1.1	222.4±4.3
τ_2	583.5±9.1	570.6	23.99		
		Toluene solution			
τ_1	153.4±1.2	8556.8	70.69	194.38±1.7	268.6±3.9
τ_2	546.5±6.8	995.9	29.31		

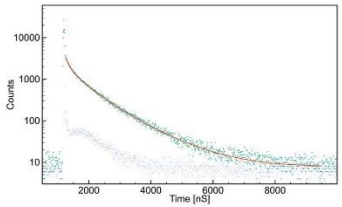


Figure S19. Luminescence decay and IRF (blue dots) obtained for **Zn1** in solid state (green dots) at room temperature after 450 nm excitation (VPL) and triexponential fit (black curve, χ^2 = 1.008).

Table S3 Parameters of triexponential fit of photoluminescence decay of **Zn1** in solid state.

	LT [ns]	pre-exponential factors	Rel. %	$\langle\tau\rangle_{amp}$ [ns]	$\langle\tau\rangle_{int}$ [ns]
τ_1	109.9±7.7	1375.5	9.44		
τ_2	509.6±38.0	1325.9	42.2	472.4±27.9	768.5±41.9
τ_3	1122.4±48.7	691.1	48.4		

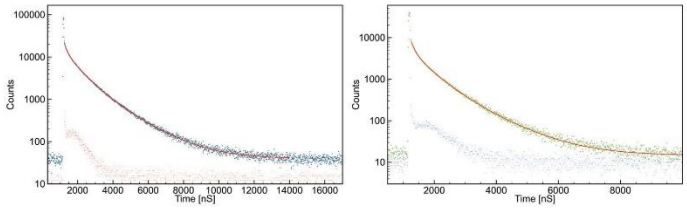


Figure S20. Luminescence decay obtained for **Zn1** in PMMA (blue dots, 10 wt%) and PS (green dots, 10 wt%) with IRF (red and blue dots, respectively) at room temperature after 380 nm excitation (VPLED) and triexponential fit (PMMA: black curve, χ^2 = 1.043, PS black curve, χ^2 = 0.999).

Table S4 Parameters of biexponential fit of photoluminescence decay of **Zn1** in PMMA and PS matrix (10 wt%).

	LT [ns]	pre-exponential factors	Rel. %	$\langle\tau\rangle_{amp}$ [ns]	$\langle\tau\rangle_{int}$ [ns]
		PMMA			
τ_1	158.9±5.4	5678.6	6.57		
τ_2	713.8+14.5	8936.6	46.46	741.4+12.4	1117.9+17.3
τ_3	1652.0±20.9	3902.7	46.96		
		PS			
τ_1	118.0±5.1	3364.7	11.25		
τ_2	509.4±21.2	3344.6	48.24	443.86±16.5	723.5±27.9
τ_3	1146.5±35.6	1248.1	40.52		

Lifetime Measurements at 77K

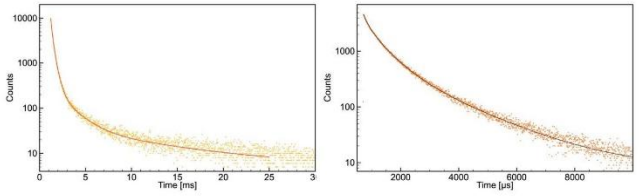


Figure S21. Luminescence decay obtained for **1** in DCM (blue dots, 2.4×10^{-5} M) and toluene (orange dots, 1.7×10^{-5} M) at 77 K after 380 nm excitation (VPL) and biexponential fits (DCM: red curve, χ^2 = 1.165; toluene: black curve, χ^2 = 1.163) of the data.

Table S5 Parameters of fit of photoluminescence decay of **Zn1** in DCM and toluene, respectively.

	LT [µs]	pre-exponential factors	Rel. %	$\langle\tau\rangle_{amp}$ [µs]	$\langle\tau\rangle_{int}$ [µs]
		DCM			
τ_1	150.3±4.0	5682.6	26.94		
τ_2	368.7±8.9	4033.7	46.94	316.5±8.8	1707.0±360.1
τ_3	1781.4±83.6	260.9	14.67		
τ_4	10769.7±1645.7	44.7	11.44		
		Toluene			
τ_1	173.7±4.4	1537.4	9.06		
τ_2	610.8±8.8	2413.4	50.04	641.2±8.4	1086.5±16.5
τ_3	1870.9±23.0	644.1	40.09		

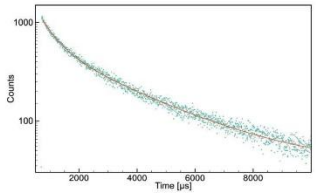


Figure S22. Luminescence decay obtained for **Zn1** in solid state (green dots) at room temperature after 450 nm excitation (VPL) and triexponential fit (red curve, χ^2 = 1.063).

Table S6 Parameters of biexponential fit of photoluminescence decay of **Zn1** in solid state.

	LT [ns]	pre-exponential factors	Rel. %	$\langle\tau\rangle_{amp}$ [ns]	$\langle\tau\rangle_{int}$ [ns]
τ_1	551.7±8.4	513.1	16.08	1703.4±16.1	2471.5±26.5
τ_2	2839.4±27.4	520.2	83.9		

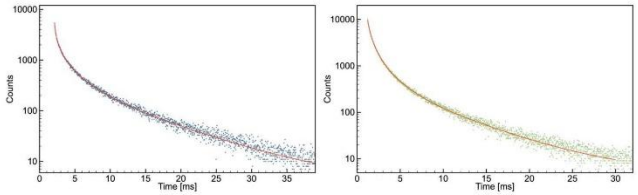


Figure S23. Luminescence decay obtained for **Zn1** in PMMA (blue dots, 10 wt%) and PS (green dots, 10 wt%) at 77K after 380 nm excitation (VPLED) and fit (PMMA: black curve, χ^2 = 1.043, PS black curve, χ^2 = 0.999).

Table S7 Parameters of multiexponential fit of photoluminescence decay of **Zn1** in PMMA and PS matrix (10 wt%).

	LT [ns]	pre-exponential factors	Rel. %	$\langle\tau\rangle_{amp}$ [ns]	$\langle\tau\rangle_{int}$ [ns]
		PMMA			
τ_1	139.1±5.2	1973.2	3.80		
τ_2	692.6±21.8	1914.4	18.37		
τ_3	2490.7±67.3	1021.4	35.24	1372.1±27.9	4723.0±107.6
τ_4	8716.3±141.7	352.8	42.60		
		PS			
τ_1	168.3±7.1	3090.8	11.25		
τ_2	601.1±18.1	4529,0	48.24		
τ_3	1823.4±52.8	1778.8	40.52	926.74±20.3	2650.4±71.5
τ_4	6315.5±117.9	412.7	40.52		

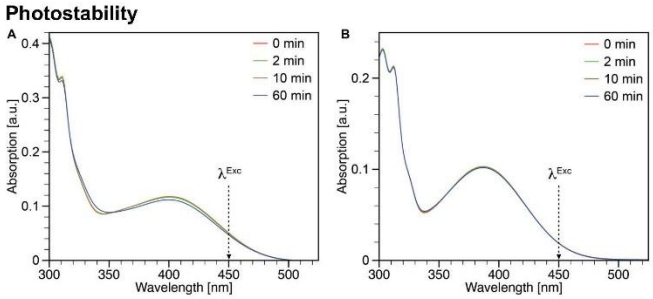


Figure S24. Photostability of **Zn1** under continuous 450 nm irradiation (18W EvoluChem™ LED) in various solvents. **A**: toluene (1.7×10^{-5} M), B: THF (3.6×10^{-5} M). Absorbance monitored at 402 (toluene) and 387 nm (THF): the 96% and 99% of original absorbance after 1 hour of irradiation in toluene and THF, respectively, showing excellent photostability of **Zn1** for photocatalytic application.

Photo-isomerization of (*E*)-stilbene

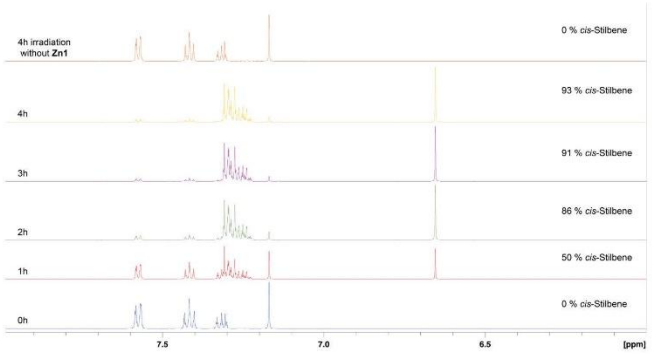


Figure S25. Photo-induced isomerization (*E*)-stilbene → (*Z*)-stilbene monitored by ^{1}H NMR spectroscopy using toluene-d_8 solution containing 2 mM of **Zn1** and 50 mM of (*E*)-stilbene. Irradiation source: 450 nm, 18W EvoluChem™ LED. Top (orange) spectrum: reference experiment using identical condition but without **Zn1** photocatalyst

Computational Methods and Technical Details

For all geometry optimizations the Gaussian 16 program was used.[5] The ground state geometries were optimized with Kohn-Sham density functional theory (DFT).[6] For the optimization of the singlet excited state geometries the time dependent DFT (TDDFT)[7] was used and for the excited triplet state geometries the Tamm-Dancoff approximation (TDA)[8] to TDDFT was chosen. The 10-mdf 6s5p3d basis set with defpp-ecp was used for the zinc atoms[9] and for sulfur the def2-SVPD basis was chosen.[10] For all other atoms the def-SV(P) basis set was used.[10] As functional BH-LYP functional was chosen for all calculations.[11,12] A THF environment was mimicked via the polarizable continuum model (PCM).[13,14] To examine the excitation energies and oscillator strengths of the spin allowed transitions DFT/MRCI calculations, were carried out.[15,16] As Hamiltonian the redesigned R2018 was selected and 30 singlet and 30 triplet roots were calculated. For the DFT/MRCI calculations, the point charges of the Gaussian 16 calculations were extracted. With the SPOCK program the spin-orbit coupling matrix elements (SOCMEs) were obtained.[17,18]

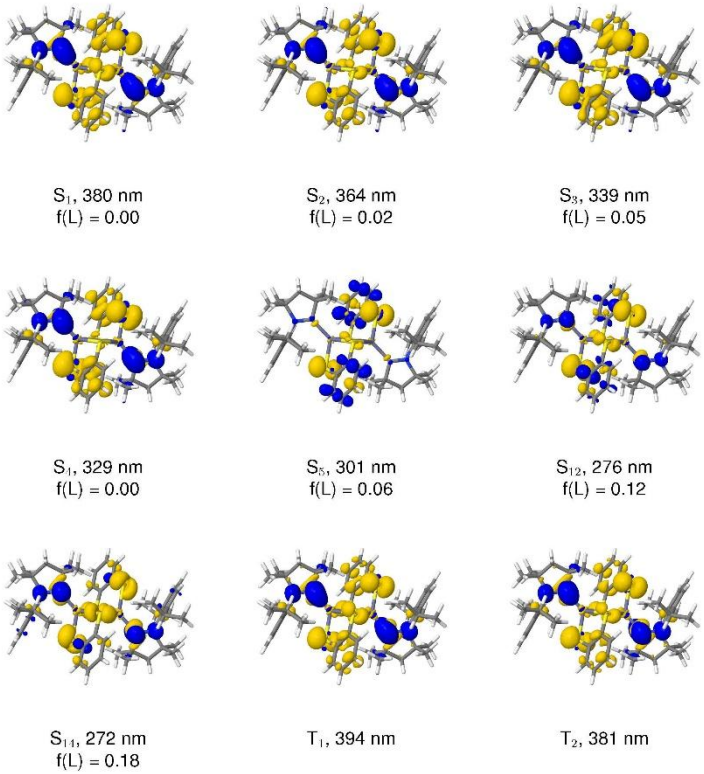


Figure S26: DFT/MRCI difference densities, excitation energies and oscillator strengths of the relevant excitations of complex **Zn1** in THF at the optimized S_0 geometry. Areas losing electron density upon electronic excitation from the ground-state are shown in gold, areas gaining electron density in blue.

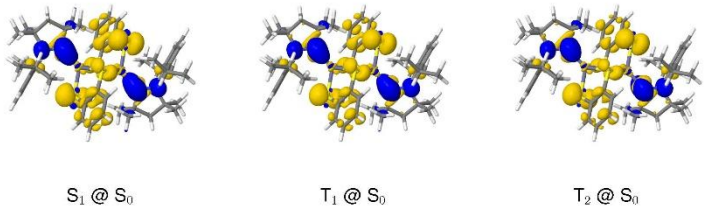


Figure S27: DFT/MRCI difference densities of the S_1, T_1 and T_2 state of complex **Zn1** in THF at the optimized S_0 geometry. For color codes, see Figure S26.

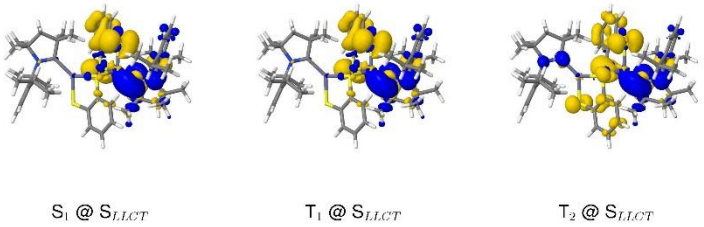
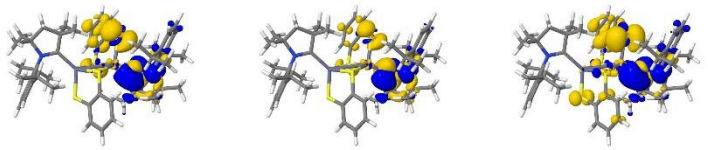
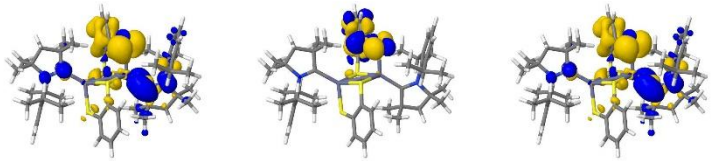


Figure S28: DFT/MRCI difference densities of the S_1, T_1 and T_2 state of complex **Zn1** in THF at the optimized S_{LLCT} geometry. For color codes, see Figure S26.



S_1 @ S_{LLCT} T_1 @ S_{LLCT} T_2 @ S_{LLCT}

Figure S29: DFT/MRCI difference densities of the S_1, T_1 and T_2 state of complex **Zn1** in THF at the optimized $T_{LL/LMCT}$ geometry. For color codes, see Figure S26.



S_1 @ T_{LC} T_1 @ T_{LC} T_2 @ T_{LC}

Figure S30: DFT/MRCI difference densities of the S_1, T_1 and T_2 state of complex **Zn1** in THF at the optimized T_{LC} geometry. For color codes, see Figure S26.

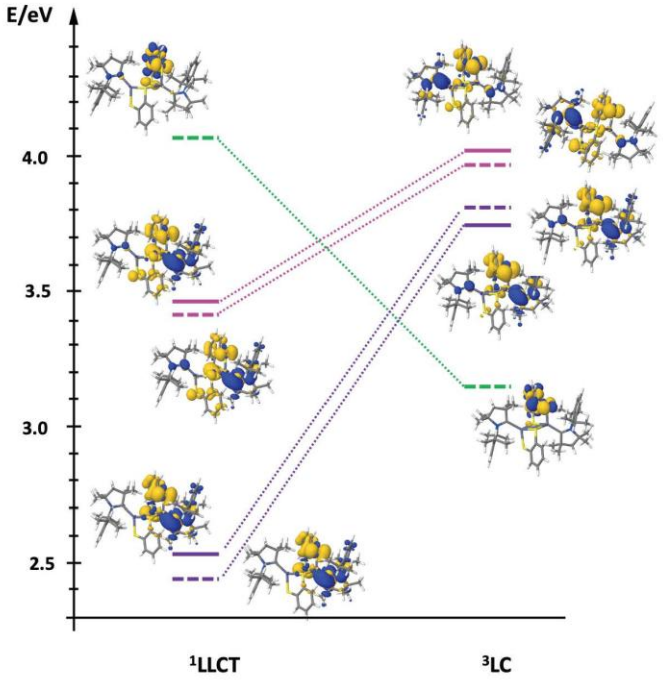


Figure S31: DFT/MRCI excitation energies and difference densities of the complex **Zn1** in THF calculated with DFT/MRCI at the optimized ^{1}LLCT and ^{3}LC geometries. The DFT/MRCI energy of the S_0 state at the DFT-optimized S_0 minimum geometry in a polarizable THF environment serves as common origin. Dashed lines represent triplet states and solid lines represent singlet states. The following color codes have been used: violet and pink LLCT ($\pi_{\mathrm{dtb}} \rightarrow \pi^*_{\mathrm{carb}}$) and green LC ($\pi_{\mathrm{thiol}} \rightarrow \pi^*_{\mathrm{thiol}}$). For color codes of the difference densities, see Figure S26.

Table S8: DFT/MRCI excitation energies (ΔE/eV) of **Zn1** in THF at various molecular geometries. The DFT/MRCI energy of the S_0 state at the DFT-optimized S_0 minimum geometry in a polarizable THF environment serves as common origin. 0–0 energies including zero-point vibrational energy corrections are given in parentheses.

state	optimized geometry			
	S_0	S_{LLCT}	$T_{LL/LMCT}$	$T_{LC(thiol)}$
S_0	0.00	0.70	1.21	0.80
S_{LLCT}	3.26	2.53 (**2.45**)	3.31	3.81
S'_{LLCT}	3.41	3.46	4.15	4.01
T_{LLCT}	3.15	2.44	2.76 (**2.66**)	3.74
T'_{LLCT}	3.25	3.42	4.00	3.96
$T_{LC(thiol)}$	3.55	4.06	4.83	3.15 (**3.04**)
$T'_{LC(thiol)}$	3.56	4.19	4.85	4.21

Table S9: SOMEs [cm^{-1}] computed at the optimized geometries.

optimized geometry	$\langle T_1 \lvert \hat{H}_{SO} \rvert S_1 \rangle$			$\sum$ (SOCMEs)^2
	x	y	z	
S_{LLCT}	0.84	0.09	1.67	3.49
$T_{LL/LMCT}$	-2.63	-1.77	2.60	16.79
$T_{LC(thiol)}$	3.41	2.43	-6.79	63.69

Table S10: Cartesian coordinates of the optimized S_0 geometry of complex **Zn1**.

atom	x	y	z
Zn	3.277080	5.187227	5.375498
S	5.052022	5.584904	6.964482
S	1.739072	5.018962	7.140121
N	2.042695	7.101935	3.304992
C	0.810124	7.171588	4.064042
C	-1.378341	6.351943	4.595452

Continued on next page

Table S10: Cartesian coordinates of the optimized S_0 geometry of complex **Zn1**.

atom	x	y	z
H	-2.170353	5.622504	4.466207
C	-1.560763	7.394619	5.484417
H	-2.491235	7.484013	6.036061
C	-0.195848	6.209138	3.870705
C	4.205396	6.632268	2.674919
C	-0.542590	8.309578	5.685567
H	-0.681597	9.105677	6.408451
C	-0.064040	4.994859	2.964178
H	0.886979	5.059891	2.436402
C	0.660679	8.219788	4.992097
C	2.673573	5.749378	8.448344
C	3.710792	7.812977	1.822405
H	4.141351	8.744656	2.202618
H	4.003230	7.721673	0.773362
C	3.079251	6.411092	3.666529
C	1.755505	9.222056	5.327354
H	2.564811	9.103114	4.606977
C	4.415129	5.363106	1.840719
H	3.515200	5.065720	1.295162
H	4.721329	4.523711	2.467284
H	5.208363	5.546060	1.107354
C	2.192462	7.854217	1.985252
C	4.060162	5.993168	8.384993

Continued on next page

Table S10: Cartesian coordinates of the optimized S_0 geometry of complex **Zn1**.

atom	x	y	z
C	-0.036134	3.694806	3.772777
H	0.787513	3.678728	4.491266
H	0.091167	2.838606	3.099614
H	-0.971348	3.550038	4.325405
C	2.355774	8.942977	6.706196
H	1.601835	9.046708	7.494965
H	3.164076	9.654101	6.915087
H	2.762894	7.931536	6.770531
C	5.510306	6.975061	3.396801
H	6.267681	7.255251	2.655042
H	5.893342	6.122381	3.966306
H	5.380805	7.818605	4.083851
C	1.456561	7.117274	0.868870
H	1.787278	6.083845	0.752858
H	1.647319	7.638295	-0.074498
H	0.377684	7.123967	1.038820
C	1.273002	10.672415	5.248199
H	0.783401	10.894522	4.294888
H	2.123219	11.354982	5.361519
H	0.562653	10.902803	6.049852
C	1.996592	6.106074	9.623220
C	-1.177647	4.924856	1.915411
H	-2.149919	4.726725	2.380185

Continued on next page

Table S10: Cartesian coordinates of the optimized S_0 geometry of complex **Zn1**.

atom	x	y	z
H	-0.978773	4.108590	1.211257
H	-1.268378	5.852215	1.341470
C	4.703832	6.589527	9.472945
H	5.770424	6.779905	9.404390
C	1.656200	9.277109	2.037824
H	0.590601	9.303836	2.284126
H	1.779987	9.719960	1.044136
H	2.202085	9.903079	2.743753
C	2.649982	6.681968	10.700092
C	4.016214	6.931840	10.626484
Zn	5.484894	3.121619	6.680555
S	3.710026	2.723944	5.091603
S	7.022997	3.289808	4.915975
N	6.719237	1.206675	8.751007
C	7.951794	1.136828	7.991956
C	10.140493	1.955967	7.460761
H	10.932687	2.685182	7.590150
C	10.322720	0.913311	6.571729
H	11.253210	0.823727	6.020146
C	8.957992	2.099004	8.185445
C	4.556611	1.676608	9.381117
C	9.304345	-0.001397	6.370454
H	9.443212	-0.797487	5.647534

Continued on next page

Table S10: Cartesian coordinates of the optimized S_0 geometry of complex **Zn1**.

atom	x	y	z
C	8.826461	3.313170	9.092167
H	7.875553	3.248121	9.620145
C	8.101053	0.088642	7.063856
C	6.088461	2.559507	3.607713
C	5.051076	0.495819	10.233603
H	4.620376	-0.435794	9.853392
H	4.758682	0.587149	11.282657
C	5.682769	1.897665	8.389493
C	7.006023	-0.913378	6.728540
H	6.196726	-0.794289	7.448903
C	4.347068	2.945784	10.215331
H	5.247063	3.243057	10.760843
H	4.040935	3.785216	9.588784
H	3.553850	2.762915	10.948734
C	6.569398	0.454390	10.070720
C	4.701865	2.315748	3.671057
C	8.798435	4.613328	8.283739
H	7.974695	4.629474	7.565353
H	8.671211	5.469443	8.957027
H	9.733569	4.758183	7.731002
C	6.405848	-0.634127	5.349697
H	7.159785	-0.737992	4.560942
H	5.597399	-1.345070	5.140762

Continued on next page

Table S10: Cartesian coordinates of the optimized S_0 geometry of complex **Zn1**.

atom	x	y	z
H	5.998940	0.377402	5.285396
C	3.251639	1.333989	8.659263
H	2.494244	1.053878	9.401034
H	2.868685	2.186715	8.089776
H	3.381024	0.490438	7.972201
C	7.305432	1.191239	11.187070
H	6.974912	2.224738	11.303023
H	7.114560	0.670299	12.130460
H	8.384309	1.184332	11.017135
C	7.488206	-2.363844	6.807681
H	7.977696	-2.586083	7.761018
H	6.637848	-3.046224	6.694290
H	8.198556	-2.594353	6.006065
C	6.765418	2.202867	2.432805
C	9.940316	3.382983	10.140683
H	10.912491	3.581107	9.675699
H	9.741666	4.199177	10.844983
H	10.031129	2.455548	10.714488
C	4.058163	1.719486	2.583070
H	2.991567	1.529136	2.651624
C	7.105514	-0.968560	10.018044
H	8.171130	-0.995365	9.771823
H	6.981608	-1.411517	11.011671

Continued on next page

Table S10: Cartesian coordinates of the optimized S_0 geometry of complex **Zn1**.

atom	x	y	z
H	6.559630	-1.594395	9.311990
C	6.112002	1.627064	1.355902
C	4.745761	1.377231	1.429502
H	7.833702	2.386670	2.376415
H	6.672079	1.366246	0.462735
H	4.220112	0.917782	0.598169
H	4.541845	7.391356	11.457791
H	2.089889	6.942830	11.593237
H	0.928311	5.922250	9.679609

Table S11: Cartesian coordinates of the optimized S_{LLCT} geometry of complex **Zn1**.

atom	x	y	z
Zn	-1.9997000	0.3548000	0.1491300
S	-0.0900200	1.1660800	-0.9398700
S	-1.9953000	2.0091500	1.7183100
N	-4.7128000	-0.5639200	-0.7094900
C	-5.3005800	0.4959400	0.0894900
C	-6.2280900	1.2697300	2.1605700
H	-6.4914200	1.1015400	3.1988800
C	-6.4801200	2.5047600	1.5923700
H	-6.9493600	3.2886600	2.1781200
C	-5.6285600	0.2426300	1.4346700
C	-3.1569000	-1.9890200	-1.6366600

Continued on next page

Table S11: Cartesian coordinates of the optimized S_{LLCT} geometry of complex **Zn1**.

atom	x	y	z
C	-6.1046700	2.7460600	0.2834800
H	-6.2708700	3.7296400	-0.1415700
C	-5.3150500	-1.0529700	2.1689000
H	-4.9226700	-1.7714000	1.4507600
C	-5.5001600	1.7616000	-0.4941600
C	-0.8318000	3.1028200	0.9533200
C	-4.4921000	-2.2199500	-2.3652700
H	-4.4448600	-1.7755400	-3.3636500
H	-4.7172100	-3.2817800	-2.4915300
C	-3.4418100	-0.8017500	-0.7486100
C	-5.0362100	2.1492800	-1.8909400
H	-4.6343600	1.2617400	-2.3817500
C	-2.7630300	-3.1735400	-0.7426500
H	-3.5591400	-3.4506600	-0.0451000
H	-1.8665400	-2.9463100	-0.1597700
H	-2.5474500	-4.0439600	-1.3720100
C	-5.5718400	-1.5101200	-1.5419900
C	-0.0356900	2.7618700	-0.1563000
C	-4.2263200	-0.8454800	3.2263200
H	-3.2996600	-0.4596300	2.7915500
H	-3.9966400	-1.7978500	3.7184300
H	-4.5505400	-0.1386400	3.9983000
C	-3.9002100	3.1755100	-1.8306400

Continued on next page

Table S11: Cartesian coordinates of the optimized S_{LLCT} geometry of complex **Zn1**.

atom	x	y	z
H	-4.2408200	4.1178300	-1.3867400
H	-3.5380400	3.3925500	-2.8423600
H	-3.0555600	2.8171900	-1.2360400
C	-2.0216100	-1.6940400	-2.6176900
H	-1.9103700	-2.5383700	-3.3076100
H	-1.0655000	-1.5544500	-2.1021900
H	-2.2275900	-0.7966600	-3.2111400
C	-6.3551000	-2.4648100	-0.6469800
H	-5.7100800	-3.0823800	-0.0190600
H	-6.9369300	-3.1352900	-1.2868300
H	-7.0570900	-1.9226100	-0.0092500
C	-6.1741900	2.6928100	-2.7592000
H	-7.0293400	2.0120300	-2.7979700
H	-5.8191200	2.8521100	-3.7839100
H	-6.5331700	3.6577100	-2.3843800
C	-0.7016400	4.3899600	1.4912300
C	-6.5537300	-1.6754300	2.8183300
H	-6.9248400	-1.0577900	3.6435700
H	-6.3043800	-2.6590400	3.2326200
H	-7.3743300	-1.8063100	2.1063300
C	0.8476700	3.7081400	-0.6838600
H	1.4535100	3.4334300	-1.5412300
C	-6.5602900	-0.7613500	-2.4223400

Continued on next page

Table S11: Cartesian coordinates of the optimized S_{LLCT} geometry of complex **Zn1**.

atom	x	y	z
H	-7.2713900	-0.1777800	-1.8302500
H	-7.1295900	-1.4990800	-2.9970300
H	-6.0609700	-0.1035600	-3.1350000
C	0.1781100	5.3171400	0.9594700
C	0.9599800	4.9765700	-0.1393600
Zn	1.6903200	-0.2050100	0.2941900
S	0.2224300	-1.4708300	1.7395900
S	1.7617700	-2.1168600	-1.1556300
N	4.5435600	0.6884800	0.3732500
C	4.9874400	-0.2263100	-0.6237200
C	5.3262600	-0.8375300	-2.9382600
H	5.2441500	-0.6015100	-3.9945100
C	5.8743600	-2.0477000	-2.5580700
H	6.2247200	-2.7510100	-3.3077200
C	4.8652200	0.0808000	-1.9929400
C	3.4477300	1.2127600	2.4050500
C	5.9664200	-2.3586700	-1.2106100
H	6.3905900	-3.3132900	-0.9165900
C	4.2293100	1.3636900	-2.4961300
H	3.8699200	1.9132300	-1.6257800
C	5.5346500	-1.4700300	-0.2303000
C	1.1218100	-3.3297500	-0.1305300
C	4.9045200	1.7295600	2.4253100

Continued on next page

Table S11: Cartesian coordinates of the optimized S_{LLCT} geometry of complex **Zn1**.

atom	x	y	z
H	5.5321800	1.0363200	2.9956000
H	4.9942100	2.7107900	2.9019600
C	3.3508200	0.5030500	1.0571900
C	5.6722300	-1.8851700	1.2251600
H	5.4596800	-1.0103500	1.8371700
C	2.4332700	2.3535500	2.5592900
H	2.5268200	3.1028300	1.7694300
H	1.4086200	1.9673300	2.5181800
H	2.5625800	2.8561500	3.5276500
C	5.3869400	1.7545000	0.9666500
C	0.4701000	-3.0567100	1.1195700
C	3.0168100	1.0865300	-3.3879900
H	2.2726400	0.4734700	-2.8706300
H	2.5318800	2.0285600	-3.6724400
H	3.3031700	0.5702700	-4.3118900
C	4.6464000	-2.9549200	1.6036800
H	4.7927400	-3.8713100	1.0183200
H	4.7405200	-3.2158000	2.6653900
H	3.6284900	-2.5951700	1.4295800
C	3.2158500	0.2373400	3.5684700
H	3.3560500	0.7430300	4.5343000
H	2.1970400	-0.1644300	3.5431500
H	3.9091400	-0.6089000	3.5231600

Continued on next page

Table S11: Cartesian coordinates of the optimized S_{LLCT} geometry of complex **Zn1**.

atom	x	y	z
C	5.1081400	3.1233100	0.3317400
H	4.0360200	3.3322400	0.2859600
H	5.5855400	3.9129400	0.9239000
H	5.5117300	3.1817700	-0.6819200
C	7.0856600	-2.3568700	1.5748500
H	7.8439500	-1.6197700	1.2881900
H	7.1687400	-2.5242700	2.6556300
H	7.3366000	-3.3018700	1.0795900
C	1.2388700	-4.6821700	-0.5493500
C	5.2370800	2.2451600	-3.2382700
H	5.5653500	1.7708700	-4.1711300
H	4.7869500	3.2112400	-3.4978400
H	6.1309100	2.4386800	-2.6356900
C	-0.0178300	-4.1537000	1.8725800
H	-0.5060600	-3.9458800	2.8181900
C	6.8784100	1.4676000	0.8516600
H	7.1987200	1.4275100	-0.1950200
H	7.4404300	2.2697500	1.3432300
H	7.1517200	0.5238900	1.3297600
C	0.7527400	-5.7133100	0.2057100
C	0.1165300	-5.4443600	1.4359500
H	1.7331000	-4.8808200	-1.4937300
H	0.8589000	-6.7368200	-0.1379600

Continued on next page

Table S11: Cartesian coordinates of the optimized S_{LLCT} geometry of complex **Zn1**.

atom	x	y	z
H	-0.2655000	-6.2622900	2.0378200
H	1.6516900	5.6933300	-0.5706900
H	0.2499200	6.3065100	1.4009900
H	-1.3135800	4.6585400	2.3465400

Table S12: Cartesian coordinates of the optimized $T_{LL/LMCT}$ geometry of complex **Zn1**.

atom	x	y	z
Zn	-1.7825400	0.2305400	0.1745700
S	-0.0506000	1.3726300	-1.1190300
S	-1.8997700	2.0202500	1.6473000
N	-4.5609200	-0.4954200	-0.7612300
C	-5.1215000	0.5157500	0.1145200
C	-6.0134300	1.1899200	2.2349000
H	-6.2593000	0.9716200	3.2682300
C	-6.2733800	2.4510000	1.7320800
H	-6.7308900	3.2058800	2.3636000
C	-5.4269100	0.1982500	1.4502300
C	-3.0535200	-1.8260200	-1.8844100
C	-5.9225500	2.7546200	0.4287800
H	-6.0956500	3.7572300	0.0539100
C	-5.1002500	-1.1288500	2.1180500
H	-4.6938200	-1.8038200	1.3652800
C	-5.3347800	1.8068800	-0.4044900

Continued on next page

Table S12: Cartesian coordinates of the optimized $T_{LL/LMCT}$ geometry of complex **Zn1**.

atom	x	y	z
C	-0.8125900	3.1869100	0.8902300
C	-4.4181600	-1.9702700	-2.5800000
H	-4.4134700	-1.4007700	-3.5143400
H	-4.6500300	-3.0082600	-2.8311100
C	-3.2925500	-0.7368600	-0.8614800
C	-4.9019100	2.2506800	-1.7942100
H	-4.5655800	1.3736600	-2.3482900
C	-2.6265900	-3.1092700	-1.1589800
H	-3.3769000	-3.4527800	-0.4408000
H	-1.6864800	-2.9659400	-0.6216600
H	-2.4773800	-3.9047900	-1.8974000
C	-5.4567800	-1.3739500	-1.6283800
C	-0.0302300	2.9307900	-0.2516200
C	-4.0216700	-0.9549200	3.1919700
H	-3.1110700	-0.5024200	2.7900600
H	-3.7543400	-1.9302200	3.6156400
H	-4.3776600	-0.3203300	4.0114200
C	-3.7085600	3.2067700	-1.7197800
H	-3.9728600	4.1286200	-1.1890000
H	-3.3841100	3.4806800	-2.7308100
H	-2.8615400	2.7544600	-1.1982100
C	-1.9595800	-1.4233700	-2.8756300
H	-1.9000100	-2.1759600	-3.6705700

Continued on next page

Table S12: Cartesian coordinates of the optimized $T_{LL/LMCT}$ geometry of complex **Zn1**.

atom	x	y	z
H	-0.9779100	-1.3681100	-2.3933500
H	-2.1748000	-0.4553800	-3.3413400
C	-6.1537500	-2.4302400	-0.7758900
H	-5.4527200	-3.0618600	-0.2270600
H	-6.7397600	-3.0764800	-1.4366600
H	-6.8437100	-1.9694400	-0.0655500
C	-6.0398700	2.8968100	-2.5883300
H	-6.9336300	2.2662800	-2.6198500
H	-5.7173400	3.0822700	-3.6194000
H	-6.3282200	3.8626000	-2.1589600
C	-0.7260500	4.4618300	1.4689500
C	-6.3320900	-1.7994000	2.7320800
H	-6.7163300	-1.2235500	3.5813200
H	-6.0690400	-2.7961700	3.1046000
H	-7.1481200	-1.9120600	2.0119400
C	0.7845100	3.9393400	-0.7731100
H	1.3724600	3.7267100	-1.6602700
C	-6.5244200	-0.5808600	-2.3665000
H	-7.1957500	-0.0603500	-1.6771100
H	-7.1256200	-1.2852600	-2.9505200
H	-6.0971500	0.1408600	-3.0632800
C	0.0927500	5.4496100	0.9494700
C	0.8554600	5.1915400	-0.1844500

Continued on next page

Table S12: Cartesian coordinates of the optimized $T_{LL/LMCT}$ geometry of complex **Zn1**.

atom	x	y	z
Zn	1.3505200	-0.1680200	0.0802300
S	-0.1869100	-1.1347100	1.6214200
S	1.7008300	-2.1840700	-0.9869100
N	4.3774600	0.5198400	0.2935900
C	4.9959500	-0.3608000	-0.6514700
C	5.4814600	-0.9640200	-2.9336800
H	5.3895300	-0.7735200	-3.9977500
C	6.2021800	-2.0627800	-2.5039900
H	6.6738100	-2.7238400	-3.2246100
C	4.8586300	-0.1053800	-2.0289700
C	3.2897200	0.8317800	2.4491600
C	6.3123300	-2.3177300	-1.1477300
H	6.8710800	-3.1863800	-0.8162300
C	4.0496800	1.0532200	-2.5832600
H	3.5585400	1.5458200	-1.7433700
C	5.7253900	-1.4810300	-0.2028500
C	0.9294600	-3.2692200	0.1709900
C	4.6326700	1.6107200	2.3581400
H	5.4163500	1.0365700	2.8620300
H	4.5691100	2.5818700	2.8572600
C	3.2881700	0.2036700	1.0552400
C	5.8771600	-1.8319000	1.2651300
H	5.5262800	-0.9800000	1.8450200

Continued on next page

Table S12: Cartesian coordinates of the optimized $T_{LL/LMCT}$ geometry of complex **Zn1**.

atom	x	y	z
C	2.1136800	1.7806100	2.7008800
H	2.0357500	2.5586100	1.9379300
H	1.1649500	1.2356800	2.7232200
H	2.2398500	2.2700300	3.6742100
C	5.0024000	1.7586100	0.8643300
C	0.1198700	-2.8424100	1.2438200
C	2.9463600	0.5820900	-3.5328700
H	2.2808200	-0.1374800	-3.0461700
H	2.3379300	1.4352400	-3.8541100
H	3.3592000	0.1105000	-4.4320100
C	5.0001300	-3.0298700	1.6369700
H	5.3165800	-3.9296600	1.0955900
H	5.0737600	-3.2409700	2.7108300
H	3.9490400	-2.8429300	1.3937600
C	3.3077800	-0.2103500	3.5701900
H	3.4049600	0.2865200	4.5435800
H	2.3730900	-0.7817700	3.5727600
H	4.1377900	-0.9139400	3.4634600
C	4.4007100	3.0306400	0.2664400
H	3.3084700	3.0026200	0.2692800
H	4.7204200	3.8988700	0.8531800
H	4.7359600	3.1842500	-0.7617800
C	7.3313100	-2.0776900	1.6711900

Continued on next page

Table S12: Cartesian coordinates of the optimized $T_{LL/LMCT}$ geometry of complex **Zn1**.

atom	x	y	z
H	7.9762200	-1.2348300	1.3976400
H	7.3985400	-2.2163900	2.7567400
H	7.7415900	-2.9786500	1.2015700
C	1.1273100	-4.6471700	-0.0041700
C	4.9438000	2.0816300	-3.2806800
H	5.4032600	1.6576300	-4.1816100
H	4.3565800	2.9559800	-3.5863100
H	5.7539300	2.4276900	-2.6299600
C	-0.4519700	-3.7994400	2.0901100
H	-1.0663100	-3.4587400	2.9176000
C	6.5098700	1.7676400	0.6608700
H	6.7728500	1.8299400	-0.3995100
H	6.9273200	2.6464000	1.1650300
H	6.9844100	0.8776800	1.0819000
C	0.5420500	-5.5804700	0.8325400
C	-0.2549500	-5.1551800	1.8915000
H	1.7558200	-4.9790900	-0.8243200
H	0.7128700	-6.6391300	0.6626400
H	-0.7158600	-5.8748200	2.5607700
H	1.4973100	5.9570800	-0.6086900
H	0.1304300	6.4236900	1.4279200
H	-1.3243900	4.6696300	2.3503400

Table S13: Cartesian coordinates of the optimized T_{LC} geometry of complex **Zn1**.

atom	x	y	z
Zn	3.264888	5.158651	5.287666
S	5.065323	5.550241	6.861546
S	1.752453	5.007947	7.074022
N	1.988639	7.103378	3.282818
C	0.813814	7.241011	4.119714
C	-1.376252	6.533728	4.787565
H	-2.207305	5.840630	4.716863
C	-1.457841	7.596278	5.668267
H	-2.350319	7.738483	6.269439
C	-0.244283	6.322648	4.002169
C	4.048989	6.468226	2.483800
C	-0.386837	8.462719	5.798434
H	-0.445545	9.273317	6.516249
C	-0.212880	5.079648	3.125652
H	0.705172	5.093609	2.539036
C	0.769081	8.305672	5.038928
C	2.708114	5.722735	8.375072
C	3.567312	7.659854	1.640225
H	4.103879	8.564295	1.943084
H	3.749424	7.514444	0.572402
C	3.008347	6.358699	3.578553
C	1.931792	9.252293	5.297768
H	2.690770	9.081597	4.534456

Continued on next page

Table S13: Cartesian coordinates of the optimized T_{LC} geometry of complex **Zn1**.

atom	x	y	z
C	4.061159	5.160928	1.680441
H	3.092059	4.945546	1.221335
H	4.335299	4.313243	2.310383
H	4.803879	5.239852	0.879065
C	2.078389	7.828292	1.942478
C	4.095755	5.953232	8.298461
C	-0.179001	3.804992	3.974077
H	0.671628	3.794812	4.660502
H	-0.099726	2.924872	3.325138
H	-1.092454	3.701405	4.570728
C	2.595508	8.954349	6.643186
H	1.895444	9.103400	7.473233
H	3.450179	9.624108	6.797077
H	2.954863	7.924226	6.694072
C	5.440147	6.719613	3.067377
H	6.145324	6.913850	2.250515
H	5.803973	5.852333	3.627481
H	5.443606	7.591047	3.731845
C	1.179737	7.153444	0.909521
H	1.412706	6.097006	0.767163
H	1.317304	7.658575	-0.051546
H	0.126963	7.247259	1.185620
C	1.523275	10.725358	5.227456

Continued on next page

Table S13: Cartesian coordinates of the optimized T_{LC} geometry of complex **Zn1**.

atom	x	y	z
H	0.995911	10.964936	4.298877
H	2.413173	11.362608	5.287574
H	0.870105	11.000182	6.063042
C	2.047476	6.078436	9.559520
C	-1.390453	5.015607	2.149389
H	-2.339438	4.875397	2.678814
H	-1.266537	4.165120	1.469005
H	-1.479426	5.922598	1.543821
C	4.758811	6.531824	9.384223
H	5.826519	6.711208	9.305320
C	1.672804	9.292725	2.026395
H	0.639279	9.411793	2.364519
H	1.746019	9.720379	1.021127
H	2.330662	9.870986	2.675661
C	2.718941	6.638681	10.633427
C	4.087491	6.872075	10.547927
Zn	5.496363	3.097432	6.646739
S	3.759997	2.694837	4.997384
S	7.151109	3.232744	4.958774
N	6.676642	1.184653	8.739241
C	7.949032	1.159774	8.045254
C	10.146691	2.036318	7.660929
H	10.913824	2.778596	7.852108

Continued on next page

Table S13: Cartesian coordinates of the optimized T_{LC} geometry of complex **Zn1**.

atom	x	y	z
C	10.402763	1.018241	6.761806
H	11.365451	0.959983	6.263955
C	8.920677	2.139171	8.316826
C	4.475418	1.599256	9.271113
C	9.417605	0.088321	6.480705
H	9.615405	-0.687403	5.749467
C	8.708579	3.333569	9.234393
H	7.732439	3.235744	9.708429
C	8.174501	0.136345	7.104787
C	6.179254	2.946183	3.556439
C	4.953623	0.415789	10.128972
H	4.559086	-0.518093	9.716758
H	4.611454	0.486614	11.164476
C	5.642803	1.856323	8.337473
C	7.127135	-0.886704	6.689205
H	6.271980	-0.796558	7.359361
C	4.205854	2.853000	10.112173
H	5.075084	3.157244	10.701934
H	3.912734	3.696779	9.484780
H	3.383819	2.645587	10.806173
C	6.478511	0.404640	10.036679
C	4.842711	2.290044	3.667008
C	8.690010	4.644241	8.442883

Continued on next page

Table S13: Cartesian coordinates of the optimized T_{LC} geometry of complex **Zn1**.

atom	x	y	z
H	7.912996	4.644986	7.674072
H	8.494802	5.486281	9.117653
H	9.652896	4.825045	7.951736
C	6.606093	-0.608776	5.278105
H	7.410665	-0.678665	4.536962
H	5.837197	-1.343902	5.011562
H	6.168191	0.388416	5.196524
C	3.209902	1.242484	8.488339
H	2.427552	0.936817	9.193146
H	2.834339	2.095706	7.914333
H	3.385703	0.411586	7.796208
C	7.148156	1.130156	11.200933
H	6.790988	2.153794	11.325389
H	6.925763	0.583579	12.122617
H	8.233482	1.148348	11.080431
C	7.641917	-2.325472	6.782260
H	8.080829	-2.546758	7.760011
H	6.818015	-3.028111	6.611758
H	8.403767	-2.527555	6.021317
C	6.891089	2.763938	2.287905
C	9.761660	3.416201	10.342828
H	10.752037	3.645944	9.934337
H	9.503649	4.216866	11.045675

Continued on next page

Table S13: Cartesian coordinates of the optimized T_{LC} geometry of complex **Zn1**.

atom	x	y	z
H	9.845545	2.483338	10.908733
C	4.460033	1.380366	2.711605
H	3.499154	0.881824	2.811159
C	7.041366	-1.007664	9.979935
H	8.118327	-1.011507	9.787744
H	6.874913	-1.475424	10.955832
H	6.542426	-1.625347	9.233170
C	6.466282	1.876461	1.361086
C	5.256025	1.119679	1.578947
H	7.792831	3.348147	2.120797
H	7.015812	1.744876	0.432900
H	4.931872	0.390003	0.844950
H	4.627204	7.318263	11.377441
H	2.171382	6.899369	11.534342
H	0.978068	5.905216	9.626187

References

(1) Sheldrick, G. M. *SHELXT* – Integrated space-group and crystal-structure determination. *Acta Crystallogr. Sect. A* **2015**, *71*, 3–8.

(2) Sheldrick, G. M. Crystal structure refinement with *SHELXL*. *Acta Crystallogr. Sect. C* **2015**, *71*, 3–8.

(3) Dolomanov, O. V.; Bourhis, L. J.; Gildea, R. J.; Howard, J. A. K.; Puschmann, H. *OLEX2*: a complete structure solution, refinement and analysis program. *J. Appl. Crystallogr.* **2009**, *42*, 339–341.

(4) Spek, A. L. *PLATON* SQUEEZE: a tool for the calculation of the disordered solvent contribution to the calculated structure factors. *Acta Crystallogr. Sect. C* **2015**, *71*, 9–18.

(5) Frisch, M. J. et al. Gaussian 16, Revision A.03. 2016; Gaussian Inc. Wallingford CT.

(6) Von Arnim, M.; Ahlrichs, R. Performance of Parallel TURBOMOLE for Density Functional Calculations. *J. Comput. Chem.* **1998**, *19*, 1746–1757.

(7) Furche, F.; Ahlrichs, R. Adiabatic Time-Dependent Density Functional Methods for Excited State Properties. *J. Chem. Phys.* **2002**, *117*, 7433–7447.

(8) Hirata, S.; Head-Gordon, M. Time-dependent density functional theory within the Tamm–Dancoff approximation. *Chem. Phys. Lett.* **1999**, *314*, 291–299.

(9) Figgen, D.; Rauhut, G.; Dolg, M.; Stoll, H. Energy-Consistent Pseudopotentials for Group 11 and 12 Atoms: Adjustment to Multi-Configuration Dirac–Hartree–Fock Data. *Chem. Phys.* **2005**, *311*, 227–244.

(10) Schäfer, A.; Horn, H.; Ahlrichs, R. Fully Optimized Contracted Gaussian Basis Sets for Atoms Li to Kr. *J. Chem. Phys.* **1992**, *97*, 2571–2577.

(11) Lee, C.; Yang, W.; Parr, R. G. Development of the Colle-Salvetti Correlation-Energy Formula into a Functional of the Electron Density. *Phys. Rev. B* **1988**, *37*, 785–789.

(12) Becke, A. D. A New Mixing of Hartree-Fock and Local Density-Functional Theories. *J. Chem. Phys.* **1993**, *98*, 1372–1377.

(13) Cancès, E.; Mennucci, B.; Tomasi, J. A new integral equation formalism for the polarizable continuum model: Theoretical background and applications to isotropic and anisotropic dielectrics. *J. Chem. Phys.* **1997**, *107*, 3032.

(14) Mennucci, B.; Cancès, E.; Tomasi, J. Evaluation of Solvent Effects in Isotropic and Anisotropic Dielectrics and in Ionic Solutions with a Unified Integral Equation Method: Theoretical Bases, Computational Implementation, and Numerical Applications. *J. Phys. Chem. B* **1997**, *101*, 10506.

(15) Grimme, S.; Waletzke, M. A Combination of Kohn–Sham Density Functional Theory and Multi-Reference Configuration Interaction Methods. *J. Chem. Phys.* **1999**, *111*, 5645–5655.

(16) Marian, C. M.; Heil, A.; Kleinschmidt, M. The DFT/MRCI Method. *WIREs Comp. Mol. Sci.* **2019**, *9*, e1394.

(17) Kleinschmidt, M.; Tatchen, J.; Marian, C. M. Spin-Orbit Coupling of DFT/MRCI Wavefunctions: Method, Test Calculations, and Application to Thiophene. *J. Comput. Chem.* **2002**, *23*, 824–833.

(18) Kleinschmidt, M.; Marian, C. M. Efficient Generation of Matrix Elements for One-Electron Spin–Orbit Operators. *Chem. Phys.* **2005**, *311*, 71–79.

5.3 Supporting information for chapter 2.3 (Structural Control of Highly Efficient Thermally Activated Delayed Fluorescence in Carbene Zinc(II) Dithiolates)

Supporting Information

Structural Control of Highly Efficient Thermally Activated Delayed Fluorescence in Carbene Zinc(II) Dithiolates

M. Mitra, O. Mrózek, M. Putscher, J. Guhl, B. Hupp, A. Belyaev, C. M. Marian, A. Steffen**

Table of Contents

1 METHODS AND MATERIALS 2

1.1 GENERAL REMARKS 2
1.2 PHOTOPHYSICAL MEASUREMENTS 2
1.3 COMPUTATIONAL METHODS AND TECHNICAL DETAILS 3

2 SYNTHETIC PROCEDURES 5

3 NMR SPECTRA 12

4 THERMOGRAVIMETRIC ANALYSIS/DIFFERENTIAL SCANNING CALORIMETRY 19

5 X-RAY CRYSTALLOGRAPHY 20

6 PHOTOPHYSICAL MEASUREMENTS 24

6.1 ABSORPTION SPECTRA 24
6.2 PHOTOPHYSICAL DATA IN DICHLOROMETHANE 25
6.3 EMISSION AND EXCITATION SPECTRA AT 297K 25
6.4 EMISSION AND EXCITATION SPECTRA AT 77 K 28
6.5 TEMPERATURE-DEPENDENT EMISSION SPECTRA 29
6.6 DETAILS OF LIFETIME MEASUREMENTS 30

7 THEORETICAL CALCULATIONS 35

7.1 TORSION PATH 35
7.2 STATES, ENERGIES AND OSCILLATOR STRENGTH 36
7.3 CROSSING POINT 39
7.4 COORDINATES 41

8 REFERENCES: 65

1 Methods and Materials

1.1 General remarks

All operations were performed under an argon atmosphere using conventional Schlenk-line techniques or glovebox. The solvents were dried using the Technology Inc. Pure-Solv system or standard methods[1], degassed and stored under activated 4Å molecular sieves. Menthyl-substituted cyclic (alkyl(amino)carbene precursor (^{Menth}cAACHBF$_4$) was prepared according to the method reported in the literature,[2] and to ensure enantiopurity, the enantiomerically pure L-menthol was used following the procedure reported by Ung et al.[3] All other starting materials were commercially available and were used without further purification. ^{1}H, ^{13}C{^{1}H} APT, ^{1}H-^{13}C HSQC, ^{1}H-^{13}C HSMB, ^{1}H-^{1}H COSY and ^{1}H-^{15}N HMBC were measured at 297 K on Bruker 500 Avance and Bruker 600 Avance spectrometer. The chemical shifts are given in ppm relative to residual signals of the solvent [^{1}H, ^{13}C: CD_3CN (1.94, 118.69 ppm), $CDCl_3$ (7.26, 77.16 ppm), CD_2Cl_2 (5.32, 53.84 ppm), C_6D_6 (7.16, 128.06 ppm)]. TGA/DSC data were recorded using a STA650 instrument (TA instruments, USA) with a heat rate of 10 °C/min and under constant flow of nitrogen gas. CHN analysis were performed with Leco CHNS-932.

1.2 Photophysical Measurements

All photophysical measurements were performed under rigorous exclusion of air and moisture. Dichloromethane (DCM) used for steady-state absorption spectroscopy was dried and degassed prior to the measurement. The solid-state measurements were performed either in single-crystalline form (sample assigned as 'crystals') or single-crystals were ground and dried under vacuum for 24 h (sample assigned as 'powder'). Photophysical measurements in the single-crystalline form of **CZT3a** and **CZT3b** were

performed either in a thin quartz EPR tube or using 4 K cryostat sample holders, which allows sample preparation without applying mechanical stress to the crystals, keeping them undamaged. PMMA and PS films were prepared by drop casting method with 1 wt-% of complexes dissolved in DCM followed by evaporation of DCM and drying of polymeric films under high vacuum. UV-visible absorption spectroscopy was performed on an Agilent Cary 5000 spectrophotometer using standard 1 cm path-length quartz cells. Excitation and emission spectra were recorded on an Edinburgh Instrument FLS1000 spectrometer, equipped with a 450 W Xenon arc lamp, double monochromators for the excitation and emission pathways, and a red-sensitive photomultiplier (PMT-980) as a detector. The excitation and emission spectra were corrected using the standard corrections supplied by the manufacturer for the excitation source's spectral power and the detector's sensitivity. Quantum yields of solid samples and polymeric matrices were measured using an integrating cryosphere (Microstat N2) from Oxford Instruments. The luminescence lifetimes were measured using a µF2 pulsed 60 W Xenon microsecond flashlamp, with a repetition rate of 10-100 Hz and a multichannel scaling (MCS) module or with VPLED (449.6 nm with 37 mW), with 100 ns pulse width and an MCS module, depending on the time range. The emission was collected at a right angle to the excitation source. The low-temperature experiments were performed using a 4 K cryostat (CS204SI-FMX-1SS) from Advanced Research System equipped with a closed cycle water-cooled helium compressor.

1.3 Computational Methods and Technical details

The Gaussian 16 software package[4] was employed for all geometry optimizations and vibrational frequency analyses. To account for electrostatic solvent-solute

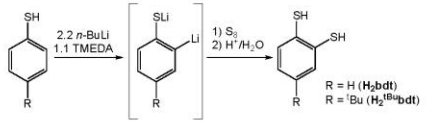
interactions, we utilized the polarizable continuum model (PCM)[5,6] (DCM, ε_r = 8.93). Equilibrium geometries of the electronic ground states were determined using Kohn–Sham (KS) DFT with the BH-LYP[7,8] functional. Excited-state geometries were calculated with time-dependent DFT (TDDFT), and the Tamm–Dancoff approximation (TDA) was added for triplet states. We used the def2-SV(P) basis set to represent hydrogen, carbon, nitrogen, and oxygen atoms. Sulfur was described using the def2-SVPD basis set.[9] To accurately represent the zinc ion, an effective core potential (ECP10MDF) was incorporated, along with the corresponding basis set (10-mdf 6s5p3d)[10].

Excitation energies were calculated using the DFT/MRCI method[11,12] with the R2018 Hamiltonian[13], employing the short parameter set and a selection threshold of 0.8 E_H. BHLYP-KS orbitals and three-index-two-electron integrals were generated with the Turbomole program package[14,15]. In our calculations, the first 21 singlet and 20 triplet roots were determined for each geometry. To account for solvent-solute interactions, we considered PCM point charges.

For the determination of spin-orbit coupling matrix elements (SOCMEs), we utilized the SPOCK program[16,17]. The effective one-electron Hamiltonian contains an atomic mean-field approximation of the Breit–Pauli spin–orbit operator[18,19] on all atoms except for zinc which comprises a relativistic ECP[10]. The phosphorescence lifetimes were computed using the variational multireference spin-orbit configuration interaction (MRSOCI) method[20]. The rate constants for intersystem crossing (ISC) and reverse ISC (rISC) were calculated within perturbation theory according to Fermi's golden rule. The vibrational density of states within the Franck-Condon (FC) approximation was calculated using the VIBES program[21,22] (65536 grid points, interval of 3000 fs, damping of 10 cm^{-1}).

2 Synthetic Procedures

Preparation of dithiols and dithiolates

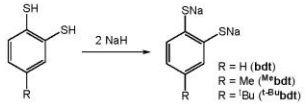


$C_6H_4S_2H_2$ (**H_2bdt**)

5 mL of benzenethiol (49 mmol) was added dropwise to a mixture of *n*-BuLi (41 mL, 2.5 M, 103 mmol) and TMEDA (54 mmol, 8.1 mL) in *n*-pentane (50 mL) at -78 °C, and the mixture was stirred overnight at room temperature. After that, the solution was cooled to -78°C and octasulfur (49 mmol) was added portion-wise. The mixture was stirred for two hours at -78°C and at room temperature overnight. Then, the mixture was carefully quenched with 100 mL of diluted hydrochloric acid solution and extracted with Et_2O (3 × 50 mL). Combined organic layers were dried over $MgSO_4$, and solvents were vacuum-evaporated. The crude product was distilled under vacuum (55 °C, 0.2 mbar) to give 1.4 mL of colorless liquid (24 %). Analytic data are in line with those published elsewhere.[23] ^{1}H NMR (C_6D_6, 500 MHz): δ [ppm] = 7.96 (m, 2H, $H^{3,6}$, $C_6H_4S_2$), 6.65 (m, $H^{4,5}$, $C_6H_4S_2$, 2H), 3.35 (s, 2H, S*H*). ^{13}C{^{1}H} NMR (C_6D_6, 125 MHz): δ [ppm] = 131.4 (s, 2C), 130.9 (s, 2C), 126.4 (s, 2C).

$C_6H_3C(CH_3)_3S_2$ (**$H_2^{t\text{-}Bu}$bdt**)

The compound was prepared following the analogous procedure as described above for **H_2bdt** but with 2.7 mL of 4-methyl benzenethiol (16 mmol), 14.8 mL of *n*-BuLi (37 mmol, 2.5 M) and 8.1 mL of TMEDA (17.6 mmol, 2.6 mL). Vacuum distillation (95 °C, 0.05 mbar) afforded 2.65 mL (82 %) of colorless, liquid product. Spectroscopic data are in line with those published elsewhere.[24] ^{1}H NMR ($CDCl_3$, 500 MHz): δ [ppm] = 7.38 (d, $^3J(^1H,^1H)$ = 2.1 Hz, 1H, H^6, $C_6H_3S_2{}^tBu$), 7.30 (d, $^3J(^1H,^1H)$ = 8.2 Hz, 1H, H^3, $C_6H_3S_2{}^tBu$), 7.10 (dd, $^3J(^1H,^1H)$ = 8.2 Hz, $^3J(^1H,^1H)$ = 2.2 Hz, 1H, H^5, $C_6H_3S_2$t-Bu), 3.77 (s, 1H, S*H*), 3.61 (s, 1H, S*H*), 1.27 (s, 9H, $C(CH_3)_3$). ^{13}C{^{1}H} NMR ($CDCl_3$, 125 MHz): δ [ppm] = 150.46, 131.33, 131.26, 128.09, 127.34, 124.49, 34.52, 31.24.



$C_6H_4S_2Na_2$ (**Na_2bdt**)

320 mg (13.3 mmol) of NaH was dispersed in 40 mL of THF, and 800 µL (1 g, 7 mmol) of benzenethiol was added dropwise, while the evolution of H_2 was observed. After complete addition, the mixture was stirred for one hour at 60 °C and then overnight at room temperature. After that, THF was filtered off, and the solid was washed with an additional portion of THF (2 × 15 mL), *n*-pentane (15 mL), and the product was vacuum-dried (6 hours at 50 °C) to give a white powder. Yield: 1.08 g (83 %, 5.81 mol). Very low solubility prevented the characterization of the compound by NMR spectroscopy.

$C_6H_3(CH_3)S_2Na_2$ (**Na_2^{Me}bdt**)

The compound was prepared following the analogous procedure as described above for **Na_2bdt** but with 930 µL of toluene-3,4-dithiol (1.09 g, 7 mmol). Yield: 1.61 g (87 %, 8.04 mol).

$C_6H_3C(CH_3)_3S_2Na2$ (**$Na_2^{t\text{-}Bu}$bdt**)

The compound was prepared following the analogous procedure as described above for **Na_2bdt** but with 1.39 g of 4-tert-butyl-1,2-benzedithiol (7 mmol). Yield: 1.89 g (90 %, 7.78 mol).

[($ZnCl_2$(^{Menth}cAAC)] (**1**)

50 mg of (107 μmol) of ^{Menth}cAACHBF$_4$ was mixed with 1.05 equiv. of NaHMDS (112 μmol, 21.5 mg) in 7 mL of toluene. The mixture was stirred at room temperature overnight. After that, the suspension was filtered, and the solvent vacuum-evaporated to dryness to give pale white powder. The free carbene was mixed with 1 equiv. of $ZnCl_2$ (107 μmol, 14.5 mg) and dissolved in 5 mL of THF. The mixture was stirred at room temperature overnight, filtrated through a celite pad and concentrated in a vacuum to a volume of ~2 mL. The gas-phase diffusion of *n*-pentane into this solution afforded white single crystals of **1**. However, characterization by NMR revealed contamination of **1** with protonated carbene, and attempts to separate this mixture were unsuccessful and/or increased concentration of the by-product, which implies high reactivity of **1**. For this reason, **1** was used for the preparation of target thiolate complexes without previous isolation or purification. ^{1}H NMR of main product (CD_3CN, 600 MHz): δ [ppm] = 7.62 (t, $^3J(^1H,^1H)$ = 7.8 Hz, 1H, H^4, $C_6H_3{}^iPr_2$), 7.48 (m, 2H, H^{3,5}, $C_6H_3{}^iPr_2$), 2.67 (sept, $^3J(^1H,^1H)$ = 6.7 Hz, 2H, CH^{iPr}), 2.13-2.30 (m, 3H), 1.80-1.84 (m, 3H), 1.28-1.69 (m, 16H), 1.10-1.15 (m, 7H), 1.05 (d, $^3J(^1H,^1H)$ = 6.8 Hz), 0.95 (d, $^3J(^1H,^1H)$ = 6.4 Hz), 0.77 (d, $^3J(^1H,^1H)$ = 6.9 Hz).

[(Zn(bdt)(^{Menth}cAAC)] (**CZT1**)

100 mg of (213 μmol) of ^{Menthc}cAACHBF$_4$ was mixed with 1.05 equiv. of NaHMDS (224 μmol, 41 mg) in 10 mL of toluene. The mixture was stirred at room temperature overnight. After that, the suspension was filtered, and the solvent vacuum-evaporated to dryness to give white powder, which was mixed with 1 equiv. of $ZnCl_2$ (213 μmol, 29 mg) and dissolved in 5 mL of THF. The mixture was stirred at room temperature for two hours. After that, the solution was cannula-transferred to a dry Schlenk tube containing 1 equiv. of **Na_2bdt** (213 μmol, 40 mg) dissolved in 7 mL of THF and the mixture was stirred overnight at room temperature. After that, solvents were vacuum evaporated to dryness, and the solid residue was extracted with toluene (3 × 5 mL). Toluene fractions were vacuum-evaporated to dryness, and the crude product was washed with *n*-pentane (3 mL) and crystalized using gas-phase diffusion of *n*-pentane into the solution of **CZT1** in DCM (1.5 mL) to give 79 mg of yellow single-crystals (63 %, 135 μmol). CHNS analysis calcd for $C_{33}H_{48}NS_2Zn$: C, 67.38; H, 8.22; N, 2.38. Found: C, 66.7; H, 8.1; N, 2.5. ^{1}H NMR (C_6D_6, 400 MHz): δ [ppm] = 8.04 (m, 2H, H^{3,6}, $C_6H_4S_2$), 7.21 (t, $^3J(^1H,^1H)$ = 7.8 Hz, 1H, H^4, $C_6H_3{}^iPr_2$), 7.05 (m, 2H, H^{3,5}, $C_6H_3{}^iPr_2$), 6.80 (m, 2H, H^{4,5}, $C_6H_4S_2$), 2.80-2.62 (m, 2H, C$H(CH_3)_2$, Dipp, 1H, C$H(CH_3)_2$, menthyl, 1H, CHCH$_3$, menthyl), 2.10 (m, 1H, CH_2, cAAC), 1.83 (m, 3H, menthyl), 1.64 (m, 1H, menthyl), 1.52 (d, $^3J(^1H,^1H)$ = 6.7 Hz, 3H, CH(C$H_3)_2$, Dipp), 1.45 (d, $^3J(^1H,^1H)$ = 6.8 Hz, 3H, -CH(C$H_3)_2$, Dipp), 1.22-1.43 (m, 3H, menthyl), 1.04 (d, $^3J(^1H,^1H)$ = 6.6 Hz, 3H, -CH(C$H_3)_2$, Dipp), 1.02 (d, $^3J(^1H,^1H)$ = 6.6 Hz, 3H, CH(C$H_3)_2$, menthyl), 0.99 (d, $^3J(^1H,^1H)$ = 6.6 Hz, 3H, CH(C$H_3)_2$, Dipp), 0.94 (s, 3H, C(C$H_3)_2$, cAAC), 0.91 (s, 3H, C(C$H_3)_2$, cAAC), 0.88 (d, $^3J(^1H,^1H)$ = 6.6 Hz, 3H, CHCH_3, menthyl), 0.86 (d, $^3J(^1H,^1H)$ = 6.9 Hz, 3H, CH(C$H_3)_2$, menthyl), 0.84 (m, 1H, CH_2, cAAC).

$^{13}C\{^1H\}$ NMR (C_6D_6, 100 MHz): δ [ppm] = 246.4 (s, $C^{carbene}$), 145.3 (s, 2C, $C^{2,6}$, $C_6H_3{}^iPr_2$), 144.8 (d, 2C, $C^{1,2}$, $C_6H_4S_2$) , 134.3 (s, 1C, C^1, $C_6H_3{}^iPr_2$), 131.1 (s, 1C, C^4, $C_6H_3{}^iPr_2$), 130.6 (s, 1C, $C^{3,6}$, $C_6H_4S_2$), 126.5 (d, 2C, $C^{3,5}$, $C_6H_3{}^iPr_2$,), 122.2 (s, 2C, $C^{4,5}$, $C_6H_4S_2$), 79.8 (s, 2 C, NCC^{carbene}), 65.6 (s, 1C, CC^{carbene}), 52.6 (s, 1C, menthyl), 52.5 (s, 1C, menthyl), 48.7 (s, 1C, menthyl), 35.1 (s, 1C, CH_2, cAAC), 30.3 (s, 1C, $(CH_3)_2$, *cAAC*) , 29.8 (s, 1C, $(CH_3)_2$, *cAAC*), 29.4 (s, 1C, $CH^{i\text{-}Pr}_2$, Dipp), 29.1 (s, 1C, $CH^{i\text{-}Pr}_2$, Dipp), 27.8 (s, 1C, menthyl), 27.4(s, 1C, menthyl), 26.9 (s, 1C, menthyl), 24.8 (s,2C, $CH_3{}^{iPr}$, Dipp), 24.34 (s,2C, $CH_3{}^{iPr}$, Dipp), 23.56 (d, 1C, menthyl), 22.9 (s, 1C, menthyl),20.3 (s, 1C, menthyl). ^{15}N (60 MHz, CD_2Cl_2): δ [ppm]= - 140.76 ppm.

[(Zn(^{Me}bdt)(^{Menth}cAAC)] (**CZT2**)

The compound was prepared following the analogous procedure as described above for **CZT1** but with 43 mg of **$Na_2{}^{Me}$bdt** (213 μmol). Yield: 83 mg (65 %, 139 μmol). CHNS analysis calcd for $C_{34}H_{50}NS_2Zn$: C, 67.80; H, 8.37; N, 2.33. Found: C, 68.3; H, 8.3; N, 2.5. ^1H NMR (C_6D_6, 600 MHz): δ [ppm] = 7.96 (d, $^3J(^1H,^1H)$ = 7.9 Hz, 1H, H^6, $C_6H_3(CH_3)S_2$), 7.86 (d, $^3J(^1H,^1H)$ = 1.5 Hz, 1H, H^5, $C_6H_3(CH_3)S_2$), 7.22 (t, $^3J(^1H,^1H)$ = 7.8 Hz, 1H, H^4, $C_6H_3{}^iPr_2$), 7.07 (m, 2H, $H^{4,5}$, $C_6H_3{}^iPr_2$), 6.64 (dd, $^3J(^1H,^1H)$ = 7.9 Hz, $^4J(^1H,^1H)$ = 1.5 Hz, 1H, H^3, $C_6H_3(CH_3)S_2$), 2.80-2.62 (m, 2H, $CH(CH_3)_2$, Dipp, 1H, $CH(CH_3)_2$, menthyl, 1H, $CHCH_3$, menthyl), 2.10 (m, 1H, CH_2, cAAC), 2.04 (s, 3H, CH_3, $C_6H_3(CH_3)S_2$), 1.87-1.77 (m, 3H, menthyl), 1.63 (m, 1H, menthyl), 1.53 (d, $^3J(^1H,^1H)$ = 6.6 Hz, 3H, $CH(CH_3)_2$, Dipp), 1.46 (d, $^3J(^1H,^1H)$ = 6.7 Hz, 3H, $CH(CH_3)_2$, Dipp), 1.20-1.06 (m, 3H, menthyl), 1.04 (d, $^3J(^1H,^1H)$ = 6.6 Hz, 3H, $CH(CH_3)_2$, Dipp), 1.02 (d, $^3J(^1H,^1H)$ = 6.6 Hz, 3H, $CH(CH_3)_2$, menthyl), 0.99 (d, $^3J(^1H,^1H)$ = 6.6 Hz, 3H, $CH(CH_3)_2$, Dipp), 0.94 (s, 3H, $C(CH_3)_2$, cAAC), 0.91 (s, 3H, $C(CH_3)_2$, cAAC), 0.87 (d, 3H, $^3J(^1H,^1H)$

= 6.3 Hz, $CHCH_3$, menthyl), 0.85 (d, 3H, $^3J(^1H,^1H)$ = 6.9 Hz, $CH(CH_3)_2$, menthyl), 0.83 (m, 1H, CH_2, cAAC). $^{13}C\{^1H\}$ NMR (C_6D_6, 100 MHz): δ [ppm] = 246.8 (s, 1C, $C^{carbene}$), 145.5 (s, 2C, $C^{2,6,}$ $C_6H_3{}^iPr_2$), 144.9 (s, 1C, $C_6H_3(CH_3)S_2$), 144.6 (s, 1C, $C_6H_3(CH_3)S_2$), 141.3 (1C, C^4, $C_6H_3(CH_3)S_2$), 134.5 (s, 1C, C^1, $C_6H_3{}^iPr_2$), 131.4 (s, 1C, C^6, $C_6H_3(CH_3)S_2$), 131.2 (s, 1C, C^4, $C_6H_3{}^iPr_2$), 130.4 (s, 1C, C^3, $C_6H_3(CH_3)S_2$), 126.6 (d, 2C, $C^{3,5}$, $C_6H_3{}^iPr_2$), 123.7 (s, 1C, C^5, $C_6H_3(CH_3)S_2$), 79.87 (s, 2C, NCC^{carbene}), 65.74 (s, 1C, CC^{carbene}), 52.80 (s, 1C, menthyl), 52.68 (s, 1C, menthyl), 48.90 (s, 1C, menthyl), 35.23 (s, 1C, CH_2, cAAC), 30.38 (s, 1C, $(CH_3)_2$, *cAAC*), 29.97 (s, 1C, $(CH_3)_2$, *cAAC*), 29.60 (s, 1C, CH^{iPr}_2, Dipp), 29.28 (s, 1C, CH^{iPr}_2, Dipp), 29.20 (s, 1C, menthyl), 28.02 (s, 1C, menthyl), 27.56 (s,1C, $CH_3{}^{iPr}$, Dipp), 27.13 (s,1C, $CH_3{}^{iPr}$, Dipp), 24.94 (s,1C, $CH_3{}^{iPr}$, Dipp), 24.51(s, 1C, $CH_3{}^{iPr}$, Dipp), 23.73 (d, 2C, menthyl), 23.14 (s, 1C, menthyl), 20.87 (s, 1C, CH_3, $C_6H_3(CH_3)S_2$), 20.41 (s, 1C, Menthyl). ^{15}N (60 MHz, CD_2Cl_2): δ [ppm]=- 141.08 ppm.

[(Zn($^{1\text{-}Bu}$bdt)(^{Menth}cAAC)] (**CZT3**)

The compound was prepared following analogous procedure as described above for **CZT1** but with 52 mg of **$Na_2{}^{t\text{-}Bu}$bdt** (213 μmol). Yield: 106 mg (77 %, 164 μmol). CHNS analysis calcd for $C_{37}H_{56}NS_2Zn$: C, 68.97; H, 8.76; N, 2.17. Found: C, 69.2; H, 9.2; N, 2.2. ^1H NMR (C_6D_6, 600 MHz): δ [ppm] = 8.03 (d, $^3J(^1H,^1H)$ = 2.2 Hz, 1H, H^3, $C_6H_3C(CH_3)_3S_2$), 7.96 (d, $^3J(^1H,^1H)$ = 8.2 Hz, 1H, H^6, $C_6H_3C(CH_3)_3S_2$), 7.22 (t, $^3J(^1H,^1H)$ = 7.8 Hz, 1H, H^4, $C_6H_3{}^iPr_2$), 7.09 (m, $H^{3,5}$, $C_6H_3{}^iPr_2$), 6.83 (dd, $^3J(^1H,^1H)$ = 8.2 Hz, $^3J(^1H,^1H)$ = 2.3 Hz, 1H, H^5, $C_6H_3C(CH_3)_3S_2$), 2.85-2.63 (m, 2H, $CH(CH_3)_2$, Dipp, 1H, $CH(CH_3)_2$, menthyl, 1H, $CHCH_3$, menthyl), 2.14 (m, 1H, CH_2, cAAC), 1.90-1.79 (m, 3H, menthyl), 1.65 (m, 1H, $CHCH_3$, menthyl), 1.54 (d, $^3J(^1H,^1H)$ = 6.7 Hz, 3H, $CH(CH_3)_2$, Dipp), 1.47 (d, $^3J(^1H,^1H)$ = 6.7 Hz, 3H, $CH(CH_3)_2$, Dipp), 1.31-1.18 (m, 3H,

menthyl), 1.17 (s, 9H, $^{tbu}CH_3$), 1.06 (m, 3H, $CH(CH_3)_2$, Dipp, $CH(CH_3)_2$, menthyl), 0.99 (d, $^3J(^1H,^1H)$ = 6.7 Hz, 3H, $CH(CH_3)_2$, Dipp), 0.96 (s, 3H, $C(CH_3)_2$, cAAC), 0.93 (s, 3H, $C(CH_3)_2$, cAAC), 0.90 (d, $^3J(^1H,^1H)$ = 6.3 Hz, 3H, $CHCH_3$, menthyl), 0.87 (d, $^3J(^1H,^1H)$ = 6.9 Hz, 3H, $CH(CH_3)_2$, menthyl), 0.85 (m, 1H, CH_2, cAAC). $^{13}C\{^1H\}$ NMR (C_6D_6, 100 MHz): δ [ppm] = 246.6 (s, 1C, $C^{carbene}$), 145.3 (s, 1C, $C_6H_3{}^iPr_2$), 144.8 (s, 1C, $C_6H_3{}^iPr_2$), 144.4 (s, 1C, $C_6H_3C(CH_3)_3S_2$), 144.2 (s, 1C, $C_6H_3C(CH_3)_3S_2$), 141.2 (1C, C^4, $C_6H_3C(CH_3)_3S_2$), 134.4 (s, 1C, C^1, $C_6H_3{}^iPr_2$), 131.0 (s, 1C, C^4, $C_6H_3{}^iPr_2$), 130.1 (s, 1C, C^6, $C_6H_3C(CH_3)_3S_2$), 127.5 (s, 1C, C^3, $C_6H_3C(CH_3)_3S_2$), 126.5 (2C, $C^{3,5}$, $C_6H_3{}^iPr_2$), 119.7 (s, 1C, C^5, $C_6H_3C(CH_3)_3S_2$), 79.8 (s, 2 C, $NCC^{carbene}$) , 65.6 (s, 1C, $CC^{carbene}$), 52.6 (s, 1C, menthyl), 52.5 (s, 1C, menthyl), 48.8 (s, 1C, menthyl), 35.1 (s, 1C, CH_2, cAAC), 33.9 (s, 1C, $C(CH_3)_3$, $C_6H_3C(CH_3)_3S_2$), 31.5 (3C, $C(CH_3)_3$, $C_6H_3C(CH_3)_3S_2$), 30.2 (s, 1C, $(CH_3)_2$, *cAAC*), 29.8 (s, 1C, $(CH_3)_2$, *cAAC*), 29.5 (s, 1C, $CH^{i\text{-}Pr}{}_2$, Dipp), 29.0 (s, 1C, $CH^{i\text{-}Pr}{}_2$, Dipp), 27.8 (s, 1C, menthyl), 27.4 (s, 1C, menthyl), 27.0 (s, 1C, menthyl), 24.8 (s, 2C, $CH_3{}^{iPr}$, Dipp), 24.4 (s, 2C, $CH_3{}^{iPr}$, Dipp), 23.6 (d, 1C, menthyl), 22.9 (s, 1C, menthyl), 20.3 (s, 1C, menthyl). ^{15}N (60 MHz, CD_2Cl_2): δ [ppm]=- 140.83 ppm. Two different types of single-crystals were obtained by gas-phase diffusion of *n*-pentane into the THF solution of **CZT3** (denoted as **CZT3_A**) and by layering cyclohexane over saturated toluene solution of **CZT3** (denoted as **CZT3_B**).

3 NMR Spectra

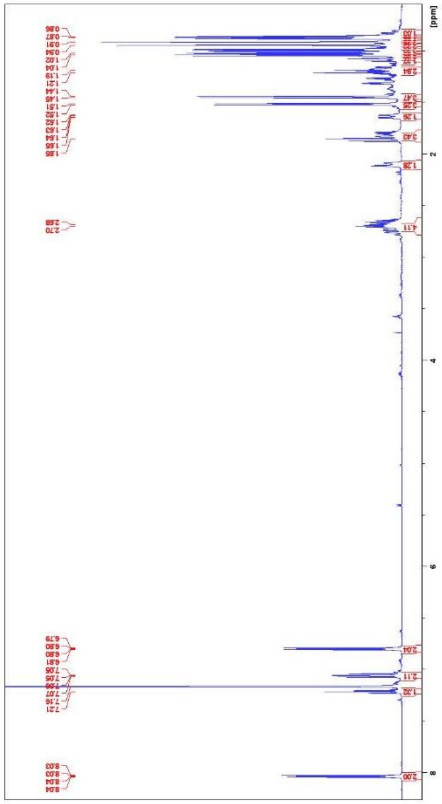


Figure S1. ^1H NMR spectrum of **CZT1** in CD_2Cl_2.

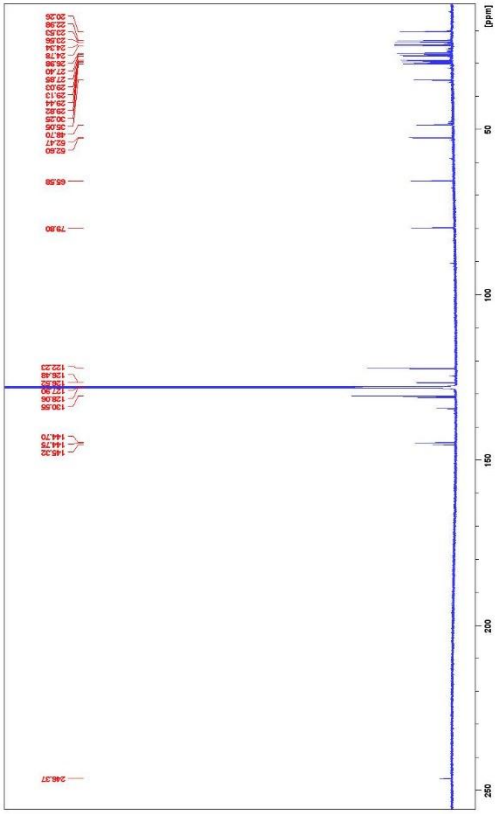


Figure S2. $^{13}C\{^{1}H\}$ NMR spectrum of **CZT1** in CD_2Cl_2.

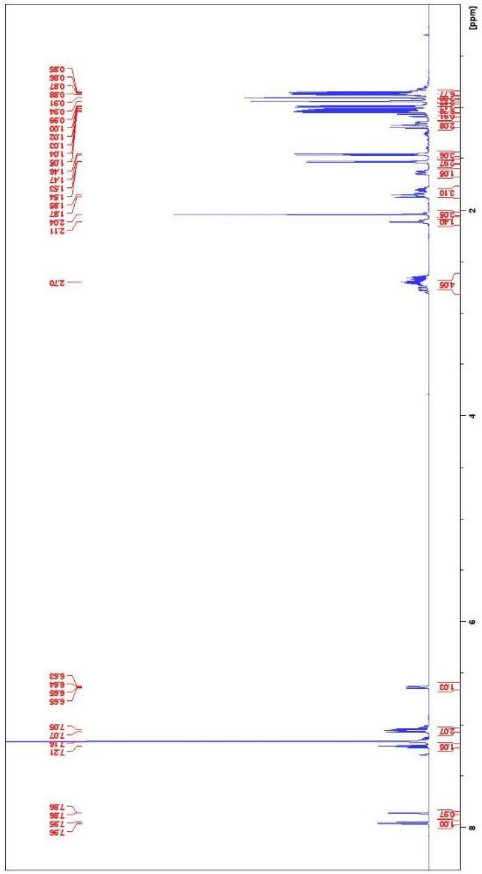


Figure S3. ^{1}H NMR spectrum of **CZT2** in C_6D_6.

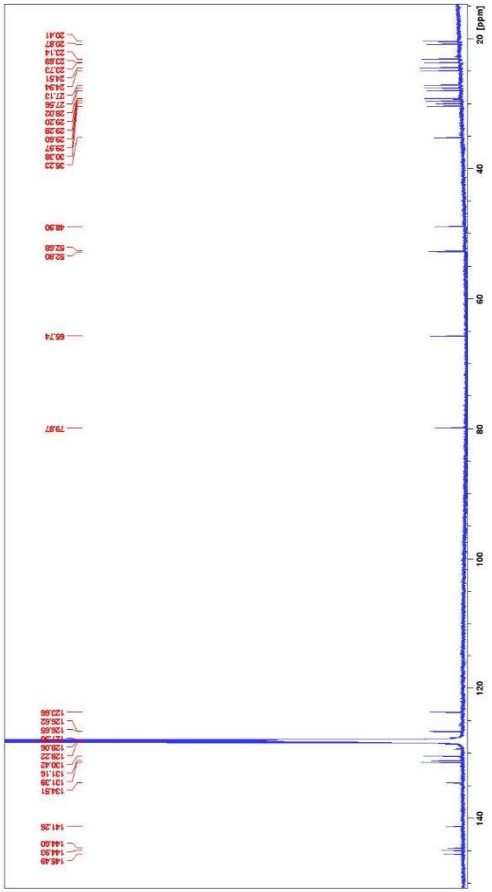


Figure S4. $^{13}C\{^{1}H\}$ NMR spectrum of **CZT2** in C_6D_6.

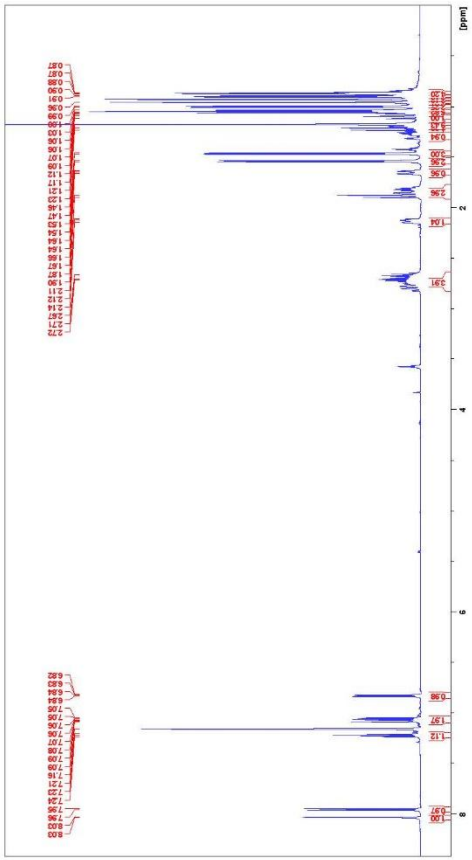


Figure S5. ^{1}H NMR spectrum of **CZT3** in CD_2Cl_2.

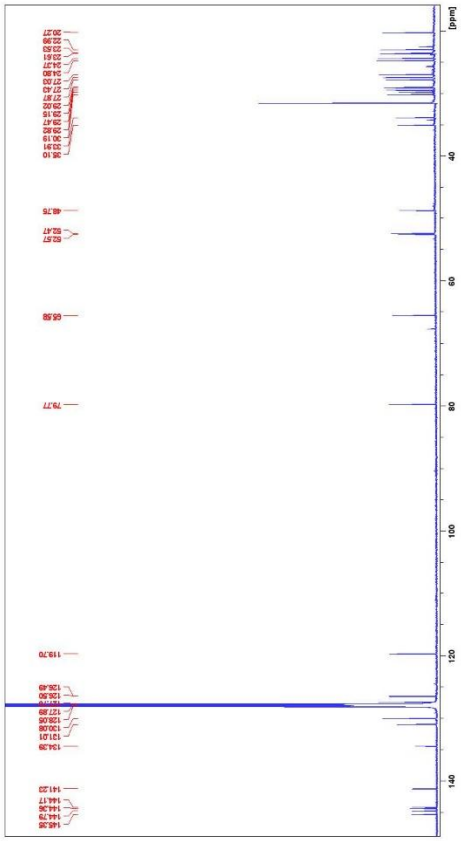


Figure S6. $^{13}C\{^{1}H\}$ NMR spectrum of **CZT3** in CD_2Cl_2.

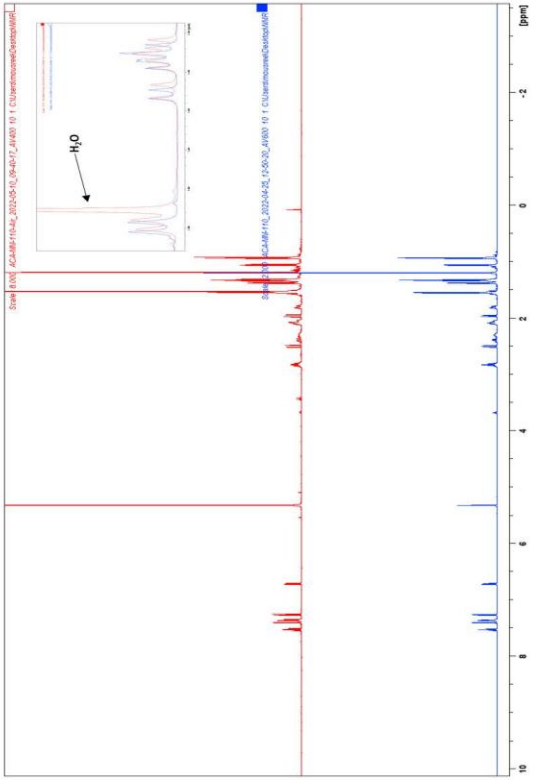


Figure S7. ^{1}H NMR spectra of **CZT3** in wet (red) and dry/degassed (blue) CD_2Cl_2. Spectra, showing no formation of protonated ^{Menth}cAAC or bdt species, were recorded after several hours of dissolution of complex in wet, air-saturated solvent.

4 Thermogravimetric analysis/differential scanning calorimetry

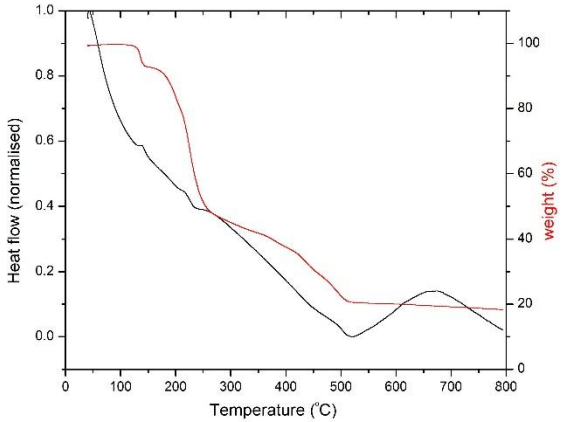


Figure S8. TGA/DSC data for compound **CZT3** in powder form.

5 X-ray Crystallography

The single crystals of **1**, **CZT1**, **CZT2**, **CZT3a** and **CZT3b** were immersed in a film of NVH or perfluoropolyether oil, mounted on a polyimide microloop (MiTeGen) and transferred to a stream of cold nitrogen (Bruker Kryoflex2/Cryostream 700 cooling system by Oxford Cryosystems), and measured at a temperature of 100 K or 120 K. The X-ray diffraction data were collected on a Bruker D8 diffractometer with a CMOS Photon 100 and multilayer optics monochromated MoKα (0.71073Å) for **1**, **CZT1**, **CZT2**, **CZT3a** or using an Agilent SuperNova dual wavelength diffractometer with a HyPix-Arc 100 detector using mirror-monochromated Cu Kα (λ = 1.54184 Å) radiation (INCOATEC microfocus sealed tube) for **CZT3b**. Using a narrow-frame algorithm, the frames were integrated with the Bruker SAINT software package or the COLLECT program for data collection and DENZO/SCALEPACK for the data reduction. The APEX3 v2018.7-0 program package was used for cell refinements and data reductions. The structure was solved using the intrinsic phasing method,[25,26] refined and visualized with the OLEX2-1.5 program.[27] A semiempirical absorption correction (SADABS) was applied to all data. All non-hydrogen atoms were refined anisotropically. Hydrogen atoms were included in structure factors calculations. All Hydrogen atoms were assigned to idealized geometric positions. The crystallographic details are summarized in Table 1. CCDC 2290921–2290925 contain supplementary crystallographic data for this paper.

Identification code	1	CZT1	CZT2	CZT3a	CZT3b
CCDC number	2290921	2290922	2290923	2290925	2290924
Empirical formula	$C_{31}H_{33}Cl_2NOZn$	$C_{32}H_{47}NS_2Zn$	$C_{34}H_{48}NS_2Zn$	$C_{37}H_{33}NS_2Zn$	$C_{88}H_{122}N_2S_4Zn_2$
Formula weight	589.99	587.20	600.22	643.31	1370.77
Temperature/K	130.00	100.00	100.0	120.15	100.00
Crystal system	orthorhombic	orthorhombic	monoclinic	monoclinic	orthorhombic
Space group	$P2_12_12_1$	$P2_12_12_1$	$P2_1$	$P2_1$	$P2_12_12_1$
a/Å b/Å c/Å α/° β/° γ/°	9.7353(4) 15.8013(6) 19.9086(11) 90 90 90	10.1678(5) 17.1888(11) 17.6290(9) 90 90 90	13.0912(4) 17.1279(5) 14.4290(5) 90 94.8230(10) 90	17.08817(8) 48.1483(3) 18.61765(10) 90 99.6409(4) 90	17.0033(4) 20.9509(6) 21.5999(6) 90 90 90
Volume/Å^3	3062.5(2)	3081.1(3)	3223.88(18)	15101.65(14)	7694.6(4)
Z	4	4	4	16	4
ρ_{calc}g/cm^3	1.280	1.266	1.237	1.132	1.183
μ/mm^{-1}	1.000	0.955	0.914	2.094	0.774
F(000)	1264.0	1256.0	1284.0	5536.0	2960.0
Crystal size/mm^3	0.47 × 0.27 × 0.18	0.122 × 0.09 × 0.06	0.32 × 0.22 × 0.18	0.21 × 0.14 × 0.12	0.172 × 0.06 × 0.03
Radiation	MoKα (λ = 0.71073)	MoKα (λ = 0.71073)	MoKα (λ = 0.71073)	CuKα (λ = 1.54184)	MoKα (λ = 0.71073)
2Θ range for data collection/°	5.548 to 54.996	6.118 to 49.996	5.536 to 51.996	6.056 to 152.8	4.322 to 49.994
Index ranges	-12 ≤ h ≤ 11, -20 ≤ k ≤ 20, -24 ≤ l ≤ 25	-12 ≤ h ≤ 12, -20 ≤ k ≤ 20, -19 ≤ l ≤ 20	-16 ≤ h ≤ 16, -21 ≤ k ≤ 21, -17 ≤ l ≤ 17	-21 ≤ h ≤ 21, -60 ≤ k ≤ 60, -23 ≤ l ≤ 22	-20 ≤ h ≤ 20, -24 ≤ k ≤ 24, -25 ≤ l ≤ 25
Reflections collected	24720	22714	75733	115095	160197
Independent reflections	7019 [R_{int} = 0.0422, R_{sigma} = 0.0483]	5410 [R_{int} = 0.0657, R_{sigma} = 0.0568]	12641 [R_{int} = 0.0370, R_{sigma} = 0.0315]	54720 [R_{int} = 0.0201, R_{sigma} = 0.0258]	13526 [R_{int} = 0.1229, R_{sigma} = 0.0489]
Data/restraints/parameters	7019/0/335	5410/0/343	12641/1/706	54720/231/3014	13526/0/817
Goodness-of-fit on F^2	1.030	1.025	1.072	1.044	1.039
Final R indexes [I>=2σ (I)]	R_1 = 0.0416, wR_2 = 0.1058	R_1 = 0.0299, wR_2 = 0.0569	R_1 = 0.0273, wR_2 = 0.0708	R_1 = 0.0400, wR_2 = 0.1091	R_1 = 0.0275, wR_2 = 0.0647
Final R indexes [all data]	R_1 = 0.0462, wR_2 = 0.1086	R_1 = 0.0363, wR_2 = 0.0591	R_1 = 0.0281, wR_2 = 0.0712	R_1 = 0.0416, wR_2 = 0.1102	R_1 = 0.0340, wR_2 = 0.0666
Largest diff. peak/hole / e Å^{-3}	1.14/-0.58	0.23/-0.24	0.83/-0.32	1.05/-0.87	0.45/-0.24
Flack parameter	0.027(15)	0.004(8)	0.028(8)	-0.002(4)	0.010(3)

Table S1: Crystal data and structure refinement for the complexes.

[a] $R_1 = \sum||F_o|-|F_c||/\sum|F_o|$; $wR_2 = [\sum[w(F_o^2-F_c^2)^2/\sum[(wF_o^2)^2]]^{1/2}$; $w = 1/[\sigma^2(F_o^2)+(aP)^2+bP]$, where $P = (F_o^2+2F_c^2)/3$ [b] GooF = S = $[[\sum w(F_o^2-F_c^2)^2]/(m-n)]^{1/2}$, where m = number of reflexes and n = number of parameters

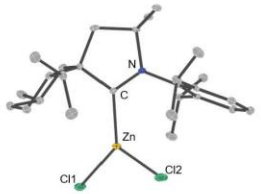


Figure S9: Crystal structure of **1**. Thermal ellipsoids are drawn at the 30 % probability level and hydrogens are omitted for clarity. Selected bond lengths (Å) and angles (°):

Zn1-C1 2.0457(39); Zn1-Cl1 2.2024(15); Zn1-Cl2 2.1971(17); C1-Zn1-Cl1 128.87(1); C1-Zn1-Cl2 130.37(4).

Table S2: Selected bond lengths and angles for **CZT1-3**.

	Zn(1)-S(1) (Å)	Zn(1)-S(2) (Å)	Zn(1)-C(1) (Å)	S(1)-Zn(1)-S(2) (°)	C(1)-Zn(1)-S(1) (°)	C(1)-Zn(1)-S(2) (°)	Ω (°)
CZT1	2.230(1)	2.238(1)	2.025(3)	97.43(4)	131.0(1)	131.5(1)	45.0
CZT2	2.230(1) 2.2447(9)	2.239(1) 2.233(1)	2.020(3) 2.029(3)	98.04(3) 97.49(4)	132.98(9) 128.41(9)	128.87(9) 133.73(9)	54.3 59.2
CZT3_A	2.232(1) 2.235(1) 2.234(1) 2.233(1) 2.234(2) 2.234(1) 2.239(1) 2.229(1)	2.232(1) 2.233(1) 2.242(1) 2.235(1) 2.221(1) 2.238(1) 2.237(1) 2.232(1)	2.032(4) 2.031(4) 2.033(5) 2.031(4) 2.032(4) 2.034(4) 2.029(4) 2.019(4)	96.93(5) 97.35(5) 97.81(4) 97.70(4) 97.50(5) 97.12(4) 97.65(4) 98.22(4)	133.2(1) 129.5(1) 128.4(1) 130.5(1) 133.3(1) 132.2(1) 128.7(1) 133.1(1)	129.8(1) 133.2(1) 133.6(1) 131.6(1) 129.2(1) 130.6(1) 133.6(1) 128.1(1)	24.2 8.5 30.1 36.1 8.6 6.4 41.3 43.1
CZT3_B	2.2235(9) 2.2394(9)	2.2337(9) 2.2396(9)	2.015(3) 2.031(3)	98.16(3) 97.24(3)	131.51(9) 130.47(9)	130.31(9) 132.23(9)	29.9 36.2

6 Photophysical Measurements

6.1 Absorption Spectra

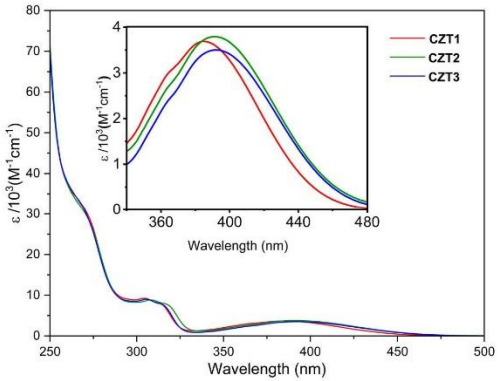


Figure S10. Absorption spectra of **CZT1**, **CZT2** and **CZT3** in DCM.

6.2 Photophysical data in dichloromethane

Table S3. Photophysical data of **CZT1**, **CZT2**, **CZT3** in DCM (10^{-5} M).

Sample no.	λ_{max} / nm	t_{exp}[μs]	ϕ	k_r / s^{-1}
CZT1	650	0.072	0.01	1.4×10^5
CZT2	670	0.064	0.01	1.6×10^5
CZT3	665	0.089	0.01	1.1×10^5

6.3 Emission and excitation spectra at 297K

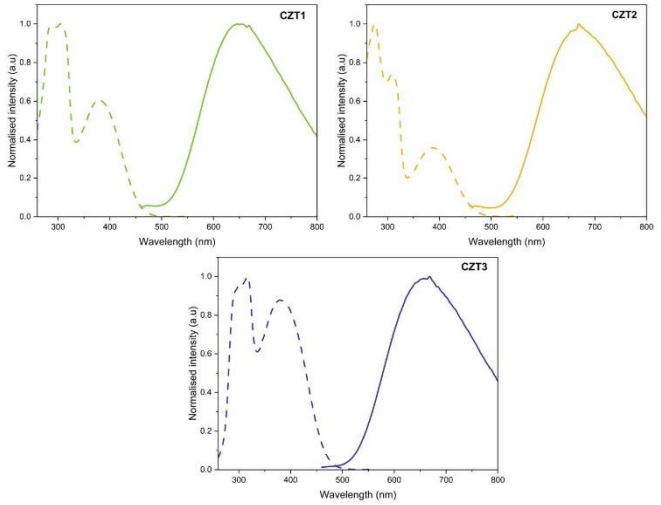


Figure S11. Emission (solid lines) and excitation spectra (dashed lines) of **CZT1**, **CZT2**, **CZT3** in DCM.

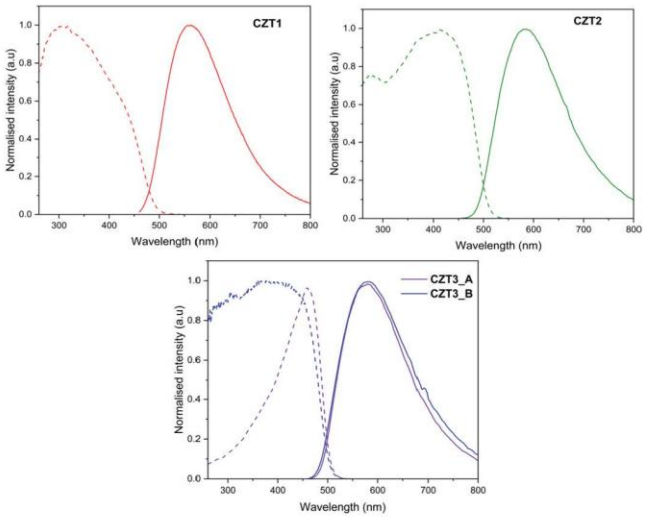


Figure S12. Emission (solid lines) and excitation spectra (dashed lines) of **CZT1**, **CZT2** and **CZT3_A** and **CZT3_B** in solid state at 297K.

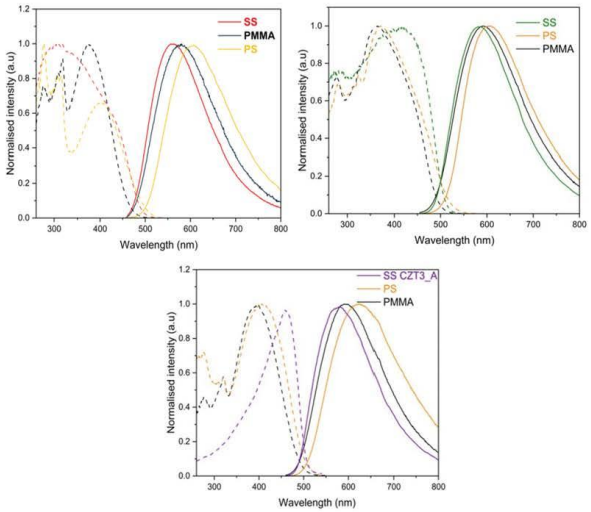


Figure S13. Comparison of emission (solid lines) and excitation (dashed lines) profiles of **CZT2** (left) and **CZT3** (right) in different media at room temperature.

6.4 Emission and Excitation Spectra at 77 K

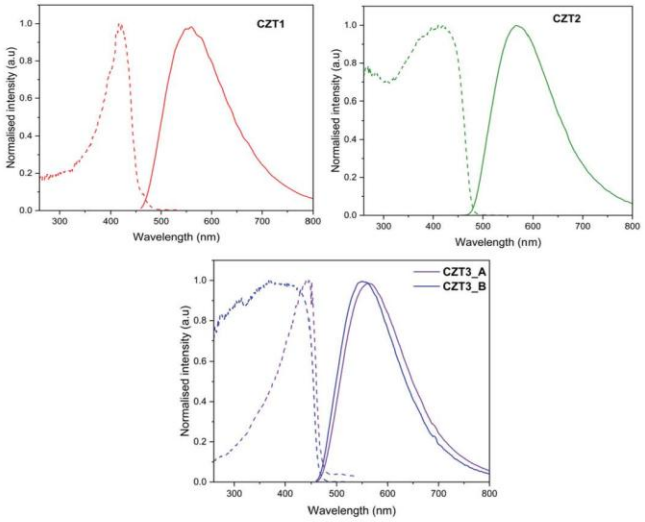


Figure S14. Emission (solid lines) and excitation spectra (dashed lines) of **CZT1**, **CZT2** and **CZT3** in solid state at 77 K.

6.5 Temperature-dependent emission spectra

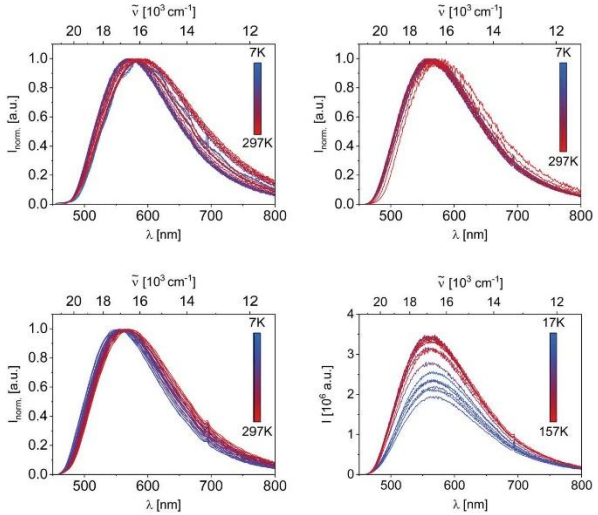


Figure S15. Normalized, temperature dependent emission spectra of **CZT2** (top left), **CZT3a** (top right), **CZT3b** (bottom left) and variation of luminescence intensity with temperature for **CZT3b** (bottom right). All data are recorded in solid state.

6.6 Details of lifetime measurements

Table S4. Lifetimes of the decay channels with the significance of their respective contribution to the decay of emission of **CZT1**, **CZT2**, **CZT3** in DCM (10^{-5} M).

Sample no.	t_1[μs]	B1	t_2[μs]	B2	[χ^2]	t_{exp}[μs]	ϕ	k_r / s^{-1}
CZT1	0.072	1.00	-	-	0.88	0.072	0.01	1.4×10^5
CZT2	0.064	1.00	-	-	0.95	0.064	0.01	1.6×10^5
CZT3	0.089	0.97	0.707	0.03	1.329	0.089	0.01	1.1×10^5

Table S5. Lifetimes of the decay channels with the significance of their respective contribution to the decay of emission of **CZT1**, **CZT2**, **CZT3**, **CZT3_A** and **CZT3_B** in solid state.

Sample no.	Temperature [K]	τ_1[μs]	B1	τ_2[μs]	B2	τ_3[μs]	B3	τ_4[μs]	B4	[χ^2]	τ_{exp}[μs]
CZT1	77	274.2	0.32	1174.6	0.43	5388.7	0.25	-	-	1.146	1944.0
	297	0.113	0.27	0.820	0.73	-	-			1.009	0.628
CZT2	77	0.029	0.95	0.224	0.04	0.738	0.01	-	-	1.292	45.7
	297	0.129	0.85	0.436	0.15	-	-	-	-	1.125	0.174
CZT3	77	297.1	0.46	1225.3	0.40	3838.9	0.14			1.030	1149.4
	297	0.133	0.40	0.670	0.60	-	-	-	-	1.103	0.454
CZT3_A	77	80.5	0.57	664.0	0.24	2985.5	0.12	8903.6	0.07	1.052	1220.7
	297	0.108	0.28	1.283	0.72	-	-	-	-	1.039	0.951
CZT3_B	77	379.2	0.80	1003.7	0.20	-	-	-	-	1.197	501.5
	297	0.152	0.24	0.469	0.76	-	-	-	-	0.909	0.394

Table S6. Lifetimes of the decay channels with the significance of their respective contribution to the decay of emission of **CZT2**, **CZT3** in different matrices

Sample no.	Medium	t_1[μs]	B1	t_2[μs]	B2	t_3[μs]	B3	[χ^2]	t_{exp}[μs]
CZT1	PS	0.051	0.39	0.177	0.44	0.563	0.17	1.104	0.192
	PMMA	0.099	0.53	0.371	0.36	0.843	0.11	1.187	0.277
CZT2	PS	0.114	0.70	0.444	0.30	-	-	1.156	0.214
	PMMA	0.68	0.39	0.219	0.42	0.546	0.19	1.149	0.222
CZT3	PS	0.075	0.47	0.266	0.42	0.607	0.11	1.175	0.211
	PMMA	0.111	0.58	0.450	0.38	1.418	0.04	1.059	0.298

Table S7. Temperature-dependent lifetimes of the decay channels with the significance of their respective contribution to the decay of emission of **CZT2** in solid state. From 17-137 K a µF2 pulsed 60 W Xenon microsecond flashlamp, and from 147 K to 297 K a 450 nm VPLED and multichannel scaling module, was used to determine the lifetimes.

Temperature [K]	τ_1 [μs]	B1	τ_2 [μs]	B2	τ_3 [μs]	B3	τ_4 [μs]	B4	[χ^2]	τ_{exp} [μs]
17	272.2	0.35	969.0	0.42	2120.9	0.22	6694.9	0.01	1.162	1022.5
27	70.6	0.11	373.3	0.21	1220.6	0.62	2668.3	0.06	1.209	995.4
37	51.3	0.11	509.0	0.41	1075.6	0.45	2553.2	0.03	1.219	786.7
47	37.3	0.27	624.1	0.65	1823.1	0.08	-	-	1.243	554.2
57	156.7	0.67	339.7	0.31	1712.5	0.02	-	-	1.257	251.6
67	64.6	0.88	173.1	0.10	968.9	0.02	-	-	1.239	97.9
77	29.1	0.95	224.5	0.04	737.7	0.01	-	-	1.291	45.7
87	17.6	0.93	120.6	0.05	339.6	0.01	1346.6	0.01	1.220	29.4
97	11.5	0.86	35.4	0.08	107.6	0.05	290.0	0.01	1.211	19.9
107	5.7	0.59	17.7	0.33	64.4	0.07	222.1	0.01	1.246	14.5
117	4.1	0.62	17.3	0.32	45.9	0.05	155.1	0.01	1.149	10.9
127	3.0	0.58	16.3	0.41	51.1	0.01	-	-	1.026	9.0
137	1.8	0.43	11.1	0.48	27.1	0.09	-	-	1.004	7.3
147	1.8	0.48	8.6	0.51	31.6	0.01	-	-	1.211	5.6

157	1.1	0.57	5.8	0.42	19.4	0.01	-	-	0.951	3.3
167	0.899	0.64	4.1	0.35	12.3	0.01	-	-	1.191	2.1
187	0.071	0.17	0.581	0.59	2.1	0.22	4.4	0.02	1.244	0.919
197	0.420	0.63	1.4	0.33	3.0	0.04	-	-	1.169	0.846
207	0.235	0.34	0.525	0.47	1.5	0.19	-	-	1.146	0.616
217	0.227	0.45	0.485	0.38	1.2	0.17	-	-	1.056	0.499
227	0.278	0.71	0.965	0.29	-	-	-	-	1.106	0.474
237	0.241	0.73	0.811	0.27	-	-	-	-	1.096	0.394
247	0.206	0.73	0.677	0.27	-	-	-	-	1.051	0.332
257	0.189	0.71	0.588	0.29	-	-	-	-	1.144	0.302
267	0.168	0.76	0.527	0.24	-	-	-	-	1.079	0.255
277	0.149	0.76	0.459	0.24	-	-	-	-	1.126	0.222
287	0.142	0.80	0.436	0.20	-	-	-	-	1.174	0.201
297	0.129	0.85	0.436	0.15	-	-	-	-	1.125	0.174

Table S8.Temperature-dependent lifetimes of the decay channels with the significance of their respective contribution to the decay of emission of **CZT3-B** in solid state. From 17-137 K a μF2 pulsed 60 W Xenon microsecond flashlamp, and from 147 K to 297 K a 450 nm VPLED and multichannel scaling module, was used to determine the lifetimes.

Temperature [K]	τ_1 [μs]	B1	τ_2 [μs]	B2	[χ^2]	τ_{exp} [μs]
7	3355.4	0.69	10437.2	0.31	1.299	5550.9
17	2877.9	0.66	8369.4	0.34	1.296	4741.3
27	2978.9	0.69	7873.8	0.31	1.263	4494.1
37	2958.8	0.71	7776.8	0.29	1.215	4351.7
47	2832.9	0.66	7481.6	0.34	1.209	4163.0
57	2202.8	0.73	5826.2	0.27	1.298	3172.2
67	1108.2	0.81	3035.3	0.19	1.220	1467.4
77	379.2	0.80	1003.7	0.20	1.196	501.5
87	155.9	0.82	389.8	0.18	1.271	198.8
97	79.7	0.84	187.6	0.16	1.253	96.5
107	47.4	0.91	108.6	0.09	1.279	53.1

117	21.3	0.65	43.1	0.35	1.194	28.9
127	12.9	0.61	25.6	0.39	1.218	17.9
137	13.2	0.62	25.8	0.38	1.210	18.0
147	5.9	0.52	10.9	0.48	1.177	8.3
157	3.0	0.34	7.0	0.66	1.086	5.7
167	2.8	0.43	5.5	0.57	1.083	4.3
177	2.1	0.38	4.1	0.62	1.185	3.3
187	1.7	0.37	3.2	0.63	1.076	2.6
197	1.4	0.34	2.5	0.66	1.199	2.1
207	1.3	0.49	2.1	0.51	1.128	1.8
217	1.2	0.62	1.8	0.38	1.046	1.5
227	0.986	0.47	1.4	0.53	1.227	1.2
237	0.205	0.16	1.1	0.84	1.066	0.934
247	0.177	0.15	0.910	0.85	1.035	0.799
257	0.132	0.19	0.776	0.81	1.080	0.656
267	0.154	0.20	0.672	0.80	1.012	0.576
277	0.112	0.19	0.581	0.81	1.161	0.492
287	0.166	0.20	0.516	0.80	1.082	0.444
297	0.152	0.24	0.469	0.76	0.909	0.394

Table S9. Temperature-dependent lifetimes of the decay channels with the significance of their respective contribution to the decay of emission of **CZT3_A** in solid state. From 17-157 K a µF2 pulsed 60 W Xenon microsecond flashlamp, and from 187 K to 297 K a 450 nm VPLED and multichannel scaling module, was used to determine the lifetimes.

Temperature [K]	τ_1 [µs]	B1	τ_2 [µs]	B2	τ_3 [µs]	B3	τ_4 [µs]	B4	[χ^2]	τ_{exp} [µs]
17	136.4	0.031	915.3	0.091	5185.4	0.109	16355.9	0.769	1.175	2552.3
27	222.8	0.076	881.5	0.072	5115.2	0.126	16350.05	0.726	1.141	2031.3
37	263.9	0.075	840.5	0.096	5550.1	0.117	15818.8	0.713	1.188	2160.7
47	255.2	0.054	787.5	0.139	4856.5	0.115	15356.8	0.692	1.161	2192.4
57	198.3	0.043	843.8	0.151	4556.2	0.149	14548.9	0.657	1.121	2109.9
67	167.1	0.037	826.9	0.126	4064.6	0.206	12543.4	0.631	1.141	2111.7
77	148.6	0.019	842.8	0.128	3287.1	0.295	9000.9	0.558	1.077	2313.8
87	510.1	0.131	1947.6	0.379	4660.8	0.310	-	-	0.963	1799.3
97	444.9	0.248	1583.2	0.722	863.4	0.211	-	-	1.055	981.6
107	167.3	0.073	413.7	0.342	794.2	0.574	6834.9	0.011	0.998	503.8
117	18.6	0.027	147.9	0.337	347.3	0.628	2418.5	0.008	1.039	181.3
127	67.4	0.240	176.7	0.751	2664.7	0.009	-	-	1.093	127.9
137	52.5	0.193	102.3	0.786	707.5	0.010	4805.0	0.011	0.836	87.9
147	2.6	0.011	29.2	0.321	62.4	0.660	1179.2	0.008	1.207	38.8
157	1.9	0.005	27.5	0.597	46.2	0.389	1024.3	0.09	1.198	30.3
187	7.2	0.205	13.6	0.787	109.9	0.008	-	-	1.187	11.5
297	0.11	0.032	1.3	0.968	-	-	-	-	1.039	0.95

7 Theoretical Calculations

7.1 Torsion Path

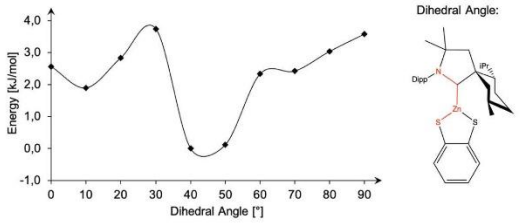


Figure S16. DFT/MRCI energies of **CZT1** with changing dihedral angles.

7.2 States, Energies and Oscillator Strength

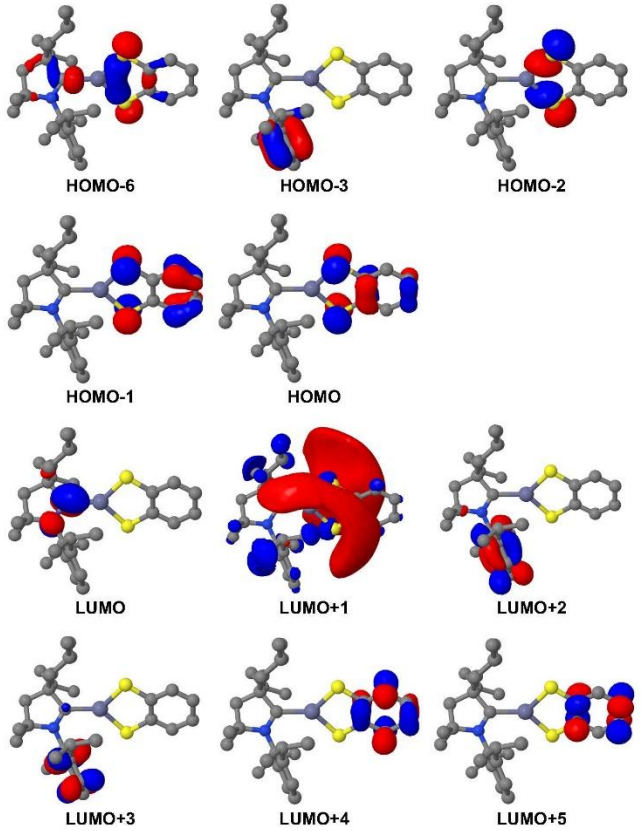


Figure S17. Selected orbitals for compound **CZT1** (tilted conformer).

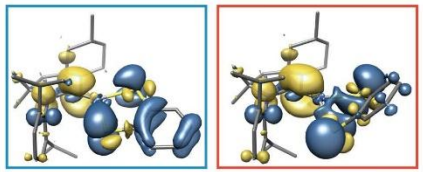


Figure S18. Electron density differences of the ^{1}LLCT(ππ*) (left) and the ^{1}LLCT(nπ*) states (right) of model compound **CZT1** (loss of electron density is indicated in blue and gain in yellow with isosurface values ±0.002, hydrogens omitted for clarity).

Table S10. Singlet states and their properties at the ground state geometry (ortho) of **CZT1.**

state	E [eV]	λ_{abs} [nm]	osc. strength	character	leading excitation
S0				S0	-
S1	3.26	380	0.00745	LLCT($\pi\pi^*$)	HOMO→LUMO
S2	3.88	320	0.00120	LLCT($\pi\pi^*$)	HOMO-1→LUMO
S3	4.34	286	0.10534	LLCT($n\pi^*$)	HOMO-2→LUMO
S4	4.37	284	0.02103	LC(bdt)	HOMO→LUMO+4
S5	4.54	273	0.05797	Rydberg	HOMO→LUMO+1
S6	4.68	265	0.00229	LC(CAAC)	HOMO-6→LUMO
S7	4.80	258	0.00512	LLCT($\pi\pi^*$)	HOMO→LUMO+2
S8	4.89	253	0.08956	LC(bdt)	HOMO→LUMO+5
S9	4.96	250	0.00858	LLCT($\pi\pi^*$)	HOMO→LUMO+3
S10	5.05	245	0.00715	LC(CAAC)	HOMO-3→LUMO+2

Table S11. Singlet states and their properties at the ground state geometry (tilted) of **CZT1.**

state	E [eV]	λ_{abs} [nm]	osc. strength	character	leading excitation
S0				S0	-
S1	3.24	383	0.03744	LLCT($\pi\pi^*$)	HOMO→LUMO
S2	3.83	323	0.00319	LLCT($\pi\pi^*$)	HOMO-1→LUMO
S3	4.25	292	0.04544	LLCT($n\pi^*$)	HOMO-2→LUMO
S4	4.37	284	0.03111	LC(bdt)	HOMO→LUMO+4
S5	4.56	272	0.05207	Rydberg	HOMO→LUMO+1
S6	4.65	267	0.00688	LC(CAAC)	HOMO-6→LUMO
S7	4.75	261	0.00398	LLCT($\pi\pi^*$)	HOMO→LUMO+2
S8	4.88	254	0.07977	LC(bdt)	HOMO→LUMO+5 HOMO→LUMO+3
S9	4.91	252	0.02445	LLCT($\pi\pi^*$)	HOMO→LUMO+3 HOMO→LUMO+5
S10	5.01	248	0.00935	LC(CAAC)	HOMO-3→LUMO HOMO-3→LUMO+2

Table S12. Singlet states and their properties at the ground state geometry (planar) of **CZT1.**

state	E [eV]	λ_{abs} [nm]	osc. strength	state	leading excitation
S0				S0	-
S1	3.17	391	0.05979	LLCT($\pi\pi^*$)	HOMO→LUMO
S2	3.76	330	0.00542	LLCT($\pi\pi^*$)	HOMO-1→LUMO
S3	4.15	299	0.00340	LLCT($n\pi^*$)	HOMO-2→LUMO
S4	4.36	284	0.03186	LC(bdt)	HOMO→LUMO+4
S5	4.50	275	0.04942	Rydberg	HOMO→LUMO+1
S6	4.63	268	0.00658	LC(CAAC)	HOMO-6→LUMO
S7	4.66	266	0.00051	LLCT($\pi\pi^*$)	HOMO→LUMO+2
S8	4.84	256	0.04559	LLCT($\pi\pi^*$)	HOMO→LUMO+3
S9	4.90	253	0.06707	LC(bdt)	HOMO→LUMO+5
S10	4.99	249	0.00982	LC(CAAC)	HOMO-3→LUMO

Table S13. Excited state geometries of **CZT1** und their S_1/T_1 state properties. [a]Vertical energy. [b]Adiabatic energy with S_0 (tilted) as reference point.

geometry		E [eV][(a)]	E [eV][(b)]	osc. strength
^{1}LLCT($\pi\pi^*$)	ortho	1.96	2.48	0.00751
	tilted	1.96	2.46	0.04670
	planar	1.93	2.44	0.06400
^{3}LLCT($\pi\pi^*$)	ortho	1.96	2.46	$< 10^{-5}$
	tilted	1.90	2.44	$< 10^{-5}$
	planar	1.86	2.42	$< 10^{-5}$
^{1}LLCT($n\pi^*$)		1.66	2.63	0.00062
^{3}LLCT($n\pi^*$)		1.66	2.61	$< 10^{-5}$

7.3 Crossing point

At the optimized geometry of the ^{3}LLCT($n\pi^*$) state, one dummy atom (D1) was placed in-between the two sulfur atoms (#2, #3) and a second one (D2) in the middle of the benzene ring, in-between the carbon atom #10 and carbon atom #37. Afterwards, the angle defined by the zinc atom, D1 and D2 was defined as an internal coordinate in TURBOMOLE, and manually set to the similarly obtained angle of the ^{3}LLCT($\pi\pi^*$) optimized state (177.09229°). Using TURBOMOLE, the cartesian coordinates were readjusted to the new internal angle, and a constrained optimization of the T_1 geometry was conducted. For that purpose, the dihedral angle spanned by atoms #66, #1, #2 and #38 and the dihedral angle between atoms #66, #1, #3 and #37 were fixed. At the thus obtained structure (crossing point), the DFT/MRCI energies of the T_1 and T_2 states differ by less than 0.01 eV.

Table S14. Cartesian coordinates of the crossing point between the ^{3}LLCT($n\pi^*$) and the ^{3}LLCT($\pi\pi^*$) at the planar conformer of **CZT1.**

atom	x	y	z
Zn	-0.024701	-0.307719	0.735251
S	-0.828927	1.206561	2.357394
S	-0.598875	-1.80747	2.521159
N	0.206548	0.709087	-1.953292
C	0.233383	-1.036544	-3.499691
H	0.934599	-1.493773	-4.202745
H	-0.768868	-1.228124	-3.887487
C	-0.237812	1.283661	5.062882
H	-0.291467	2.365703	4.993584
C	-0.008622	0.666802	6.287837
H	0.134268	1.273800	7.175836
C	1.175511	2.697585	-0.86524
C	1.853511	0.881148	-3.851487
H	2.002621	1.958666	-3.750083
H	1.976955	0.628895	-4.910288
H	2.63773	0.365795	-3.293783
C	0.008507	-0.719946	6.37869

H	0.158294	-1.201625	7.339439
C	-1.372388	3.825333	-0.670114
H	-2.359315	4.265974	-0.574218
C	-2.508385	1.835392	-1.663658
H	-2.212985	0.898229	-2.133609
C	-0.271518	4.530184	-0.216632
H	-0.39567	5.516558	0.219896
C	0.986642	3.961729	-0.307933
H	1.843093	4.509531	0.071383
C	0.05237	2.003748	-1.370114
C	0.447152	0.478482	-3.401379
C	3.565149	2.996098	-1.660985
H	3.209568	3.204784	-2.673616
H	4.53777	2.495686	-1.740291
H	3.731247	3.959169	-1.164421
C	-3.331095	2.639294	-2.673847
H	-4.1706	2.036841	-3.041232
H	-2.733272	2.948294	-3.536588
H	-3.752209	3.543132	-2.218529
C	-0.371513	-0.8833	4.010032
C	-0.424955	0.505385	3.926274
C	-0.181379	-1.497838	5.24196
H	-0.195651	-2.581568	5.31058
C	-0.538834	1.232087	-4.292006
H	-1.570908	0.926747	-4.110978
H	-0.309444	1.018347	-5.341711
H	-0.462997	2.315143	-4.148448
C	1.20328	-4.150228	-0.620206
H	1.438214	-4.821948	-1.458922
H	1.371416	-4.7262	0.298847
C	1.845222	-2.123444	-1.913605
H	2.091097	-2.74184	-2.788854
H	2.519663	-1.26143	-1.943432
C	-0.254333	-3.722985	-0.705214
H	-0.519269	-3.180994	0.207613
H	-0.893333	-4.613753	-0.719841
C	-3.37876	1.46911	-0.459246
H	-3.727557	2.362134	0.072899
H	-2.829792	0.84626	0.252362
H	-4.262291	0.908659	-0.788331
C	2.585787	2.12771	-0.864719
H	2.544024	1.142444	-1.32581
C	0.379278	-1.630158	-2.079767

C	-1.239982	2.560259	-1.24044
C	2.142441	-2.952331	-0.67083
H	1.950099	-2.330855	0.213983
C	-2.078679	-2.596547	-2.117248
H	-2.189952	-1.626871	-2.612848
C	0.090403	-0.42862	-1.182937
C	3.133669	1.941498	0.553608
H	3.298135	2.909678	1.039457
H	4.100297	1.424635	0.516206
H	2.460994	1.354322	1.187423
C	3.60619	-3.370248	-0.624063
H	3.822387	-3.953071	0.279752
H	4.270189	-2.497017	-0.627482
H	3.866658	-3.990762	-1.491661
C	-2.699682	-3.64557	-3.039508
H	-2.58249	-4.654944	-2.623218
H	-2.226869	-3.638289	-4.029028
H	-3.773319	-3.468326	-3.178293
C	-2.894389	-2.502658	-0.828908
H	-3.931514	-2.237564	-1.068524
H	-2.508992	-1.732744	-0.155369
H	-2.918808	-3.452888	-0.284037
C	-0.557441	-2.87076	-1.939318
H	-0.265907	-3.494686	-2.795894

7.4 Coordinates

Table S15. Cartesian coordinates of the optimized S_0 (ortho) geometry of **CZT1.**

atom	x	y	z
Zn	1.179492	-0.019319	-0.045352
S	2.450926	-0.740747	-1.803754
S	2.947244	0.149599	1.410710
N	-1.763309	-0.271608	0.267959
C	-2.834474	1.807206	0.466649
H	-3.321645	2.379841	1.257793
H	-3.240608	2.170119	-0.478805
C	5.127269	-1.227011	-1.757209
H	4.964253	-1.508961	-2.792962
C	6.400767	-1.304181	-1.218573
H	7.228685	-1.644706	-1.833027
C	-1.292779	-2.555681	1.120864
C	-3.545693	-0.055418	2.025692

H	-3.697744	-1.131243	2.126183
H	-4.500563	0.435424	2.237095
H	-2.828256	0.276573	2.778567
C	6.605114	-0.943669	0.109291
H	7.595648	-0.997674	0.550774
C	-1.636832	-3.573084	-1.461147
H	-1.751604	-3.978020	-2.460260
C	-2.014663	-1.341480	-2.496388
H	-2.143538	-0.307074	-2.176808
C	-1.362061	-4.431991	-0.413206
H	-1.272670	-5.498980	-0.590098
C	-1.185496	-3.920677	0.858037
H	-0.948197	-4.597472	1.671070
C	-1.601313	-1.699805	0.043690
C	-3.126578	0.316183	0.607401
C	-1.969609	-2.760974	3.558972
H	-3.022185	-2.653489	3.282884
H	-1.830843	-2.309980	4.548247
H	-1.761546	-3.832229	3.655910
C	-3.278179	-1.762611	-3.252852
H	-3.489230	-1.045425	-4.054392
H	-4.156376	-1.814935	-2.603538
H	-3.150599	-2.745297	-3.719906
C	4.238103	-0.426285	0.343386
C	4.031162	-0.793820	-1.001217
C	5.532355	-0.512827	0.871693
H	5.689147	-0.230687	1.908367
C	-4.217893	-0.147630	-0.345171
H	-4.029230	0.160351	-1.374301
H	-5.159028	0.315034	-0.031031
H	-4.353397	-1.232529	-0.312890
C	0.775348	4.096128	1.147595
H	0.108683	4.934136	1.398515
H	1.801618	4.467992	1.252070
C	-0.871612	2.395743	1.941301
H	-1.579040	3.172741	2.256377
H	-1.023604	1.554441	2.627321
C	0.527624	3.658059	-0.286721
H	1.286987	2.923252	-0.572348
H	0.672529	4.510076	-0.960722
C	-0.816922	-1.367779	-3.448123
H	-0.658645	-2.371956	-3.857602
H	0.105211	-1.065396	-2.946859

H	-0.989755	-0.686369	-4.288899
C	-1.021147	-2.105175	2.549582
H	-1.161433	-1.026057	2.605463
C	-1.299832	1.983859	0.500984
C	-1.760040	-2.199719	-1.265685
C	0.536079	2.953491	2.124993
H	1.268424	2.170405	1.903856
C	-1.218521	2.843856	-1.989906
H	-2.005967	2.083131	-2.031612
C	-0.783536	0.579317	0.216296
C	0.425386	-2.391025	2.963264
H	0.632661	-3.467164	2.964267
H	0.600291	-2.019200	3.979940
H	1.148711	-1.904448	2.303504
C	0.750546	3.384467	3.569974
H	1.767659	3.766692	3.715442
H	0.605271	2.546742	4.262768
H	0.049076	4.180416	3.852818
C	-1.794465	4.100701	-2.641342
H	-1.078874	4.931533	-2.598491
H	-2.714028	4.425751	-2.140410
H	-2.030646	3.922482	-3.697012
C	-0.059762	2.312520	-2.829405
H	-0.416730	2.063601	-3.835429
H	0.387741	1.406515	-2.411922
H	0.737670	3.055315	-2.939361
C	-0.886847	3.113657	-0.495870
H	-1.553192	3.929871	-0.187021

Table S16. Cartesian coordinates of the optimized S_0 (tilted) geometry of **CZT1.**

atom	x	y	z
Zn	1.585936	7.602213	12.354441
S	0.184753	6.998921	10.646816
S	1.495390	9.844978	11.889668
N	3.373010	5.486372	13.391352
C	3.874450	5.712420	15.674466
H	4.742309	6.015242	16.262840
H	3.255930	5.093052	16.325495
C	-0.929677	8.676928	8.817773
H	-1.355092	7.759044	8.423656
C	-1.211691	9.883422	8.199422
H	-1.855537	9.905991	7.325359

C	4.129391	5.276702	11.035951
C	5.757911	5.131768	14.081953
H	6.026975	4.581225	13.178866
H	6.379786	4.753199	14.898868
H	5.998919	6.187435	13.942351
C	-0.664267	11.057613	8.706238
H	-0.873022	12.013463	8.235318
C	2.262842	3.231529	10.639977
H	1.528445	2.453156	10.466184
C	1.285481	3.425027	12.922380
H	1.496589	3.946985	13.856306
C	3.121644	3.588679	9.617114
H	3.066963	3.085492	8.657165
C	4.033597	4.607209	9.816917
H	4.681846	4.902675	8.999649
C	3.275336	4.866118	12.079249
C	4.296560	4.903571	14.451363
C	6.555599	6.008743	10.821615
H	6.883918	5.174566	11.446788
H	7.236117	6.850195	10.995420
H	6.672306	5.704474	9.775649
C	1.328141	1.920085	13.204013
H	0.666488	1.678972	14.043924
H	2.333764	1.569725	13.452350
H	0.979377	1.345143	12.339170
C	0.448562	9.790779	10.460940
C	-0.103916	8.600748	9.946488
C	0.153381	11.001665	9.822456
H	0.581438	11.916295	10.221367
C	4.087814	3.410572	14.654734
H	3.079819	3.176075	14.999194
H	4.785896	3.075201	15.428583
H	4.299499	2.841086	13.745382
C	2.308041	9.736644	16.033282
H	2.768529	9.758658	17.031735
H	1.818339	10.707219	15.890364
C	4.031900	8.169116	15.140337
H	4.567969	8.158850	16.097407
H	4.795376	8.027736	14.366577
C	1.275925	8.622220	15.970883
H	0.729973	8.693939	15.025334
H	0.528355	8.770648	16.758195
C	-0.129918	3.826046	12.499710

H	-0.428013	3.311732	11.579085
H	-0.211010	4.900878	12.320635
H	-0.846200	3.554012	13.283552
C	5.113157	6.437044	11.111386
H	5.079924	6.856128	12.117416
C	3.079155	6.936734	15.169198
C	2.313011	3.854227	11.884426
C	3.395340	9.545313	14.984770
H	2.922798	9.612264	14.000393
C	0.832787	6.114827	16.281520
H	1.315228	5.158179	16.052024
C	2.725080	6.557849	13.736371
C	4.728802	7.559630	10.141174
H	4.821273	7.230587	9.100202
H	5.398148	8.416585	10.279624
H	3.703346	7.906123	10.289506
C	4.457592	10.634167	15.056493
H	4.008956	11.625669	14.924822
H	5.217016	10.503301	14.276257
H	4.968220	10.622854	16.028421
C	0.342703	6.012553	17.725656
H	-0.130271	6.946101	18.054447
H	1.168729	5.795519	18.413017
H	-0.400085	5.212955	17.829443
C	-0.357997	6.238760	15.335768
H	-1.009235	5.363409	15.439016
H	-0.052142	6.287623	14.287016
H	-0.962455	7.125953	15.552059
C	1.897373	7.235346	16.146161
H	2.414547	7.269270	17.114338

Table S17. Cartesian coordinates of the optimized S_0 (planar) geometry of **CZT1.**

atom	x	y	z
Zn	1.591797	7.556923	12.319013
S	0.866501	7.065522	10.208485
S	0.618427	9.632668	12.379712
N	3.390217	5.460936	13.388112
C	3.870183	5.703945	15.676074
H	4.747314	5.996842	16.255760
H	3.235577	5.119702	16.343478
C	-0.544125	8.720325	8.572031
H	-0.462802	7.891689	7.875100

C	-1.211804	9.872206	8.191359
H	-1.650108	9.941042	7.200277
C	4.228095	5.241403	11.068070
C	5.746967	4.990233	14.129954
H	5.999372	4.428880	13.228328
H	6.327425	4.568983	14.956436
H	6.056909	6.029447	14.004191
C	-1.313476	10.932620	9.085988
H	-1.832255	11.844604	8.806434
C	2.330665	3.242611	10.587697
H	1.584967	2.483479	10.379840
C	1.253523	3.473580	12.825928
H	1.448078	3.983689	13.769730
C	3.242470	3.580025	9.604386
H	3.217343	3.078903	8.642131
C	4.168237	4.578211	9.843918
H	4.856316	4.860758	9.055073
C	3.320742	4.847997	12.071964
C	4.267893	4.852806	14.472508
C	6.672066	5.927281	10.920112
H	6.966270	5.059719	11.516901
H	7.368271	6.743763	11.143741
H	6.805353	5.664713	9.864892
C	1.221808	1.968618	13.105494
H	0.507290	1.753904	13.908465
H	2.198524	1.580096	13.407551
H	0.897732	1.407016	12.222439
C	-0.066217	9.661973	10.745505
C	0.037822	8.586784	9.839321
C	-0.744717	10.819153	10.343514
H	-0.821511	11.645098	11.044141
C	3.968688	3.377297	14.694865
H	2.939082	3.207096	15.013222
H	4.624040	3.016644	15.494218
H	4.172486	2.780662	13.801286
C	2.419803	9.786369	15.903690
H	2.874268	9.834540	16.904031
H	1.955309	10.762610	15.720818
C	4.101150	8.139773	15.080583
H	4.626958	8.145405	16.043375
H	4.867510	7.946152	14.320858
C	1.359893	8.696336	15.874769
H	0.831213	8.738378	14.918353

H	0.606690	8.898498	16.644187
C	-0.124901	3.938105	12.348298
H	-0.412011	3.432841	11.418970
H	-0.143981	5.013988	12.157526
H	-0.882134	3.705927	13.106107
C	5.234687	6.376786	11.199967
H	5.194517	6.756685	12.220327
C	3.109878	6.938156	15.142394
C	2.340274	3.864332	11.833932
C	3.510640	9.530134	14.872065
H	3.050058	9.586076	13.879868
C	0.843750	6.219915	16.291315
H	1.305084	5.238474	16.135903
C	2.753792	6.544163	13.715088
C	4.887592	7.547545	10.274659
H	4.965819	7.254612	9.221512
H	5.586767	8.374949	10.443623
H	3.871195	7.914628	10.436375
C	4.607211	10.586039	14.924396
H	4.192707	11.587202	14.758333
H	5.370858	10.407728	14.157635
H	5.106748	10.587416	15.902049
C	0.323134	6.222866	17.728687
H	-0.138339	7.183853	17.986651
H	1.131403	6.036007	18.445365
H	-0.436696	5.445198	17.868939
C	-0.325675	6.309645	15.314987
H	-1.009748	5.468475	15.475916
H	-0.003389	6.261686	14.271011
H	-0.900906	7.232164	15.445984
C	1.940701	7.301724	16.110376
H	2.459978	7.356192	17.076667

Table S18. Cartesian coordinates of the optimized ^{1}LLCT($\pi\pi^*$) (ortho) geometry of **CZT1.**

atom	x	y	z
Zn	1.079243	-0.000996	0.081254
S	2.437013	-0.966061	-1.621118
S	3.043786	0.112838	1.474085
N	-1.805625	-0.304036	0.326752
C	-2.820619	1.789026	0.421109
H	-3.347795	2.438150	1.125682

H	-3.198576	2.032816	-0.574268
C	5.082023	-1.427491	-1.679413
H	4.878624	-1.799461	-2.677031
C	6.357605	-1.423570	-1.191817
H	7.172628	-1.794938	-1.803663
C	-1.264351	-2.593240	1.088971
C	-3.465741	0.078476	2.175226
H	-3.675024	-0.976629	2.366107
H	-4.372061	0.644334	2.418491
H	-2.676052	0.402733	2.855708
C	6.622171	-0.933646	0.109448
H	7.638179	-0.932305	0.489096
C	-1.587636	-3.531113	-1.518499
H	-1.699220	-3.902716	-2.531862
C	-2.061659	-1.271629	-2.453693
H	-2.216320	-0.263025	-2.073155
C	-1.275566	-4.419808	-0.505337
H	-1.151925	-5.476773	-0.721208
C	-1.109323	-3.945923	0.782417
H	-0.846070	-4.642685	1.571488
C	-1.624282	-1.693785	0.058945
C	-3.100707	0.307465	0.704219
C	-1.973275	-2.847037	3.508070
H	-3.019308	-2.717375	3.215872
H	-1.847886	-2.427939	4.513790
H	-1.780979	-3.924281	3.574542
C	-3.326151	-1.702559	-3.202500
H	-3.583774	-0.960459	-3.967872
H	-4.184130	-1.809713	-2.532084
H	-3.181396	-2.661577	-3.713350
C	4.257750	-0.456926	0.421016
C	3.990472	-0.944688	-0.909768
C	5.601484	-0.465881	0.885394
H	5.798345	-0.091443	1.883395
C	-4.271656	-0.201670	-0.132359
H	-4.148224	0.030022	-1.191503
H	-5.194814	0.280793	0.207435
H	-4.402991	-1.283867	-0.024643
C	0.831936	4.085186	1.055509
H	0.217202	4.972792	1.266025
H	1.879285	4.400229	1.148828
C	-0.921179	2.524722	1.891932
H	-1.586130	3.370122	2.123827

H	-1.138282	1.747341	2.630659
C	0.555367	3.604773	-0.360255
H	1.269519	2.815300	-0.624478
H	0.746327	4.423693	-1.063951
C	-0.884030	-1.206801	-3.429174
H	-0.674695	-2.188755	-3.870291
H	0.026793	-0.858644	-2.934847
H	-1.107582	-0.513096	-4.248311
C	-1.007146	-2.173905	2.527605
H	-1.146191	-1.095726	2.591428
C	-1.289319	1.999327	0.475726
C	-1.757684	-2.170787	-1.266122
C	0.511650	3.007599	2.081573
H	1.189477	2.164081	1.900303
C	-1.199585	2.794454	-2.040430
H	-1.897820	1.953010	-2.063015
C	-0.749375	0.597399	0.211927
C	0.431235	-2.472028	2.961388
H	0.630834	-3.549899	2.979317
H	0.606476	-2.087456	3.973638
H	1.166728	-2.007107	2.297555
C	0.750353	3.485922	3.507419
H	1.787041	3.817218	3.645630
H	0.553144	2.687752	4.233760
H	0.093913	4.331044	3.753845
C	-1.903246	3.981775	-2.696430
H	-1.271561	4.879666	-2.666360
H	-2.843499	4.221381	-2.185053
H	-2.135529	3.776194	-3.748925
C	-0.005255	2.372211	-2.894989
H	-0.351416	2.060418	-3.887701
H	0.533411	1.528320	-2.454609
H	0.706409	3.192543	-3.040721
C	-0.879031	3.106369	-0.550986
H	-1.517785	3.957363	-0.274683

Table S19. Cartesian coordinates of the optimized ^{1}LLCT($\pi\pi^*$) (tilted) geometry of **CZT1.**

atom	x	y	z
Zn	0.875320	0.292289	0.124899
S	2.318501	-1.340907	-0.843760
S	2.797306	1.586879	0.670210

N	-1.851279	-0.643005	0.463968
C	-3.336817	1.139977	0.291332
H	-4.031964	1.722994	0.901648
H	-3.718728	1.164138	-0.731844
C	4.932311	-1.165647	-1.429370
H	4.777985	-2.137107	-1.885057
C	6.159447	-0.569289	-1.471748
H	6.989344	-1.067156	-1.961441
C	-0.775988	-2.587305	1.546147
C	-3.618115	-0.459173	2.242157
H	-3.572765	-1.504764	2.556163
H	-4.642327	-0.107776	2.409734
H	-2.955668	0.123122	2.884992
C	6.349708	0.702369	-0.881764
H	7.325781	1.173895	-0.921418
C	-0.812925	-3.954343	-0.886202
H	-0.810375	-4.488266	-1.830820
C	-1.797947	-2.036047	-2.137721
H	-2.201379	-1.051550	-1.905145
C	-0.310325	-4.577327	0.241976
H	0.072987	-5.591534	0.183886
C	-0.286430	-3.889792	1.441274
H	0.127121	-4.374256	2.319752
C	-1.327031	-1.969585	0.400385
C	-3.268595	-0.320570	0.756212
C	-1.450668	-2.643758	3.988283
H	-2.490816	-2.819330	3.699692
H	-1.450552	-2.061970	4.918002
H	-1.000721	-3.618431	4.210477
C	-2.900356	-2.863045	-2.805126
H	-3.306705	-2.324183	-3.669642
H	-3.726397	-3.076042	-2.120033
H	-2.515021	-3.822287	-3.169879
C	4.021560	0.749315	-0.183995
C	3.821096	-0.536089	-0.804783
C	5.310332	1.336944	-0.260972
H	5.457232	2.309966	0.193639
C	-4.256335	-1.191799	-0.015371
H	-4.160638	-1.063274	-1.094597
H	-5.277715	-0.909430	0.262842
H	-4.128170	-2.253015	0.223618
C	-0.357290	4.295007	0.702848
H	-1.173826	5.025956	0.797254

H	0.580473	4.860820	0.774679
C	-1.727969	2.466088	1.688761
H	-2.582074	3.149463	1.806020
H	-1.790867	1.748027	2.511697
C	-0.445112	3.605490	-0.649587
H	0.450344	2.989129	-0.790695
H	-0.417125	4.360322	-1.444467
C	-0.644511	-1.823495	-3.120103
H	-0.202310	-2.777877	-3.430607
H	0.148879	-1.215026	-2.677121
H	-1.003419	-1.312084	-4.021568
C	-0.661381	-1.906819	2.901313
H	-1.066587	-0.900690	2.802994
C	-1.901836	1.714823	0.338240
C	-1.314786	-2.654798	-0.836156
C	-0.458304	3.293130	1.844714
H	0.402853	2.616314	1.779101
C	-1.874038	2.201963	-2.252630
H	-2.358169	1.223576	-2.179890
C	-1.039786	0.462135	0.243640
C	0.795411	-1.768307	3.355285
H	1.255022	-2.747094	3.535395
H	0.844793	-1.202530	4.293507
H	1.410868	-1.245837	2.616817
C	-0.402734	3.972149	3.206567
H	0.520785	4.553054	3.321344
H	-0.441166	3.237799	4.020554
H	-1.248289	4.660384	3.337488
C	-2.798973	3.102239	-3.071073
H	-2.392062	4.119373	-3.147985
H	-3.792128	3.177008	-2.611807
H	-2.928164	2.719733	-4.091287
C	-0.575527	1.970303	-3.025606
H	-0.799036	1.488131	-3.985036
H	0.115284	1.315038	-2.486135
H	-0.054351	2.908658	-3.245641
C	-1.711487	2.759568	-0.809081
H	-2.545538	3.459714	-0.658223

Table S20. Cartesian coordinates of the optimized ^{1}LLCT($\pi\pi^*$) (planar) geometry of **CZT1.**

atom	x	y	z

Zn	0.859819	0.383777	0.057729
S	2.308736	-1.493979	-0.283305
S	2.738275	1.816300	-0.065725
N	-1.832487	-0.626413	0.445129
C	-3.378120	1.118138	0.327041
H	-4.058295	1.652784	0.995615
H	-3.802955	1.192635	-0.675894
C	4.901100	-1.516179	-0.976374
H	4.756047	-2.589227	-1.029749
C	6.118628	-0.968114	-1.260241
H	6.951022	-1.604406	-1.540508
C	-0.756685	-2.545409	1.560711
C	-3.657259	-0.595989	2.173201
H	-3.554928	-1.650497	2.440946
H	-4.707386	-0.318419	2.317262
H	-3.057016	-0.001532	2.865145
C	6.293559	0.433099	-1.191755
H	7.261183	0.867248	-1.419880
C	-0.713565	-3.925364	-0.864854
H	-0.672425	-4.462138	-1.807006
C	-1.616416	-1.993418	-2.162978
H	-2.037933	-1.011591	-1.949548
C	-0.259088	-4.545684	0.285188
H	0.120926	-5.562037	0.245902
C	-0.268718	-3.850230	1.480438
H	0.120532	-4.328464	2.373373
C	-1.276943	-1.939928	0.395216
C	-3.267357	-0.362867	0.710903
C	-1.400829	-2.568506	4.018770
H	-2.442072	-2.774071	3.755358
H	-1.396594	-1.966378	4.935370
H	-0.923602	-3.526792	4.254605
C	-2.665721	-2.815861	-2.915063
H	-3.008785	-2.269672	-3.802075
H	-3.539185	-3.033750	-2.293104
H	-2.255048	-3.772027	-3.259595
C	3.971250	0.716692	-0.529930
C	3.788043	-0.710467	-0.608202
C	5.249524	1.243793	-0.839319
H	5.386740	2.317904	-0.787555
C	-4.196961	-1.220981	-0.145052
H	-4.049873	-1.040419	-1.211496
H	-5.237404	-0.973676	0.093547

H	-4.054634	-2.288934	0.051881
C	-0.475795	4.329634	0.787668
H	-1.310040	5.027233	0.952675
H	0.446020	4.921949	0.852364
C	-1.752503	2.414186	1.731107
H	-2.617948	3.068147	1.914246
H	-1.767072	1.652407	2.517539
C	-0.597235	3.707257	-0.594733
H	0.307821	3.128153	-0.803870
H	-0.624306	4.501310	-1.350676
C	-0.396302	-1.764207	-3.058311
H	0.076302	-2.712235	-3.342079
H	0.355459	-1.152434	-2.550816
H	-0.692165	-1.246885	-3.978965
C	-0.650507	-1.836414	2.902129
H	-1.084978	-0.844382	2.786815
C	-1.955798	1.724037	0.352099
C	-1.212665	-2.623619	-0.839415
C	-0.498619	3.267537	1.878984
H	0.380147	2.622184	1.742345
C	-2.030372	2.340793	-2.212791
H	-2.602468	1.408215	-2.184201
C	-1.061320	0.499025	0.196416
C	0.809394	-1.644368	3.326771
H	1.298930	-2.605932	3.521342
H	0.858772	-1.054099	4.249882
H	1.395130	-1.126994	2.560653
C	-0.404856	3.876531	3.271581
H	0.505225	4.479386	3.379681
H	-0.387610	3.099914	4.046157
H	-1.263967	4.529927	3.473359
C	-2.861851	3.347115	-3.007708
H	-2.372579	4.329380	-3.040662
H	-3.854417	3.485529	-2.562151
H	-3.002296	3.014438	-4.043692
C	-0.741769	2.021998	-2.967988
H	-0.980802	1.582378	-3.944190
H	-0.129283	1.299070	-2.421214
H	-0.139101	2.918618	-3.151854
C	-1.839221	2.825673	-0.749823
H	-2.693310	3.485275	-0.538675

Table S21. Cartesian coordinates of the optimized ^{3}LLCT($\pi\pi^*$) (ortho) geometry of **CZT1.**

atom	x	y	z
Zn	0.906627	0.205751	0.210753
S	2.439308	-1.042316	-1.089169
S	2.764457	1.445142	1.097723
N	-1.818042	-0.547940	0.875461
C	-3.307544	1.077995	0.135734
H	-3.990548	1.841530	0.518185
H	-3.710980	0.744643	-0.823222
C	5.000518	-0.485795	-1.684753
H	4.889642	-1.291323	-2.401647
C	6.191670	0.172270	-1.566031
H	7.032102	-0.112332	-2.189965
C	-0.726774	-2.065033	2.492767
C	-3.526427	0.259992	2.529956
H	-3.479003	-0.614028	3.184145
H	-4.541439	0.667547	2.595975
H	-2.836852	1.014234	2.912848
C	6.334789	1.226142	-0.632041
H	7.283506	1.744502	-0.544254
C	-0.843158	-4.133513	0.623616
H	-0.871291	-4.940345	-0.101344
C	-1.859486	-2.701384	-1.145707
H	-2.272633	-1.696737	-1.224403
C	-0.311706	-4.372993	1.878378
H	0.063546	-5.358840	2.135928
C	-0.250110	-3.341019	2.796044
H	0.184656	-3.527668	3.772527
C	-1.307948	-1.835067	1.224493
C	-3.225240	-0.129571	1.078300
C	-1.332343	-1.327021	4.838833
H	-2.382898	-1.561495	4.644416
H	-1.297420	-0.480879	5.535721
H	-0.890147	-2.191274	5.348096
C	-2.964986	-3.702119	-1.492562
H	-3.400453	-3.459770	-2.469507
H	-3.770488	-3.696276	-0.751780
H	-2.576168	-4.725154	-1.553834
C	4.025526	0.928924	0.069585
C	3.880927	-0.146401	-0.880343
C	5.280745	1.589923	0.155547

C	-1.722256	2.222382	-1.490293
H	-2.551604	2.940887	-1.556371

Table S22. Cartesian coordinates of the optimized ^{3}LLCT($\pi\pi^*$) (tilted) geometry of **CZT1.**

atom	x	y	z
Zn	0.878205	0.285312	0.150457
S	2.313197	-1.352819	-0.807655
S	2.786200	1.581661	0.681530
N	-1.851329	-0.645390	0.452339
C	-3.323616	1.148853	0.282660
H	-4.021274	1.729388	0.892423
H	-3.695339	1.187019	-0.743761
C	4.885612	-1.104593	-1.536193
H	4.719550	-2.055316	-2.029672
C	6.108577	-0.501997	-1.589178
H	6.924180	-0.972780	-2.127347
C	-0.790187	-2.584424	1.560893
C	-3.636342	-0.467624	2.212382
H	-3.599556	-1.516475	2.516355
H	-4.660615	-0.112910	2.372138
H	-2.978028	0.105229	2.867909
C	6.315631	0.739717	-0.942432
H	7.289728	1.214675	-0.988737
C	-0.814938	-3.972359	-0.859999
H	-0.807447	-4.514356	-1.799987
C	-1.787091	-2.063057	-2.135038
H	-2.188499	-1.075052	-1.914475
C	-0.323017	-4.587408	0.277037
H	0.056845	-5.603520	0.230470
C	-0.305758	-3.889727	1.470687
H	0.098888	-4.368436	2.356417
C	-1.331316	-1.974553	0.405422
C	-3.269917	-0.316497	0.732053
C	-1.486573	-2.616159	3.997898
H	-2.525825	-2.784985	3.702741
H	-1.488721	-2.027364	4.923205
H	-1.046866	-3.592941	4.231035
C	-2.889126	-2.892869	-2.799500
H	-3.288716	-2.361677	-3.671884
H	-3.719637	-3.095493	-2.116755
H	-2.505280	-3.857267	-3.152045

H	5.383579	2.398099	0.870660
C	-4.238190	-1.203512	0.687955
H	-4.179724	-1.458560	-0.371214
H	-5.249799	-0.830752	0.883120
H	-4.102232	-2.117945	1.275490
C	-0.347014	4.179160	-0.632605
H	-1.171794	4.892079	-0.779844
H	0.583865	4.741225	-0.782673
C	-1.665346	2.787175	0.959847
H	-2.528597	3.463777	0.873945
H	-1.687052	2.385805	1.977265
C	-0.453939	3.062792	-1.658990
H	0.437743	2.427583	-1.591956
H	-0.439919	3.493684	-2.666951
C	-0.729700	-2.796451	-2.172128
H	-0.251252	-3.783068	-2.153770
H	0.037429	-2.041509	-1.981749
H	-1.119359	-2.631254	-3.183851
C	-0.566050	-0.990436	3.555537
H	-0.963633	-0.059830	3.152621
C	-1.872984	1.624878	-0.053601
C	-1.337286	-2.878893	0.270768
C	-0.409495	3.632896	0.786451
H	0.467397	2.991212	0.934068
C	-1.931905	1.214640	-2.657442
H	-2.378618	0.308194	-2.238620
C	-1.014220	0.401928	0.251874
C	0.905962	-0.744266	3.901376
H	1.357969	-1.620965	4.380055
H	0.992476	0.094980	4.602327
H	1.504879	-0.502440	3.017316
C	-0.344526	4.740857	1.829276
H	0.568352	5.338586	1.715167
H	-0.352625	4.331647	2.847166
H	-1.202283	5.420198	1.736001
C	-2.919465	1.778008	-3.678489
H	-2.545764	2.716230	-4.110241
H	-3.892763	1.989824	-3.219327
H	-3.082954	1.075683	-4.505504
C	-0.661994	0.758815	-3.374752
H	-0.910572	-0.019581	-4.106298
H	0.069424	0.334705	-2.681742
H	-0.181030	1.577697	-3.921375

C	4.005774	0.753950	-0.186295
C	3.795793	-0.513783	-0.838453
C	5.294640	1.343040	-0.264098
H	5.452494	2.296061	0.227682
C	-4.255304	-1.172592	-0.058941
H	-4.147065	-1.034393	-1.135848
H	-5.277484	-0.885166	0.210938
H	-4.137831	-2.236943	0.171261
C	-0.333889	4.286231	0.729700
H	-1.147863	5.021117	0.815528
H	0.605673	4.847645	0.812060
C	-1.725555	2.466146	1.701852
H	-2.576724	3.155050	1.807223
H	-1.803493	1.749094	2.524693
C	-0.410092	3.598321	-0.624559
H	0.485385	2.980529	-0.758743
H	-0.373170	4.354335	-1.417898
C	-0.628793	-1.863138	-3.114107
H	-0.185151	-2.821098	-3.411418
H	0.161426	-1.249827	-2.672863
H	-0.982912	-1.361887	-4.023241
C	-0.681634	-1.894288	2.912039
H	-1.075769	-0.884822	2.802556
C	-1.886045	1.715162	0.350952
C	-1.313059	-2.670754	-0.824747
C	-0.452835	3.285643	1.871380
H	0.404768	2.603133	1.816919
C	-1.829612	2.192287	-2.239753
H	-2.292664	1.204066	-2.163521
C	-1.026838	0.458041	0.271145
C	0.772227	-1.767056	3.379376
H	1.218630	-2.749008	3.574922
H	0.817931	-1.192041	4.312176
H	1.400834	-1.259157	2.641872
C	-0.408783	3.965996	3.233004
H	0.516726	4.541605	3.357908
H	-0.461037	3.232797	4.047274
H	-1.251774	4.659315	3.353385
C	-2.774160	3.071233	-3.058716
H	-2.386257	4.095283	-3.141484
H	-3.766795	3.130143	-2.595988
H	-2.900117	2.681880	-4.076746
C	-0.528690	1.983606	-3.015361

H	-0.747488	1.504915	-3.977750
H	0.170174	1.333406	-2.480123
H	-0.019881	2.929915	-3.230057
C	-1.676916	2.756344	-0.796661
H	-2.509249	3.460535	-0.655743

Table S23. Cartesian coordinates of the optimized ^{3}LLCT($\pi\pi^*$) (planar) geometry of **CZT1.**

atom	x	y	z
Zn	0.842202	0.391835	-0.012883
S	2.279456	-1.476352	-0.351336
S	2.696519	1.830113	-0.166293
N	-1.832910	-0.627047	0.422900
C	-3.377153	1.122133	0.354129
H	-4.037285	1.648889	1.048530
H	-3.829599	1.212931	-0.635164
C	4.912774	-1.514837	-0.862156
H	4.766400	-2.587081	-0.925582
C	6.150155	-0.972896	-1.050280
H	6.998782	-1.612957	-1.265488
C	-0.737530	-2.542051	1.527967
C	-3.628223	-0.614242	2.180524
H	-3.516189	-1.670745	2.436615
H	-4.677228	-0.343359	2.344030
H	-3.019890	-0.022945	2.868318
C	6.327670	0.428434	-0.964901
H	7.313166	0.856029	-1.115466
C	-0.732980	-3.927861	-0.895148
H	-0.706686	-4.466725	-1.836677
C	-1.653982	-1.996006	-2.182209
H	-2.071586	-1.013969	-1.962171
C	-0.261604	-4.545760	0.249422
H	0.116679	-5.562654	0.206869
C	-0.251992	-3.847392	1.443110
H	0.150755	-4.323821	2.331033
C	-1.277282	-1.939658	0.369505
C	-3.262038	-0.364180	0.714996
C	-1.333207	-2.560995	3.998693
H	-2.378098	-2.773677	3.756072
H	-1.315125	-1.955041	4.912613
H	-0.845892	-3.515409	4.229605
C	-2.714956	-2.818071	-2.918002
H	-3.071026	-2.272327	-3.800147

H	-3.579099	-3.034824	-2.282746
H	-2.310158	-3.774820	-3.267927
C	3.961333	0.724776	-0.494813
C	3.778923	-0.702234	-0.578632
C	5.265876	1.245164	-0.695557
H	5.404337	2.318420	-0.632389
C	-4.206725	-1.209760	-0.136755
H	-4.074712	-1.017421	-1.203256
H	-5.242961	-0.962972	0.119943
H	-4.064071	-2.280283	0.045644
C	-0.443286	4.317211	0.744356
H	-1.265010	5.026230	0.922949
H	0.487048	4.898134	0.787171
C	-1.722586	2.420958	1.722286
H	-2.578429	3.084761	1.914849
H	-1.731651	1.663562	2.513405
C	-0.601673	3.691395	-0.633048
H	0.291955	3.101249	-0.861119
H	-0.636797	4.482923	-1.391204
C	-0.447228	-1.766596	-3.095405
H	0.026532	-2.713857	-3.379981
H	0.306265	-1.146786	-2.600452
H	-0.757932	-1.255970	-4.014947
C	-0.608695	-1.828701	2.865255
H	-1.049109	-0.838833	2.755736
C	-1.953074	1.724692	0.351742
C	-1.230948	-2.625857	-0.864532
C	-0.457155	3.260855	1.841726
H	0.409734	2.602396	1.691197
C	-2.089607	2.336190	-2.213727
H	-2.657364	1.401701	-2.167918
C	-1.057368	0.499931	0.189637
C	0.858180	-1.627460	3.259774
H	1.360527	-2.585956	3.436525
H	0.922571	-1.042720	4.185546
H	1.418881	-1.097954	2.483616
C	-0.327586	3.875812	3.228720
H	0.591859	4.467954	3.315029
H	-0.303797	3.102838	4.006767
H	-1.174286	4.540769	3.444810
C	-2.949537	3.340815	-2.980088
H	-2.463856	4.324338	-3.027324
H	-3.927384	3.476389	-2.502260

H	-3.122789	3.009191	-4.011435
C	-0.826221	2.021767	-3.012457
H	-1.098168	1.590566	-3.983863
H	-0.197398	1.294217	-2.491419
H	-0.228703	2.919201	-3.209162
C	-1.854728	2.821555	-0.756519
H	-2.696886	3.489416	-0.524654

Table S24. Cartesian coordinates of the optimized ^{1}LLCT($n\pi^*$) geometry of **CZT1.**

atom	x	y	z
Zn	-0.225399	3.792147	0.678535
S	-1.502664	5.811585	0.971328
S	-0.914185	3.829200	2.984046
N	0.515098	3.078234	-2.008071
C	1.105922	0.823096	-2.124148
H	2.008901	0.224510	-2.269419
H	0.269148	0.215862	-2.474570
C	-0.296349	7.755569	2.589947
H	-0.531114	8.499946	1.835784
C	0.366636	8.115689	3.758694
H	0.651691	9.150991	3.915782
C	0.911271	5.494901	-2.331494
C	2.598095	2.500093	-3.291889
H	2.631491	3.434728	-3.856042
H	3.034896	1.717443	-3.921872
H	3.227022	2.604405	-2.404942
C	0.660435	7.158930	4.724345
H	1.174437	7.447668	5.635520
C	-1.718762	5.797835	-3.218535
H	-2.744769	5.930182	-3.545659
C	-2.314171	3.415140	-2.784637
H	-1.800494	2.497164	-2.501561
C	-0.867044	6.888113	-3.211265
H	-1.219235	7.860544	-3.541789
C	0.430036	6.733032	-2.758166
H	1.084581	7.597747	-2.724411
C	0.054740	4.373779	-2.400183
C	1.157880	2.119042	-2.942502
C	3.374517	5.897002	-2.796988
H	3.291031	5.354717	-3.742939
H	4.384100	5.733604	-2.401225
H	3.278972	6.965927	-3.020148

C	-2.971284	3.192858	-4.149482
H	-3.612709	2.303890	-4.119218
H	-2.230251	3.049053	-4.941764
H	-3.603301	4.041842	-4.434416
C	-0.370084	5.470709	3.368683
C	-0.662838	6.429304	2.400950
C	0.294135	5.830324	4.533929
H	0.516260	5.082378	5.288349
C	0.390190	1.976088	-4.254232
H	-0.626780	1.613635	-4.092336
H	0.903917	1.250888	-4.894898
H	0.340650	2.925649	-4.797796
C	1.442066	0.179333	2.165659
H	1.925201	-0.784801	1.949168
H	1.396280	0.268943	3.258545
C	2.295385	1.198727	0.059677
H	2.798744	0.257057	-0.202904
H	2.907856	2.004743	-0.358101
C	0.036829	0.186049	1.584240
H	-0.492026	1.079230	1.934092
H	-0.525688	-0.666045	1.984196
C	-3.390644	3.667310	-1.725171
H	-3.957200	4.581274	-1.939317
H	-2.954071	3.765416	-0.726386
H	-4.099730	2.831429	-1.699034
C	2.325659	5.451315	-1.773109
H	2.539724	4.423034	-1.484242
C	0.905793	1.203151	-0.637859
C	-1.288519	4.537687	-2.807238
C	2.290157	1.300570	1.580835
H	1.826050	2.252905	1.869476
C	-1.411867	-0.063651	-0.511587
H	-1.430246	0.360993	-1.520082
C	0.329323	2.613199	-0.726986
C	2.465847	6.313217	-0.513127
H	2.324154	7.376724	-0.738431
H	3.470400	6.196334	-0.088635
H	1.739461	6.039412	0.258270
C	3.707768	1.297153	2.137264
H	3.703184	1.382610	3.230868
H	4.295122	2.133042	1.737481
H	4.230590	0.367267	1.877280
C	-1.752752	-1.547327	-0.648532

H	-1.707047	-2.055492	0.323611
H	-1.054228	-2.057456	-1.322768
H	-2.765771	-1.686493	-1.045825
C	-2.516292	0.648382	0.266810
H	-3.470282	0.545222	-0.264424
H	-2.311829	1.717469	0.369365
H	-2.653145	0.224923	1.268124
C	0.024391	0.112179	0.055225
H	0.556554	-0.818084	-0.189250

Table S25. Cartesian coordinates of the optimized ^{3}LLCT($n\pi^*$) geometry of **CZT1.**

atom	x	y	z
Zn	-0.225399	3.792147	0.678535
S	-1.502664	5.811585	0.971328
S	-0.914185	3.829200	2.984046
N	0.515098	3.078234	-2.008071
C	1.105922	0.823096	-2.124148
H	2.008901	0.224510	-2.269419
H	0.269148	0.215862	-2.474570
C	-0.296349	7.755569	2.589947
H	-0.531114	8.499946	1.835784
C	0.366636	8.115689	3.758694
H	0.651691	9.150991	3.915782
C	0.911271	5.494901	-2.331494
C	2.598095	2.500093	-3.291889
H	2.631491	3.434728	-3.856042
H	3.034896	1.717443	-3.921872
H	3.227022	2.604405	-2.404942
C	0.660435	7.158930	4.724345
H	1.174437	7.447668	5.635520
C	-1.718762	5.797835	-3.218535
H	-2.744769	5.930182	-3.545659
C	-2.314171	3.415140	-2.784637
H	-1.800494	2.497164	-2.501561
C	-0.867044	6.888113	-3.211265
H	-1.219235	7.860544	-3.541789
C	0.430036	6.733032	-2.758166
H	1.084581	7.597747	-2.724411
C	0.054740	4.373779	-2.400183
C	1.157880	2.119042	-2.942502
C	3.374517	5.897002	-2.796988
H	3.291031	5.354717	-3.742939

H	4.384100	5.733604	-2.401225
H	3.278972	6.965927	-3.020148
C	-2.971284	3.192858	-4.149482
H	-3.612709	2.303890	-4.119218
H	-2.230251	3.049053	-4.941764
H	-3.603301	4.041842	-4.434416
C	-0.370084	5.470709	3.368683
C	-0.662838	6.429304	2.400950
C	0.294135	5.830324	4.533929
H	0.516260	5.082378	5.288349
C	0.390190	1.976088	-4.254232
H	-0.626780	1.613635	-4.092336
H	0.903917	1.250888	-4.894898
H	0.340650	2.925649	-4.797796
C	1.442066	0.179333	2.165659
H	1.925201	-0.784801	1.949168
H	1.396280	0.268943	3.258545
C	2.295385	1.198727	0.059677
H	2.798744	0.257057	-0.202904
H	2.907856	2.004743	-0.358101
C	0.036829	0.186049	1.584240
H	-0.492026	1.079230	1.934092
H	-0.525688	-0.666045	1.984196
C	-3.390644	3.667310	-1.725171
H	-3.957200	4.581274	-1.939317
H	-2.954071	3.765416	-0.726386
H	-4.099730	2.831429	-1.699034
C	2.325659	5.451315	-1.773109
H	2.539724	4.423034	-1.484242
C	0.905793	1.203151	-0.637859
C	-1.288519	4.537687	-2.807238
C	2.290157	1.300570	1.580835
H	1.826050	2.252905	1.869476
C	-1.411867	-0.063651	-0.511587
H	-1.430246	0.360993	-1.520082
C	0.329323	2.613199	-0.726986
C	2.465847	6.313217	-0.513127
H	2.324154	7.376724	-0.738431
H	3.470400	6.196334	-0.088635
H	1.739461	6.039412	0.258270
C	3.707768	1.297153	2.137264
H	3.703184	1.382610	3.230868
H	4.295122	2.133042	1.737481

H	4.230590	0.367267	1.877280
C	-1.752752	-1.547327	-0.648532
H	-1.707047	-2.055492	0.323611
H	-1.054228	-2.057456	-1.322768
H	-2.765771	-1.686493	-1.045825
C	-2.516292	0.648382	0.266810
H	-3.470282	0.545222	-0.264424
H	-2.311829	1.717469	0.369365
H	-2.653145	0.224923	1.268124
C	0.024391	0.112179	0.055225
H	0.556554	-0.818084	-0.189250

8 References:

[1] W. L. F. Armarego, *Purification of laboratory Chemicals*, Butterworth Heinemann, Oxford; Boston, **1996**.

[2] R. Jazzar, J. Bourg, R. D. Dewhurst, B. Donnadieu, G. Bertrand, *J. Org. Chem.* **2007**, *72*, 9, 3492–3499.

[3] M. Deng, N. F. M. Mukhtar, N. D. Schley, G. Ung, *Angew. Chem., Int. Ed.* **2020**, *59*, 1228.

[4] M. J. Frisch, G. W. Trucks, H. B. Schlegel, G. E. Scuseria, M. A. Robb, J. R. Cheeseman, G. Scalmani, V. Barone, G. A. Petersson, H. Nakatsuji, et al., Gaussian 16, revision A.03; Gaussian Inc.: Wallingford CT, 2016.

[5] E. Cancès, B. Mennucc, J. Tomasi, *J. Chem. Phys.* **1997**, 107, 3032

[6] B. Mennucci, E. Cancès, J. Tomasi, *J. Phys.* Chem. B **1997**, 101, 10506

[7] C. Lee, W. Yang, R. G. Parr, *Phys. Rev. B* **1988**, 37, 785–789

[8] A. D. Becke, *J. Chem. Phys.* **1993**, 98, 1372–1377

[9] A. Schäfer, H. Horn, R. Ahlrichs, *J. Chem. Phys.* **1992**, 97, 2571–2577

[10] D. Figgen, G. Rauhut, M. Dolg, H. Stoll, *Data. Chem. Phys.* **2005**, 311, 227–244

[11] S. Grimme, M. Waletzke, *J. Chem. Phys.* **1999**, 111, 5645–5655

[12] C. M. Marian, A. Heil, M. Kleinschmidt, *Wiley Interdiscip. Rev.: Comput. Mol. Sci.* **2019**, 9, e1394

[13] A. Heil, M. Kleinschmidt, C. M. Marian *J. Chem. Phys.* **2018**, 149, 164106

[14] R. Ahlrichs, M. Bär, M. Häser, H. Horn, C. Kölmel, *Chem. Phys. Lett.* **1989**, 162, 165–169

[15] TURBOMOLE V6.6 2014, a development of University of Karlsruhe and Forschungszentrum Karlsruhe GmbH, 1989–2007, TURBOMOLE GmbH, since 2007; available from http://www.turbomole.com

[16] M. Kleinschmidt, J. Tatchen, C. M. Marian, J. Comput. Chem. **2002**, 23, 824–833

[17] M. Kleinschmidt, C. M. Marian, *Chem. Phys.* **2005**, 311, 71–79

[18] B. A. Heß, C. M. Marian, U. Wahlgren, O. Gropen, O *Chem. Phys. Lett.* **1996**, 251, 365– 371

[19] AMFI is an atomic spin-orbit integral program written by B. Schimmelpfennig, University of Stockholm, 1996.

[20] M. Kleinschmidt, J. Tatchen, C. M. Marian, *J. Chem. Phys.* **2006**, 124, 124101

[21] M. Etinski, J. Tatchen, C. M. Marian *J. Chem. Phys.* **2011**, 134, 154105

[22] M. Etinski, J. Tatchen, C. M. Marian, *Phys. Chem. Chem. Phys.* **2014**, 16, 4740–4751

[23] P. S. Nejman, B. Morton-Fernandez, N. Black, D. B. Cordes, A. M. Slawin, P. Kilian, J. D.Woollins, *J. Organomet. Chem.* **2015**, *776*, 7–16.

[24] S. I. Etkind, J. Lopez, Y. G. Zhu, J. Fang, W. J. Ong, Y. Shao-Horn, T. M. Swager, *ACS Sustainable Chem. Eng.* **2022**, *10*, 36, 11739–11750.

[25] G. M. Sheldrick, *Acta Crystallogr.* C **2015**, 71, 3-8.

[26] G. M. Sheldrick, *Acta Crystallogr. A* **2015**, *71*, 3-8.

[27] O. V. Dolomanov, L. J. Bourhis, R. J. Gildea, J. A. K. Howard, H. Puschmann, *J. Appl. Crystallogr.* **2009**, *42*, 339.

5.4 Supporting Information for TADF Zn(II) Bicyclic(Alkyl)(Amino)Carbene Thiolate Complexes with Near-Unity Quantum Yield

TADF Zn(II) Bicyclic(Alkyl)(Amino)Carbene Thiolate Complexes with Near-Unity Quantum Yield

Methods and Materials

All operations were performed under an argon atmosphere by using conventional Schlenk-line techniques or glovebox. The solvents were dried using Technology Inc. Pure-Solv system or standard methods[1] and degassed and stored under activated 4Å molecular sieves. Bicyclic (alkyl(amino)carbene precursor (^{Me}bicAAC.HBF$_4$ and ^{tpr}bicAAC.HBF$_4$), Benzene-1,2-dithiol and its disodium salt, [(Zn$_2$(^{Me}bicAAC)$_2$(Cl)$_4$] (**1**) were prepared according to procedure reported in the literature[2,3,4]. All other starting materials were available commercially and were used without further purification. ^{1}H, ^{13}C{^{1}H} APT, ^{1}H-^{13}C HSQC, ^{1}H-^{13}C HSMB, ^{1}H-^{1}H COSY and ^{1}H-^{15}N HMBC were measured at 300 K on Bruker 500 Avance and Bruker 600 Avance spectrometer. The chemical shifts are given in ppm relatively to residual signals of the solvent [^{1}H, ^{13}C: CD_3CN (1.94,118.69 ppm), CD_2Cl_2 (5.32, 53.84 ppm).].

All photophysical measurements were performed under inert atmosphere. Dichloromethane (DCM) used for steady-state absorption spectroscopy was dried and degassed prior to the measurement. The solid-state measurements were performed in powder form where single crystals were ground and dried under high vacuum for 24 h to remove co-crystallised solvent molecules. PMMA and PS and mCP films were prepared by drop casting method with 2 wt-% of complexes dissolved in DCM followed by evaporation of DCM and drying of polymeric films under high vacuum. UV-visible absorption spectroscopy was performed on an Agilent Cary 5000 spectrophotometer using standard 1 cm path length quartz cells. Excitation and emission spectra were recorded on an Edinburgh Instrument FLS1000 spectrometer, equipped with a 450 W Xenon arc lamp, double monochromators for the excitation and emission pathways, and a red-sensitive photomultiplier (PMT-980) as a detector. The excitation and emission spectra were corrected using the standard corrections supplied by the manufacturer for the excitation source's spectral power and the detector's sensitivity. Quantum yields of solid samples and polymeric matrices were measured using an integrating cryosphere (Microstat N2) from Oxford Instruments. The luminescence lifetimes were measured using a µF2 pulsed 60 W Xenon microsecond flashlamp, with a repetition rate of 10 100 Hz and a multichannel scaling (MCS) module or with VPLED (449.6 nm with 37 mW), with 100 ns pulse width and an MCS module, depending on the time range. The emission was collected at a right angle to the excitation source. The low-temperature experiments were performed using a 4 K cryostat (CS204SI-FMX-1SS) from Advanced Research System equipped with a closed cycle water-cooled helium compressor.

Synthetic Procedures

[(Zn(^{tpr}bicAAC)(Cl)$_2$] (**2**)

200 mg of (589 µmol) of ^{tpr}bicAAC was mixed with 1 equiv. of $ZnCl_2$ (589 µmol, 81 mg) and dissolved in 10 mL of THF. The mixture was stirred at room temperature overnight, filtrated through celite pad and concentrated in vacuum to total volume of 2 mL. The gas-phase diffusion of *n*-pentane into this solution afforded white single crystals of product. The crude product was washed with *n*-pentane (5 mL) and dried under vacuum to give 198 mg of white crystals (71 %, 416 µmol).

^{1}H NMR (400 MHz, CD_3CN): δ [ppm] = 7.48 (t, $^3J(^1H,^1H)$ = 7.8 Hz,1H, H^4, $C_6H_3{}^iPr_2$), 7.39 (d, $^3J(^1H,^1H)$ = 4.1 Hz,1H, H^{3,5}, $C_6H_3{}^iPr_2$), 3.29 (sept, $^3J(^1H,^1H)$ = 6.7 Hz,1H, CH^{iPr}), 2.99 (sept, $^3J(^1H,^1H)$ = 6.7 Hz,1H, CH^{iPr}), 2.63 (sept, $^3J(^1H,^1H)$ = 6.7 Hz,1H, CH^{iPr}), 2.34 (m,1H), 2.23 (m, 1H), 1.82-1.71 (m, 3H), 1.59 (m, 2H), 1.40 (d, $^3J(^1H,^1H)$ = 6.9 Hz, 3H),

1.35 (dq, $^3J(^1H,^1H)$ = 6.9 Hz, 6H), 1.30 (d, $^3J(^1H,^1H)$ = 6.9 Hz, 3H), 1.24 (d, $^3J(^1H,^1H)$ = 6.9 Hz, 3H), 1.09 (d, $^3J(^1H,^1H)$ = 6.9 Hz, 3H), 1.02 (m, 6H).

^{13}C NMR (100 MHz, CD_3CN): δ [ppm] = 256.2(s, $C^{carbene}$), 145.8, 145.3, 141.3, 130.8, 126.1, 125.8, 66.1, 56.4, 43.6, 34.4, 32.4, 29.8, 29.3, 28.6, 25.1, 24.9, 24.6, 24.0, 23.4, 22.8, 20.5, 20.1, 16.9.

^{15}N (60 MHz, CD_3CN): δ [ppm]=-138.26 ppm.

[$(Zn_2(^{Me}$bicAAC$)_2$(bdt$)_2$] (**3**)

44 mg of (234 µmol) disodium benzene-1,2-dithiolate (**bdt**) was mixed with 100 mg (111 µmol) of [$(^{Me}$bicAAC$)_2Zn_2Cl_4$] (**1**) in 7 mL of THF and the resulting mixture was stirred overnight at room temperature. After that, the solvents were vacuum-evaporated, and the solid residue was extracted with DCM (3x5 mL) and filtered over celite. The combined organic fractions were concentrated by vacuum evaporation to a final volume of 3 mL and crystallization was induced by gas phase diffusion of n-pentane. The obtained single-crystals were collected, washed with *n*-pentane (2×5 mL) and vacuum dried. Yield: 75 mg (65 %, 72 µmol) of yellow crystalline material. CHNS analysis calcd for $C_{58}H_{74}N_2S_4Zn$: C, 65.03; H, 7.21; N, 2.71. Found: C, 64.7; H, 7.1; N, 2.9.

^{1}H NMR (600 MHz, CD_2Cl_2): δ [ppm]=7.51 (t, $^3J(^1H,^1H)$=7.8 Hz, 2H, H^4, $C_6H_3{}^iPr_2$), 7.42 (m, 4H, $C_6H_4S_2$), 7.34 (d, $^3J(^1H,^1H)$=7.8 Hz, 4H, $H^{3,5}$, $C_6H_3{}^iPr_2$), 6.71 (m, 4H, $C_6H_4S_2$), 2.93 (sept, $^3J(^1H,1H)$=6.7 Hz, 2H, $CH^{(iPr)}$), 2.60 (sept, $^3J(^1H,1H)$=6.7 Hz, 2H, $CH^{(iPr)}$), 2.29 (m, 2H), 2.19 (m, 2H), 1.91 (m, 6H), 1.78 (s, 6H), 1.69 (m, 6H), 1.34 (m, 17H), 1.29 (d, $^3J(^1H,^1H)$=6.7 Hz, 6H), 1.19 (s, 6H), 1.11 (d, $^3J(^1H,^1H)$=6.7 Hz, 6H). ^{13}C NMR (125 MHz, CD_2Cl_2): δ [ppm]=252.6 (s, 2 C, $C^{carbene}$), 144.1, 143.9, 143.8, 140.6, 130.6, 129.9, 125.9, 125.8, 121.8, 66.1, 49.4, 43.9, 37.4, 34.2, 32.8, 30.7, 29.1, 28.5, 28.2, 25.2, 24.9, 24.8, 24.7, 23.9, 22.9, 20.3.

^{15}N (60 MHz, CD_2Cl_2): δ [ppm]=-141.86 ppm.

[(Zn (^{bi}bicAAC)(bdt)] (**4**)

42 mg of (221 µmol) disodium benzene-1,2-dithiolate (**bdt**) was mixed with 100 mg (210 µmol) of [$(Zn(^{bi}$bicAAC$)(Cl)_2$] (**2**) in 7 mL of THF and the resulting mixture was stirred overnight at room temperature. After that, the solvents were vacuum-evaporated, and the solid residue was extracted with DCM (3x5 mL) and filtered over celite. The combined organic fractions were concentrated by vacuum evaporation to a final volume of 3 mL and crystallization was induced by gas phase diffusion of n-pentane. The obtained single-crystals were collected, washed with *n*-pentane (2×5 mL) and vacuum dried. Yield: 98 mg (85 %, 180 µmol) of yellow crystalline material. CHNS analysis calcd for $C_{30}H_{41}NS_2Zn$: C, 66.10; H, 7.58; N, 2.57. Found: C, 65.8; H, 7.4; N, 2.6.

^{1}H NMR (600 MHz, CD_2Cl_2): δ [ppm]=7.52 (t, $^3J(^1H,^1H)$=7.8 Hz, 2H, H^4, $C_6H_3{}^iPr_2$), 7.40 (m, 3H, $C_6H_4S_2$), 7.31 (d, $^3J(^1H,^1H)$=7.8 Hz, 2H, $H^{3,5}$, $C_6H_3{}^iPr_2$), 6.69 (q, $^3J(^1H,^1H)$ = 3.1 Hz, 2H, $C_6H_4S_2$), 3.12 (sept, $^3J(^1H,^1H)$ = 6.7 Hz,1H, $CH^{(iPr)}$), 2.61 (sept, $^3J(^1H,^1H)$ = 6.7 Hz,1H, $CH^{(iPr)}$), 2.47 (m, 1H), 2.29 (m,1H), 1.92-1.81 (m, 3H), 1.69 (m, 1H), 1.59-1.51 (m,1H), 1.34-1.29 (m, 12H), 1.22-1.20 (m, 6H), 1.12 (q, $^3J(^1H,^1H)$ = 7.8 Hz ,6H).

^{13}C NMR (125 MHz, CD_2Cl_2): δ [ppm]=254.1 ($C^{carbene}$), 144.2, 143.9, 143.8, 141.1, 130.6, 129.9, 126.91, 125.7, 121.8, 65.7, 44.3, 34.4, 32.1, 29.9, 28.8, 28.6, 25.5, 24.5, 24.2, 24.1, 20.9, 20.3.

^{15}N (60 MHz, CD_2Cl_2): δ [ppm]=-136 ppm.

NMR Spectra

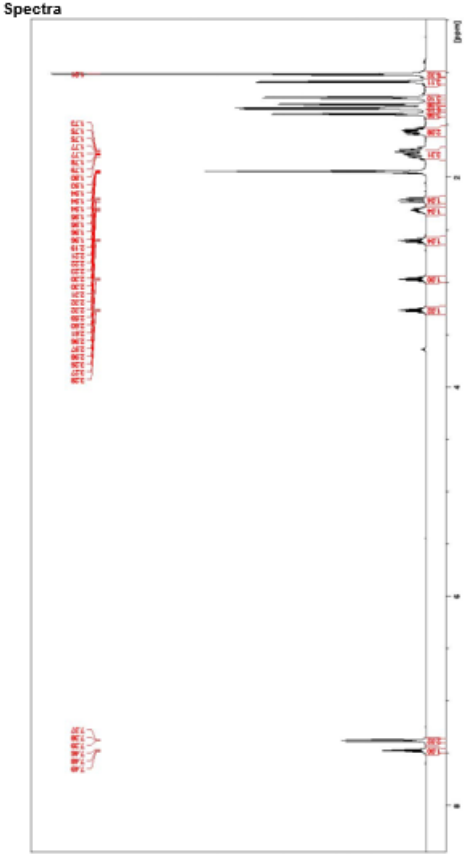


Fig S1. ^{1}H NMR spectrum of **2** in CD_3CN.

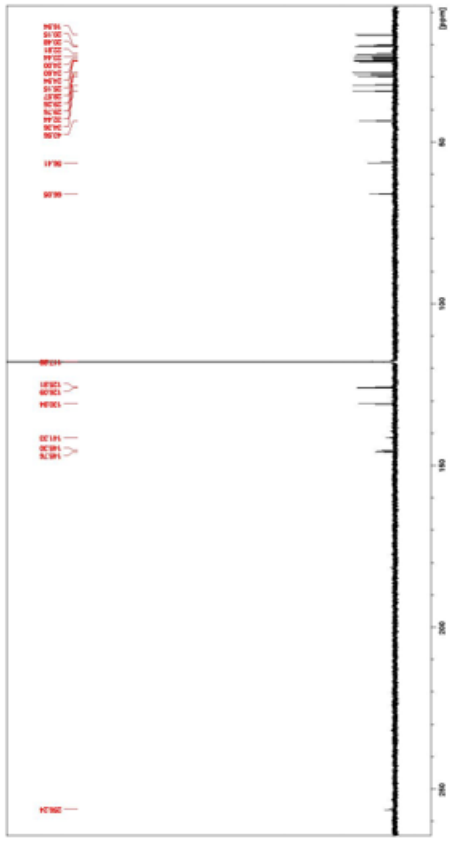


Fig S2. ^{13}C NMR spectrum of **2** in CD_3CN.

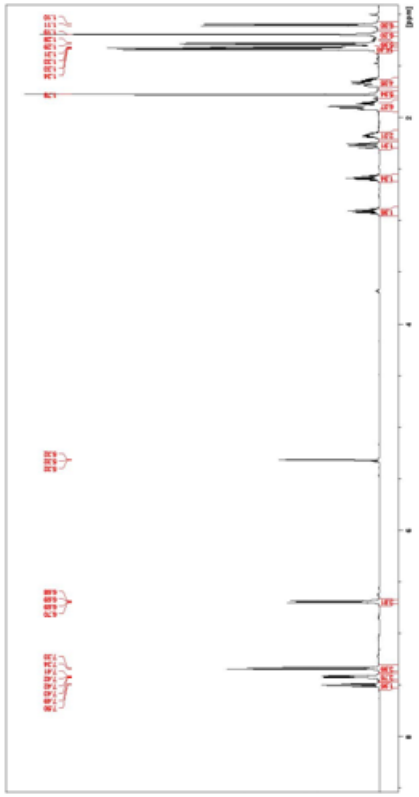


Fig S3. ^{1}H NMR spectrum of 3 in CD_2Cl_2.

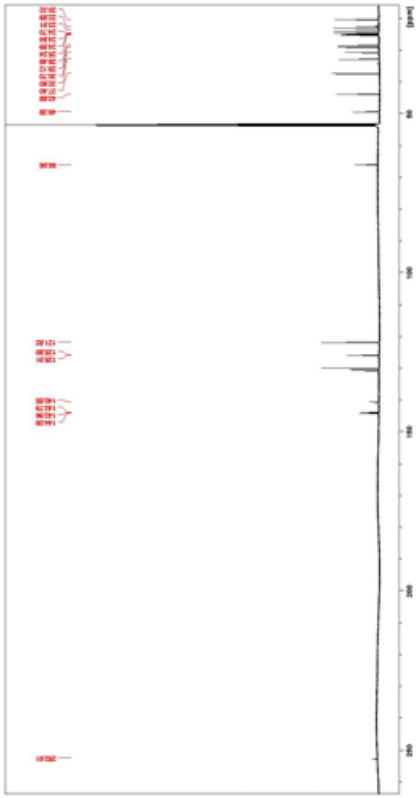


Fig S4. ^{13}C NMR spectrum of 3 in CD_2Cl_2.

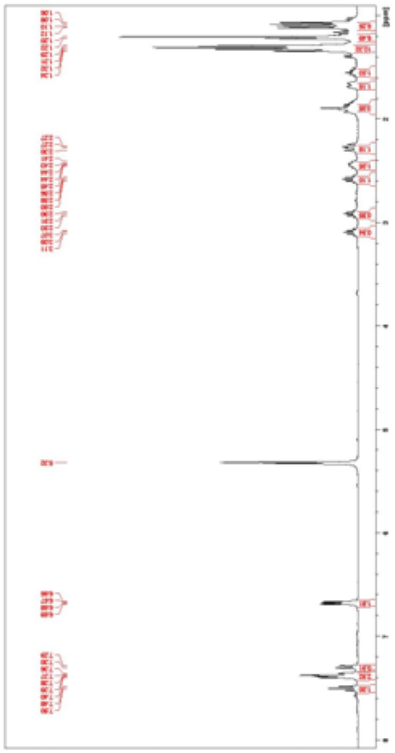


Fig S5. ^{1}H NMR spectrum of **4** in CD_2Cl_2.

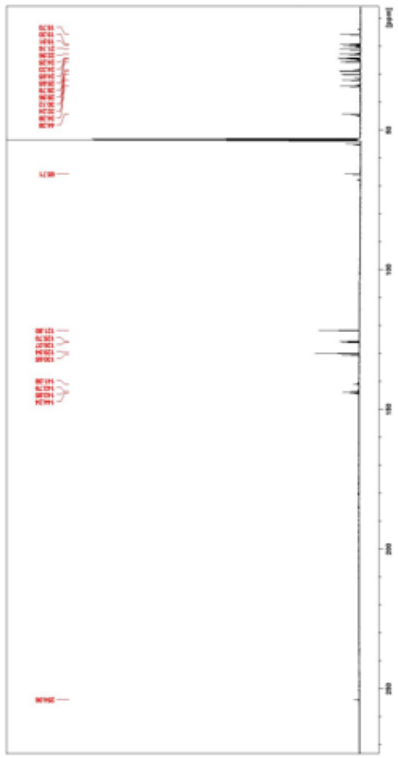


Fig S6. ^{13}C NMR spectrum of **4** in CD_2Cl_2.

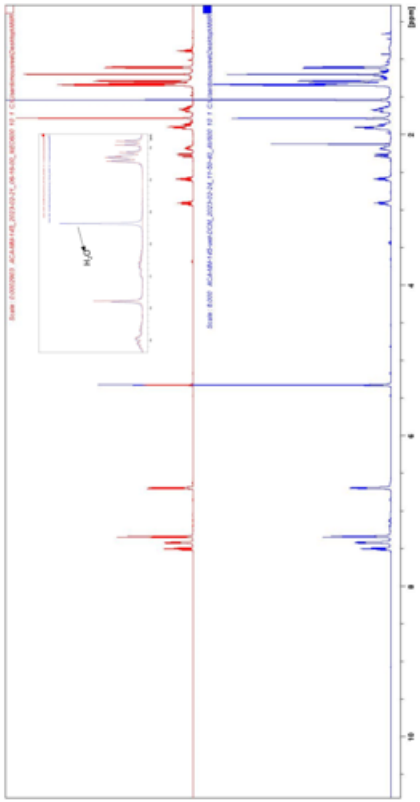


Fig S7. ^{1}H NMR spectra of **3** in wet (blue) and dry/degassed (red) CD_2Cl_2. Spectra, showing no formation of protonated ^{Me}bicAAC or bdt species, were recorded after several hours of dissolution of complex in wet, air-saturated solvent.

Thermogravimetric analysis/differential scanning calorimetry

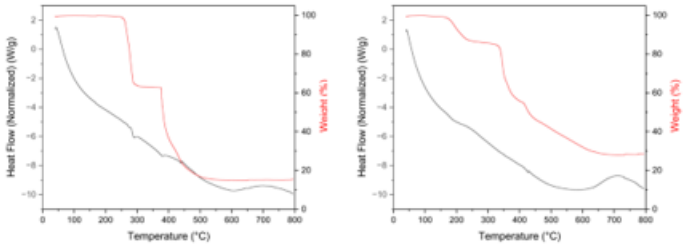


Fig S8. TGA/DSC data for compound 3 (left) and 4 (right) in powder form.

Burried volume

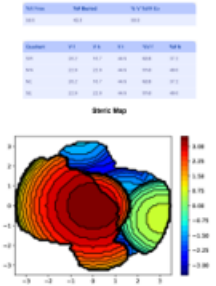


Fig S8. Burried volume of carbene in 3.

V

Photophysical Measurements

Absorption Spectra

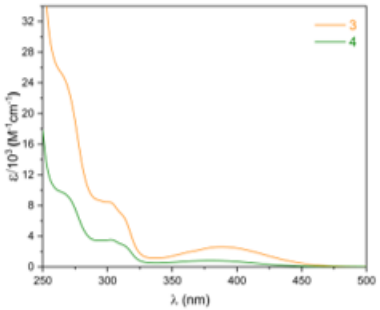


Fig S9. Absorption spectra of **3** and **4** in DCM.

Photophysical data in dichloromethane

Table S1. Photophysical data of **3** and **4** in DCM.

Sample no.	λ_{em}^{max} [nm]	τ [ns]	Φ_{PL}	k_r [s^{-1}]	k_{nr} [s^{-1}]
3	645	160	0.01	6.2×10^{4}	6.2×10^{6}
4	645	105	0.01	9.5×10^{4}	9.4×10^{6}

Emission and excitation spectra

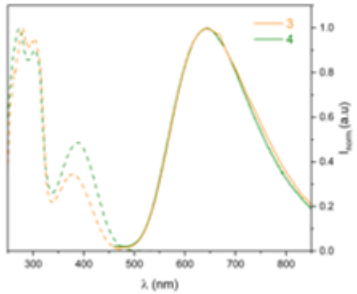


Fig S10. Emission (solid lines) and excitation (dashed lines) spectra of **3** and **4** in DCM.

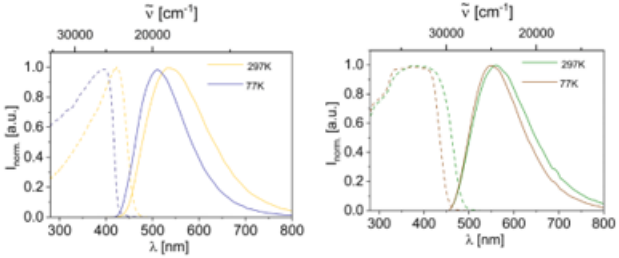


Fig S11. Emission (solid lines) and excitation (dashed lines) spectra of **3** (left) and **4** (right) in powder form at RT and 77K.

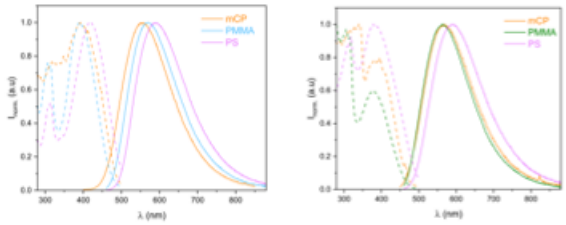


Fig S12. Emission (solid lines) and excitation (dashed lines) spectra of **3** (left) and **4** (right) in different matrices at RT.

Details of lifetime measurements

Table S2. Lifetimes of the decay channels with the significance of their respective contribution to the decay of emission of **3** and **4** in DCM (10-5 M).

Sample no.	τ_1 [µs]	B1	τ_2 [µs]	B2	τ_3 [µs]	B3	[χ^2]	τ_{avg} [µs]
3	0.021	0.09	0.131	0.83	0.595	0.08	1.021	0.160
4	0.089	0.97	0.645	0.03	-	-	1.228	0.105

Table S3. Temperature-dependent lifetimes of the decay channels with the significance of their respective contribution to the decay of emission of **3** in solid state. From 17-137 K a µF2 pulsed 60 W Xenon microsecond flashlamp, and from 147 K to 297 K a 450 nm VPLED and multichannel scaling module, was used to determine the lifetimes.

Temperature [K]	τ_1 [µs]	B1	τ_2 [µs]	B2	τ_3 [µs]	B3	[χ^2]	τ_{avg} [µs]
17	52.9	0.79	284.8	0.18	1236.7	0.03	1.105	130.5
27	111.5	0.73	385.8	0.22	1245.0	0.05	1.157	221.6
37	124.9	0.79	405.9	0.17	1167.5	0.04	1.090	213.5
47	101.8	0.82	319.0	0.15	968.8	0.03	1.190	160.4
57	65.8	0.89	237.6	0.10	602.0	0.01	1.147	88.7
67	43.7	0.93	155.3	0.07	-	-	1.261	51.8
77	30.5	0.96	93.1	0.04	-	-	1.258	34.9
87	22.5	0.99	74.5	0.01	-	-	1.169	23.4
97	11.9	0.88	24.4	0.12	-	-	1.122	13.4
107	9.3	0.92	18.7	0.08	-	-	1.083	10.0
117	7.4	0.92	13.2	0.08	-	-	1.040	7.9

127	6.1	0.96	11.7	0.04	-	-	1.098	6.3
137	5.0	0.96	9.3	0.04	-	-	1.028	5.3
147	4.2	0.87	6.3	0.13	-	-	1.100	4.5
157	3.8	0.98	9.4	0.02	-	-	1.069	3.9
167	3.3	0.96	6.6	0.04	-	-	1.020	3.5
177	2.9	0.96	5.8	0.04	-	-	1.052	3.1
187	2.7	0.98	6.8	0.02	-	-	1.062	2.8
197	2.5	0.97	4.9	0.03	-	-	1.077	2.5
207	2.3	0.98	5.1	0.02	-	-	1.023	2.3
217	2.1	0.98	4.9	0.02	-	-	1.054	2.2
227	1.9	0.97	4.0	0.03	-	-	1.154	2.0
237	1.8	0.99	4.6	0.01	-	-	1.061	1.9
247	1.6	0.90	2.6	0.10	-	-	1.153	1.7
257	1.6	0.99	3.7	0.01	-	-	1.069	1.6
267	1.5	0.99	4.8	0.01	-	-	1.117	1.5
277	1.4	0.99	7.1	0.01	-	-	0.981	1.5
287	0.024	0.04	1.4	0.96	-	-	1.093	1.3
297	1.3	0.99	8.7	0.01	-	-	1.011	1.3

Table S4. Temperature-dependent lifetimes of the decay channels with the significance of their respective contribution to the decay of emission of **4** in solid state. From 17-137 K a µF2 pulsed 60 W Xenon microsecond flashlamp, and from 147 K to 297 K a 450 nm VPLED and multichannel scaling module, was used to determine the lifetimes.

Temperature [K]	τ_1 [µs]	B1	τ_2 [µs]	B2	τ_3 [µs]	B3	$[\chi^2]$	τ_{avg} [µs]
17	381.5	0.25	2472.3	0.72	6923.3	0.03	1.189	2094.5

27								
37	124.9	0.79	405.9	0.17	1167.5	0.04	1.090	213.5
47	101.8	0.82	319.0	0.15	968.8	0.03	1.190	160.4
57	65.8	0.89	237.6	0.10	602.0	0.01	1.147	88.7
67	43.7	0.93	155.3	0.07	-	-	1.261	51.8
77	30.5	0.96	93.1	0.04	-	-	1.258	34.9
87	22.5	0.99	74.5	0.01	-	-	1.169	23.4
97	11.9	0.88	24.4	0.12	-	-	1.122	13.4
107	9.3	0.92	18.7	0.08	-	-	1.083	10.0
117	7.4	0.92	13.2	0.08	-	-	1.040	7.9
127	6.1	0.96	11.7	0.04	-	-	1.098	6.3
137	5.0	0.96	9.3	0.04	-	-	1.028	5.3
147	4.2	0.87	6.3	0.13	-	-	1.100	4.5
157	3.8	0.98	9.4	0.02	-	-	1.069	3.9
167	3.3	0.96	6.6	0.04	-	-	1.020	3.5
177	2.9	0.96	5.8	0.04	-	-	1.052	3.1
187	2.7	0.98	6.8	0.02	-	-	1.062	2.8
197	2.5	0.97	4.9	0.03	-	-	1.077	2.5
207	2.3	0.98	5.1	0.02	-	-	1.023	2.3
217	2.1	0.98	4.9	0.02	-	-	1.054	2.2
227	1.9	0.97	4.0	0.03	-	-	1.154	2.0
237	1.8	0.99	4.6	0.01	-	-	1.061	1.9
247	1.6	0.90	2.6	0.10	-	-	1.153	1.7
257	1.6	0.99	3.7	0.01	-	-	1.069	1.6
267	1.5	0.99	4.8	0.01	-	-	1.117	1.5
277	1.4	0.99	7.1	0.01	-	-	0.981	1.5
287	0.024	0.04	1.4	0.96	-	-	1.093	1.3
297	1.3	0.99	8.7	0.01	-	-	1.011	1.3

Eidesstattliche Versicherung (Affidavit)

Mitra, Mousree

Name, Vorname
(Surname, first name)

231465

Matrikel-Nr.
(Enrolment number)

Belehrung:

Wer vorsätzlich gegen eine die Täuschung über Prüfungsleistungen betreffende Regelung einer Hochschulprüfungsordnung verstößt, handelt ordnungswidrig. Die Ordnungswidrigkeit kann mit einer Geldbuße von bis zu 50.000,00 € geahndet werden. Zuständige Verwaltungsbehörde für die Verfolgung und Ahndung von Ordnungswidrigkeiten ist der Kanzler/die Kanzlerin der Technischen Universität Dortmund. Im Falle eines mehrfachen oder sonstigen schwerwiegenden Täuschungsversuches kann der Prüfling zudem exmatrikuliert werden, § 63 Abs. 5 Hochschulgesetz NRW.

Die Abgabe einer falschen Versicherung an Eides statt ist strafbar.

Wer vorsätzlich eine falsche Versicherung an Eides statt abgibt, kann mit einer Freiheitsstrafe bis zu drei Jahren oder mit Geldstrafe bestraft werden, § 156 StGB. Die fahrlässige Abgabe einer falschen Versicherung an Eides statt kann mit einer Freiheitsstrafe bis zu einem Jahr oder Geldstrafe bestraft werden, § 161 StGB.

Die oben stehende Belehrung habe ich zur Kenntnis genommen:

Official notification:

Any person who intentionally breaches any regulation of university examination regulations relating to deception in examination performance is acting improperly. This offence can be punished with a fine of up to EUR 50,000.00. The competent administrative authority for the pursuit and prosecution of offences of this type is the chancellor of the TU Dortmund University. In the case of multiple or other serious attempts at deception, the candidate can also be unenrolled, Section 63, paragraph 5 of the Universities Act of North Rhine-Westphalia.

The submission of a false affidavit is punishable.

Any person who intentionally submits a false affidavit can be punished with a prison sentence of up to three years or a fine, Section 156 of the Criminal Code. The negligent submission of a false affidavit can be punished with a prison sentence of up to one year or a fine, Section 161 of the Criminal Code.

I have taken note of the above official notification.

Ort, Datum
(Place, date)

Unterschrift
(Signature)

Titel der Dissertation:
(Title of the thesis):

Ich versichere hiermit an Eides statt, dass ich die vorliegende Dissertation mit dem Titel selbstständig und ohne unzulässige fremde Hilfe angefertigt habe. Ich habe keine anderen als die angegebenen Quellen und Hilfsmittel benutzt sowie wörtliche und sinngemäße Zitate kenntlich gemacht.
Die Arbeit hat in gegenwärtiger oder in einer anderen Fassung weder der TU Dortmund noch einer anderen Hochschule im Zusammenhang mit einer staatlichen oder akademischen Prüfung vorgelegen.

I hereby swear that I have completed the present dissertation independently and without inadmissible external support. I have not used any sources or tools other than those indicated and have identified literal and analogous quotations.

The thesis in its current version or another version has not been presented to the TU Dortmund University or another university in connection with a state or academic examination.*

*Please be aware that solely the German version of the affidavit ("Eidesstattliche Versicherung") for the PhD thesis is the official and legally binding version.

Ort, Datum
(Place, date)

Unterschrift
(Signature)

The End